Curso 2010/11
CIENCIAS Y TECNOLOGÍAS/11
I.S.B.N.: 978-84-15287-31-5

TOBÍAS FELIPE GARCÍA

Ondas MHD en la fotosfera y cromosfera de manchas solares

Directores
MANUEL COLLADOS VERA
ELENA KHOMENKO

SERVICIO DE PUBLICACIONES
UNIVERSIDAD DE LA LAGUNA

SOPORTES AUDIOVISUALES E INFORMÁTICOS
Serie Tesis Doctorales

A mis padres

Resumen

En esta tesis estudiamos la propagación de ondas magneto-acústicas en manchas solares, desde debajo de la fotosfera hasta la cromosfera. La motivación de este estudio va más allá de la simple derivación de las propiedades de las oscilaciones, ya que las ondas pueden ser usadas como herramienta de diagnóstico independiente para derivar la estructura de atmósferas estelares, y además tienen un papel relevante en el balance energético de la atmósfera del Sol y otras estrellas.

Como principal novedad, en esta tesis se estudian los diferentes modos de ondas en una situación real, donde la configuración del campo magnético y la estratificación atmosférica se parecen a las de manchas solares. Las propiedades de la atmósfera magnetizada de las manchas solares cambian con la altura, pasando de estar dominada por el gas en la fotosfera, y capas inferiores, a estar dominada por el campo en la alta cromosfera, por lo que el parámetro β del plasma (el cociente de la presión gaseosa con la presión magnética) varía de valores mucho mayores que la unidad a valores mucho más pequeños. La velocidad de propagación de los modos magneto-acústicos depende de la velocidad del sonido y Alfvén, ambas estratificadas con la altura. En la región donde estas dos velocidades características son similares se produce la transformación de modos, permitiendo la conversión de energía acústica de la onda a magnética y viceversa.

La complejidad de la atmósfera solar hace que sea imposible resolver analíticamente las ecuaciones MHD en este caso realista, por lo que hemos abordado este problema mediante simulaciones numéricas. Para este trabajo se ha desarrollado un código MHD paralelizado no lineal en tres dimensiones, al cual le hemos realizado una serie de tests numéricos para verificar su robustez. Las simulaciones excitadas con una fuerza armónica de periodo corto muestran una gran variedad de modos de ondas y transformaciones en un rango de frecuencias por encima de la frecuencia de corte, de tal forma que el modo lento acústico en la región con bajo β puede propagarse hacia alturas cromosféricas y desarrollar choques, mientras el modo rápido magnético en esa región es refractado hacia la fotosfera debido al fuerte gradiente de la velocidad Alfvén. Hemos obtenido medidas cuantitativas del flujo de energía de los diferentes modos de ondas después de la transformación de modos y se ha identificado el modo Alfvén en las regiones con bajo β en aquellas simulaciones en las que la fuerza excitadora está situada en regiones con una cierta inclinación de campo magnetico, aunque la eficiencia de la transformación a este modo Alfvén es muy baja. Las simulaciones numéricas obtenidas utilizando una fuerza excitadora con un espectro similar al solar, con un pico central a la frecuencia correspondiente a los 5 minutos y excitando una banda ancha de frecuencias, reproducen el cambio con la altura observado en el periodo, que varía de 5 minutos en la fotosfera a 3 minutos en la cromosfera. Estas simulaciones confirman que las ondas acústicas con frecuencia inferior a la frecuencia de corte atmosférica (alrededor de 5.7 mHz) no se pueden propagar hacia arriba y forman ondas evanescentes, cuya amplitud aumenta ligeramente con la altura. Por otro lado, la ondas acústicas con frecuencia por encima del valor de corte se propagan hacia arriba y, debido al aumento de su amplitud de acuerdo con la disminución de la densidad, dominan en las alturas cromosféricas, donde encontramos un pico de potencia alrededor de 5.8 mHz correspondiente a las oscilaciones de 3 minutos. De este modo, se puede decir que el mecanismo que produce el cambio de la frecuencia con la altura es la propagación lineal de ondas en la banda de 3 minutos que

son excitadas en la fotosfera y dominan sobre las ondas evanescentes con frecuencia por debajo de la frecuencia de corte. Las simulaciones numéricas en las que la fuerza excitadora está ubicada a distinta distancia radial desde el eje de la mancha muestran que la frecuencia dominante en la cromosfera disminuye con la distancia radial, debido a la reducción de la frecuencia de corte lejos del centro de la mancha. Estas simulaciones muestran que las ondas en la banda de 5 minutos no pueden proporcionar energía a las capas altas de la umbra debido a que forman ondas evanescentes, que no transportan energía, u ondas rápidas magnéticas, que son refractadas hacia la fotosfera. Por el contrario, la energía de las altas frecuencias de la fuerza excitadora puede llegar a capas más altas en forma de ondas acústicas a lo largo de las líneas campo magnético y formar choques, proporcionando energía a la cromosfera.

La segunda parte de esta tesis se centra en un estudio observacional. Hemos analizado espectros de intensidad de Ca II H, incluyendo las líneas superpuestas de Fe I, y espectros polarimétricos de Si I λ 10827 y el multiplete de He I λ 10830. Las distintas líneas espectrales tienen información complementaria sobre diferentes alturas de la atmósfera solar. La región espectral de 10830 Å es especialmente interesante porque contiene la línea fotosférica de Si I y la cromosférica de He I. Mediante el uso de varias líneas espectrales formadas a profundidades intermedias entre el Si I y el He I hemos mejorado el muestreo de la propagación de ondas a través de la atmósfera, cubriendo el vacío de información entre estas dos capas. Del desplazamiento Doppler de estas líneas obtuvimos las variaciones temporales de la velocidad a lo largo de la línea de visión. Tras calcular el espectro de diferencia de fase y de amplificación entre diversos pares de líneas, los resultados han sido ajustados a un modelo de propagación vertical de ondas magneto-acústicas lentas en una atmósfera estratificada con pérdidas radiativas de acuerdo con la ley de enfriamiento de Newton. El modelo funciona para la atmósfera por debajo de la altura de formación del núcleo de la línea de Ca II H, pero no puede reproducir el espectro de amplificación entre el núcleo de Ca II H y la línea de He I. El acuerdo obtenido, con un modelo simple de propagación lineal, en las regiones de la baja y media atmósfera, y el desacuerdo en las capas más altas, indican que la transferencia de energía debida a la formación y disipación de choques ocurre a una altura entre la altura de formación de las líneas de Fe I y el núcleo de Ca II H. Encontramos propagación de ondas de alta frecuencia (por encima de la frecuencia de corte) a lo largo de las líneas de campo hacia capas más altas, correspondiente al modo acústico lento. Las ondas con frecuencia inferior a la de corte forman ondas evanescentes y no se pueden propagar hacia las capas más altas. El espectro de potencias a diferentes alturas no se desplaza gradualmente desde la banda de 5 minutos en la fotosfera hasta frecuencias más altas en capas superiores, hasta alcanzar la banda de 3 minutos en la cromosfera. En su lugar, todas las líneas fotosféricas (formadas a diferentes alturas) presentan su potencia máxima a la misma frecuencia, y lo mismo ocurre para las dos líneas cromosféricas. Por lo tanto, el espectro de potencias muestra un comportamiento discontinuo con la altura, y la frecuencia con máxima potencia cambia abruptamente de 3.5 mHz en la fotosfera a 6 mHz en la cromosfera. Estos resultados están de acuerdo con los obtenidos con las simulaciones, y confirman que el cambio en la frecuencia con la altura es debido al mayor incremento de la amplitud de las ondas que se propagan en comparación con las ondas evanescentes. También hemos podido inferir algunas propiedades de la atmósfera de la mancha solar (temperatura y tiempo de relajación radiativo) mediante el análisis de la propagación de ondas y estimar la altura de formación de las líneas espectrales usadas en este estudio. El análisis muestra que las ondas primero alcanzan la altura de formación de la línea de Si I, luego las líneas de Fe I procedentes de las alas de la línea de Ca II H, a continuación la altura de formación del núcleo de la línea de Ca II H y finalmente la de la línea de He I.

En la última parte de esta tesis, hemos intentado reproducir los resultados observacionales a través de cálculos numéricos. Hemos construido un modelo tridimensional de mancha solar basado en las observaciones, y hemos desarrollado simulaciones numéricas introduciendo como elemento excitador en la fotosfera las fluctuaciones medidas con la línea de Si I. Los resultados son comparados con las oscillaciones obtenidas a diferentes alturas con la línea de He I, el núcleo de la línea de Ca II H y las líneas de Fe I superpuestas en las alas de la línea de Ca II H. Las simulaciones muestran un gran acuerdo con las observaciones. Reproducen los mapas de velocidades y los espectros de potencias a las alturas de formación de las líneas espectrales, así como los espectros de fase y amplificación entre varios pares de líneas. Los choques más fuertes están acompañados de un retraso de la señal cromosférica observada respecto a la simulada a la altura correspondiente, debido a que los choques desplazan la altura de formación de las líneas cromosféricas hacia capas más altas. Hemos demostrado que la propagación de ondas simulada tiene propiedades muy similares a la observada, y esto nos ha permitido utilizar los cálculos numéricos para cuantificar la contribución energética de las ondas acústicas al calentamiento cromosférico en manchas solares. Nuestros resultados indican que la energía suministrada por estas ondas es muy baja para compensar las pérdidas radiativas de la cromosfera. La energía contenida en forma de potencia acústica a la altura de formación de la línea de Si I ya es insuficiente para calentar las capas superiores, mientras que la que alcanza la cromosfera es alrededor de 70 veces inferior a la cantidad de energía requerida.

Abstract

In this thesis we investigate the propagation of magneto-acoustic waves from below the photosphere to the chromosphere of sunspots. The motivation of this work extends beyond the simple derivation of the properties of the oscillations, since waves can be used as an independent diagnostic tool of the structure of stellar atmospheres, having a relevant role in the energy balance of the upper atmosphere of the Sun and stars.

The novelty of the approach used in this thesis consists in the study of the different wave modes in a realistic situation, where the magnetic field configuration and the atmospheric stratification resembles that of solar sunspots. The magnetized atmosphere of sunspots changes from being gas dominated at the photosphere and below to field dominated at the high chromosphere, so the plasma β parameter (the ratio of the gas pressure to the magnetic pressure) varies from values much higher than unity to values much lower than unity. The velocity of propagation of the magneto-acoustic modes depends on the acoustic and Alfvén speeds, both stratified with height. At the height where both characteristic velocities are similar the mode transformation is produced, allowing for the wave energy conversion from acoustic to magnetic and vice versa.

The complexity of the solar atmosphere makes it impossible to solve analytically the MHD equations in this realistic case. For this reason, we have faced this problem using numerical simulations. A parallel 3D nonlinear MHD code, which allows to excite a sunspot-like flux tube and study its oscillations, has been developed. A set of numerical tests has been developed to prove to robustness of the code. Simulations with a short period harmonic driver show a rich variety of wave modes and transformations in a frequency range above the cutoff frequency. The slow acoustic mode in the low-β region can propagate toward chromospheric heights and develop into shocks, while the fast magnetic mode in that region is refracted back toward the photosphere due to the strong gradient of the Alfvén speed. We have obtained quantitative measures of the energy flux of the different wave modes after the mode conversion and we have identified the Alfvén mode in the low-β regions, in those simulations with the driver force located in regions with a certain inclination of the magnetic field, although the efficience of the transformation to this Alfvén mode is very low. The numerical simulations which have been performed with a driving force spectrum resembling the solar one, with a central peak at the frequency corresponding to 5 minutes and exciting a broad band of frequencies, reproduce the observed change in the period of the oscillations with height in sunspots from 5 minutes at the photosphere to 3 minutes at the chromosphere. The simulations show that the acoustic waves with frequency below the cutoff frequency of the atmosphere (around 5.7 mHz) cannot propagate upward and they form evanescent waves, whose amplitude slightly increases with height. On the other hand, those acoustic waves with frequency above the cutoff value propagate upward and, due to the increase of their amplitude according to the drop of the density, dominate at high chromospheric heights, where we find a power peak around 5.8 mHz, corresponding to the 3 minute oscillations. Therefore, the mechanism that produces the change in frequency with height is the linear propagation of waves in the 3 min band which are excited at the photosphere and dominate over the evanescent waves with frequencies below the cutoff frequency. Numerical simulations with the driver located at different radial distances from the axis of the sunspot show that the dominant wave frequency in the chromosphere decreases with the radial

distance, due to the reduction of the cutoff frequency far form the axis. These simulations show that waves in the band of the 5 min cannot supply energy to higher layers of the umbra because these waves either form evanescent waves, which do not carry energy, or fast magnetic waves, which are refracted back toward the photosphere. Instead, a part of the high-frequency driver power can reach higher layers in form of acoustic field-aligned waves that develop into shocks, providing energy to the chromosphere.

In the second, observational, part of this thesis work, we have analyzed co-spatial Ca II H intensity spectra, including its line blends, and polarimetric spectra of the Si I λ 10827 and the He I λ 10830 multiplet. Different spectral lines contain complementary information about different heights of the solar atmosphere. The spectral region of 10830 Å is very interesting because it includes the photospheric Si I and the chromospheric He I lines. We have improved the sampling of the wave propagation through the atmosphere by using more spectral lines formed at intermediate depths between Si I and He I, covering the gap between the layers where these two lines are formed. From the Doppler shifts of these lines we retrieved the temporal variations of the velocity along the line-of-sight. We built the phase difference and amplification spectra and fit them with a model of vertical propagation of slow magneto-acoustic waves in a stratified atmosphere with radiative losses according to Newton's cooling law. The model works at layers below the formation height of the Ca II H core, but it cannot reproduce the amplification spectra between the Ca II H core and the He I lines. The agreement with a simple model of linear wave propagation in the lower and mid parts of the atmosphere, and the disagreement in the very high layers, also indicates that the energy transfer due to shock formation and dissipation occurs at some height between the formation height of the Fe I lines and the Ca II H core. We find upward propagation of field aligned high-frequency waves above the cutoff, corresponding to a slow acoustic mode. Waves with frequency below the cutoff value form evanescent waves and cannot propagate to higher layers. The power spectra at different heights is not gradually shifted from the 5 minute band at the photosphere to higher frequencies at higher layers, until reach the 3 minute band at the chromosphere. Instead, all photospheric lines (formed at different heights) peak at the same frequency, and the same happen to both chromospheric lines. Thus, the power spectra shows a discontinuous behavior with height, and the frequency with maximum power changes abruptly from 3.5 mHz at the photosphere to 6 mHz at the chromosphere. These findings agree with those obtained from the simulations, and confirm that the frequency change with height is due to the larger increase of the amplitude of the propagating waves compared to the evanescent waves. We were also able to infer the properties of the atmosphere (temperature and radiative relaxation time) from the propagation of waves and estimate the formation height of the spectral lines used in this study. The analysis shows that waves first reach the formation height of the Si I line, then the Fe I lines from the wings of the Ca II H line, then the formation height of the Ca II H core, and finally that of the He I line.

In the last part of this thesis, we have attempted to reproduce the observational signatures discussed above through numerical simulations with our 3D MHD code. We have constructed a sunspot model based on the properties of the observed one, and we have developed numerical simulations introducing the fluctuations measured with the Si I line as a driver at the photosphere. The results are compared with the oscillations obtained at different heights from the He I line, the Ca II H core and the Fe I blends at the wings of the

Ca II H line. The simulations show a remarkable agreement with the observations. They reproduce the velocity maps and power spectra at the formation heights of the observed lines, as well as the phase and amplification spectra between several pair of lines. We find that the stronger shocks at the chromosphere are accompanied with a delay between the observed signal and the simulated one at the corresponding height, since the shocks shift the formation height of the chromospheric lines to higher layers. Since we have proven that the simulated wave propagation has the properties of the observed one, we are able to use the numerical calculations to quantify the energy contribution of the acoustic waves to the chromospheric heating in sunspots. Our findings indicate that the energy supplied by these waves is too low to balance the chromospheric radiative losses. The energy contained at the formation height of the lowermost Si I line in the form of acoustic power is already insufficient to heat the higher layers, and the acoustic energy which reaches the chromosphere is around 70 times lower than the required amount of energy.

Index

1

Introduction

The response of a medium to a small perturbation generates an oscillatory movement when its restoring forces try to recover the initial equilibrium. In sunspots, the complex structure of their atmosphere produces a rich variety of wave phenomena with different temporal and spatial scales, for which still does not exist a clear theoretical picture. Wave propagation is affected by the gradients of the thermodynamic magnitudes, as the density or the temperature, while the presence of a magnetic field imposes a spatial order which affects the oscillatory character of the atmosphere.

1.1 Sunspots

Sunspots are one of the most evident manifestation of the magnetic activity in the solar atmosphere. They are observed as dark regions on the photosphere, composed by two distinct parts: a central dark area, called umbra, which is surrounded by the penumbra, formed by light and dark radial filaments. Sunspots are formed by strong concentrations of magnetic flux. The magnetic field inhibits the convection and avoids the heating of the photosphere in these regions, making them to be cooler than the quiet Sun regions around them. The typical life time for most of the sunspots is around some weeks, but the larger ones can last much longer. During this time they move across the surface of the Sun, following the solar rotation. Figure 1.1 shows an image of the sunspot analyzed in this thesis.

The central region, the umbra, is the darkest part of the sunspot. Its diameter is typically between 10 and 20 Mm, about 40% of the total sunspot diameter. The continuum intensity in visible light is around 15% of the photospheric value. The temperature of the umbra is around 3700 K, and the magnetic field is between 2000 and 3000 G, being mostly perpendicular to the surface inside the umbra and becomes slightly inclined near the umbra/penumbra boundary. The darkness of the umbra is not uniform, and in high resolution some bright umbral dots can be visible inside it. Their diameter is around 150 km and their brightness is similar to the photospheric one. Other structures can appear inside the umbra, like light bridges, which consist on a bright band that connects two boundaries of the umbra.

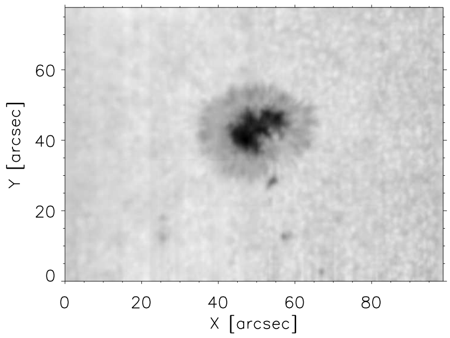

Figure 1.1: Map of the continuum intensity of the sunspot observed on August 28th 2007.

When the sunspot is completely developed, the penumbra appears around the umbra. It is seen in continuum images as alternating light and dark radial filaments (Collados et al. 1988) which are 5 to 7 Mm long and 300 to 400 km in width. The penumbra exhibits an intermediate brightness between the umbra and the quiet Sun photosphere. The continuum intensity of the bright filaments is 95% of the surrounding photosphere, while for the dark filaments is 60%. The strength of the magnetic field is stronger near the umbra, and it decreases at the outer regions of the penumbra. The current accepted model of the penumbral topology is formed by at least two different inclinations of the magnetic field lines which coexist on a small scale. One of the main inclinations corresponds to a component whose magnetic field is inclined abound 50 degrees with respect to the vertical to the solar surface, with a strength around 2000 G. The other component is almost horizontal and weaker (Lites et al. 1993). The Evershed flow (a stream of material emanating radially from sunspots at velocities of up to 6 km s^{-1}) is found to follow the more horizontal magnetic field lines toward deeper layers at the middle penumbra and beyond (Westendorp Plaza et al. 1997; Bellot Rubio et al. 2003).

1.2 Why study wave propagation in sunspots?

Sunspots can be considered as laboratories for studies of magnetized plasma in conditions that are inaccessible on Earth. They give clues about the physics of energy propagation (*e.g.*, in the form of different oscillatory modes) in fluids permeated by strong magnetic fields. The restoring forces associated with the magnetic field allow the generation of new wave modes that are not present in quiet Sun, and they have a large enough spatial coherence length to be observable. The study of waves in sunspots is interesting under several points of view.

Firstly, the analysis of the oscillations measured with several spectral lines may be used to infer the characteristics of the atmosphere which supports them. Spectral lines with different formation heights provide a magnificent sample of the sunspot structure, spanning from the photosphere to the chromosphere, and give information about the stratification of its thermodynamic magnitudes. A slow wave propagating through a plasma dominated by the magnetic field (where the magnetic pressure is much higher than the gas pressure) behaves in a similar way to an acoustic wave. Thus, the difference in the oscillatory signals obtained at these two layers will depend on the geometrical distance between them, the frequency of the wave, and the characteristic propagation speed of this wave. The latter weakly depends on the temperature of the atmosphere, and the analysis of oscillations may be used to retrieve the height difference between both layers.

Secondly, understanding wave propagation in the solar interior makes it possible to infer the structure of the layers they propagate through. Global helioseismology interprets the resonant modes of solar oscillations, and it has retrieved several important results about solar interior. It is complemented by local helioseismology, which uses the full wave field observed at some location of the surface as a probe to determine the properties of solar interior and surface. Local helioseismology uses several different and complementary techniques: ring diagram analysis (Hill 1988), which analyses frequencies of oscillations in small regions on the Sun; and time-distance helioseismology (Duvall et al. 1993) and helioseismic holography (Lindsey & Braun 1990), which derive the sub-surface properties of the atmosphere from the evaluation of the time employed by the waves to travel though the solar interior between two surface locations. One of the most important challenges of local helioseismology is to obtain a complete understanding of how the magnetic fields affect the travel times and the properties of wave propagation, and use them to determine the atmosphere below magnetic structures, like sunspots. For a review in local helioseismology see Gizon & Birch (2005).

Finally, sunspot waves should have its relevant role in the energy balance of the upper solar atmosphere. Semi-empirical models of the solar atmosphere show an increase of the temperature at the chromosphere (Figure 1.2). Acoustic waves have been early suggested as a possible candidate to explain chromospheric heating (Biermann 1948; Schwarzschild 1948). Sunspots are ideal systems to study the energy that is propagated upward in magnetized atmospheres by means of magneto-acoustic waves, and the amount of energy that is supplied at each layer.

1.3 Observations: historical approach and properties

Waves in sunspots are known since more than forty years ago, when Beckers & Tallant (1969) detected what they called "Umbral Flashes". Those observations showed periods of 50 s, in which the brightness suddenly increased, followed by slow decreases and accompanied by Doppler shifts of 6 km s^{-1}. Nowadays, it is known that these observations correspond to chromospheric umbral oscillations. After this first detection, many studies have been carried out in order to understand the physics of these waves from an observational as well as a theoretical point of view. Waves in sunspots are different from those observed in quiet Sun due to the presence of magnetic field. They show a variety of behaviors depending on the height and region of the sunspot where they are observed. From the Doppler shift, the oscillations of the line-of-sight velocity can be inferred, and they are related to the fluctuations in the other thermodynamic magnitudes. These variations are accompanied by oscillations in the intensity and also in the geometrical shift of the layer where the spectral line and the continuum are formed. Taking into account all these features, the analysis of spectral lines with different formation heights makes it possible to study wave propagation.

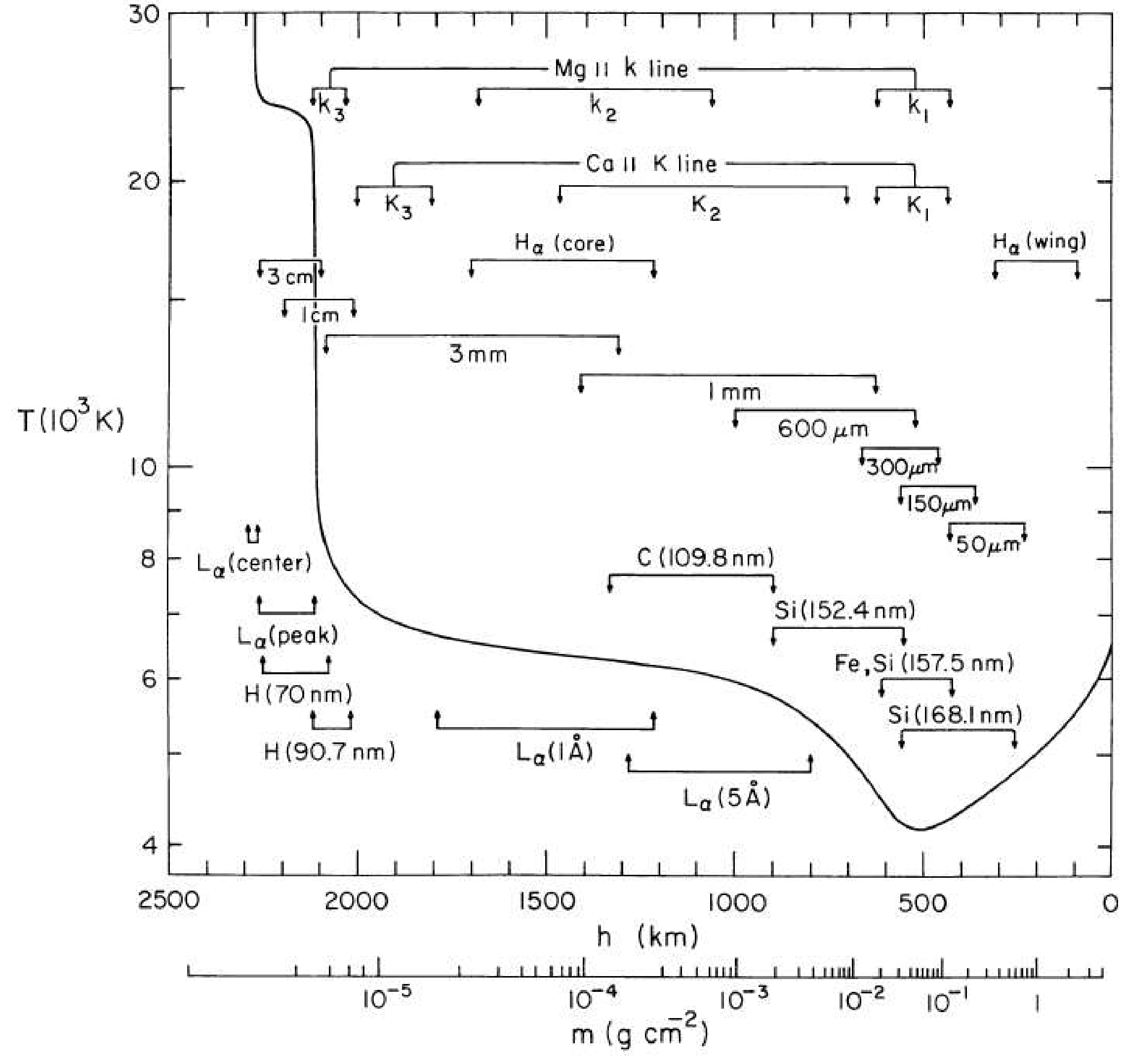

Figure 1.2: Average quiet Sun temperature. The approximate depths where various continua and spectral lines originate are indicated. Extracted from Vernazza et al. (1981).

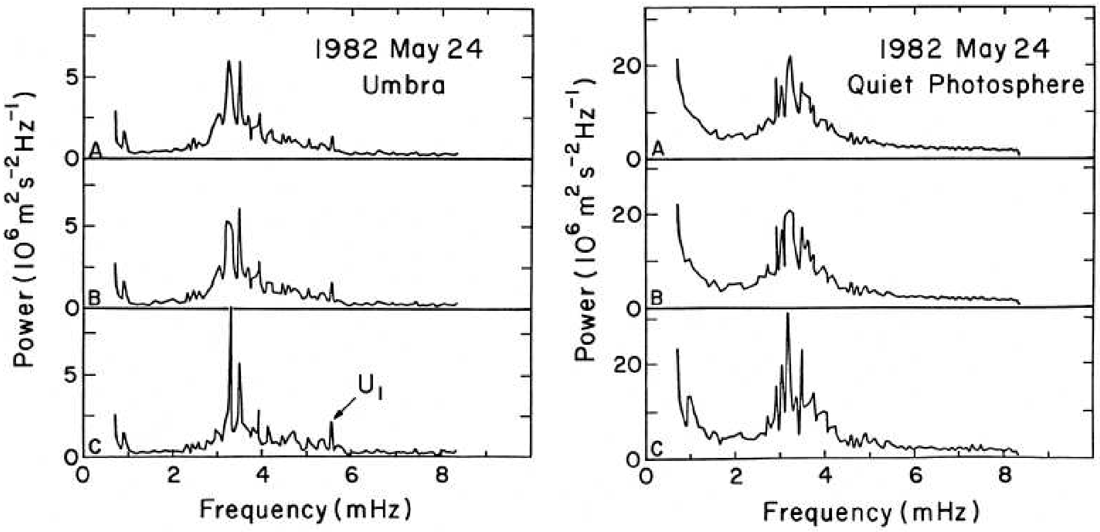

Figure 1.3: Examples of mean power spectra of velocity oscillations measured in Ti I 6304 Å in a sunspot umbra (left panel) and outside the sunspot (right panel). The power spectra A, B, and C refer to averages in successively smaller areas. Extracted from Abdelatif et al. (1986).

Usually, waves in sunspots are classified as photospheric umbral oscillations, chromospheric umbral oscillations and running penumbral waves (Lites 1992). However, all these kind of waves seem to be different manifestations of the same global propagation of magneto-acoustic waves (Maltby et al. 1999, 2001; Brynildsen et al. 2000, 2002; Rouppe van der Voort et al. 2003; Centeno et al. 2006).

At the photosphere, in the umbra, the power spectra of the oscillations is quite similar to the corresponding one of the quiet Sun, with a broad distribution of frequencies and a clear peak at about 3 mHz, corresponding to a period of 5 minutes. Thomas et al. (1982) found that the oscillations in the 5-minute band are composed by a set of individual modes of different period, which they interpret as the response of the sunspot to the 5-minute p-modes in the surrounding quiet Sun atmosphere. Abdelatif et al. (1986) obtained the power spectra of velocity oscillations measured with the Ti I 6304 Å line in an umbra (left panel) and a quiet Sun region around the sunspot (right panel), shown in Figure 1.3. In both regions the power is concentrated in the 5 minute band (3.3 mHz), but the power is significatively lower in the umbra of the sunspot. They concluded that the umbra acts as a filter in transmitting selected frequencies in the power spectrum of 5-minute p-modes of the surrounding quiet atmosphere. Several works have studied this reduction of the oscillations (*e.g.* Brown et al. 1992; Kumar et al. 2000; Balthasar et al. 1996), and several mechanisms have been proposed to explain this power suppression: reduction of wave excitation inside sunspots (Goldreich & Keeley 1977; Goldreich & Kumar 1988, 1990), p-mode absorption inside sunspots (Cally 1995), different heights of spectral line formation due to the Wilson depression, and altering of p-mode eigenfunctions by the magnetic field (Hindman et al. 1997).

Kobanov (1990) studied the spatial characteristics of the oscillations in the sunspot umbra using Fe I λ 5434 Å and Fe I λ 5576 Å spectral lines and found that most of the photospheric umbra is covered by coherent 5 minute oscillations. However, in a later work, Kobanov & Makarchik (2004) detected, using observations in Fe I λ 6569.2 Å, that the spatial coherence of the 5 minute oscillations at the umbra center is lower than 2", and they propagate completely across all the sunspot.

The finite spatial and temporal extent of the wavetrains inside the umbra produces a smooth distribution of the power in the 5-minute band. There are not preferred frequencies for the highest power peaks in the umbra or the penumbra, and the frequency where the power is concentrated varies when the power spectra is calculated using different spatial positions and time intervals, but always inside the 5-minute band. An example of this result is the work by Balthasar & Wiehr (1984). They studied the umbral Doppler oscillations free from scattered light coming from the non-magnetized quiet Sun atmosphere by using the inversion point of the Stokes V profiles of magnetically sensitive lines and also analyzing pure umbral lines as Zr I λ 6127.5 and Ti I λ 6359.9. The periods of the observed waves showed significant variations from 5 minutes and changed with time.

Sunspot waves are usually studied by measuring the fluctuations of intensity and line-of-sight velocity derived from Doppler shift. The development of accurate spectropolarimetric techniques and sophisticated inversion methods also make it possible to measure magnetic field oscillations. From full Stokes inversions of the line profiles of Fe I λ 6301.5 and Fe I λ 6302.5, Lites et al. (1998) found an upper limit of 4 G for the amplitude of 5 minute oscillations in magnetic field strength. Moreover, they considered that their measurement could be overestimated due to instrumental and inversion cross talk between the velocity and magnetic signals. From a theoretical model of sunspot umbra they deduced that the maximum expected magnetic field variations are 0.5 G. Bellot Rubio et al. (2000) detected magnetic field fluctuations with amplitudes around 7-11 G based on inversions of the full Stokes vector of three Fe I lines at 15650 Å. From the analysis of the amplitude of the oscillations and the phase shift between the oscillations in magnetic field strength and line-of-sight velocity they suggest that the obtained magnetic field variations are caused by changes in the opacity which move upward and downward the height where the spectral lines are sensitive to the magnetic field. In a later work, Khomenko et al. (2003) interpreted magnetic field oscillations as due to fast and slow MHD modes. They developed a mathematical formalism based on the analytical solution of the MHD equations to separate intrinsic variations of magnetic field from those due to the shift of line forming region, and, from the comparison of these theoretical results with the observations presented by Bellot Rubio et al. (2000), they found that a part of the detected oscillations in magnetic field strength is due to intrinsic magnetic field fluctuations caused by magnetoacoustic waves.

The chromosphere of sunspots is dominated by 3 minute oscillations. The power spectra usually show sharp peaks around 5-6 mHz, with power gradually dropping to noise values at 8–15 mHz. Several lines have been used to obtain the chromospheric power spectra. One of the first studies is the work by Kneer et al. (1981), who analized the Ca II H, Ca II K, Na I D_1, and Na I D_2 lines obtaining a 160 s period for velocity and intensity chromospheric fluctuations. The oscillations in the Ca II λ 8542 Å infrared triplet, measured by Lites et al. (1982) and Lites (1984), show a sharp peak at a period of around 180 s in both the velocity and intensity signals. Lites (1986) observed the Ca II H and He I λ 10830 Å lines and he retrieved the umbral power spectra of velocity and intensity oscillations shown in Figure 1.4.

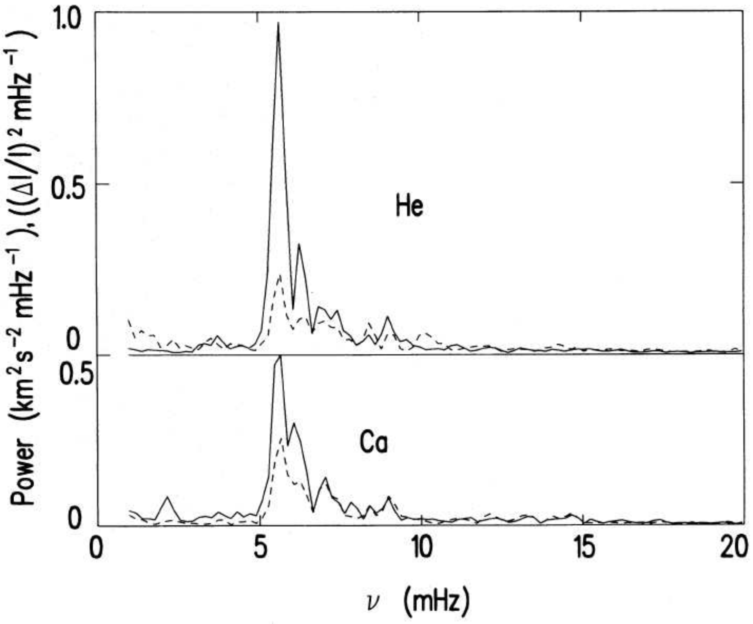

Figure 1.4: Mean power spectra of velocity (solid line) and intensity (dashed line) oscillations measured in He I λ 10830 (top panel) and Ca II H in a sunspot umbra. Extracted from Lites (1986).

The power has a prominent peak at 5.5 mHz, and it decreases for higher frequencies until it reaches noise values at 10 mHz. This pair of chromospheric lines is specially interesting in the context of this thesis, since an analysis of the oscillations measured with these two lines will be presented in Chapter 6. Thomas et al. (1987) also observed them and they found a similar result in the velocity power spectra, with multiple peaks in the 3-minute band and a strong peak at 5.5 mHz, but covering a broad band of frequencies between 4.5 and 10 mHz. Lites (1984, 1986, 1988) and Lites & Thomas (1985) studied the properties of the absortion neutral iron line at 5434.5 Å. Its velocity power spectrum shows two peaks, one in the 3 mHz (5 minute) band and the other in the 5 mHz (3 minute) band, both with similar power. This behavior was explained considering that the contribution function of this line has significant contributions from two different heights, one of them in the photosphere and the other in the chromosphere. The oscillations with 3-minute period come from the higher layer, while probably, most of the contribution to the 5-minute signal comes from the photosphere. Chromospheric umbral oscillations have amplitudes of several kilometers per second, and the velocities measured in chromospheric umbrae show saw-tooth temporal profiles, typical for shock waves (Lites 1986; Centeno et al. 2006).

There have been many attemps to explain the chromospheric 3 minute oscillations. Thomas & Scheuer (1982) proposed a resonant cavity for fast magneto-acoustic waves at photospheric and subphotospheric layers. Alternatively, Zhugzhda et al. (1983) presented a model of a resonant chromospheric cavity for slow mode waves responsible for the multiple peaks in the oscillation power spectrum, including peaks in the 5 mHz band. In Zhugzhda et al. (1985) they discussed the suitability of their model rather than the one by Thomas & Scheuer (1982) to explain chromospheric umbral oscillations. Gurman &

Leibacher (1984) also investigated a resonator for the slow mode waves at chromospheric levels. Recently, Centeno et al. (2006) reproduced the phase spectra between chromospheric and photospheric velocity oscillations with a model of linear vertical propagation of slow magnetoacoustic waves in a stratified magnetized atmosphere that accounts for radiative losses, finding a good agreement between the theoretically computed time delay and that obtained from the cross-correlation of photospheric Si I λ 10827 and chromospheric He I λ 10830 velocity maps, both filtered around the 6 mHz band. From these results they concluded that the chromospheric 3 minute power comes directly from the photosphere by means of linear wave propagation.

Several spectral lines, formed at different heights from the photosphere to the chromosphere, can be used to sample the wave propagation properties. Simultaneous time-series of suited spectral lines are a powerful tool for studying sunspot waves. This analysis gives information about the properties of the different wave modes as they propagate along the atmosphere, the cutoff frequency value, or the amplification and phase delay of the perturbations in their propagation. Using phase difference spectra between the umbral oscillations observed in the photospheric line Fe I λ 5233 Å and in Hα, Giovanelli et al. (1978) found that the phase delay indicates upward wave propagation. Lites (1984) inferred that slow mode waves propagate upward into the chromosphere in the frequency band around 6.5 mHz, based on the phase differences between the oscillations of Ca II λ 8498, Ca II λ 8542 and Fe I λ 5434. From the study of the Doppler shifts observed in the intensity profiles of the He I λ 10830 multiplet, Lites (1986) presented evidence of shock wave formation at the chromosphere. This line, together with the photospheric Si I λ 10827, was used by Centeno et al. (2006) to study the propagation of waves between the photosphere and the chromosphere by the analysis of the phase and amplification spectra. The study presented in Chapter 6 of this thesis is an extention of that work, with more spectral lines formed at intermediate heights between the layers where the Si I and the He I lines are formed.

In the sunspot penumbra, the most characteristic wave phenomenon is running penumbral waves. They are observed as velocity and intensity wavefronts moving out from the inner to the outer edges of the penumbra. The first detection of these waves by Giovanelli (1972) comes from observations in Hα, finding transverse waves that develop in the outer umbra and propagate outwards with a velocity of 20 km s^{-1}. He interpreted them as Alfvén type waves. Just before, Zirin & Stein (1972) also observed running intensity waves in sunspot penumbrae, what they called "running penumbral waves", which appeared to be connected with umbral flashes. From their observations of Hα intensity they inferred for these waves a period of 5 minutes and a constant velocity around 10 km s^{-1}, and considered that they were probably sound waves. Since these first observations, many new works have claimed the detection of running penumbral waves. Figure 1.5(a) shows a velocity map covering the umbra and penumbra of a sunspot. The region above the white line corresponds to the umbra, while the region below is the penumbra. In the penumbra, the wavefront increases its radial distance to the center of the sunspot with time. Panels (b) and (c) show how the frequency of the oscillations change between these two regions in the filtered maps in the ranges 2.5–3.5 minutes and 4.5–5.5, respectively. The umbra is dominated by waves with 3-minute period, while in the penumbral region the 5-minute waves are the most important. As the running penumbral waves move across the penumbra, their radial velocity is apparently reduced and their frequencies decrease from 4–5 mHz near the umbral/penumbral boundary to around 0.7–1.5 mHz at the outer edge of the penumbra (Bogdan & Judge 2006). Two most probable interpretations were brought forward to explain these oscillatory disturbances: they are believed to be either propagating waves through the penumbra generated in the umbra or a visual pattern resulting from the delayed wavefront arrival of field-aligned slow magnetoacoustic waves propagating up from the photosphere. Rouppe van der Voort et al. (2003) presented a set of Ca II H and Ca II K data obtained with the former Swedish Vacuum Solar Telescope (Scharmer et al. 1985), its successor the Swedish 1-m Solar Telescope (Scharmer et al. 2003), and the Dutch Open Telescope (Hammerschlag & Bettonvil 1998), all of them operated on the island of La Palma in the Spanish Observatorio del Roque de los Muchachos. They found that umbral flashes and running penumbral waves are closely related oscillatory phenomena, and suggested that they share a common source below the visible photosphere. This explanation is also supported by Bogdan & Judge (2006). Tziotziou et al. (2006) performed simultaneous two-dimensional observations in Ca II 8542 and Hα to analyze the Doppler velocity of the oscillations and the relationship between umbral flashes and running penumbral waves. However, their study was not able to support the preference of one of the proposed scenarios over the other. Bloomfield et al. (2007) analyzed one of the temporal series of Si I and He I observations obtained by Centeno et al. (2006), but while the latter considered vertical propagation along umbral field lines, they extended the analysis to waves traveling along the penumbra. They concluded that running penumbral waves are a visible pattern of low-β slow mode waves propagating and expanding their wavefront along the inclined magnetic field lines in the penumbra.

1.4 Numerical simulations

The theoretical study of wave propagation in atmospheres permeated by a magnetic field needs a very complex mathematical description. A full analysis of these processes should include magnetohydrodynamics and radiative transfer, considering non local thermodynamic equilibrium situations. Although a lot of analytical work was done in simple atmospheres (Ferraro & Plumpton 1958; Zhugzhda & Dzhalilov 1984a), those works were restricted to very idealized cases. Thus, numerical simulations face the challenge of clarifying the theoretical scenario, although their development entails great conceptual and computational deals.

The recent progress in observations and numerical simulations of sunspot waves is summarized in Khomenko (2009). In most cases, two-dimensional (2D) situations were considered. Despite this limitation, several important aspects were learned from these models. One of the first numerical simulations of magnetoacoustic waves in a bidimensional stratified atmosphere was done by Shibata (1983), who introduced a pressure pulse in uniformly magnetized atmosphere to excite slow and fast magnetoacoustic waves. Over the last years, several attempts were done to perform numerical simulations of waves in non-trivial magnetic field configurations. Cargill et al. (1997) obtained numerical solutions for the propagation of Alfvénic wave pulses in two dimensional magnetic field geometries from the photosphere to the corona. While Cargill et al. (1997) centered their study in Alfvénic solutions, Rosenthal et al. (2002) and Bogdan et al. (2003) were interested in magnetoacoustic waves. Similar calculations for conditions appropriate for sunspot rather than flux tubes

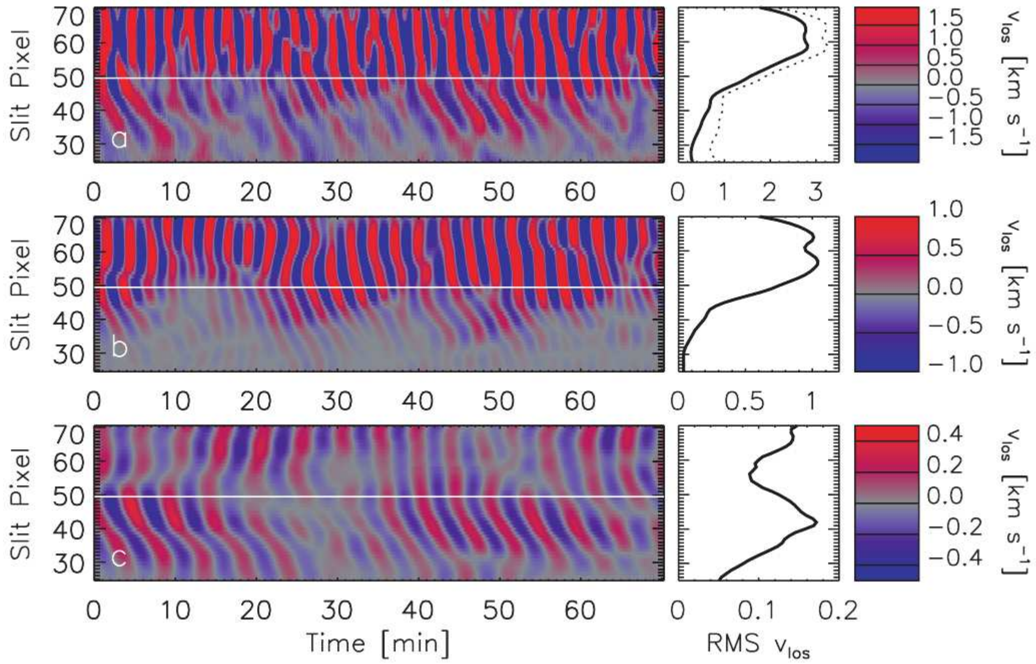

Figure 1.5: Velocity map covering the umbra and penumbra measured with He I. Original map (a), filtered in the range 2.5 − 3.5 minutes (b), and filtered in the range 4.5 − 5.5 (c). The white line marks the umbra/penumbra boundary (umbra above the line and penumbra below it), while right-hand side panels show rms velocities.

were carried by Khomenko & Collados (2006). In all these works waves were generated by a photospheric piston introduced as a bottom boundary condition in the magnetic region, and they propagate upward from the photosphere to the chromosphere. These authors found that the fast magneto-acoustic mode in the magnetically dominated region (*i.e.*, where the sound speed c_S is much lower than the Alfvén speed v_A) is refracted down and it comes back to the gas pressure dominated atmosphere due to the gradients of the Alfvén speed. Khomenko & Collados (2006) have shown that this is a robust feature of the simulations and happens for a wide frequency range and at different distances from the axis of the magnetic structure. Earlier, Rosenthal et al. (2002) demonstrated that the inclination of the magnetic field lines is important for the fast mode refraction, *i.e.*, in those regions where the inclination angle is large almost all of the fast mode wave energy is refracted back down. Another important feature of all these simulations is the presence of mode transformation at the layer where $v_A = c_S$. Around this layer, the phase speeds of all modes are similar and different waves can interact (Bogdan et al. 2003; Cally 2006; Khomenko & Collados 2006). Several works by Cally have gone deeper into the issue of mode transformation. According to Cally (2006), the direction and efficiency of the mode transformation depend on the frequency of the wave and the angle between the wavevector and the magnetic field. When this angle is small, the fast mode can be converted into the slow mode and vice versa. During this transformation, the wave conserves its physical nature (magnetic or acoustic). On the other hand, when this angle is arbitrary but different from zero, the fast (slow) mode in the region below $v_A = c_S$ can remain as a fast (slow) solution above this layer. In this case, as the fast (slow) wave propagates through the transformation region it changes its nature from acoustic (magnetic) to magnetic (acoustic). In the case of the fast-to-fast mode transformation, Cally (2005) pointed out that it is more efficient with increasing angle between the wave vector and the magnetic field and for lower wave frequencies.

Other works have studied wave propagation in magnetic structures corresponding to flux tubes. Many of them use the assumption of "thin" flux tube, where the horizontal dimensions of the structure are much smaller than the characteristic vertical scales of the atmosphere (Hasan et al. 2003; Hasan & Ulmschneider 2004). These structures present differents oscillatory modes, including kink, sausage and torsional modes (Spruit 1981). The topology of the flux tube was improved, leaving the "thin" flux tube aproximation, in Hasan et al. (2005) and Khomenko et al. (2008). In these simulations the slow magneto-acoustic mode reaches the layer where $v_A = c_S$ and its energy is transformed into a slow acoustic mode in the high atmosphere where $v_A > c_S$. Then this slow acoustic mode propagates vertically along the field lines and stepeens into shocks.

Several numerical codes have been developed by the solar physics community to study the propagation of waves in the magnetized atmospheres. They adopt different strategies for the numerical scheme, boundary conditions and wave driving, having their advantages and disadvantages (Moradi et al. 2009a). In the nonlinear 2D codes used by Rosenthal et al. (2002), Hasan et al. (2005) and Khomenko et al. (2008), the waves are driven in the simulation domain as initial condition at the lower boundary.

The upper boundary typically represents a problem in the wave simulations, since waves should not artificially be reflected there back into the physical domain. Rosenthal et al. (2002) apply characteristic boundary conditions at the top boundary; Hasan et al. (2005) use the open boundary concept; while Khomenko et al. (2008) introduced a special medium at the top called Perfectly Matched Layer (PML) which absorbs with almost no reflections the waves that reach the upper boundary. Rosenthal et al. (2002) and Hasan et al. (2005) solve the complete MHD equations, while Khomenko et al. (2008) solve equations for perturbations with all nonlinear terms retained. This strategy gives them an advantage for the precision of the numerical scheme and for the application of the boundary conditions.

3D MHD codes for wave simulations also start being available. Cameron et al. (2007) presented the semi-spectral linear MHD code SLiM, developed for helioseismology purposes. In this code, the horizontal derivatives are evaluated in Fourier space while the vertical derivatives are calculated with a two-step Lax-Wendroff scheme and the upper boundary is treated as a sponge layer. Figure 1.6 shows an example of the results obtained with this code. It illustrates a comparison of the observed cross-covariance of a wavepacket which traverses a sunspot with a numerical simulation whose set up was chosen to mimic the observations. Most of the features of the wavepacket once it has passed through the sunspot seem to be reproduced by the simulations, like the amplitudes, phase, and spatial spectrum. The amplitude of the wave is clearly reduced in the proximity of the sunspot. This absorption is caused by the partial conversion of these modes into slow magnetoacoustic waves which propagate downward along field lines inside the sunspot. The mode transformation removes energy from the wave that reaches the sunspot, whose amplitude is reduced in the region after the sunspot.

Another 3D linear MHD code for wave propagation has been developed by Parchevsky & Kosovichev (2007). The authors use the realistic OPAL equation of state and PML layer

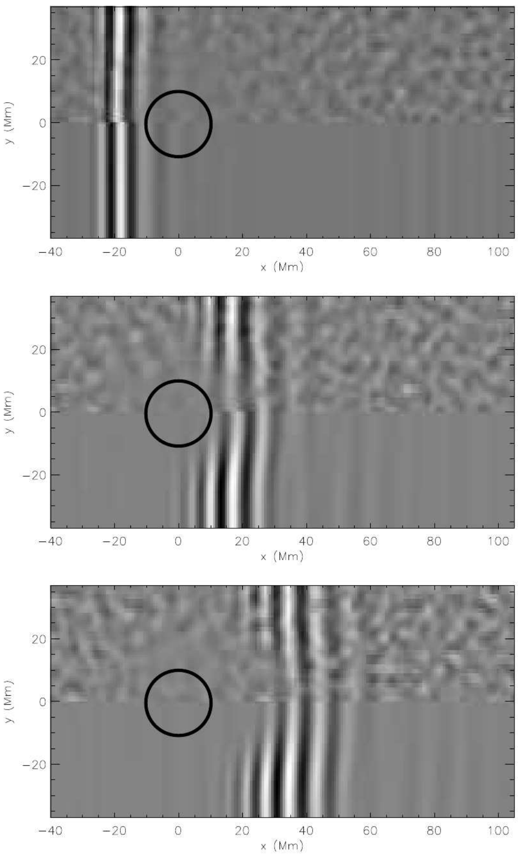

Figure 1.6: Comparison of the simulated vertical velocity and the observed cross-covariance at different time steps, increasing from top to bottom. In each panel the upper frame shows the observed cross-covariance and the bottom frame the simulated wave packet. The black circles of radius $R_0 = 10$ Mm indicates the location of the sunspots. Extracted from Cameron et al. (2007).

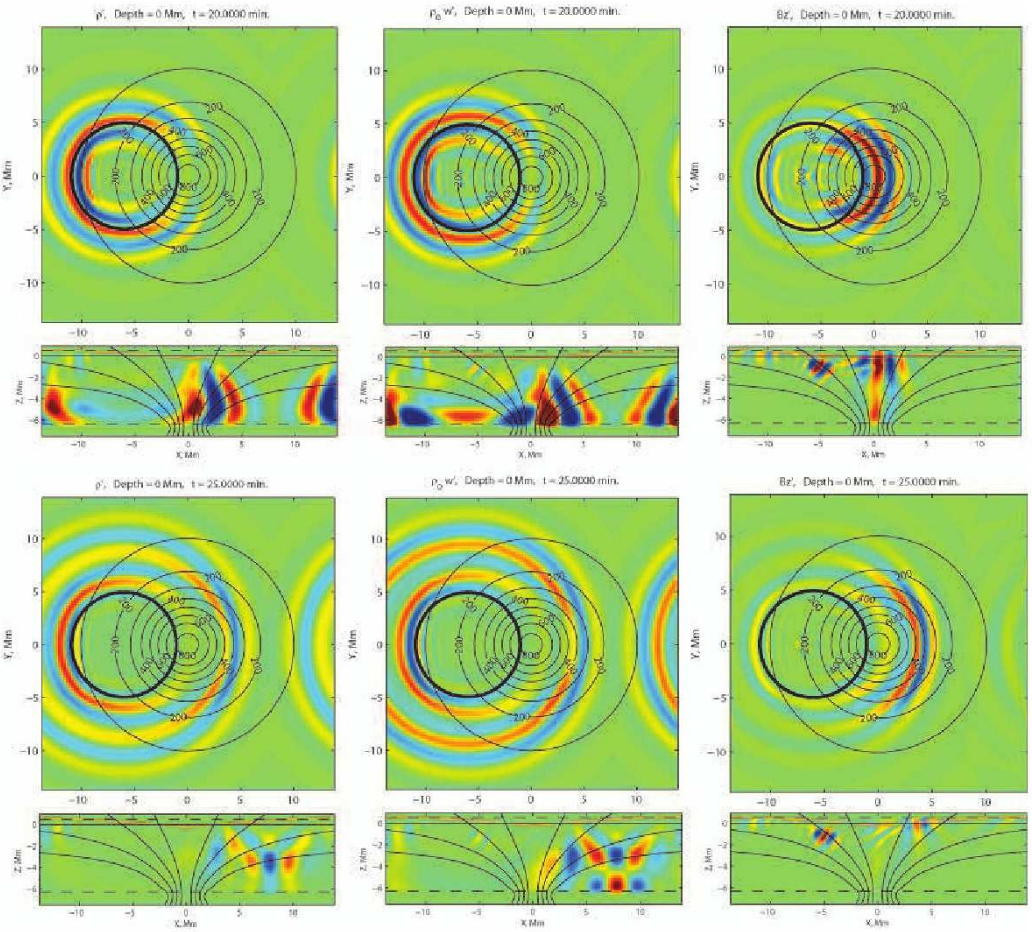

Figure 1.7: Snapshot of density (left), z-momentum (middle) and vertical magnetic field (right) perturbations at two different time steps: $t = 20$ min (top) and $t = 25$ min (bottom). Each panel includes two pictures: a horizontal cut at the photosphere (top) and a vertical vut (bottom). Extracted from Parchevsky et al. (2010).

as the upper boundary condition. Figure 1.7 illustrates the wave propagation obtained with this code in a sunspot model. It shows the perturbations of density, z-momentum and vertical magnetic field at two different time steps: at $t = 20$ min in top panels and $t = 25$ min in bottom panels. Each panel consists of a horizontal cut at photospheric level (top) and a vertical cut through the center of the sunspot (bottom). The amplitude of the wavefront is clearly anisotropic due to the non-uniform background model.

Numerically, the upper magnetized atmospheric layers represent an additional problem, strongly limiting the time step of the simulations due to the high values of the Alfvén speed. To overcome this problem, one of the strategies used is the Lorentz force controller. This method consists in reducing the amplitude of the Lorentz force in the layers where the Alfvén speed is large. This method is used by Hanasoge (2008) in his 3D linear code. However, the influence of this artificial procedure on the simulated wave properties has not been verified yet.

Recently, Shelyag et al. (2008) presented a nonlinear 3D parallel code developed on the base of the VAC code (Tóth 1996). In this code, they use the same philosophy as Khomenko et al. (2008), solving nonlinear equations for perturbations. There are also codes aiming at modeling waves in coronal loops and low$-\beta$ enviroments. An example of such codes is the one by Terradas et al. (2008). In this work the authors use the code to study numerically the kink oscillation in a flux tube, and find that the shear motion associated to this wave might be unstable and produce significant deformations of the tube boundary.

1.5 Objectives of this thesis

Despite the recent progress in the analysis of sunspot waves, to date no comprehensive model is available due to the complicated mathematical description of the physical processes playing a role in realistic magneto-atmospheres in three spatial dimensions. The aim of this thesis is to advance our understanding of the wave phenomena in sunspots by means of numerical simulations and spectropolarimetric observations.

The first objetive is the study of mode transformation and propagation of waves in 3D numerical simulations. Both simulations and analytical theory of the mode refraction, transformation, etc., were developed mostly for waves with high-frequencies, *i.e.* above, or just at, the cutoff frequency of the solar atmosphere. It is not clear what the response of the magnetic atmospheres to oscillations with long periods, like 5 minute waves, will be. This response can be studied with the help of simulations of waves with low frequencies in stratified magnetic atmospheres. The presence of magnetic field generates new wave modes, whose propagation properties are different from those of quiet Sun waves. We address the problem of the identification of these modes and evaluate their contribution to the energy transport to the upper atmosphere.

The second objective is the analysis of observations obtained with several spectral lines. Many observational works have been limited to the study of oscillations at only two heights, one photospheric and one chromospheric. It is thus interesting to perform a more detailed sampling of the sunspot atmosphere, using more spectral lines which are formed at several intermediate heights between these two regions. For this observational study we have a double aim. On the one hand, we expect to analyze the properties of wave propagation, including amplitude amplification, phase difference spectrum, and cutoff frequency. On the other hand, we aim to characterize the sunspot atmosphere and retrieve an estimation of the formation height of the spectral lines used in this work.

Our last objective is the development of numerical simulations of the real wave pattern observed between the photosphere and the chromosphere. Most of the simulations in realistic magnetized atmospheres with long periods, like those observed in the Sun, address questions related with helioseismic wave propagation below sunspots. With our code we have a different aim, *i.e.*, study these waves in the upper layers of the photosphere and chromosphere of the Sun. At these heights the simulations can be compared with direct measures obtained from spectropolarimetric observations. Such numerical calculations should account for several observed issues, like the change of wave frequency with height or the formation of shocks at chromospheric layers. These simulations will also allow us to evaluate the contribution of magnetoacoustic waves to the chromospheric heating. Understanding this phenomenon is one of the greatest challenges of modern solar physics. It is related to the presence of magnetic structures at the solar surface, and the propagation of energy by waves is one of the mechanisms proposed to explain the high temperatures prevailing in the upper layers of the solar atmosphere.

1.6 Organization

In the next chapter we introduce the theoretical basis needed to understant the bulk of this work, which consists on the magnetohydrodynamic equations and the theory of wave propagation and mode transformation.

In Chapter 3 we explain the main tool used in this thesis: the numerical code. This chapter introduces the equations solved by the code and the employed numerical techniques, including the spatial and temporal discretization, artificial diffusivity, boundary conditions and parallelization. The robustness of the code is verified in Chapter 4, where we show the results of several numerical tests.

Chapter 5 presents the analysis of a set of simulations where different drivers are introduced in a magnetohydrostatic model spanning from the photosphere to the chromosphere of a sunspot. The propagation of waves through this height range is studied from an observational point of view in Chapter 6. In Chapter 7 we combine the numerical and observational work, and develop a simulation which reproduces the observed wave propagation.

Finally, we present a summary of the conclusions extracted from this thesis and the future prospects in Chapter 8.

2

Theoretical concepts

The Sun is a huge sphere which maintains its cohesion thanks to its own gravity, and where matter is in a *plasma* state. The study of this star needs the knowledge of the physical laws that control its interior, that is, the plasma. A plasma is a highly ionized fluid which macroscopically is neutral, with many free electrons and ions in order to compensate the charge, and whose behavior is collective and is dominated by free electrons. In plasmas, charge neutrality is not satisfied at spatial scales smaller than a Debye length $\lambda_D = (KT\epsilon_0/(n_e e^2))^{1/2}$, where K is the Boltzmann constant, T is the temperature, ϵ_0 is the permittivity, n_e is the electronic density, and e is the charge of the electron. It means that the medium must be big enough, much bigger than a Debye length in order to be considered as a plasma. In the solar atmosphere λ_D is of the order of 10^{-6} m and the spatial scales are usually bigger than 10^5 m, so this condition is well satisfied.

This chapter deals with the basic physics of this study, which includes the magnetohydrodinamic theory (Section 2.1) and its aplication to linear and non-linear wave propagation (Sections 2.2 and 2.3, respectively), as well as the mode transformation phenomenon (Section 2.4).

2.1 Magnetohydrodynamic basic equations

The behavior of a plasma can be described by Maxwell's equations and Ohm's law together with the equations for hydrodynamics, *i.e.*, mass continuity, motion and energy equations. This set is known as magnetohydrodynamic equations (MHD) and it allows us to study the coupling between the magnetic field and the plasma fluid.

2.1.1 Electromagnetic equations

Maxwell's equations

The Maxwell's equations relate the electric and magnetic field to their sources, that is, the charge density and current density. They can be written as

$$\nabla \times \mathbf{B} = \mu_0 \Big(\mathbf{j} + \epsilon_0 \frac{\partial \mathbf{E}}{\partial t} \Big), \tag{2.1}$$

$$\nabla \times \mathbf{E} = -\frac{\partial \mathbf{B}}{\partial t}, \tag{2.2}$$

$$\nabla \cdot \mathbf{E} = \frac{\rho^*}{\epsilon_0}, \tag{2.3}$$

$$\nabla \cdot \mathbf{B} = 0, \tag{2.4}$$

where $\mathbf{E}$ is the electric field, $\mathbf{B}$ is the magnetic field, $\mathbf{j}$ is the current density, ρ^* is the charge density, μ_0 is the magnetic permeability, and ϵ_0 is the permittivity of free space. Equation (2.1) can be simplified using the so-called *MHD approximation*, for which the following hypothesis are applied:

(i) Electromagnetic variations are non relativistic. Considering L and T as the spatial and temporal scales, respectively, in which a magnitude changes, the characteristic velocity is

$$V = \frac{L}{T} \tag{2.5}$$

and it has to satisfy

$$V \ll c, \tag{2.6}$$

where c is the speed of light.

(ii) From Equation (2.2), the order of magnitude of the spatial variations of the electric field can be estimated as

$$\frac{E}{L} \sim \frac{B}{T} \Rightarrow E \sim B\frac{L}{T}. \tag{2.7}$$

Thus, comparing the left hand side term of Equation (2.1) with the second term of the right hand side (displacement current), the last one is much smaller than the first one:

$$\frac{|\mu_0\epsilon_0\frac{\partial \mathbf{E}}{\partial t}|}{|\nabla \times \mathbf{B}|} \sim \frac{\frac{1}{c^2}\frac{\mathbf{E}}{T}}{\frac{\mathbf{B}}{L}} = \frac{L^2/T^2}{c^2} = \frac{V^2}{c^2} \ll 1 \tag{2.8}$$

Neglecting the displacement current term, Equation (2.1) is simplified to

$$\nabla \times \mathbf{B} = \mu_0 \mathbf{j}. \tag{2.9}$$

One of the consequences of this equation can be analyzed by the calculation of its divergence, resulting in $\nabla \mathbf{j} = 0$. Physically, it means that charge accumulations are negligible.

Ohm's law

According to Ohm's law, the current density is proportional to the total electric field in a frame of reference moving with the plasma. When the movement of this plasma is at a non-relativistic speed and the medium is permeated by a magnetic field, the Ohm's law may be written as

$$\mathbf{j} = \sigma(\mathbf{E} + \mathbf{v} \times \mathbf{B}) - \frac{\sigma}{n_e e}(\mathbf{j} \times \mathbf{B}), \tag{2.10}$$

where σ is the electric conductivity. The last term corresponds to the Hall term. It is produced by the drifting of charged particles across the magnetic field. It vanishes when the collisions dominate over the cyclotron frequency, since the electrons cannot complete their spiral motion. In the following we will neglect this term. Applying the rotational to both sides of Equation (2.10), and replacing $\mathbf{j}$ and $\nabla \times \mathbf{E}$ according to Equations (2.9) and (2.2), respectively, we may retrieve the *induction equation*

$$\frac{\partial \mathbf{B}}{\partial t} = \nabla \times (\mathbf{v} \times \mathbf{B}) - \nabla \times (\eta \nabla \times \mathbf{B}), \tag{2.11}$$

where we have defined the magnetic diffusivity $\eta = (\mu_0 \sigma)^{-1}$. In this equation, $\nabla \times (\mathbf{v} \times \mathbf{B})$ is called advective term, since its effect is to couple the magnetic field with the plasma motion, while $-\nabla \times (\eta \nabla \times \mathbf{B})$ is the difusive term, as it produces the elimination of magnetic field. The *magnetic Reynolds number* estimates the relative importance between these two terms in order of magnitude, and it is defined as

$$R_m = \frac{|\nabla \times (\mathbf{v} \times \mathbf{B})|}{|\nabla \times (\eta \nabla \times \mathbf{B})|} \sim \frac{|\mathbf{v}||\mathbf{B}|/L}{\eta |\mathbf{B}|/L^2} = vL/\eta. \tag{2.12}$$

The induction equation determines the behavior of the magnetic field once the velocity of the plasma is known, and it depends on the value of R_m. When R_m is high, the diffusive term is almost zero, while in those cases where R_m is very low the advective term is negligible. In general, in astrophysics and in the Sun, R_m has very high values, so the diffusion is usually negligible.

The limit $R_m \gg 1$ corresponds to a perfectly conductive plasma. The reason of the high values presented by R_m is the high electric conductivity σ, which implies a low magnetic diffusivity, together with the large characteristic distances. The magnetic Reynolds number at the photosphere has been estimated to be of the order of 10^3-10^6 (Stix 1989). Mathematically, $R_m \to \infty$ is equivalent to $\sigma \to \infty$, and in this case the Ohm's law is simplified to

$$\mathbf{E} + \mathbf{v} \times \mathbf{B} = 0 \tag{2.13}$$

in order to keep the current density with finite values.

In addition, the Alfvén's theorem of flux-freezing states that in a perfectly conductive plasma, magnetic field lines move together with the plasma, and the fluid motions are only possible along field lines.

2.1.2 Plasma equations

The behavior of the magnetic field is described by the induction equation (Equation 2.11), and its relation with the fluid comes from the presence of the velocity term in that equation. The dynamics of the plasma depends on the equations of continuity, motion and energy, which will be discussed in the next sections together with their coupling to the magnetic field.

Mass continuity

It represents mass conservation, and may be written as

$$\frac{\partial \rho}{\partial t} + \nabla(\rho \mathbf{v}) = 0, \tag{2.14}$$

where ρ is the mass density and $\mathbf{v}$ is the velocity. At a fixed location, the density increases ($\frac{\partial \rho}{\partial t} > 0$) if there exists a mass flux towards its surroundings, while it decreases in the opposite case.

Equation of motion

It indicates the conservation of the momentum, and it is given by

$$\frac{\partial \rho \mathbf{v}}{\partial t} + \nabla \cdot (\rho \mathbf{v}\mathbf{v}) = \rho \mathbf{g} - \nabla p + \mathbf{j} \times \mathbf{B} + \nabla \cdot \bar{\tau}, \tag{2.15}$$

where p is gas pressure, $\mathbf{g}$ is the aceleration of gravity, and $\mathbf{vv}$ indicates the tensor product of the velocity. The last term of the previous equation is the viscous force. In the case of a compressible gas, the components of the viscous stress tensor $\bar{\tau}$ are

$$\tau_{ij} = \mu\Big(\frac{\partial v_i}{\partial x_j} + \frac{\partial v_j}{\partial x_i} - \frac{2}{3}\delta_{ij}(\nabla \cdot v)\Big), \qquad i, j = 1, 2, 3 \tag{2.16}$$

with μ being the dynamic viscosity. The *Reynolds number* R_e evaluates the importance of the viscosity, and it is obtained as the ratio in order of magnitude between the advective and viscous terms of Equation (2.15). Defining the kinematic viscosity $\nu = \frac{\mu}{\rho}$, the Reynolds number is given by

$$R_e = \frac{\nabla \cdot \rho \mathbf{v}\mathbf{v}}{\nabla \cdot \bar{\tau}} \sim \frac{\rho V^2/L}{\mu V/L^2} = \frac{\rho V L}{\mu} = \frac{V L}{\nu}. \tag{2.17}$$

At the photosphere, the Reynolds number has values of the order of $R_e \sim 10^8$, so the effect of viscous forces is negligible. Although the Sun is a rotating system, the rotational terms can be ignored for the calculation of the momentum balance. In the photosphere, the centrifugal aceleration is about four orders of magnitude lower than the gravitational aceleration, while the ratio of advective term of Equation (2.15) ($\nabla \cdot \rho \mathbf{vv}$) to the momentum due to the Coriolis force ($2\rho \mathbf{\Omega} \times \mathbf{v}$), the so-called *Rossby number*, is around 10^2-10^3.

Energy equation

The conservation of energy is represented by

$$\begin{aligned} &\frac{\partial e}{\partial t} + \nabla \cdot [\mathbf{v}(e + p + \frac{\mathbf{B}^2}{\mu_0}) - \frac{1}{\mu_0}\mathbf{B}(\mathbf{v} \cdot \mathbf{B})] = \\ &\quad = \frac{1}{\mu_0}\nabla \cdot (\mathbf{B} \times \eta(\nabla \times \mathbf{B})) + \nabla \cdot (\bar{\tau} \cdot \mathbf{v}) + \nabla \cdot (\kappa \nabla T) + \rho(\mathbf{g} \cdot \mathbf{v}) + Q_{rad}. \end{aligned} \tag{2.18}$$

In this equation, e is the total energy density per volume unity, which is obtained as the sum of the kinetic $e_{kin} = \rho v^2/2$, magnetic $e_{mag} = B^2/(2\mu_0)$ and internal $e_{int} = p/(\gamma - 1)$ energy densities.

Looking to the left hand side of the equations, the term $\partial e/\partial t$ indicates the variation of the energy at a fixed location, which depends on the rest of the terms. The term $\nabla \cdot (\mathbf{v}e)$ is the convective transport of the energy, that is, the energy that a fluid element transports from one location to another if it interchanges no heat or work with its surroundings, while $\nabla \cdot (\mathbf{v}p)$ is the compression-expansion work. The same reasoning may be applied to the other two terms of the left hand side, which indicate the magnetic energy transport ($|\mathbf{B}|^2/\mu_0$) and magnetic pressure work ($-\mathbf{B}(\mathbf{v}\cdot\mathbf{B})/\mu_0$).

Another set of terms which also affect the energy balance appears on the right hand side of the equation. The first term shows the loss of magnetic energy due to the diffusion of the magnetic field, while the second is the energy dissipated by the viscous forces. The third term is the transport by thermal conduction, where T is the temperature and κ is the thermal conductivity, and the fourth term is the work produced by the gravity. Finally, Q_{rad} is a source term produced by radiative transfer, which takes into account the heating or cooling due to the interaction of the plasma with radiation.

The conservation of internal energy is expressed by

$$\frac{\partial}{\partial t}\Big(\frac{p}{\gamma-1}\Big) + \mathbf{v}\nabla\frac{p}{\gamma-1} + \frac{\gamma}{\gamma-1}p\nabla\cdot\mathbf{v} = \rho\nabla\cdot(\kappa\nabla T) + \rho Q_{rad} + \rho\frac{\mathbf{j}^2}{\sigma}. \tag{2.19}$$

This equation can be related with Equation (2.18) by means of the equations of continuity, motion and Ohm's law.

Equation of state

In order to close the system of MHD equations, it is necessary to write an equation of state which relates the thermodynamic variables of the fluid. For simplicity, the perfect gas law can be taken, and it may be written in the form

$$p = \frac{k_B}{m}\rho T, \tag{2.20}$$

where k_B is the Boltzmann constant and m represents the mean particle mass. Usually, instead of m the mean atomic weight $\tilde{\mu} = m/m_p$ is used, which is the mean particle mass in units of proton mass m_p. Equation (2.20) becomes

$$p = \frac{R}{\tilde{\mu}}\rho T, \tag{2.21}$$

where $R = k_B/m_p$ is the gas constant. A fully-ionized hidrogen plasma is composed by the same number of protons and electrons. Since the mass of the electron is negligible in comparison with the mass of the proton, in this plasma $\tilde{\mu} = 0.5$. In the solar atmosphere the presence of other elements modifies $\tilde{\mu}$, taking values around 0.6 except near the photosphere, where hydrogen and helium are not fully ionized.

2.1.3 Assumptions

This section encompasses the set of assumptions that have been made in the derivation of the magnetohydrodynamic equations written for an inertial frame, and are briefly stated in the following:

(1) The plasma is treated as a continuum, since the length scale of the variations greatly exceeds the characteristic plasma length, *i.e.*, the Debye length.

(2) The plasma is in thermodynamic equilibrium, *i.e.*, it is dominated by collisions (with velocity distribution functions close to Maxwellian).

(3) All the plasma properties, as the coefficients η and μ, are considered constant.

(4) The typical velocity of the studied phenomena is much lower than the speed of light, so relativistic effects are neglected. This assumption allows us to neglect the displacement current term ($\frac{1}{c}\frac{\partial E}{\partial t}$) in the Maxwell's Equation (2.1)

(5) The plasma is treated as a single fluid, without considering a "three-fluid" model for electrons, protons and neutral atoms. Thus, a simple Ohm's law is suitable, instead of a generalized Ohm's law that would be necessary if the plasma would not be dominated by collisions.

2.2 Waves

Waves are generated due to the appearance of restoring forces when the fluid is slightly perturbed from an equilibrium state. The Sun is a dynamic body where different movements appears at a variety of scales, and they act as driver elements which allow for the creation of several wave types in the solar atmosphere. Depending on the restoring force considered, these waves will present different characteristics. Thus, magnetic tension generates *Alfvén waves*, magnetic pressure produces *compressional Alfvén waves*, plasma pressure creates *acoustic waves* and gravity force generates *gravity waves.* In the situation considered in this thesis, all forces are present and have the same order of magnitude in a general case.

2.2.1 Basic equations

Simple wave modes will be considered in this section. To that aim the equations of continuity, motion and energy, together with the induction equation and the Maxwell's Equation (2.4) will be considered. This set of equations may be written as:

$$\frac{\partial \rho}{\partial t} + \nabla(\rho \mathbf{v}) = 0 \tag{2.22}$$

$$\frac{\partial \rho \mathbf{v}}{\partial t} + \nabla \cdot (\rho \mathbf{v} \mathbf{v}) = \rho \mathbf{g} - \nabla p + \frac{1}{\mu_0}(\nabla \times \mathbf{B}) \times \mathbf{B} \tag{2.23}$$

$$\frac{\partial}{\partial t}\Big(\frac{p}{\rho^\gamma}\Big) + \mathbf{v} \cdot \nabla\Big(\frac{p}{\rho^\gamma}\Big) = 0 \tag{2.24}$$

$$\frac{\partial \mathbf{B}}{\partial t} = \nabla \times (\mathbf{v} \times \mathbf{B}) \tag{2.25}$$

$$\nabla \cdot \mathbf{B} = 0 \tag{2.26}$$

As can be seen, the viscous term of the equation of motion has been neglected, as well as the diffusive term in the induction equation, since the conditions of the solar atmosphere impose a high R_m. The energy loss terms have been dropped from the energy Equation (2.19), which yields Equation (2.24). It is valid for a plasma where the period of the wave is much shorter than the characteristic time of the losses of energy due to heat flux, radiative cooling or ohmic heating, and it indicates that the ratio p/ρ^γ keeps constant for a fluid element following the movement (adiabatic oscillations).

First, we present the equations for the equilibrium state, that is, with the temporal derivatives and the velocity set to zero:

$$0 = \rho_0 \mathbf{g} - \nabla p_0 + \frac{1}{\mu_0}(\nabla \times \mathbf{B}_0) \times \mathbf{B}_0 \tag{2.27}$$

$$\nabla \cdot \mathbf{B}_0 = 0. \tag{2.28}$$

Next, we introduce small departures from the equilibrium in ρ, p, $\mathbf{B}$ y $\mathbf{v}$ according to

$$\begin{aligned} \rho &= \rho_0 + \rho_1 \qquad (2.29) \\ p &= p_0 + p_1 \\ \mathbf{B} &= \mathbf{B}_0 + \mathbf{B}_1 \\ \mathbf{v} = \mathbf{v}_0 + \mathbf{v}_1 = \mathbf{v}_1 &= v_x \mathbf{e}_x + v_y \mathbf{e}_y + v_z \mathbf{e}_z \end{aligned}$$

and linearize the Equations (2.22)-(2.26) by neglecting the products between the perturbations (denoted by subindex 1). Taking into account the equations for the equilibrium (Equations 2.27 and 2.28), for an isothermal atmosphere we obtain the system

$$\frac{\partial \rho_1}{\partial t} + (\mathbf{v}_1 \cdot \nabla)\rho_0 + \rho_0(\nabla \cdot \mathbf{v}_1) = 0, \tag{2.30}$$

$$\rho_0 \frac{\partial \mathbf{v}_1}{\partial t} = -\nabla p_1 + \frac{1}{\mu_0}(\nabla \times \mathbf{B}_1) \times \mathbf{B}_0 - \rho_1 \mathbf{g}, \tag{2.31}$$

$$\frac{\partial p_1}{\partial t} + (\mathbf{v}_1 \cdot \nabla)p_0 - c_S^2\Big(\frac{\partial \rho_1}{\partial t} + (\mathbf{v}_1 \cdot \nabla)\rho_0\Big) = 0, \tag{2.32}$$

$$\frac{\partial \mathbf{B}_1}{\partial t} = \nabla \times (\mathbf{v}_1 \times \mathbf{B}_0), \tag{2.33}$$

$$\nabla \cdot \mathbf{B}_1 = 0, \tag{2.34}$$

where the speed of sound $c_S = (\gamma \frac{p_0}{\rho_0})^{1/2}$ has a constant value since the temperature is constant. Setting the gravity in the direction $-\hat{\mathbf{z}}$ and after calculating the time derivative of Equation (2.31), substituting $\partial \rho_1/\partial t$, $\partial p_1/\partial t$ and $\partial \mathbf{B}_1/\partial t$ from Equations (2.30), (2.32), and (2.33), a single equation for velocity perturbations is obtained:

$$\frac{\partial^2 \mathbf{v}_1}{\partial t^2} = c_S^2 \nabla(\nabla \cdot \mathbf{v}_1) - (\gamma - 1) g \hat{\mathbf{z}}(\nabla \cdot \mathbf{v}_1) - g \nabla v_{1z} + [\nabla \times (\nabla \times (\mathbf{v}_1 \times \mathbf{B}_0)] \times \frac{\mathbf{B}_0}{\mu_0 \rho_0}. \tag{2.35}$$

2.2.2 Waves in an unstratified atmosphere

The characteristic length of a stratified atmosphere is given by the pressure scale height $H_0 = c_S^2/(\gamma g)$. If the wavelength of a perturbation is much smaller than the scale height, gravity can be neglected in Equation (2.35). With this approximation, this is reduced to

$$\frac{\partial^2 \mathbf{v}_1}{\partial t^2} = c_S^2 \nabla(\nabla \cdot \mathbf{v}_1) + [\nabla \times (\nabla \times (\mathbf{v}_1 \times \mathbf{B}_0)] \times \frac{\mathbf{B}_0}{\mu_0 \rho_0}. \tag{2.36}$$

In this limit we can consider for all the variables a solution of plane waves of the form

$$\mathbf{v}_1(\mathbf{r}, t) = V e^{i(\mathbf{k}\cdot\mathbf{r} - \omega t)}. \tag{2.37}$$

The period of the wave is $2\pi/\omega$, its wavelength is $2\pi/k$, and its direction of propagation is $\hat{\mathbf{k}}$. Applying solutions like Equation (2.37) is equivalent to replace $\partial/\partial t$ by $-i\omega$ and ∇ by $i\mathbf{k}$. Thus, Equation (2.36) becomes

$$\omega^2 \mathbf{v}_1 = c_S^2 \mathbf{k}(\mathbf{k} \cdot \mathbf{v}_1) + \Big[\mathbf{k} \times (\mathbf{k} \times (\mathbf{v}_1 \times \mathbf{B}_0))\Big] \times \frac{\mathbf{B}_0}{\mu_0 \rho_0}. \tag{2.38}$$

It is convenient to define the *Alfvén speed*

$$\mathbf{v}_A = \frac{\mathbf{B}_0}{(\mu_0 \rho_0)^{1/2}}. \tag{2.39}$$

The values of the Alfvén speed are below 5 km s^{-1} in the photosphere, and reach around 1000 km s^{-1} in the chromosphere of sunspots. Introducing the definition of the Alfvén speed in Equation (2.38), and after some vectorial calculations, we obtain

$$\omega^2 \mathbf{v}_1 = (c_S^2 + v_A^2)(\mathbf{k} \cdot \mathbf{v}_1)\mathbf{k} + (\mathbf{v}_A \mathbf{k})\Big[(\mathbf{v}_A \cdot \mathbf{k})\mathbf{v}_1 - (\mathbf{v}_1 \cdot \mathbf{k})\mathbf{v}_A - (\mathbf{v}_A \cdot \mathbf{v}_1)\mathbf{k}\Big]. \tag{2.40}$$

Assuming an arbitrary direction of propagation, without loss of generality we can assign the Z axis to the direction of the magnetic field and choose the orientation of the X and Y axes in such a way that the propagation is confined to the plane XZ. The cartesian components of Equation (2.40) are

$$\Big[\omega^2 - v_A^2 k^2 - c_S^2 k_x\Big] v_{1x} = c_S^2 k_x k_z v_{1z} \tag{2.41}$$

$$\omega^2 v_{1y} = v_A^2 k_z^2 v_{1y} \tag{2.42}$$

$$c_S^2 k_x k_z v_{1x} = (\omega^2 - c_S^2 k_z^2) v_{1z} \tag{2.43}$$

The set of Equations (2.41)–(2.43) is decoupled into two independent systems, which give rise to three types of wave modes: fast and slow magneto-acoustic waves and the Alfvén wave. Each of these modes is described by its own dispersion relation. Dispersion relations $\omega = \omega(\mathbf{k})$ give the frequency as a function of the wave number, and they allow for the calculation of the phase velocity, $\mathbf{v}_{ph} = \omega/\mathbf{k}$, and the group velocity, $\mathbf{v}_g = \partial\omega/\partial\mathbf{k}$. The first one corresponds to the velocity propagation of a plane wave in the direction of $\mathbf{k}$, while the second one is the velocity of the energy propagation, whose magnitude and direction generally do not coincide with those of $\mathbf{v}_{ph}$. When $\mathbf{v}_{ph}$ depends on the wavelength the wave is dispersive. If ω is proportional to k, the wave is non-dispersive (ω/k = constant). The phase velocity and the group velocity of a non-dispersive wave coincide.

In the next sections we will discuss the solutions of the two independent system of the set of Equations (2.41)–(2.43).

Alfvén wave

From Equation (2.42), taking into account that $k_z = k\cos\theta_B$, where θ_B is the angle between the magnetic field and the direction of propagation, we obtain the dispersion relation

$$\omega = kv_A \cos\theta_B = \pm\mathbf{v}_A\mathbf{k} \tag{2.44}$$

for Alfvén waves.

- *Phase and group velocities*

  Their phase velocity $v_{ph} = v_A \cos\theta_B$ varies with the direction of propagation, reaching its maximum value along magnetic field and vanishing in the direction normal to it. According to the definition of the group velocity, we obtain $\mathbf{v_g} = \partial\omega/\partial\mathbf{k} = \pm\mathbf{v}_A$. It means that Alfvén waves transport energy in the direction of the magnetic field, although the wave perturbation in velocity can propagate forming any angle θ_B with $\mathbf{B}_0$, except $\theta_B = \pi/2$.

- *Oscillations in velocity and magnetic field*

  From Equation (2.42) we find that for v_{1y} different from 0 there is a wave with velocity oscillations in the direction $\mathbf{e}_y$, and according to the chosen system of reference they are perpendicular to $\mathbf{k}$ and $\mathbf{B}_0$. From Equation (2.34) we obtain $\mathbf{k}\cdot\mathbf{B}_1 = 0$, which implies that magnetic fields fluctuations are perpendicular to the direction of propagation.

  The introduction of the solution for plane waves in the induction equation for perturbations (Equation 2.33) gives

$$-\omega\mathbf{B}_1 = \mathbf{k}\times(\mathbf{v}_1\times\mathbf{B}_0), \tag{2.45}$$

  or equivalently

$$-\omega\mathbf{B}_1 = (\mathbf{k}\cdot\mathbf{B_0})\mathbf{v}_1 - (\mathbf{k}\cdot\mathbf{v}_1)\mathbf{B}_0. \tag{2.46}$$

  Since the velocity is perperdicular to the direction of propagation, *i.e.*, $\mathbf{k}\cdot\mathbf{v_1} = 0$, Equations (2.44) and (2.46) lead to the equation

$$\frac{\mathbf{v}_1}{v_A} = -\frac{\mathbf{B}_1}{B_0}, \tag{2.47}$$

which means that the perturbations in velocity and magnetic field are parallel, both perpendicular to the direction of propagation.

As stated before, $\mathbf{B}_0 \cdot \mathbf{v}_1 = 0$, and this expression together with Equation (2.47) results

$$\mathbf{B}_0 \cdot \mathbf{B}_1 = 0, \tag{2.48}$$

indicating that the magnetic field perturbation is normal to $\mathbf{B}_0$.

- *Oscillations in pressure and density*

  Equations (2.30) and (2.32) imply that, with ρ_0 and p_0 uniform, these waves do not produce changes in pressure and density.

- *Restoring force*

  In the case of Alfvén waves, the Lorentz force is the cause of the oscillation, and it may be written as

$$\mathbf{j}_1 \times \mathbf{B}_0 = i(\mathbf{k} \times \mathbf{B}_1) \times \mathbf{B}_0/\mu_0 = i(\mathbf{k} \cdot \mathbf{B}_0) \times \mathbf{B}_1/\mu_0 - i(\mathbf{B}_0 \cdot \mathbf{B}_1) \times \mathbf{k}/\mu_0. \tag{2.49}$$

  The first term of the right hand side of Equation (2.49) comes from magnetic tension and the second is due to magnetic pressure. According to Equation (2.48), magnetic pressure term vanishes, so the restoring force of Alfvén waves is magnetic tension. In addition, following Equation (2.47), the ratio of the magnetic energy to the kinetic energy ($\frac{B_1^2/(2\mu_0)}{\rho_0 v_1^2/2}$) is unity, meaning that magnetic and kinetic energies are in equipartition for Alfvén waves.

Magneto-acoustic waves

The system formed by Equations (2.41) and (2.43) can be combined in a single equation which gives the dispersion relation

$$\omega^4 - \omega^2 k^2 (c_S^2 + v_A^2) + c_S^2 v_A^2 k^4 \cos^2\theta_B = 0 \tag{2.50}$$

for *magnetoacoustic waves.* The phase velocity of these waves is

$$v_{ph}^2 = \left(\frac{\omega}{k}\right)^2 = \frac{1}{2}(v_A^2 + c_S^2) \pm \frac{1}{2}\sqrt{(v_A^2 + c_S^2)^2 - 4v_A^2 c_S^2 \cos^2\theta_B}, \tag{2.51}$$

where the positive sign corresponds to *fast magnetoacoustic waves* and the negative sign to *slow magnetoacoustic waves.* Moreover, after applying the square root to the previous expression, the two different signs of the solution indicate the opposite directions in which the waves can propagate.

Phase velocity of magneto-acoustic waves depends on the direction of propagation given by the angle between $\mathbf{k}$ and $\mathbf{B}_0$. For propagation along magnetic field ($\theta_B = 0$) the ratio

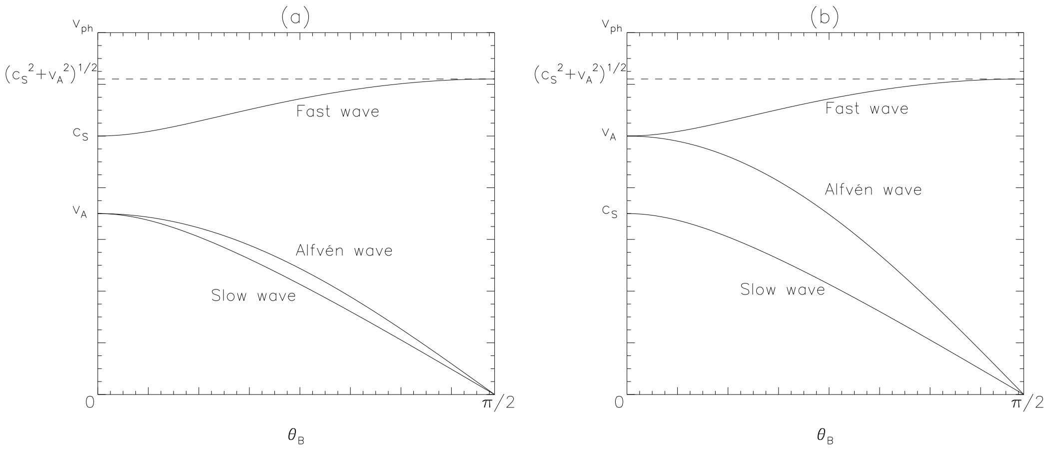

Figure 2.1: Variation of the phase velocity with the angle θ_B for magnetoacoustic and Alfvén waves. *(a)* $c_S > v_A$; *(b)* $c_S < v_A$.

ω/k takes the value v_A or c_S for fast or slow mode. For propagation across magnetic field ($\theta_B = \pi/2$) the phase velocity of the fast wave is $v_{ph} = (v_A^2 + c_S^2)^{1/2}$ and that of the slow wave vanishes (see Figure 2.1).

When one of the characteristic speeds is much higher than the other, the dispersion relation can be simplified to $\omega = kv_{fast}$ for the fast mode and $\omega = kv_{slow}\cos\theta_B = v_{slow}\mathbf{k}\cdot\mathbf{B}_0/|B_0|$ for the slow mode, where v_{fast} is the largest velocity between v_A and c_S, while v_{slow} is the smallest. In the case of the fast mode, the direction of the phase and group velocity is $\mathbf{k}$ and their magnitude is either c_S or v_A, and the energy is propagated in the same direction of the wave. In the case of the slow mode, the energy is propagated along magnetic field lines, according to the group velocity. When the sound and Alfvén speeds are similar, the direction of the group velocity and phase velocity is different for fast and slow modes, as can be retrieved from the derivation of $\mathbf{v}_g$ from Equation (2.50). The angle α between both directions depends on the local values of v_A, c_S and θ_B. Following Khomenko & Collados (2006) it is given by

$$\tan\alpha = \frac{c_S^2 v_A^2 \sin(2\theta_B)}{2v_{ph}(2v_{ph}^2 - v_A^2 - c_S^2)}, \tag{2.52}$$

where v_{ph} is the phase velocity obtained from Equation (2.51).

In those regions where the sound speed is much higher than the Alfvén speed, the fast wave propagates in all directions at the sound speed with longitudinal oscillations, while the behavior of the slow wave is similar to a magnetic wave and it produces transversal oscillations to the magnetic field and propagates along field lines. On the other hand, in the region where the magnetic field dominates over pressure forces, the fast mode has a magnetic nature, while the slow mode is acoustic-like and it mainly propagates along field lines at the sound speed.

2.2.3 Waves in a stratified atmosphere

In all the cases of MHD waves studied until this point we have considered that the gravity is negligible, so we have presented waves in the limit where the wavelength is much lower than the scale height. Zhugzhda & Dzhalilov (1984a) obtained an exact solution of the equations for magneto-acoustic-gravity waves in a conductive isothermal atmosphere in the presence of a uniform oblique magnetic field. According to their work, when the wave propagation direction lies in the plane including the gravity and oblique magnetic field vectors, the analytical solution can be expressed in terms of the Meijer functions. In this section we analyze the effects of the introduction of the gravity in the equations in an isothermal, plane-parallel atmosphere, which is vertically stratifed due to the gravity and has a constant vertical magnetic field following the work by Ferraro & Plumpton (1958). With this approximation, the introduction of a small perturbation which propagates vertically in a linear regime produces the generation of two types of waves. One of them is an acoustic wave with longitudinal oscillations. The other is an Alfvén wave with fluctuations in the transversal velocity.

If the atmosphere is permeated with a constant magnetic field in the direction of the Z axis, then $\mathbf{B}_0=(0,0,B_0)$, and Equation (2.35) becomes:

$$\frac{\partial^2\mathbf{v}_1}{\partial t^2}=c_S^2\nabla(\nabla\cdot\mathbf{v}_1)-(\gamma-1)g\hat{\mathbf{z}}(\nabla\cdot\mathbf{v}_1)-g\nabla v_{1z}+v_A^2\nabla(\nabla\cdot\mathbf{v}_1)- \\ -\hat{\mathbf{z}}v_A^2\frac{\partial(\nabla\cdot\mathbf{v}_1)}{\partial z}-\frac{B_0}{\mu_0\rho_0}[\mathbf{B}_0\times(\nabla\times\mathbf{v}_1)]. \tag{2.53}$$

This equation may be decomposed in its three Cartesian components

$$\frac{\partial^2 v_{1x}}{\partial t^2}=(c_S^2+v_A^2)\frac{\partial(\nabla\cdot\mathbf{v}_1)}{\partial x}-g\frac{\partial v_{1z}}{\partial x}+v_A^2\Big(\frac{\partial v_{1x}}{\partial z}-\frac{\partial v_{1z}}{\partial x}\Big), \tag{2.54}$$

$$\frac{\partial^2 v_{1y}}{\partial t^2}=(c_S^2+v_A^2)\frac{\partial(\nabla\cdot\mathbf{v}_1)}{\partial y}-g\frac{\partial v_{1z}}{\partial y}+v_A^2\Big(\frac{\partial v_{1y}}{\partial z}-\frac{\partial v_{1z}}{\partial y}\Big), \tag{2.55}$$

$$\frac{\partial^2 v_{1z}}{\partial t^2}=\frac{\partial}{\partial z}\Big[c_S^2(\nabla\cdot\mathbf{v}_1)-gv_{1z}\Big]-(\gamma-1)g(\nabla\cdot\mathbf{v}_1). \tag{2.56}$$

Without loss of generality, we can choose the direction of the X and Y axes in order to make $\mathbf{v}_1$ independent of y. Equation (2.55) is simplified to

$$\frac{\partial^2 v_{1y}}{\partial t^2}=v_A^2\Big(\frac{\partial v_{1y}}{\partial z}\Big). \tag{2.57}$$

The set of equations needed in this study is formed by Equations (2.54), (2.56), and (2.57), and they are clearly separated into two independent systems. Equation (2.57) represents an Alfvén wave with fluctuations in the transversal velocity. The other two equations correspond to an acoustic wave with both horizontal and vertical components of the velocity perturbations. Considering a harmonic solution of the form

$$\mathbf{v}_1(x,z,t)=\mathbf{A}(z)e^{i(kx+\omega t)}, \tag{2.58}$$

where $\mathbf{A} = (A_x, A_y, A_z)$, the above set of equations can be written as

$$\Big[v_A^2\Big(\frac{d^2}{dz^2} - k^2\Big) - k^2 c_S^2 + \omega^2\Big] A_x = -ik\Big(c_S^2 \frac{d}{dz} - g\Big) A_z, \tag{2.59}$$

$$\Big(c_S^2 \frac{d^2}{dz^2} - \gamma g \frac{d}{dz} + \omega^2\Big) A_z = -ik\Big[c_S^2 \frac{d}{dz} - (\gamma - 1)g\Big)\Big] A_x, \tag{2.60}$$

$$v_A^2 \frac{\partial^2 A_y}{\partial z^2} + \omega^2 A_y = 0. \tag{2.61}$$

If $k = 0$ (vertical propagation), Equation (2.59) yields two solutions:

$$A_x = 0, \tag{2.62}$$

$$v_A^2 \frac{\partial^2 A_x}{\partial z^2} + \omega^2 A_x = 0, \tag{2.63}$$

while Equation (2.60) is reduced to

$$c_S^2 \frac{d^2 A_z}{dz^2} - \gamma g \frac{dA_z}{dz} + \omega^2 A_z = 0. \tag{2.64}$$

Equations (2.61) and (2.63) represent an Alfvén wave, since when $k = 0$ both X and Y axes are equivalent, and Equation (2.64) corresponds to an acoustic wave propagating vertically upward, without fluctuations in the horizontal direction according to Equation (2.62). In the following, we discuss both waves independently.

Acoustic wave

The amplitude A_z of this wave is given by Equation (2.64). If we consider solutions of the form

$$A_z(z) = D e^{z/2H_0} e^{ik_z z}, \tag{2.65}$$

being $H_0 = c_S^2/(\gamma g)$ the pressure scale height, Equation (2.64) gives the dispersion relation

$$k_z = \frac{1}{c_S}\Big(\mp \sqrt{\omega^2 - \omega_c^2}\Big). \tag{2.66}$$

In this expression, $\omega_c = \gamma g/(2c_S)$ corresponds to the acoustic cutoff frequency of the atmosphere. The posible solutions for the vertical displacement of the wave are given by

$$\begin{aligned} A_z(z) &= D e^{[1/2H_0 \mp (\sqrt{\omega_c^2 - \omega^2})/c]z} && (\omega < \omega_c), \\ A_z(z) &= D e^{z/2H_0} e^{\mp i[(\sqrt{\omega^2 - \omega_c^2})/c]z} && (\omega > \omega_c). \end{aligned} \tag{2.67}$$

When $\omega < \omega_c$, $A(z)$ is a real exponential, so there is no wave propagation. In this case, the perturbation has an evanescent behavior that produces a stationary wave. On the other hand, when $\omega > \omega_c$, the vertical wave number k_z is real and the solution $A(z)$ gives rise to an exponential growth with height of the amplitude of the perturbation. The complex exponential includes the oscillatory character of the wave.

Alfvén wave

If we change the independent variable of Equation (2.61) from z to v_A, it yields to

$$v_A^2\frac{d^2A_y(z)}{dv_A^2}-v_A\frac{dA_y(z)}{dv_A}+\frac{4\omega^2H_0^2}{v_A^2}A_y(z)=0. \qquad (2.68)$$

The form of the general solution of this equation is

$$A_y(z)=CJ_0\Big(\frac{2\omega H_0}{v_A}\Big)+DY_0\Big(\frac{2\omega H_0}{v_A}\Big), \qquad (2.69)$$

where J_0 and Y_0 are the Bessel functions of order zero of first and second type, respectively, and C and D are arbitrary constants. The transversal velocity and magnetic field perturbation are given by

$$v_y(z,t)=i\omega CJ_0\Big(\frac{2\omega H_0}{v_A}\Big)e^{i\omega t}+i\omega DY_0\Big(\frac{2\omega H_0}{v_A}\Big)e^{i\omega t}, \qquad (2.70)$$

$$B_{y1}(z,t)=\frac{C\omega B_{z0}}{v_A}J_1\Big(\frac{2\omega H_0}{v_A}\Big)e^{i\omega t}+\frac{D\omega B_{z0}}{v_A}Y_1\Big(\frac{2\omega H_0}{v_A}\Big)e^{i\omega t}, \qquad (2.71)$$

respectively, where J_1 is the Bessel function of order one. In these solutions, the height dependence is included in $v_A=v_A(z)$.

2.3 Shock waves

In the previous sections we have considered the propagation of linear waves in some idealized atmospheres. Since the numerical code includes the nonlinear terms, it is interesting to address how these terms affect the wave propagation. Firstly, we will show an example of a nonlinear acoustic oscillation.

Considering a one-dimensional flux with the movement in the direction x whithout gravity, magnetic field and viscosity. Continuity and motion equations are written as

$$\frac{\partial\rho}{\partial t}+\frac{\partial}{\partial x}(\rho v)=0, \qquad (2.72)$$

$$\frac{\partial v}{\partial t}+v\frac{\partial v}{\partial x}=-\frac{1}{\rho}\frac{\partial p}{\partial x}, \qquad (2.73)$$

respectively. We suppose an isothermal atmosphere. In general, we have two independent thermodynamic variables, and taking them as ρ and T, since T is constant, we obtain from the equation of state $p=p(\rho,T)=p(\rho)$. From the continuity equation (2.72) we retrieve

$$\frac{\partial\rho}{\partial t}+\frac{\mathrm{d}(\rho v)}{\mathrm{d}\rho}\frac{\partial\rho}{\partial x}=0. \qquad (2.74)$$

Since $\partial p/\partial x=(\mathrm{d}p/\mathrm{d}v)(\partial v/\partial x)$, the motion equation (2.73) yields

$$\frac{\partial v}{\partial t}+\Big(v+\frac{1}{\rho}\frac{\mathrm{d}p}{\mathrm{d}v}\Big)\frac{\partial v}{\partial x}=0, \qquad (2.75)$$

that is:

$$\frac{\mathrm{d}v}{\mathrm{d}\rho}\frac{\partial\rho}{\partial t}+\Big(v+\frac{1}{\rho}\frac{\mathrm{d}p}{\mathrm{d}v}\Big)\frac{\mathrm{d}v}{\mathrm{d}\rho}\frac{\partial\rho}{\partial x}=0, \tag{2.76}$$

and

$$\frac{\partial\rho}{\partial t}+\Big(v+\frac{1}{\rho}\frac{\mathrm{d}p}{\mathrm{d}v}\Big)\frac{\partial\rho}{\partial x}=0. \tag{2.77}$$

In general $\rho=\rho(x,t)$, and taking infinitesimal differences

$$\delta\rho=\frac{\partial\rho}{\partial x}\delta x+\frac{\partial\rho}{\partial t}\delta t. \tag{2.78}$$

Considering changes at constant ρ, *i.e.*, $\delta\rho=0$:

$$\frac{\partial\rho}{\partial x}\delta x=-\frac{\partial\rho}{\partial t}\delta t, \tag{2.79}$$

resulting

$$\frac{\partial\rho/\partial t}{\partial\rho/\partial x}=-\Big(\frac{\partial x}{\partial t}\Big)_\rho, \tag{2.80}$$

where the subindex ρ at the bracket indicates changes with constat ρ. Introducing this relation into continuity (Equation 2.74) and motion (Equation 2.77) equations we find

$$\Big(\frac{\partial x}{\partial t}\Big)_\rho=\frac{\mathrm{d}(\rho v)}{\mathrm{d}\rho}=v+\rho\frac{\mathrm{d}v}{\mathrm{d}\rho}, \tag{2.81}$$

$$\Big(\frac{\partial x}{\partial t}\Big)_\rho=v+\frac{1}{\rho}\frac{\mathrm{d}p}{\mathrm{d}v}, \tag{2.82}$$

respectively. Equating both expresions we obtain

$$\frac{\mathrm{d}v}{\mathrm{d}\rho}=\frac{1}{\rho^2}\frac{\mathrm{d}p}{\mathrm{d}v}. \tag{2.83}$$

In this case with constant temperature $c_S^2=\mathrm{d}p/\mathrm{d}\rho$, and Equation (2.83) is equivalent to

$$\frac{\mathrm{d}v}{\mathrm{d}\rho}=\frac{c_S^2}{\rho^2}\frac{\mathrm{d}\rho}{\mathrm{d}v}, \tag{2.84}$$

which leads to

$$\frac{\mathrm{d}v}{\mathrm{d}\rho}=\pm\frac{c_S}{\rho}. \tag{2.85}$$

From Equation (2.85), together with the isothermal relation $c_S^2=\mathrm{d}p/\mathrm{d}\rho$ and Equation (2.81) we obtain

$$\Big(\frac{\partial x}{\partial t}\Big)_\rho=v\pm c_S. \tag{2.86}$$

Since once ρ is known v is determined, we can express any thermodynamic magnitude as function of v instead of ρ, and Equation (2.86) results

$$\left(\frac{\partial x}{\partial t}\right)_v = v \pm c_S(v). \tag{2.87}$$

Thus, the velocity of propagation of the wave u is written as

$$u = v \pm c_S(v). \tag{2.88}$$

The two signs correspond to the waves that propagate in opposite directions. When the wave has a finite non-infinitesimal amplitude and the nonlinear terms in the equations become important, the velocity of propagation of the wave depends on the velocity of the perturbation, opposite to the case of a linear acoustic wave where each part of the wave moves with the same speed c_S. In the latter, the wave profile maintains a fixed shape. However, in the nonlinear case the crest of the sound wave moves faster than its leading or trailing edge, producing a progressive steepening of the wavefront as the faster parts catch the slower ones, and the wave forms a sawtooth profile. The large values of the gradients of the velocity, density, pressure and temperature at the wavefronts produces that the dissipative processes are no longer negligible. Thus, the profile of the shock is determined by a balance between the steepening produced by the nonlinear terms and the broadening generated by the dissipative terms. Since the shock travels faster than c_S, the information (which travels at c_S relative to the equilibrium) cannot be propagated to the medium ahead the shock wavefront. The dissipation inside the shock produces a conversion of the energy carried by the wave into thermal energy by means of particle collisions and also to compress and heat the gas.

2.4 Mode transformation

In the atmosphere of a sunspot, the Alfvén velocity increases very fast, starting from a region where it is lower than the sound speed and reaching several orders of magnitude larger values in higher layers. In this way, an upward propagating wave which travels from the photosphere to the chromosphere will reach a layer where both characteristic velocities are equal, $v_A = c_S$. Around this height, different wave modes can interact, producing wave transformation (see, for example, Zhugzhda & Dzhalilov 1982, 1984b; Bogdan et al. 2002, 2003; Rosenthal et al. 2002; Cally 2005, 2006; Khomenko & Collados 2006).

The phase velocity, v_{ph}, is a continuous function which depends on the spatial coordinates, and this fact must remain after wave transformation. As the wave reaches the transformation layer $v_A \simeq c_S$, the phase velocity of both modes becomes similar, and the energy may be transferred among the different modes of the dispersion relation. The direction and efficiency of the transformation depends on, among other parameters, the frequency of the wave and the angle between the wave vector and the magnetic field.

When the angle θ_B between the wave vector $\mathbf{k}$ and the magnetic field $\mathbf{B}_0$ is small in the region where $v_A \simeq c_S$, the fast mode may be transformed partially in the slow mode and vice versa. In this transformation, the wave keeps its physical nature (magnetic of acoustic). In the case of high frequencies (above the cutoff frequency) in a vertical magnetic field, according to (Cally 2006) the coefficient of the transformation from the fast to the slow mode is aproximately given by

$$C = exp\Big[- \frac{k\pi sin^2\theta_B}{|(d/ds)(c_S^2/v_A^2)|}\Big], \tag{2.89}$$

where s is the distance along the direction defined by the vector $\mathbf{k}$. This coefficient must be evaluated at the point where $v_A = c_S$. As this expression shows, the fast-to-slow conversion is complete for the wave with $\mathbf{k}$ in the direction of $\mathbf{B}_0$. When the angle between these two vectors is different from zero, the energy fraction which is transformed from the fast to the slow mode is reduced as the angle θ_B increases. Moreover, the value of C depends on the frequency by means of the wave number k, in such a way that for higher frequencies the set of angles θ_B for which the conversion is effective is reduced.

If the angle between the wave vector $\mathbf{k}$ and the magnetic field $\mathbf{B}_0$ is arbitrary but different from zero, the fast solution below the region $v_A \simeq c_S$ may follow its upward propagation as a fast solution above it, but its nature changes from acoustic ($v_A < c_S$) to magnetic ($v_A > c_S$). The same happens to the slow wave, which keeps as a slow solution but changes from magnetic to acoustic. According to Cally (2005), the fast-to-fast coefficient of conversion increases with the angle θ_B and with the increase of the frequency of the wave, ω. For waves with $\mathbf{k}$ along magnetic field ($\theta_B = 0$), the conversion coefficient is zero independently of the frequency, and there is no conversion of energy between the acoustic and magnetic modes.

Only few studies have analyzed the transformation to an Alfvén mode, since most of the models have been two dimensional. In three dimensions the Alfvén wave may couple to the magnetoacoustic modes, and there may appear mode conversion among these modes. One of the pioneering works on this subject is the one presented by Cally & Goossens (2008). They find that energy transformation from magnetoacoustic waves to Alfvén waves can be important for magnetic field inclinations of $30^o - 40^o$ from the vertical, with the direction of propagation of the waves forming an angle of $60^o - 80^o$ with the plane which contains the magnetic field lines. This conversion to Alfvén wave occurs over a wide height range of several hundreds of kilometers, different from the fast/slow transformation that is confined to a layer near the height where the sound speed and the Alfvén speed are similar. For these angles, the efficiency of the conversion from fast (acoustic) mode to an Alfvén mode is almost two times larger than the slow mode for 5 mHz waves.

3

The MHD code

This chapter describes the development of the numerical MHD code. The code calculates the response of magnetic structures in equilibrium to an arbitrary perturbation. It solves the three dimensional nonlinear MHD equations for perturbations. It is an extension to three dimensions of the code described in Khomenko & Collados (2006), and it was parallelized to perform simulations in large 3D domains. It is written in Fortran 90.

The organization of the chapter is as follows: the first section presents the MHD equations which are solved by the code; Sections 3.2 and 3.3 explain the numerical procedures of the spatial and temporal derivatives, respectively; in Section 3.4 we discuss the artificial difusivity introduced in the code; Section 3.5 sets the criteria to estimate the time step for each iteration; Section 3.6 accounts for the filtering which is applied to the variables; Section 3.7 presents the Perfect Matched Layer boundary conditions; and the last section briefly explains the parallelization.

3.1 MHD equations

In Section 2.1 we have discussed the MHD equations which must be solved by the code. Written in conservative form, these equations are:

$$\frac{\partial \rho}{\partial t} + \nabla(\rho \mathbf{v}) = 0\,, \tag{3.1}$$

$$\frac{\partial(\rho \mathbf{v})}{\partial t} + \nabla\cdot\Big[\rho\mathbf{v}\mathbf{v} + \Big(p + \frac{\mathbf{B}^2}{2\mu_0}\Big)\mathbf{I} - \frac{\mathbf{B}\mathbf{B}}{\mu_0}\Big] = \rho\mathbf{g} + \mathbf{S}(t)\,, \tag{3.2}$$

$$\frac{\partial e}{\partial t} + \nabla\cdot\Big[\mathbf{v}\Big(e + p + \frac{\mathbf{B}^2}{2\mu_0}\Big) - \frac{1}{\mu_0}\mathbf{B}(\mathbf{v}\cdot\mathbf{B})\Big] = \rho(\mathbf{g}\cdot\mathbf{v}) + Q_{\rm rad}\,, \tag{3.3}$$

$$\frac{\partial \mathbf{B}}{\partial t} = \nabla\times(\mathbf{v}\times\mathbf{B})\,, \tag{3.4}$$

where $\mathbf{I}$ is the identity tensor, ρ is the density, $\mathbf{v}$ is the velocity, p is the gas pressure, $\mathbf{B}$ is the magnetic field, $\mathbf{g}$ is the gravitational acceleration and e is the total energy per unit volume,

$$e = \frac{1}{2}\rho v^2 + \frac{p}{\gamma - 1} + \frac{B^2}{2\mu_0}\,. \tag{3.5}$$

The dot '·' represents the scalar product of vectors, while the notation '**BB**' stands for the tensor product. The energy losses $Q_{\rm rad}$ are approximated by the Newton law of cooling. We neglect the viscous force, the thermal conduction and the terms describing the diffusion of the magnetic field. However, artificial equivalents of some of these terms are introduced later for the issue of numerical stability of the simulations. The term **S**(t) in Equation 3.2 represents a time-dependent external force, to account for the driver exciting the perturbation.

For numerical reasons, the MHD equations should be expressed in conservative form, written schematically as

$$\frac{\partial \mathbf{u}}{\partial t} + \frac{\partial \mathbf{F}(\mathbf{u})}{\partial x} + \frac{\partial \mathbf{G}(\mathbf{u})}{\partial y} + \frac{\partial \mathbf{K}(\mathbf{u})}{\partial z} = \mathbf{H}(\mathbf{u}), \tag{3.6}$$

where $\mathbf{u}$ is the considered variable, $\mathbf{F}(\mathbf{u})$, $\mathbf{G}(\mathbf{u})$ and $\mathbf{K}(\mathbf{u})$ are the fluxes of this variable in the directions x, y, or z, respectively, and $\mathbf{H}(\mathbf{u})$ represents sink or source terms. The set of Equations (3.1)-(3.4) is written in this way to show a conservation law, meaning that the variations of a magnitude (mass, energy or momentum) in a spatial element depend on the amount of that magnitude which enters or goes out through the boundaries and the amount of it which is destroyed or created. A numerical scheme written following Equation (3.6) is called conservative.

We assume that magnetohydrostatic equilibrium holds. In an equilibrium state, where temporal derivatives and velocities are zero, and in the absence of external forces ($\mathbf{S} = 0$), the previous equations reduce to the equations of the force balance for a gravitationally stratified magnetized plasma:

$$\nabla \cdot \left[\left(p_0 + \frac{{\mathbf{B}_0}^2}{2\mu_0} \right) \mathbf{I} - \frac{\mathbf{B}_0 \mathbf{B}_0}{\mu_0} \right] = \rho_0 \mathbf{g}\,. \tag{3.7}$$

The code solves the system of non-linear equations for perturbations. Considering departures from the equilibrium state induced by an external force $\mathbf{S}$, variables ρ, p and $\mathbf{B}$ can be expressed as the sum of the background value (subindex 0) and the perturbation (subindex 1):

$$\rho = \rho_0 + \rho_1\,, \tag{3.8}$$

$$p = p_0 + p_1\,, \tag{3.9}$$

and

$$\mathbf{B} = \mathbf{B}_0 + \mathbf{B}_1\,, \tag{3.10}$$

while the velocity only corresponds to a perturbed value $\mathbf{v} = \mathbf{v}_1$. The non-linear equations for perturbations are obtained by introducing expressions (3.8–3.10) into Equations (3.1–3.4) and subtracting the equation of the magnetohydrostatic equilibrium (Equation 3.7). The equations include first-order terms as well as higher orders (products of perturbed variables). The following system of MHD equations for perturbations of density, pressure, magnetic field and velocities is obtained in conservative form:

$$\frac{\partial \rho_1}{\partial t} + \nabla \Big[(\rho_0 + \rho_1) \mathbf{v}_1 \Big] = 0\,, \tag{3.11}$$

$$\frac{\partial[(\rho_0+\rho_1)\mathbf{v}_1]}{\partial t}+\nabla\cdot\Big[(\rho_0+\rho_1)\mathbf{v}_1\mathbf{v}_1+\Big(p_1+\frac{\mathbf{B}_1^2}{2\mu_0}+\frac{\mathbf{B}_1\cdot\mathbf{B}_0}{\mu_0}\Big)\mathbf{I}- \\ -\frac{1}{\mu_0}(\mathbf{B}_0\mathbf{B}_1+\mathbf{B}_1\mathbf{B}_0+\mathbf{B}_1\mathbf{B}_1)\Big]=\rho_1\mathbf{g}+\Big(\frac{\partial[(\rho_0+\rho_1)\mathbf{v}_1]}{\partial t}\Big)_{\text{diff}}+\mathbf{S(t)}\,, \tag{3.12}$$

$$\frac{\partial e_1}{\partial t}+\nabla\cdot\Big[\mathbf{v_1}\Big((e_0+e_1)+(p_0+p_1)+\frac{|\mathbf{B}_0+\mathbf{B}_1|^2}{2\mu_0}\Big)- \\ -\frac{1}{\mu_0}(\mathbf{B}_0+\mathbf{B}_1)\Big(\mathbf{v}_1\cdot(\mathbf{B}_0+\mathbf{B}_1)\Big)\Big]=(\rho_0+\rho_1)(\mathbf{g}\cdot\mathbf{v_1})+Q_{\text{rad}}+\Big(\frac{\partial e_1}{\partial t}\Big)_{\text{diff}}\,, \tag{3.13}$$

$$\frac{\partial\mathbf{B}_1}{\partial t}=\nabla\times[\mathbf{v}_1\times(\mathbf{B}_0+\mathbf{B}_1)]+\Big(\frac{\partial\mathbf{B}_1}{\partial t}\Big)_{\text{diff}}\,, \tag{3.14}$$

Artificial diffusion terms have been added to Equations (3.12–3.14) compared to Equations (3.2–3.4). The diffusivity terms in Equations (3.12–3.14) have their physical counterparts (see Equations 2.15, 2.18, and 2.11, respectively) and are needed for reasons of stability of the simulations (see Section 3.4). A similar strategy is applied in the MURAM code (Vögler et al. 2005).

Taking into account the non-linear terms, the code can reproduce the phenomena which depend on them, as for example the development of shocks. The use of equations for perturbations instead of complete equations has two big advantages for wave simulations. Firstly, the terms describing the static model and those for perturbations can vary by orders of magnitude. Thus, by excluding equilibrium terms we avoid important numerical precision problems. Secondly, the boundary conditions are easier to implement on equations for perturbations (see Section 3.7).

The code has to deal with variables which present high constrast in their values, with differences of several orders of magnitude. For example, in the same region the temperature may reach thousands of kelvin while the density may be around 10^{-8} g cm^{-3}. Numerically, it may be problematic, so we have used dimensionless variables, taking as a reference their value at some location or using a characteristic magnitude of the atmosphere. In the following expressions, the symbols with a hat (ˆ) represent the adimensional variables, which are related with the original as

$$\begin{aligned}\rho&=\rho_*\hat{\rho}\\ p&=p_*\hat{p}\\ \mathbf{v}&=c_*\hat{\mathbf{v}}\\ \vec{B}&=B_*\hat{\mathbf{B}}\\ x&=2H_*\hat{x}\\ \frac{\partial}{\partial x}&=\frac{1}{2H_*}\frac{\partial}{\partial\hat{x}}\\ t&=\frac{\hat{t}}{\omega_c}\\ \frac{\partial}{\partial t}&=\omega_c\frac{\partial}{\partial\hat{t}}.\end{aligned} \tag{3.15}$$

In these relations, the asterisks indicate the equilibrium values of the variables at a fixed position of the computatial domain. The parameter $c_* = \sqrt{\gamma \frac{p_*}{\rho_*}}$ is the sound speed, $\omega_c = \gamma g / 2c_*$ is the cutoff frequency of the plasma, and $H_* = c_*^2/(2g)$ is the pressure scale height.

This procedure has been performed with all the equations, and finally we have obtained a set of equations in a suitable form to be solved numerically. The next sections show briefly the process carried out with each of them.

3.1.1 Mass continuity

Starting with the continuity equation (Equation 3.11), if we express it in terms of the three spatial coordinates, the equation results

$$\frac{\partial \rho_1}{\partial t} + \frac{\partial}{\partial x}[(\rho_0 + \rho_1)v_x] + \frac{\partial}{\partial y}[(\rho_0 + \rho_1)v_y] + \frac{\partial}{\partial z}[(\rho_0 + \rho_1)v_z] = 0\,. \tag{3.16}$$

3.1.2 Equation of motion

According to the vector nature of Equation (3.12), we can extract three different scalar equations from it, one for each component. The last terms on the right hand side of each equation represent the diffusivity terms. They will be explained in Section 3.4. Assuming the external force has only a vertical component, the scalar equations are

$$\begin{aligned}
&\frac{\partial}{\partial t}[(\rho_0 + \rho_1)v_x] + \\
&+ \frac{\partial}{\partial x}\Big\{(\rho_0 + \rho_1)v_x^2 + p_1 + \frac{1}{\mu_0}[B_{y0}B_{y1} + B_{z0}B_{z1} - B_{x0}B_{x1} + \frac{1}{2}(B_{y1}^2 + B_{z1}^2 - B_{x1}^2)]\Big\} + \\
&+ \frac{\partial}{\partial y}\Big\{(\rho_0 + \rho_1)v_x v_y - \frac{1}{\mu_0}[B_{x1}B_{y0} + B_{x0}B_{y1} + B_{x1}B_{y1})]\Big\} + \\
&+ \frac{\partial}{\partial z}\Big\{(\rho_0 + \rho_1)v_x v_z - \frac{1}{\mu_0}[B_{x1}B_{z0} + B_{x0}B_{z1} + B_{x1}B_{z1})]\Big\} = \Big(\frac{\partial(\rho_0 + \rho_1)v_x}{\partial t}\Big)_{\text{diff}}
\end{aligned} \tag{3.17}$$

$$\begin{aligned}
&\frac{\partial}{\partial t}[(\rho_0 + \rho_1)v_y] + \\
&+ \frac{\partial}{\partial x}\Big\{(\rho_0 + \rho_1)v_y v_x - \frac{1}{\mu_0}[B_{y1}B_{x0} + B_{y0}B_{x1} + B_{y1}B_{x1}]\Big\} + \\
&+ \frac{\partial}{\partial y}\Big\{(\rho_0 + \rho_1)v_y^2 + p_1 + \frac{1}{\mu_0}[B_{x0}B_{x1} + B_{z0}B_{z1} - B_{y0}B_{y1} + \frac{1}{2}(B_{x1}^2 + B_{z1}^2 - B_{y1}^2]\Big\} + \\
&+ \frac{\partial}{\partial z}\Big\{(\rho_0 + \rho_1)v_y v_z - \frac{1}{\mu_0}[B_{y1}B_{z0} + B_{y0}B_{z1} + B_{y1}B_{z1}]\Big\} = \Big(\frac{\partial(\rho_0 + \rho_1)v_y}{\partial t}\Big)_{\text{diff}}
\end{aligned} \tag{3.18}$$

$$
\begin{aligned}
&\frac{\partial}{\partial t}[(\rho_0+\rho_1)v_z]+\\
&+\frac{\partial}{\partial x}\Big\{(\rho_0+\rho_1)v_z v_x-\frac{1}{\mu_0}[B_{z1}B_{x0}+B_{z0}B_{x1}+B_{z1}B_{x1}]\Big\}+\\
&+\frac{\partial}{\partial y}\Big\{(\rho_0+\rho_1)v_z v_y-\frac{1}{\mu_0}[B_{z1}B_{y0}+B_{z0}B_{y1}+B_{z1}B_{y1}]\Big\}+\\
&+\frac{\partial}{\partial z}\Big\{(\rho_0+\rho_1)v_z^2+p_1+\frac{1}{\mu_0}[B_{x0}B_{x1}+B_{y0}B_{y1}-B_{z0}B_{z1}+\frac{1}{2}(B_{x1}^2+B_{y1}^2-B_{z1}^2]\Big\}=\\
&=-\rho_1 g+S_z(t)+\Big(\frac{\partial(\rho_0+\rho_1)v_z}{\partial t}\Big)_{\text{diff}}. \qquad (3.19)
\end{aligned}
$$

3.1.3 Induction equation

In the case of the induction equation, the high values of the characteristic length of the solar atmosphere give a very high Reynolds number R_m, of the order of 10^3-10^6 at the photosphere, which allows to neglect the diffusive term. In this limit of high conductivity, only the advection term is important. However, as we will see later, we keep a diffusive term for numerical stability reasons. Thus, the induction equation solved by the code is given by Equation (3.14). Again, we can retrieve one equation for each coordinate:

$$
\begin{aligned}
\frac{\partial B_{x1}}{\partial t}&+\frac{\partial}{\partial y}[v_y(B_{x0}+B_{x1})-v_x(B_{y0}+B_{y1})]\\
&+\frac{\partial}{\partial z}[v_z(B_{x0}+B_{x1})-v_x(B_{z0}+B_{z1})]=\Big(\frac{\partial B_{x1}}{\partial t}\Big)_{\text{diff}} \qquad (3.20)
\end{aligned}
$$

$$
\begin{aligned}
\frac{\partial B_{y1}}{\partial t}&+\frac{\partial}{\partial z}[v_z(B_{y0}+B_{y1})-v_y(B_{z0}+B_{z1})]\\
&+\frac{\partial}{\partial x}[v_x(B_{y0}+B_{y1})-v_y(B_{x0}+B_{x1})]=\Big(\frac{\partial B_{y1}}{\partial t}\Big)_{\text{diff}} \qquad (3.21)
\end{aligned}
$$

$$
\begin{aligned}
\frac{\partial B_{z1}}{\partial t}&+\frac{\partial}{\partial x}[v_x(B_{z0}+B_{z1})-v_z(B_{x0}+B_{x1})]\\
&+\frac{\partial}{\partial y}[v_y(B_{z0}+B_{z1})-v_z(B_{y0}+B_{y1})]=\Big(\frac{\partial B_{z1}}{\partial t}\Big)_{\text{diff}} \qquad (3.22)
\end{aligned}
$$

3.1.4 Energy equation

After expanding the divergence in terms of spatial derivatives, the perturbed energy equation (Equation 3.13) can be written as

$$
\begin{aligned}
\frac{\partial e_1}{\partial t} &+ \frac{\partial}{\partial x}\Big\{v_x\Big((e_0+e_1)+(p_0+p_1)+\frac{(\mathbf{B}_0+\mathbf{B}_1)^2}{2\mu_0}\Big)-\frac{1}{\mu_0}(B_{x0}+B_{x1})\Big(\mathbf{v}_1\cdot(\mathbf{B}_0+\mathbf{B}_1)\Big)\Big\}+\\
&+\frac{\partial}{\partial y}\Big\{v_y\Big((e_0+e_1)+(p_0+p_1)+\frac{(\mathbf{B}_0+\mathbf{B}_1)^2}{2\mu_0}\Big)-\frac{1}{\mu_0}(B_{y0}+B_{y1})\Big(\mathbf{v}_1\cdot(\mathbf{B}_0+\mathbf{B}_1)\Big)\Big\}+\\
&+\frac{\partial}{\partial z}\Big\{v_y\Big((e_0+e_1)+(p_0+p_1)+\frac{(\mathbf{B}_0+\mathbf{B}_1)^2}{2\mu_0}\Big)-\frac{1}{\mu_0}(B_{z0}+B_{z1})\Big(\mathbf{v}_1\cdot(\mathbf{B}_0+\mathbf{B}_1)\Big)\Big\}=\\
&=-(\rho_0+\rho_1)gv_{1z}+Q_{rad}+\Big(\frac{\partial e_1}{\partial t}\Big)_{\rm diff}. \qquad (3.23)
\end{aligned}
$$

In high layers, where the magnetic pressure is much larger than the gas pressure, Equation (3.23) is numerically problematic, as recovering the thermal energy (p) from the total energy (e) leads to numerical errors. We have used Equation (2.19) for the balance of internal energy, instead, written as

$$
\frac{\partial}{\partial t}\Big(\frac{p}{\gamma-1}\Big)+\mathbf{v}\nabla\frac{p}{\gamma-1}+\frac{\gamma}{\gamma-1}p\nabla\cdot\mathbf{v}=\rho Q_{rad}+\Big(\frac{\partial p_1}{\partial t}\Big)_{\rm diff}, \qquad (3.24)
$$

or equivalently introducing the perturbed variables

$$
\begin{aligned}
\frac{\partial p_1}{\partial t}&+\frac{\partial}{\partial x}\Big[\gamma(p_0+p_1)v_x\Big]+\frac{\partial}{\partial y}\Big[\gamma(p_0+p_1)v_y\Big]+\frac{\partial}{\partial z}\Big[\gamma(p_0+p_1)v_z\Big]-\\
&-(\gamma-1)\Big[v_x\frac{\partial(p_0+p_1)}{\partial x}+v_y\frac{\partial(p_0+p_1)}{\partial y}+v_z\frac{\partial(p_0+p_1)}{\partial z}\Big]=\\
&=(\rho_0+\rho_1)Q_{rad}+\Big(\frac{\partial p_1}{\partial t}\Big)_{\rm diff}. \qquad (3.25)
\end{aligned}
$$

The radiative losses are implemented following Newton's cooling law

$$
Q_{rad}=-c_v\frac{T_1}{\tau_R}, \qquad (3.26)
$$

where T_1 is the perturbation in the temperature, τ_R is the radiative relaxation time, and c_v is the specific heat at constant volume. This expression is valid for optically thin disturbances, for which the wavelength is much smaller than the photon mean free path. The study of propagation of acoustic waves in a radiating fluid using Newton's cooling law predicts an adiabatic propagation for high frequency waves or long damping times, while in the case of low frequencies or short radiative relaxation time acoustic waves propagate isothermally. However, at a low enough frequency the wavelength of the fluctuations is so long than it becomes optically thick, and the Newtonian cooling approximation no longer applies.

We have considered the equation of state of an ideal gas to link the thermodynamic variables.

3.2 Spatial discretization

The computational domain is discretized using a three-dimensional Cartesian grid with constant spatial step in each dimension. The spatial derivatives are approximated by a centered, fourth order accurate, explicit finite differences scheme using five grid points (Vögler et al. 2005). Considering i as an index which covers one of the spatial directions, the expression of the first derivative of a magnitude u is

$$\left(\frac{\partial u}{\partial x}\right)_i = \frac{1}{12\Delta x}(-u_{i+2} + 8u_{i+1} - 8u_{i-1} + u_{i-2}), \tag{3.27}$$

All the equations of Section (3.1) are written in conservative form following Equation (3.6). The MHD code calculates the fluxes which appear in Equations (3.16), (3.17), (3.18), (3.19), (3.20), (3.21), (3.22), and (3.25), and calculates their derivatives in the corresponding coordinate following Equation (3.27).

3.3 Temporal discretization

The solution is advanced in time by an explicit fourth-order Runge-Kutta. The fourth order differences give an accurate solution, since they have been widely tested in previous numerical codes (Vögler et al. 2005; Khomenko & Collados 2006). The vector $\mathbf{u}_0$ describes the state of the system at time t_0 and, according to the equations of Section (3.1), it will have the form and dependences

$$\mathbf{u_0} = \Big(\rho_1, (\rho_0 + \rho_1)\mathbf{v}, \mathbf{B}_1, e\Big)(x, y, z, t_0). \tag{3.28}$$

The system of differential equations may be written as

$$\frac{\partial \mathbf{u}}{\partial t} = \mathbf{R}(\mathbf{u}), \tag{3.29}$$

where $\mathbf{R}(\mathbf{u}) = -\partial \mathbf{F}(\mathbf{u})/\partial x - \partial \mathbf{G}(\mathbf{u})/\partial y - \partial \mathbf{K}(\mathbf{u})/\partial z + \mathbf{H}(\mathbf{u})$ represents the set of spatial derivatives of the fluxes and the source terms of the equations. The next time step is calculated by means of four steps

$$\begin{aligned}
\mathbf{u}_{1/4} &= \mathbf{u}_0 + \frac{\Delta t}{4}\mathbf{R}(\mathbf{u}_0) \\
\mathbf{u}_{1/3} &= \mathbf{u}_0 + \frac{\Delta t}{3}\mathbf{R}(\mathbf{u}_{1/4}) \\
\mathbf{u}_{1/2} &= \mathbf{u}_0 + \frac{\Delta t}{2}\mathbf{R}(\mathbf{u}_{1/3}) \\
\mathbf{u}_1 &= \mathbf{u}_0 + \Delta t\mathbf{R}(\mathbf{u}_{1/2})
\end{aligned} \tag{3.30}$$

where $\mathbf{u}_1$ corresponds to the numerical solution for the time step $t_1 = t_0 + \Delta t$.

3.4 Artificial diffusivity

The general equations of momentum and energy take into account the diffusivity caused by the viscous forces. However, in the conditions of the solar atmosphere, the Reynolds number has a very high value due to the low viscosity, making the characteristic lenghts, in which the diffusivity acts, too small to be resolved by current computers. Variations of these small scales can grow exponentially in time in numerical simulations, and must be damped for the numerical stability of the code.

To damp high-frequency numerical noise on sub grid scales, we replace the physical diffusive terms in the equations of momentum and energy by artificial equivalents. In the induction equation we also replace the magnetic diffusion term by an artificial value. In general, we use a philosophy similar to Stein & Nordlund (1998), Caunt & Korpi (2001) and Vögler et al. (2005). Each physical quantity has its own diffusivity coefficient (scalar/vectorial for scalar/vectorial quantities), which is formed by a shock resolving term, a hyperdiffusivity part, and a constant contribution

$$\nu_l(u) = \nu_l^{\mathrm{shk}}(u) + \nu_l^{\mathrm{hyp}}(u) + \nu_l^0, \tag{3.31}$$

where u is the corresponding quantity and l is one of the spatial coordinates. The shock resolving term takes high values in those regions where there are strong gradients with sudden variations in the velocity between nearby points. Thus, ν^{shk} is selected to be proportional to the absolute value of the divergence of the velocity only in those locations where there are converging flows, being zero in the rest of the domain:

$$\begin{aligned} \nu_l^{\mathrm{shk}} &= c_{\mathrm{shk}} \cdot (\Delta x_l)^2 \cdot |\nabla \cdot \mathbf{v}| \qquad && \nabla \cdot \mathbf{v} < 0 \\ \nu_l^{\mathrm{shk}} &= 0 && \nabla \cdot \mathbf{v} \geq 0 \end{aligned} \tag{3.32}$$

The parameter c_{shk} is a scaling factor of order unity, and Δx_l is the spatial step of the grid in the direction l. We have applied this shock diffusivity in the momentum, energy, and induction equations.

The hyperdiffusivity part is needed to eliminate the noise that can appear due to fluctuations at unresolved scales. With this aim, the ν_{hyp} coefficient is defined in such a way that it detects fluctuations at small scales and takes significant values only in those regions where the numerical noise must be disipated.

The hyperdifusive coefficient acquires different values depending on the physical magnitude u and the coordinate l according to

$$\nu_l^{\mathrm{hyp}}(u) = c_{\mathrm{hyp}} \cdot c_{\mathrm{tot}} \cdot \Delta x_l \cdot \frac{\max_3 \Delta_l^3 u}{\max_3 \Delta_l^1 u}, \tag{3.33}$$

where c_{hyp} is a scaling factor and c_{tot} takes at each point the value extracted from the equation

$$c_{tot} = v + c_S + v_A. \tag{3.34}$$

The expressions $\Delta_l^3 u$ and $\Delta_l^1 u$ represent the third and first absolute differences of u, and they are calculated as

$$(\Delta_l^3 u)_{i+1/2} = |3(u_{i+1} - u_i) - (u_{i+2} - u_{i-1})| \tag{3.35}$$

$$(\Delta_l^1 u)_{i+1/2} = |u_{i+1} - u_i|. \tag{3.36}$$

The $\max_3$ indicates that a maximum over three adjacent i points is taken in the l direction.

The last constant contribution to artificial diffusivity coeficient ν_l, ν_l^0, is introduced in the following way

$$\nu_l^0 = (c_S + v_A)\Delta x_l F(x, y, z). \tag{3.37}$$

It is constant at every grid point of the domain along all the time of the simulation. The function $F(x, y, z)$ gives the spatial form of the constant contribution.

Once the coefficients ν_l of the artificial diffusivity are obtained, they need to be introduced into the MHD equations of Section 3.1. In the case of the motion equation, the term of artificial diffusivity which must be added to Equations (3.17), (3.18), and (3.19) is similar to the one which represents the viscous forces in Equation (2.16), that is

$$\Big(\frac{\partial(\rho \mathbf{v}_1)}{\partial t}\Big)_{\text{diff}} = \nabla \cdot \bar{\tau}, \tag{3.38}$$

but in this case the components of the tensor $\bar{\tau}$ for the artificial diffusivity correspond to

$$\tau_{kl} = \frac{1}{2}\rho\Big(\nu_k(v_l)\frac{\partial v_l}{\partial x_k} + \nu_l(v_k)\frac{\partial v_k}{\partial x_l}\Big). \tag{3.39}$$

In the previous expression, k and l represent again the three coordinates x, y and z, and they complete the nine components of the tensor $\bar{\tau}$. In the induction equation (Equations 3.20, 3.21, and 3.22) the variation of the magnetic field due to the diffusivity is

$$\Big(\frac{\partial \mathbf{B}_1}{\partial t}\Big)_{\text{diff}} = -\nabla \times \varepsilon, \tag{3.40}$$

The vector ε is defined as

$$\varepsilon = \begin{pmatrix} \nu_y(B_z)\frac{\partial B_z}{\partial y} - \nu_z(B_y)\frac{\partial B_y}{\partial z} \\ \nu_z(B_x)\frac{\partial B_x}{\partial z} - \nu_x(B_z)\frac{\partial B_z}{\partial x} \\ \nu_x(B_y)\frac{\partial B_y}{\partial x} - \nu_y(B_x)\frac{\partial B_x}{\partial y} \end{pmatrix}.$$

Finally, the diffusivity term of the internal energy equation (Equation 3.25) takes the form

$$\Big(\frac{\partial p_1}{\partial t}\Big)_{\text{diff}} = \sum_l \frac{\partial}{\partial x_l}\Big(\nu_l(p)\frac{\partial p}{\partial x_l}\Big). \tag{3.42}$$

or

$$\Big(\frac{\partial e_1}{\partial t}\Big)_{\text{diff}} = \sum_l \frac{\partial}{\partial x_l}\Big(\nu_l(p)\frac{\partial e_1}{\partial x_l}\Big). \tag{3.43}$$

if the complete energy equation (Equation 3.23) is used.

All the second derivatives that appear in the diffusive terms are discretized by means of second order central differences. In the case of the terms of the form $\frac{\partial}{\partial x}\Big(\nu\frac{\partial u}{\partial x}\Big)$, at every grid cell i they are calculated as

$$\frac{\partial}{\partial x}\Big(\nu\frac{\partial u}{\partial x}\Big)_i = \frac{1}{\Delta x}\Big(\nu_{i+1/2}\cdot\frac{u_{i+1}-u_i}{\Delta x} - \nu_{i-1/2}\cdot\frac{u_i-u_{i-1}}{\Delta x}\Big). \tag{3.44}$$

In the case of terms with cross derivatives of the form $\frac{\partial}{\partial y}\Big(\nu\frac{\partial u}{\partial x}\Big)$, the values of the hyperdiffusivity are interpolated from the interfaces to the center of the grid points, and the inner part is obtained as

$$\Big(\nu\frac{\partial u}{\partial x}\Big)_i = \Big(\frac{\nu_{i+1/2}+\nu_{i-1/2}}{2}\Big)\cdot\Big(\frac{u_{i+1}-u_{i-1}}{2\Delta x}\Big). \tag{3.45}$$

Finally, we apply again a second order center derivative in the other coordinate, indicated by the subindex j:

$$\begin{aligned}\frac{\partial}{\partial y}\Big(\nu\frac{\partial u}{\partial x}\Big)_i = \Big[&\Big(\frac{\nu_{i+1/2,j+1}+\nu_{i-1/2,j+1}}{2}\Big)\cdot\Big(\frac{u_{i+1,j+1}-u_{i-1,j+1}}{2\Delta x}\Big) - \\ &\Big(\frac{\nu_{i+1/2,j-1}+\nu_{i-1/2,j-1}}{2}\Big)\cdot\Big(\frac{u_{i+1,j-1}-u_{i-1,j-1}}{2\Delta x}\Big)\Big]\frac{1}{2\Delta y}\end{aligned} \tag{3.46}$$

3.5 Time step

The determination of the maximum time step that may be advanced at each time interval is a key issue. Usually, this limit is imposed by the *CFL criterion*, which establishes that a convergent scheme needs the dependence domain of the differential equation to be inside the dependence domain of the numerical scheme. According to this, the mesh width must be larger than the distance traveled by the information in a single time step due to mass flow, waves or diffusion transport. The term "dependence domain" means the region from which the solution depends on for obtaining the next time steps, and the numerical dependence domain is the set of grid points that are used for its calculation. The time step must be chosen to be smaller than the advective time step and the time step imposed by the diffusion terms

$$\Delta t = min(\Delta t_{\mathrm{adv}}, \Delta t_{\mathrm{diff}}). \tag{3.47}$$

In this expression, Δt_{v} is the time step imposed by characteristic speeds. Since it is not possible to define a strict convergence criterion for a non-linear system of equations, the analysis of the linear equations gives a modified CFL criterion approximately valid for MHD equations,

$$\Delta t_{\mathrm{adv}} = \Big[\frac{c_{\mathrm{adv}}}{1/\Delta x^2 + 1/\Delta y^2 + 1/\Delta z^2}\Big]^{1/2}\frac{1}{v_{\max}}, \tag{3.48}$$

where $v_{\max}$ is the maximum value of the sound and Alfvén speed. The time step imposed by the diffusion Δt_{diff} corresponds to the minimum of the diffusion time across the three dimensions,

$$\Delta t_{\mathrm{diff}} = c_{\mathrm{diff}}\min\Big(\frac{\Delta x^2}{\nu_x}, \frac{\Delta y^2}{\nu_y}, \frac{\Delta z^2}{\nu_z}\Big), \tag{3.49}$$

where the constant coefficients c_{adv} and c_{diff} are taken to be below one to ensure the stability of the solution. The diffusion coefficients $\nu_{x,y,z}$ are those defined in Section (3.4).

3.6 Filtering

In the particular case of wave simulations, a high diffusion is not desirable since it modifies the wave amplitudes. At the same time, a low diffusion cannot always prevent the development of high frequency noise. For that reason we perform an additional filtering of small wavelengths. Following Parchevsky & Kosovichev (2007), we use a sixth-order digital filter to eliminate unresolved short-wave components

$$u_{\mathrm{filt}} = u(x) - D(x) = u(x) - \sum_{m=-3}^{3} d_{\mathrm{m}} u(x + m\Delta x), \tag{3.50}$$

where u is a variable before filtering, u_{filt} is after filtering, and $D(x)$ is the damping funtion. The filter can be applied in the three spatial coordinates independently. In the frequency domain, the response function $G(k)$ of the filter relates the Fourier Transform of the original function $\tilde{u}$ with the filtered $\tilde{u}_{\mathrm{filt}}$ according to $\tilde{u}_{\mathrm{filt}}(k) = G(k)\tilde{u}(k)$. The coefficients d_{m} have been chosen as

$$G(k\Delta x) = 1 - \sum_{m=-3}^{3} d_m e^{imk\Delta x} = 1 - sin^6\Big(\frac{k\Delta x}{2}\Big), \tag{3.51}$$

and they are symmetric, taking the values:

$$d_0 = \frac{5}{16}, \quad d_1 = d_{-1} = -\frac{15}{64}, \quad d_2 = d_{-2} = \frac{3}{32}, \quad d_3 = d_{-3} = -\frac{1}{64}. \tag{3.52}$$

3.7 Boundary conditions

Boundary conditions are an important issue for wave simulations. One usually wants to prevent spurious wave reflections at the boundaries. Two strategies commonly applied are based on characteristic boundary conditions or sponge layers. Calculating characteristic conditions (Rosenthal et al. 2002), apart from tricky, gives good results in simple magnetic field configurations, when the wave propagation directions are easily predictable. For more complex magnetic field configurations the calculation of the characteristic directions is not an easy task. The other alternative, the sponge layer, consists in locating an absorbing layer at the boundary to dissipate the wave energy and prevent it from coming back to the physical domain. This strategy is implemented in the code SLiM (Cameron et al. 2007). Absorbing layers give good results only when the absorption is gradual and need a large amount of grid points. Thus, numerically they are very costly. In our code we used, though, another alternative, the Perfectly Matched Layer (Berenger 1994).

The Perfect Matched Layer (PML) is designed to absorb waves without reflections. This method was first introduced by Berenger (1994) to absorb electromagnetic waves in numerical solutions of Maxwell equations. Later, it has been applied to Euler equations (Hu 1996) and to simulations of acoustic waves in a strongly stratified solar convection zone (Parchevsky & Kosovichev 2007). In our code, we extend the method to the full set of the MHD equations. The PML layer for MHD equations was applied previously by Parchevsky & Kosovichev (2009), though its stability is not discussed. According to Hesthaven (1998), the application of a filter allows the scheme to improve stability, and we have verified empirically that our PML scheme, together with the high frequency filter, allows us to delay the effects of possible instabilities the necessary time to complete long enough simulations. The PML layer is introduced in the boundaries of the computational domain, and in this region the MHD equations are modified in order to add a term that damps the perturbations that reach the boundary.

The expressions of the fluxes $\mathbf{F}(\mathbf{u})$, $\mathbf{G}(\mathbf{u})$, and $\mathbf{K}(\mathbf{u})$ and the term $\mathbf{H}(\mathbf{u})$ can be found in the system of MHD equations (Section 3.1). Inside the PML, variables $\mathbf{u}$ are split into three components in such a way that $\mathbf{u} = \mathbf{u_1} + \mathbf{u_2} + \mathbf{u_3}$ and also $\mathbf{H}(\mathbf{u}) = \mathbf{H}_1(u) + \mathbf{H}_2(u) + \mathbf{H}_3(u)$. The system of MHD equations is split into a set of three coupled, one dimensional equations:

$$\frac{\partial \mathbf{u}_1}{\partial t} + \frac{\partial \mathbf{F}(\mathbf{u})}{\partial x} + \sigma_x(x)\mathbf{u}_1 = \mathbf{H}_1(\mathbf{u}), \tag{3.53}$$

$$\frac{\partial \mathbf{u}_2}{\partial t} + \frac{\partial \mathbf{G}(\mathbf{u})}{\partial y} + \sigma_y(y)\mathbf{u}_2 = \mathbf{H}_2(\mathbf{u}), \tag{3.54}$$

$$\frac{\partial \mathbf{u}_3}{\partial t} + \frac{\partial \mathbf{K}(\mathbf{u})}{\partial z} + \sigma_z(z)\mathbf{u}_3 = \mathbf{H}_3(\mathbf{u}). \tag{3.55}$$

These split Equations (3.53)–(3.55) are solved independently in the PML, in contrast to the unsplit forms (Equation 3.6) which are solved in the physical domain. When the damping coeficients σ are zero, the equations in the PML layer are the same of the rest of the domain, so PML equations include the general equations as a particular case.

To understand the effects of the absortion terms of Equations (3.53)–(3.55) in the solution of the system of MHD equations, we consider a linear one-dimensional case, with no magnetic field and no diffusion, in a homogeneous atmosphere in equilibrium. Note that as we only study one dimension, there is no need to split the density variable into several components. With these simplifications, the linearized equations of continuity (Equation 3.16) and motion (Equation 3.17) for the PML media are:

$$\frac{\partial \rho_1}{\partial t} + \frac{\partial}{\partial x}(\rho_0 v_x) + \sigma_x \rho_1 = 0 \tag{3.56}$$

$$\frac{\partial}{\partial t}(\rho_0 v_x) + \frac{\partial p_1}{\partial x} + \sigma_x \rho_0 v_x = 0. \tag{3.57}$$

Assuming the propagation of plane damped waves, the velocity and the perturbation in pressure and density take the form

$$[v_1, p_1, \rho_1] = [V, P, R]e^{i\omega(t-\alpha x)}, \tag{3.58}$$

where ω is the frequency of the wave, and α is a complex constant. Introducing this type of solutions into Equations (3.56) and (3.57), we retrieve the expresions

$$R - \alpha V \rho_0 - \frac{i\sigma_x}{\omega} R = 0, \tag{3.59}$$

$$\rho_0 V - P\alpha - \frac{i\sigma_x \rho_0}{\omega} V = 0. \tag{3.60}$$

From the continuity and internal energy equations, the following relation between the perturbations of the density and pressure is obtained

$$\frac{p_1}{p_0} = \gamma \frac{\rho_1}{\rho_0}. \tag{3.61}$$

The combination of Equations (3.59), (3.60) and (3.61), after introducing the definition of the sound speed $c_S = (\gamma p_0/\rho_0)^{1/2}$, yields the following expression for α:

$$\alpha = \frac{1}{c_S}\Big(1 - \frac{i\sigma_x}{\omega}\Big) \tag{3.62}$$

Finally, with the resulting α, we obtain from Equation (3.58) that all the magnitudes have the form

$$\phi_1 = \phi_0 e^{i\omega(t - x/c_S)} e^{-\sigma_x x/c_S}. \tag{3.63}$$

This equation shows that the perturbation keeps the behavior of a plane wave propagating with frequency ω and wavenumber $k = \omega/c_S$, but its amplitude is modulated by an exponentially decreasing factor along the direction x. This example illustrates the desired action of the PML in our code.

The coefficients $\sigma_x(x)/\sigma_y(y)/\sigma_z(z)$ only depend on x/y/z coordinate and are non-zero in the x/y/z PML faces, respectively. Thus, at the six faces of the computational domain the damping coefficients $(\sigma_x, \sigma_y, \sigma_z)$ are chosen in such a way that those which are far from their corresponding boundaries are zero. For example, in the top and bottom boundaries, the coefficients are $(0, 0, \sigma_z)$, absorbing the waves which move toward out of the domain. In the twelve edges, one of the damping coefficients σ is set to zero, while the two that have a value different from zero at the adjacent sides keep their value, for example $(\sigma_x, 0, \sigma_z)$. In the case of the eight corners, all the σ components are different from zero.

Theoretically, a PML with constant absorption coefficient produces no reflections for plane waves incident on a flat interface for any angle of incidence and any frequency. However, due to the finite difference implementation of the PML equations in numerical calculations, reflections may appear when σ has a steep gradient (Berenger 1996). To solve this problem it is necessary to include smooth variations in the absorption coefficients from small values at the interface between the PML medium and the physical domain to large values at the outer boundary. Following Hu (2001), good results are obtained with absorption coefficients of the form

$$\sigma_x = \frac{a}{\Delta x}\Big(\frac{x - x_{PML}}{x_{PML}}\Big)^2, \tag{3.64}$$

$$\sigma_y = \frac{b}{\Delta y}\Big(\frac{y - y_{PML}}{y_{PML}}\Big)^2, \tag{3.65}$$

$$\sigma_z = \frac{c}{\Delta z}\Big(\frac{z - z_{PML}}{z_{PML}}\Big)^2, \tag{3.66}$$

where Δx, Δy and Δz are the discretization steps, a, b and c are constants controlling the damping amplitude, and x_{PML}, y_{PML} and z_{PML} are the thickness of the PML domain in each spatial direction. In a typical calculation we need PML to be of 10–15 grid points. The coefficients a, b and c depend on each particular simulation and must be proportional to the wave speed at the boundaries. We locate PMLs at all boundaries of our simulation domain. The results presented in Khomenko et al. (2008) show that this strategy gives good results even for strong shocks.

For some simulations it is interesting to use other boundary conditions. The code can also account for periodic and closed boundary conditions. The design of the code allows us to choose the appropriate condition for a specific numerical simulation. According to the numerical scheme introduced for the calculation of the spatial derivatives (Equation 3.27), the two cells next to the limit of the computational domain have to be filled by the boundary conditions. The closed boundaries are implemented as

$$\begin{aligned} u_1 &= u_3, \\ u_2 &= u_3, \\ u_{n-1} &= u_{n-2}, \\ u_n &= u_{n-2}, \end{aligned} \tag{3.67}$$

where u is a certain magnitude, i is an index which covers one of the spatial dimensions, and n is the number of cells in that dimension. When the simulation uses PML layers, closed boundaries are set at the limits of the computational domain.

The form of periodic boundary conditions is

$$\begin{aligned} u_1 &= u_{n-3}, \\ u_2 &= u_{n-2}, \\ u_{n-1} &= u_3, \\ u_n &= u_4. \end{aligned} \tag{3.68}$$

In all the numerical simulations of wave propagation we have used PML layers in order to avoid interferences between the different modes which could appear from the boundaries.

3.8 Parallelization

Parallelization has been done with MPI following a distributed memory concept in which all data used by a processor are situated on the memory partition accessible to it. Data are split in a certain number of processors by means of a domain decomposition scheme. The full numerical domain is divided into a set of three dimensional subdomains, with communication between processors occurring only at their common data boundaries. For this purpose, each domain includes three layers of "ghost" cells at each boundary. The 5-point stencil of the fourth-order scheme needs two cells outside the subdomain, while for the filtering it is necessary to include one more "ghost" layer. The boundaries of the subdomains which are neighbors of other subdomains receive directly the required information and store it in the "ghost" layers, while when the boundary of the subdomain coincides with the global boundary, the "ghost" layers are settled with the values imposed by the boundary condition.

4

Tests on numerical performance

In this section we describe the results of standard numerical tests that have been performed to verify the code performance and prove its robustness.

4.1 1D Riemann shock tube test

The Riemann shock tube test (Sod 1978; Caunt & Korpi 2001) has been simulated in order to test the behavior of the hydrodynamical part of the code, including discontinuities in the properties of the fluid. This allows us to analyze how the artificial viscosity copes with shock capturing. To that aim, we have taken a 1D physical domain (with unity size, for simplicity) whose initial state includes a discontinuity at $x = 0.5$. On one side of the discontinuity we have density $\rho_1 = 1$ and pressure $p_1 = 1$, while on the other side $\rho_1 = 0.125$ and $p_1 = 0.1$. The ratio of specific heats is $\gamma = 1.4$ and the initial velocity as well as the magnetic field are set to zero. The problem has been simulated with a resolution of 256 grid points and closed boundaries.

Figure 4.1 shows the density, velocity, internal energy density per unit mass and pressure at time t=0.2 for the simulation compared to the analytical solution. From left to right the plot shows a rarefaction wave (from $x = 0.25$ to $x = 0.5$), a contact discontinuity (at $x = 0.68$) and a shock front ($x = 0.85$). The position of all of them matches precisely with the analytical solution and the magnitudes of the fluid properties are correct. The contact discontinuity for the energy was inevitably smoothed, as shown in the plot at the botton left where a region around it is amplified, but still 93% of the amplitude of the discontinuity is covered with 10 grid points. Moreover, the shock front is resolved with three grid points, which proves the good performance of the code in shock capturing.

4.2 1.5D Brio and Wu shock tube

To test the formation of MHD shock waves we use the MHD analog of the Sod shock tube problem described by Brio & Wu (1988), which has been widely used in previous works (Stone & Norman 1992; Caunt & Korpi 2001; Shelyag et al. 2008). We can compare our results with those given in the literature, since no known analytical solution exists for the

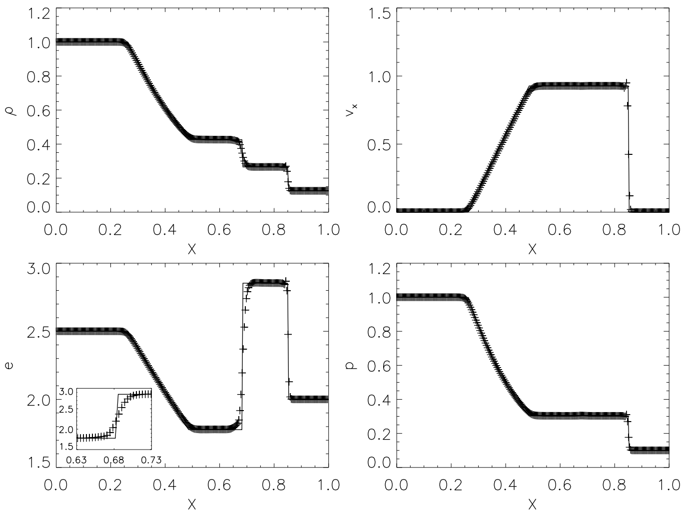

Figure 4.1: Standard Riemann shock tube problem at $t = 0.2$. Crosses represent the numerical solution, while lines represent the analytic solution with an exact nonlinear Riemann solver. The inner plot on the left bottom pannel helps to visualize better the discontinuity at $x = 0.68$.

evolution of this problem. In this 2D test the fluid is initialized in a physical domain from $x = 0$ to $x = 1$ and with a discontinuity in density, pressure, and magnetic field normal to the direction of motion located at $x = 0.5$. Parameters at the left-hand side from the discontinuity are $\rho_1 = 1$, $p_1 = 1$, and $B_{y1} = \sqrt{\mu_0}$, and at the right hand side are $\rho_2 = 0.1$, $p_2 = 0.1$ and $B_{y2} = -\sqrt{\mu_0}$. All the domain is permeated with a constant magnetic field along the direction of motion $B_x = 0.75\sqrt{\mu_0}$ and the adiabatic index γ is set to 2. In this case, the resolution is 800 grid points in the direction of the shock wave propagation, similar to the other published works. All the boundaries are closed.

The density, velocity in the x direction, pressure, and magnetic field in the y-direction are shown in Figure 4.2. This MHD Riemann problem produces a complex solution with several components: the waves moving to the left are a fast rarefaction wave and a slow compound wave (consisting of a slow rarefaction together with a slow shock), and the waves moving to the right include a contact discontinuity, a slow shock, and a fast rarefaction wave. Comparison of our results with other works show that the waves have propagated with the correct velocities and have similar magnitudes, indicating that they are in good agreement with the other solutions. The slow shock is resolved again with only three grid points.

4.3 2D Ország-Tang vortex

The next test is the Orszag-Tang vortex, which was originally studied by Orszag & Tang (1979) and has been used to probe several codes (Ryu et al. 1995; Dai & Woodward 1998; Londrillo & Del Zanna 2000; Shelyag et al. 2008). This problem allows us to demonstrate the robustness of the numerical scheme used in our code solving the two-dimensional interaction of nonlinear shock waves and also to compare qualitatively the code with other codes. The initial conditions for density and gas pressure are constant, with $\rho = 25/(36\pi)$ and $p = 5/(12\pi)$, the magnetic field $B_x = -\sin(2\pi y)$ and $B_y = \sin(4\pi x)$ and the initial

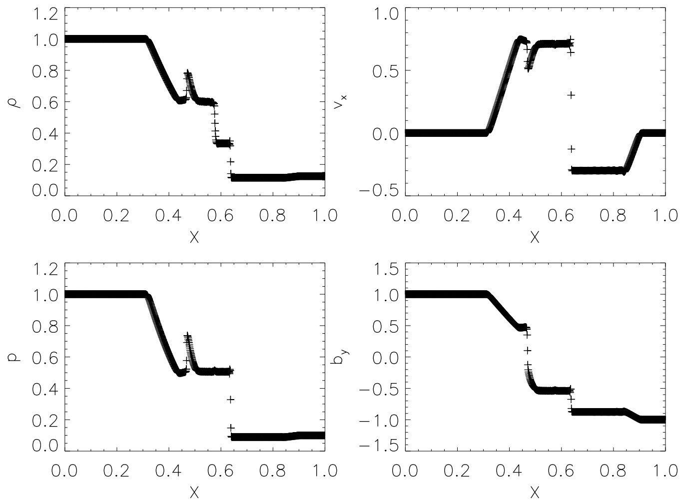

Figure 4.2: Numerical solution of the Brio & Wu problem at $t = 0.11$ (see Section 4.2).

velocity $v_x = -\sin(2\pi y)$ and $v_y = \sin(2\pi x)$. Therefore, the initial flow is a velocity vortex superimposed to a magnetic vortex, with a common X-point, but with different structure. The initial Mach number is $M_0 = 1$ and the adiabatic index is set to $\gamma = 5/3$. In our simulation for this problem we have chosen a unit size in horizontal and vertical dimensions and the resolution of the simulation box is set to 512 × 512 grid points. Figure 4.3 presents the density at time $t = 0.5$, showing precise agreement with the other published works.

4.4 3D Acoustic wave

Since our code is oriented to the simulations of waves, it is necessary to test how well it can approximate the known analytical solutions for different types of waves in a stratified atmosphere, their propagation speeds, amplitudes and shock development. The analytical solution of a linear acoustic wave propagating in an isothermal atmosphere with vertical stratification due to gravity and permeated with a constant vertical magnetic field is known from Ferraro & Plumpton (1958), see Section (2.2.3). The vertical velocity for a wave with frequency ω, above the cutoff frequency $\omega_c = \gamma g/(2c_s)$, is as follows:

$$v_z(z,t) = De^{z/2H_0} \sin\left[(\sqrt{\omega^2 - \omega_c^2})/c_s z + \omega t\right], \tag{4.1}$$

where $H_0 = c_s^2/(\gamma g)$ is the pressure scale height and c_s is the sound speed. This analytical solution, with a period of 15 s and starting amplitude of 10 m s^{-1}, has been introduced as a bottom boundary condition without variations in the horizontal directions and its evolution in time has been calculated with the numerical code. The physical domain is set to 1000 km in the vertical direction with a resolution of 200 grid points, using 20 of them as PML domain at the top. In both horizontal dimensions the computational domain consists of seven grid points, covering 35 km, and periodic boundary conditions were used in these directions. In Figure 4.4, we show the comparison between the numerical and the analytical linear solution for the vertical velocity after 197 s of simulations. The numerical solution

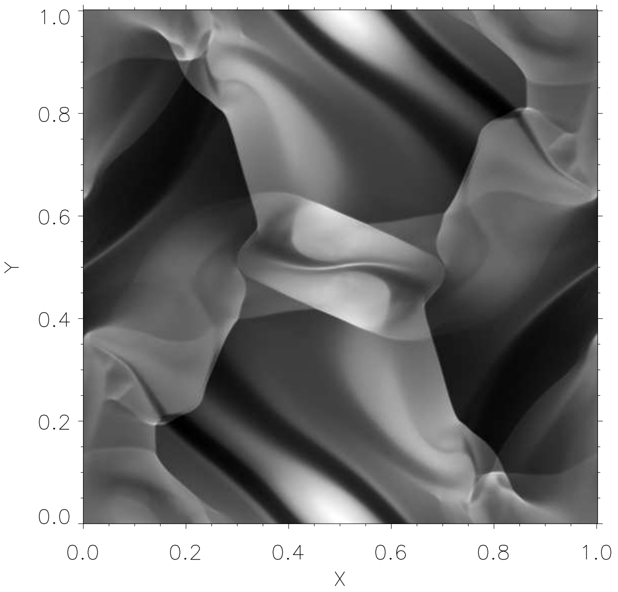

Figure 4.3: Mass density at $t = 0.5$ of the Ország-Tang vortex simulation

matches the exact solution in the computational domain, while it is damped effectively by the PML layer. It is important to note that the amplitude and propagation speeds are both described correctly by the numerical solution and that the numerical diffusion does not affect the amplitude increase with height.

The dashed line represents the difference between both solutions, which also increases with height. The main contribution to this difference comes from the nonlinear terms that are taken into account in the numerical calculation, while the analytical solution is restricted to the linear case. This was verified since a bottom boundary with half initial amplitude produces a reduction of the difference by exactly a factor 4, and the wavelength of the difference is half of the corresponding to the wave. Also, it is important to note that no spurious reflections are present and that the PML boundary works well.

4.5 3D Alfvén wave

As a next step, the response of the numerical scheme to the propagation of an Alfvén wave in an isothermal, stratified atmosphere with a vertical magnetic field is analyzed. The analytical solution was developed by Ferraro & Plumpton (1958) (see Section 2.2.3), and, according to Khomenko et al. (2003), the solution for the horizontal velocity can be written as

$$v_y(z,t) = i\xi_0\omega\sqrt{J_0^2 + Y_0^2}\exp\Big[i\Big(\omega t + \text{arctang}\frac{Y_0}{J_0}\Big)\Big] \tag{4.2}$$

where J_0 and Y_0 are Bessel functions. The same atmosphere as in the previous section was

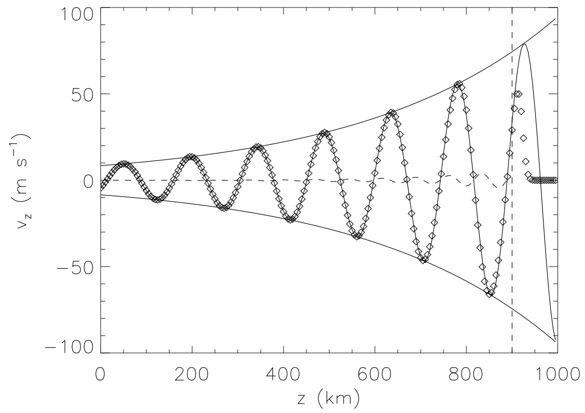

Figure 4.4: Vertical velocity profile of vertically propagating acoustic waves in an isothermal, stratified atmosphere with the vertical constant magnetic field at $t = 197$ s. Solid line: exact solution; diamonds: numerical solution. The dashed line is the difference between both solutions. The vertical dashed line indicates the location of the PML interface.

used in this test, but now the bottom layers were excited with the solution of an Alfvén wave of period 10 s and an amplitude of 10 m s^{-1} as a boundary condition. This driver generates the propagation of Alfvén waves toward higher layers of the atmosphere. The horizontal velocity of both the numerical and exact solutions for time $t = 115$ s is shown in Figure 5.27, demonstrating a very good match. The dashed line shows the difference between the numerical and the analytical solution. In this case, the nonlinearities are not so important since the amplitude is lower than the one of the acoustic wave, and the discrepancy between both solution is due to the reflection produced at the top boundary. The PML layer results more problematic for transversal waves which oscillate parallel to the interface between the PML media and the physical domain, and they give rise to reflections of 5%-6% of the velocity.

4.6 3D Strong blast wave

Our last test consists of the explosion of a spherical high gas pressure region in a magnetized, initially static 3D medium. It has been commonly used for code validation (see, for example Balsara & Spicer 1999; Londrillo & Del Zanna 2000), and the setup consists of a cubic domain with 256 grid points in the three spatial dimensions spanning from 0 to 1. The initial density, ρ_0, is set to unity in all the domain, while the initial pressure is set to unity all over except a spheric hot gas region located at the center of the domain of radius $r_0 = 0.125$, which is a hundred times overpressured ($p_1 = 100$). A constant magnetic field with a strength of $B_{0x} = 10\sqrt{\mu_0}$ is initialized along the $x-$direction.

In Figure 4.6, we show a cut of the density in the plane x-y at $z = 0.5$ and $t = 0.02$. The system shows the axial symmetry imposed by the magnetic field. We can identify the different wave modes present in the simulations. The outermost wave corresponds to the fast magnetoacoustic mode, and inside this region there are two wave fronts propagating along the magnetic field, which is a slow magnetoacoustic shock. This test verifies that our

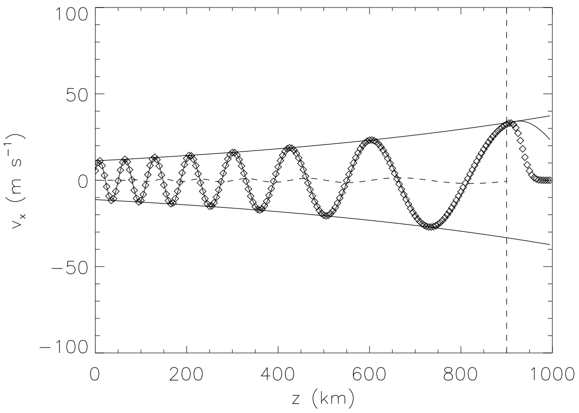

Figure 4.5: Horizontal velocity profile of Alfvén waves in an isothermal, stratified atmosphere with a vertical constant magnetic field at $t = 115$ s. Solid line: exact solution; diamonds: numerical solution. The dashed line is the difference between both solutions. The vertical dashed line indicates the position of the PML interface.

code can handle the 3D propagation of highly nonlinear waves at the correct propagation speed, resolving the shocks thanks to the hyperdiffusive terms.

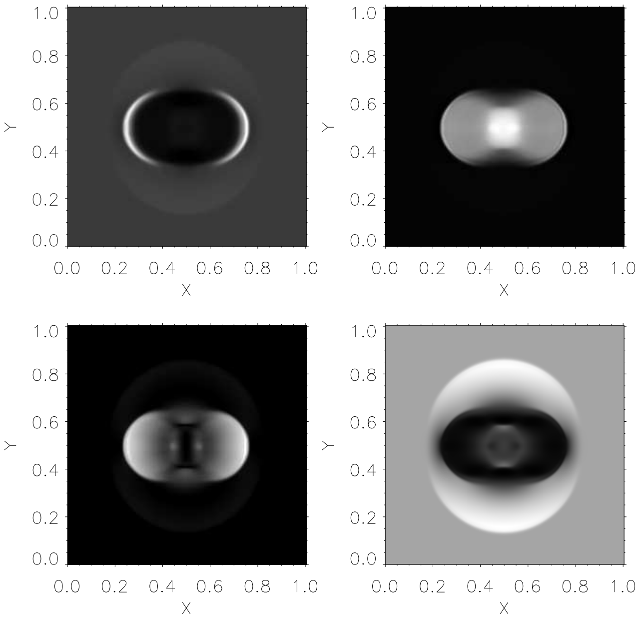

Figure 4.6: Numerical solution of the 3D strong blast wave density at the plane x-y and $z = 0.5$ at t=0.02. From left to right and from top to bottom: mass density, pressure, velocity squared, and magnetic pressure.

5

Mode transformation in 3D numerical simulations

The objetive of this chapter is to investigate the response of magnetic atmospheres in equilibrium to an arbitrary perturbation propagating in the form of waves. We address the problem in three dimensions and discuss the propagation and transformation of the waves in a wide range of periods, from about 1 to 5 min, in the upper layers of sunspots.

We perform several simulations where the static structure in equilibrium is perturbed, and it generates a set of wave modes. We have identified the presence of different magneto-acoustic and Alfvén modes, and analyzed their propagation between the photosphere and the chromosphere, including their energy contribution. At the height where the sound and Alfvén speeds are similar different wave modes can interact, and wave transformation takes place. Our aim is to perform simulations realistic enough to imitate the wave excitation in sunspots, reproduce the change of wave frequency with height and the formation of shocks at chromospheric layers, and to be at the level of allowing the comparison with photospheric and chromospheric observations by spectral synthesis.

Most of the works on the simulations of wave propagation in the upper layers of sunspots, as well as the analytical theories of mode transformation, were developed for high-frequency waves with frequencies above, or just at, the cutoff frequency. There is another class of simulations where the problem of helioseismic wave propagation below sunspots is addressed and waves with realistic solar frequencies in the 3-5 mHz range are considered (Cally & Bogdan 1997; Parchevsky & Kosovichev 2009; Hanasoge 2008; Cameron et al. 2008; Moradi et al. 2009b; Khomenko et al. 2009). In the latter works most attention has been paid to the wave propagation in sub-surface layers, rather than in upper photospheric and chromospheric layers. Thus, there is gap between these two kind of models. With the development of our code we pretend to cover this gap and study waves with 3–5 mHz frequency above the photosphere.

The organization of the chapter is as follows. Section 5.1 describes the configuration of the simulations. In Section 5.2 the description of the magneto-static sunspot model in equilibrium is included and in Section 5.3 we explain the projection of the vectorial

Table 5.1: Summary of the simulation runs

Section	Driving	$[x_{\rm src}, z_{\rm src}]$ (Mm)	$R_{\rm src}$ (Mm)	Duration (s)	Domain	Figures
5.4.1	50 s, harmonic	[0,-0.5]	0.15	904	Small	5.2–5.7
5.4.2	50 s, harmonic	[-3,-0.5]	0.15	1023	Small	5.8–5.13
5.4.3	180 s, harmonic	[0,-0.5]	0.15	930	Small	5.14–5.16
5.4.4	300 s, wavelet	[0,-0.5]	0.9	1511	Small	5.17–5.19
5.4.4	300 s, harmonic	[0,-0.5]	0.9	1212	Small	–
5.4.5	300 s, wavelet	[-5,-1]	2.25	1682	Large	5.20, 5.21, 5.23, 5.24
5.4.5	300 s, wavelet	[-10,-1]	2.25	1636	Large	5.22, 5.23, 5.25
5.4.5	300 s, wavelet	[-15,-1]	2.25	1636	Large	5.23, 5.26

quantities and the calculation of the energy fluxes developed to identify the wave modes. The simulations are analized in Section 5.4 and the results are discussed in Section 5.5.

5.1 Set up of the simulations

Below in this section we discuss several simulations of the propagation and transformation of MHD waves in a magnetostatic sunspot model, excited by pulses with different periods and locations. To facilitate the reading of this section, Table 1 summarizes the simulation runs. It gives the number of the subsection where the results are presented, the properties of the driver, its location, horizontal source size, the duration of the simulations, the computational domain used (defined in Section 5.2), and the numbers of the corresponding figures. In all cases, to identify the different wave modes in three spatial dimensions we use projections of the velocity into three characteristic directions. To quantify the mode transformation we calculate the acoustic and magnetic energy fluxes (see Section 5.3).

We use a vertical force $\mathbf{S}(t)$ in the momentum equation (Equation 3.2) to perturb a magnetostatic sunspot atmosphere in equilibrium and study the waves generated by this perturbation. We have performed several numerical simulations, all of them with the source situated at $y_{\rm src} = 0$ Mm and below the photosphere, but with differences in the period, the horizontal x location of the source relative to the axis of the sunspot, the depth, as well as the horizontal size of the source $R_{\rm src}$.

In the simulations described in Sections 5.4.1, 5.4.2, and 5.4.3 the temporal behavior of the driver is harmonic and is described by the expression

$$S_z(r,t) = AP(r) \sin \frac{2\pi t}{\tau} \tag{5.1}$$

In this equation, A is the amplitude of the source, $P(r) = \left[1 - (r/R_{\rm src})^2\right]^2$ describes the source shape, $R_{\rm src}$ is the source radius, $r = \sqrt{(x-x_{\rm src})^2 + (y-y_{\rm src})^2 + (z-z_{\rm src})^2}$ is the distance from the source center, and τ is the period of the harmonic source. $P(r)$ is zero if $r > R_{\rm src}$. The x and y components of $\mathbf{S}$, $S_x(r,t)$ and $S_y(r,t)$, are set to zero.

In the simulations described in Sections 5.4.4 and 5.4.5, the behavior of the driver is not harmonic in time, but rather has the shape of a Ricker wavelet:

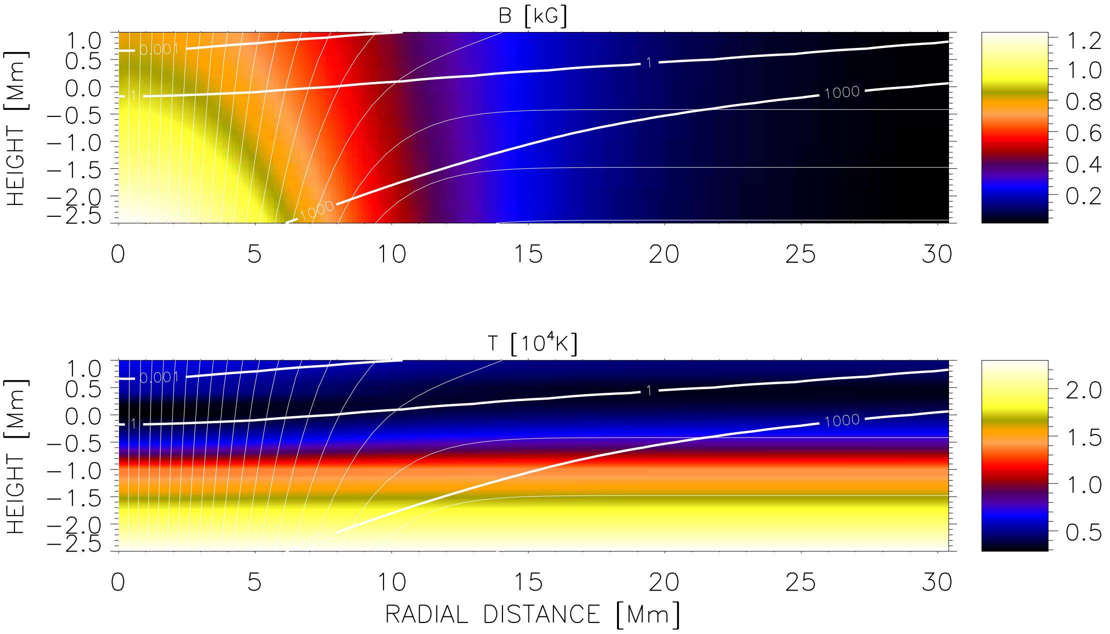

Figure 5.1: Topology of the sunspot model. Top: Magnetic field strength; bottom: Temperature. White thin lines are magnetic field lines. White thick lines with labels are the contours of c_S^2/v_A^2.

$$S_z(r,t) = AP(r)\left(1 - 2\tau_0^2\right) e^{-\tau_0^2}, \tag{5.2}$$

where $\tau_0 = \omega_0 t/2 - \pi$. Such driver produces a spectrum of waves with a central frequency ω_0 (Parchevsky & Kosovichev 2009). We set $\omega_0 = 3.33$ mHz, so the spectrum of our driver resembles a solar one and covers a broad range of frequencies.

These latter runs are particularly interesting, as they allow us to study the behavior of a realistic spectrum of solar waves in the upper layers (photosphere and chromosphere) of a sunspot model, including the propagation of individual wave modes and wave energy fluxes. As far as we are aware of, no such investigation has been performed as of today.

5.2 Magnetostatic sunspot model

We use a magnetostatic (MHS) model atmosphere in equilibrium representative of a sunspot, adopted from Khomenko & Collados (2008). This MHS model is a thick flux tube with distributed currents, it is azimuthally symmetric and has no twist. The variations of field strength and gas pressure are continuous across the spot. At 40 Mm far from the sunspot axis the model merges smoothly into a quiet Sun atmosphere taken from the model S (Christensen-Dalsgaard et al. 1996) in the deep sub-photosphere layers and continuing as a VAL-C model (Vernazza et al. 1981) in the photospheric and chromospheric layers. The sunspot axis in the atmospheric layers is given by the semi-empirical model of Avrett (1981).

In this set of simulations we have used two different computational domains. In both the optical depth $\tau_{5000} = 1$ at the photospheric quiet Sun atmosphere was chosen as the zero level of the coordinate z. In the first set of simulations, the dimensions of the computational domain (denoted as “Small” in Table 5.1) are 2.5 Mm in the vertical direction and 15 Mm in each horizontal direction with a grid step size of $\Delta z = 25$ km and $\Delta x = \Delta y = 75$ km. The bottom level is 1.25 Mm below z=0 Mm. The top level is 1.25 Mm above this height. A PML layer of 10 grid points was used at both bottom and top boundaries. With this, the physical domain occupies from $z = -1$ Mm to $z = 1$ Mm. The axis of the sunspot is placed at the center of the simulation domain. The magnetic field at the axis is about 900 G at $z = 0$ Mm. For the second set of simulations we used the same magneto-static model, but the computational domain is larger, covering 60 Mm in both horizontal directions (named “Large” in Table 5.1). It spans from $z = -2.5$ to $z = 1$ Mm (excluding PML layer). These simulations have a coarser resolution of $\Delta z = 50$ km and $\Delta x = \Delta y = 150$ km.

5.3 Identification of the wave modes in simulations

In the case of a real atmosphere, the division into pure wave modes is not so simple as in the idealized case described in Section 2.2.2, as often no clear distinction between the modes can be done neither physically nor mathematically. Even in the simple case discussed in Section 2.2.2, the governing partial differential equation factors into a single second-order wave equation for the Alfvén mode and a fourth-order wave equation for the coupled fast-slow modes, so the idea that there are three distinct modes may not always be correct. However, the simplicity of this picture makes it attractive and we will discuss the properties of the waves in realistic atmospheres in terms of the three modes.

To help the identification of the wave modes in simulations, we use the mode properties described in Section 2.2.2. We project the vectorial quantities (velocity and magnetic field perturbations) into the directions aligned/normal to the equilibrium magnetic field $\mathbf{B}_0$.

At each location of the computational domain, we calculated the projections of the $\mathbf{v_1}$ and $\mathbf{B_1}$ into the following Cartesian directions:

$$\hat{e}_{\text{long}} = [\cos\phi\sin\theta,\, \sin\phi\sin\theta,\, \cos\theta], \tag{5.3}$$

$$\hat{e}_{\text{perp}} = [-\cos\phi\sin^2\theta\sin\phi,\, 1-\sin^2\theta\sin^2\phi,\, -\cos\theta\sin\theta\sin\phi], \tag{5.4}$$

$$\hat{e}_{\text{trans}} = [-\cos\theta,\, 0,\, \cos\phi\sin\theta], \tag{5.5}$$

where θ is the magnetic field inclination from the vertical and ϕ is the field azimuth, measured from the XZ plane. The direction of $\hat{e}_{\text{long}}$ is along the magnetic field $\mathbf{B}_0$. The direction of $\hat{e}_{\text{perp}}$ is normal to the field and was chosen following Cally & Goossens (2008) as the asymptotic polarization direction of the Alfvén mode in the low-β regime. The last component $\hat{e}_{\text{trans}} = \hat{e}_{\text{long}} \times \hat{e}_{\text{perp}}$ is set in the direction normal to the other two.

We expect that in a region where $c_S > v_A$, the slow magneto-acoustic mode will be identified in $\hat{e}_{\text{trans}}$ projection of the velocity vector, while the fast magneto-acoustic mode will be equally visible in all velocity components as it propagates isotropically. In a region where $c_S < v_A$, the slow magneto-acoustic mode will be identified projected into the $\hat{e}_{\text{long}}$ direction, the Alfvén mode projected into the $\hat{e}_{\text{perp}}$ direction and the fast magneto-acoustic mode in the direction normal to these two.

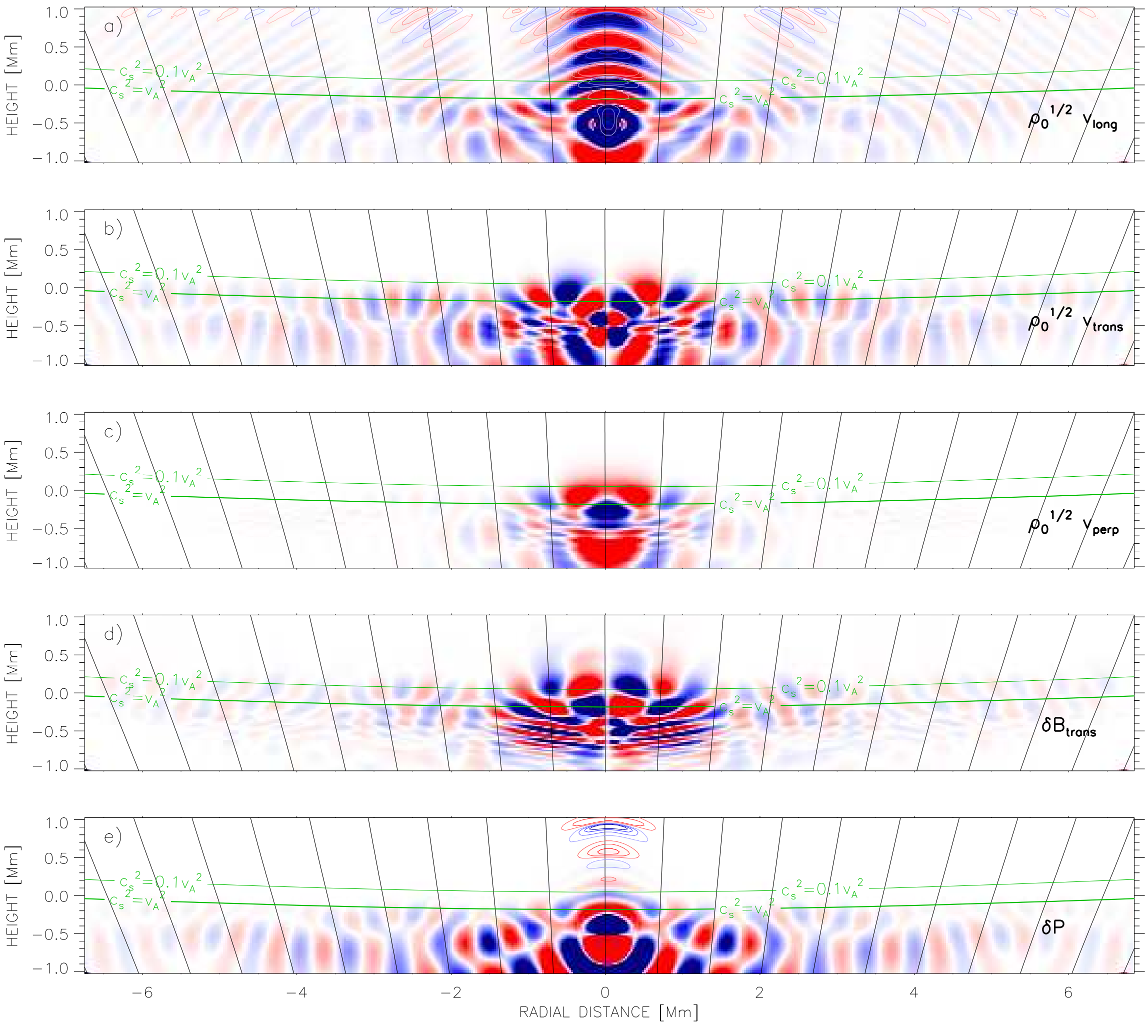

Figure 5.2: Variations of the velocity in the direction $\hat{e}_{\rm long}$ (a), $\hat{e}_{\rm trans}$ (b), and $\hat{e}_{\rm perp}$ (c), all of them scaled with factor $\sqrt{\rho_0}$ of the unperturbed density; the magnetic field in the direction $\hat{e}_{\rm trans}$ (d), and pressure (e) at an elapsed time $t = 820$ s after the beginning of the simulations for the 50 s harmonic force located at $x = 0$ km, $y = 0$ km and $z = -500$ km. All panels show the plane $y = 0$ km, except panel (c), which shows $y = 400$ km. Black inclined lines are magnetic field lines. Green lines are contours of constant v_A^2/c_S^2. The image color coding is such that blue colors represent lower values and red colors are higher values with respect to the mean. Scaling in panels (a), (b), and (c) is the same. Panel (a) shows contours of equal longitudinal velocity and panel (d) shows contours of equal p_1/p_0.

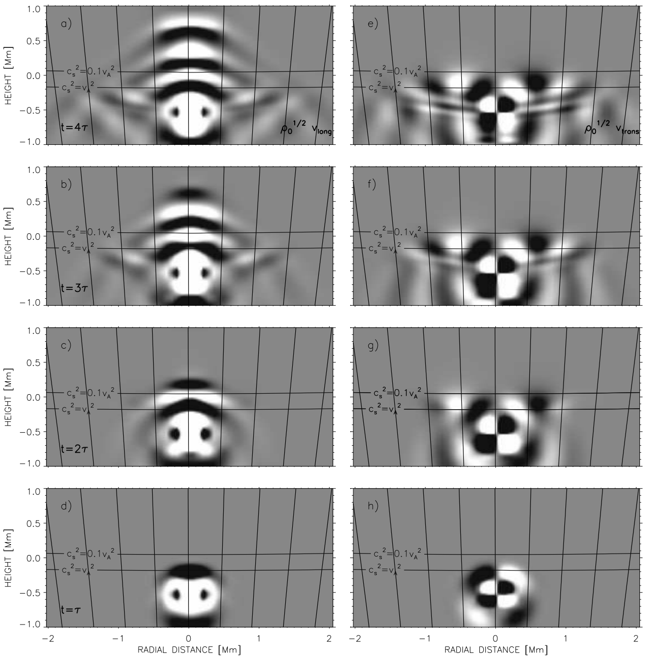

Figure 5.3: Time evolution of $\sqrt{\rho_0}v_{\mathrm{long}}$ (left) and $\sqrt{\rho_0}v_{\mathrm{trans}}$ (right) for the simulation with 50 s harmonic driver. Time increases from bottom to top, with an elapsed time between panels of a period (τ). The image color coding is such that black represents negative values and white represents positive values. Horizontal lines are contours of constant v_A^2/c_S^2.

To quantify the amount of energy contained in different wave modes and to develop a measure of the mode transformation, suitable in the case of complex magnetic field configurations like the one considered here, we found it useful to calculate the wave energy fluxes (Bray & Loughhead 1974). The acoustic energy flux is given by the expression:

$$\mathbf{F}_{\mathrm{ac}} = p_1 \mathbf{v}_1, \tag{5.6}$$

and the magnetic energy flux is given by

$$\mathbf{F}_{\mathrm{mag}} = \mathbf{B}_1 \times (\mathbf{v}_1 \times \mathbf{B}_0)/\mu_0. \tag{5.7}$$

The acoustic energy flux contains the energy of the wave with acoustic nature, which corresponds to the fast mode in the region where $v_A < c_S$ and to the slow mode in the region where $v_A > c_S$. In this region, the magnetic flux includes the fast and the Alfvén modes. Since, as we will see in the next section, in the region above the layer where $v_A = c_S$ the fast mode is refracted down toward the photosphere, the magnetic energy which propagates upward along field lines must correspond to the Alfvén wave, making possible the identification of this mode.

5.4 Numerical simulations

5.4.1 Case of 50 s harmonic force located at the axis

Figure 5.2 presents a two-dimensional snapshot of some variables and Figure 5.3 gives the temporal evolution of the projected velocities in the simulation run with a harmonic 50 s force located at the sunspot axis (Equation 5.1 with $\tau = 50$ s). Panels (a)–(c) in Figure 5.2 show the longitudinal, transversal, and perpendicular velocities scaled with a factor $\sqrt{\rho_0}$. These magnitudes provide the square root of the kinetic energy associated with the waves. Some perturbations at high layers have so low amplitude that makes them indistinguishable in this representation. To make them visible, we have plotted additional contours of constant velocity. In the case of the pressure (Figure 5.2(e)), its drop with height makes the absolute value of the perturbations at the lower layers much higher than at the upper layers. In this case, the contours represent the ratio of constant p_1/p_0.

Propagation below the surface

The vertical force acts in a region where $c_S^2/v_A^2 \approx 9.1$ and it generates mainly an acoustic fast mode, whose oscillations can be seen in the longitudinal velocity and pressure snapshots in Figure 5.2. This vertical impulse produces initially a deficit in density and pressure at the place where the source is located and, because of that, horizontal motions also appear, creating a magnetic slow mode seen in the transversal velocity and magnetic field snapshots in Figure 5.2.

At a photospheric level, the longitudinal velocity has an amplitude of about 200 m s^{-1}, the amplitude of transversal velocity is 50 m s^{-1} and the transversal magnetic field oscillates with a maximum deviation from the equilibrium value of 4 G.

The temporal evolution given in Figure 5.3 shows the fast mode (acoustic in nature) propagating in the deep layers upward to the region where $v_A \approx c_S$. It appears as a perturbation in the longitudinal velocity (panels (c) and (d)). Variations in longitudinal velocity are accompanied by acoustic variations of pressure and density (not shown in the figure). The slow mode (of magnetic nature) is visible in the transverse velocity variations (panels g–h). In this region $v_A < c_S$, so the acoustic perturbation reaches the surface $v_A^2 = c_S^2$ earlier than the magnetic perturbation. In these deep layers, the acoustic oscillations have a wavelength larger than the magnetic ones. As the fast (acoustic) wave propagates in the region $v_A < c_S$, its energy is distributed in the three spatial dimensions and it decreases away from the source as $1/r^2$. Once it reaches the $v_A > c_S$ region, the energy redistribution in horizontal directions is not so important because it is channeled along the field lines and is only affected by the density falloff.

Three-dimensional mode transformation

When the waves reach the $v_A^2 = c_S^2$ layer from below, several mode transformations take place in the simulation.

First of all, the fast acoustic mode moves from a region where $v_A < c_S$ to another where $v_A > c_S$ keeping its acoustic nature but changing from the fast mode to the slow mode. This transformation can be seen in the snapshots of longitudinal velocity and relative pressure in

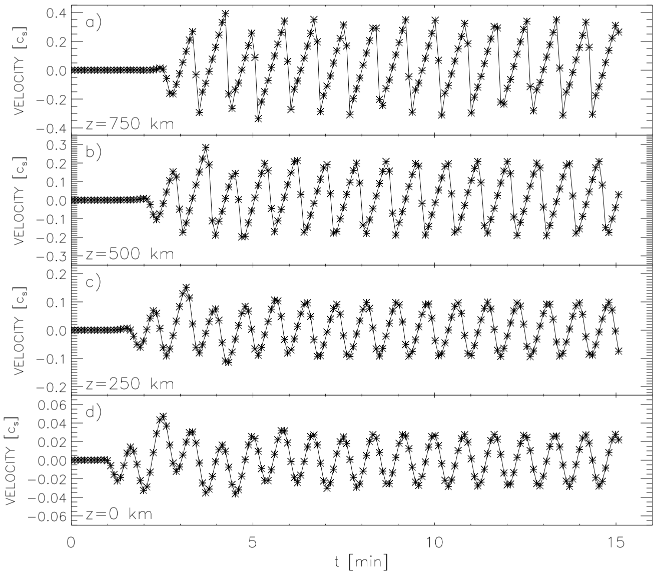

Figure 5.4: Vertical velocity in the units of local sound speed at the axis of the sunspot at several heights in the simulations with 50 s harmonic force. From bottom to top: $z = 0$ km, $z = 250$ km, $z = 500$ km and $z = 750$ km. The average speed of sound from 0 to 750 km of height is 7.9 km s^{-1}.

Figure 5.2 (panels (a) and (e)) as the wavefronts above the layer $v_A^2 = c_S^2$. The atmosphere above $v_A^2 = c_S^2$ is dominated by the magnetic field and this slow acoustic mode propagates upward along field lines (Figures 5.3(a)–5.3(c)). The amplitude of this wave increases according to the density drop and it develops into shocks above $z = 500$ km. Figure 5.4 shows that the oscillations in the vertical velocity develop a clear saw-tooth shape with sudden decreases of the velocity followed by slower increases. They present peak-to-peak variations of almost 8 km s^{-1} and their period is 50 s, the same period imposed by the excitation pulse.

The second mode transformation is the acoustic fast mode which is transmitted as a magnetic fast mode in the region $v_A > c_S$, where the magnetic field dominates. The evolution of this magnetic mode in the first 200 s of the simulation is clearly seen in Figure 5.3 (panels (e)–(g)) in the transversal velocity as the wave which moves away from the axis of the sunspot just above the surface $v_A^2 = c_S^2$. This mode is also visible in the transversal magnetic field variations (Figure 5.2(d)). Due to the large horizontal variations of v_A (large at the axis and decreasing outwards) the fast magnetic mode refracts and reflects back to the sub-photosphere, showing a behavior similar to the two-dimensional case considered by Khomenko & Collados (2006).

When the reflected magnetic fast wave reaches again the $v_A^2 = c_S^2$ layer, it suffers two new transformations: a fast-to-slow transformation, resulting in a magnetic wave in the $v_A < c_S$ region; and a fast-to-fast transmission, which produces a new acoustic wave below $v_A = c_S$. First, we discuss the slow magnetic wave. In Figure 5.2 (panels (b)–(d)), it is clearly visible in the transversal and perpendicular velocities and the magnetic field variations, at horizontal locations inside a radius of 1.5 Mm around the axis and at heights

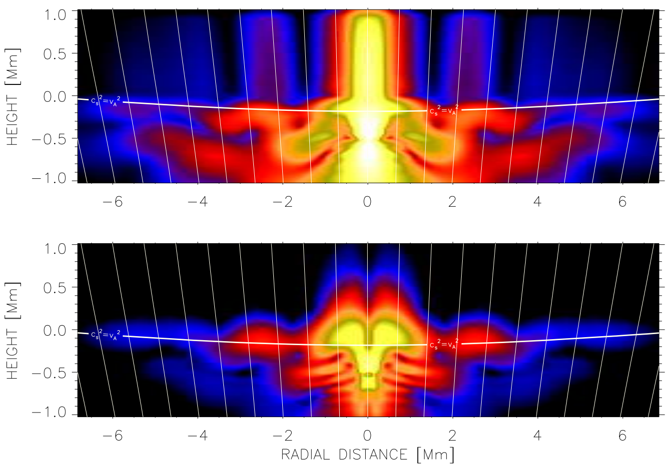

Figure 5.5: Acoustic (top) and magnetic (bottom) flux for the simulation with a 50 s harmonic driver located at the axis of the sunspot averaged over the stationary stage of the simulations. The horizontal white line is the height where sound speed and Alfvén speed are equal. Vertical lines are magnetic field lines. The axis is not to scale.

between $z = -1$ Mm and $z = 0$ Mm. Observing the temporal evolution at the beginning of the simulation one can see that in Figure 5.3(g) the fast magnetic wave above $v_A^2 = c_S^2$ has been refracted down and it is located between the two horizontal lines which indicate surfaces of constant v_A^2/c_S^2, but it has not arrived to the lower one, so the new transformation has not been produced. In the next time step (Figure 5.3(f)), the wave has already been transformed in a slow magnetic mode in the region below $v_A^2 = c_S^2$. The wavelength of this slow mode decreases as the wave propagates to deeper layers because of the drop of the Alfvén speed, which falls from 15 km s^{-1} at $z = 0$ Mm to 2 km s^{-1} at $z = -1$ Mm. Due to the higher density at the deeper layers the amplitude of this wave also decreases as it propagates down.

On the other hand, after the downward fast-to-fast transmission has occurred from the refracted fast wave, another fast acoustic wave appears in the region $v_A < c_S$. It is visible in longitudinal velocity in Figure 5.2(a) and in pressure in Figure 5.2(d) below the layer $v_A^2 = c_S^2$. The presence of this new acoustic mode can be checked comparing Figures 5.3(c) and 5.3(b). In the latter one, there is a new wave situated at both sides of the axis of the sunspot at a radial distance between 0.5 and 1.5 Mm which can be seen in longitudinal velocity. This mode appears after the reflected fast mode in the region $v_A > c_S$ reaches the surface $v_A^2 = c_S^2$. It propagates faster than the slow magnetic wave mentioned before, with a speed close to the sound speed, and its wavelength is larger than that of the slow mode. It keeps the direction of the incidence of the fast magnetic wave in the layer where $v_A^2 = c_S^2$, so it propagates down with some inclination with respect to the vertical, moving away from the axis.

In order to investigate the presence of the Alfvén mode in this simulation (either before of after the transformations) we have plotted in Figure 5.2(c) the velocity component in the direction $\hat{e}_{\rm perp}$. As expected, this velocity component has a node in the plane $y = 0$ Mm. Thus, we present in Figure 5.2(c) a vertical cut out of this plane, at 0.4 Mm from the

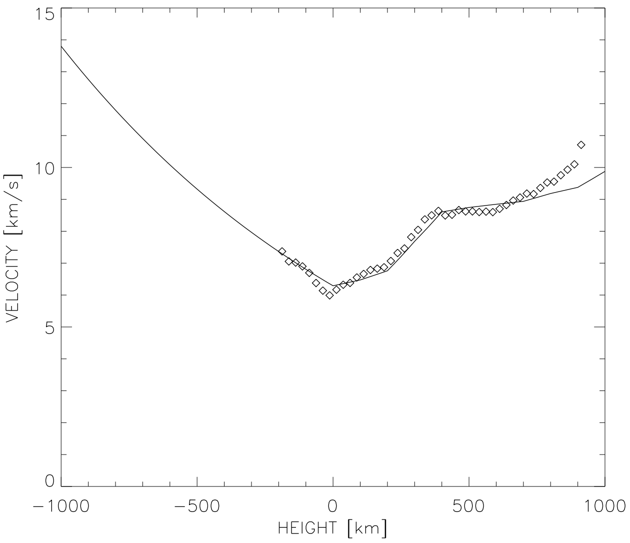

Figure 5.6: Sound speed profile (solid line) at the axis of the sunspot. Diamonds represent the phase velocity of the slow acoustic mode measured from the simulations with 50 s harmonic force.

center of the computational domain. In this projection, the Alfvén wave, if present, should appear as velocity oscillation above $v_A^2 = c_S^2$ layer. The inspection of Figure 5.2(c) shows that there are no oscillations in the magnetically dominated layers that can be identified as an Alfvén mode. Our conclusion is that when the wave driving occurs at the axis of the sunspot, no conversion to Alfvén waves happens.

Propagation in the upper atmosphere

Velocity contours in Figure 5.2(a) show the presence of some waves at a radial distance between ±1.5 and ±6 Mm near the top of the computational domain. These waves are specially tricky. From the first look at the figures and from the time evolution of the snapshots one may have an impression (from the inclination of the wavefront) that they propagate across field lines, opposite to the normal behavior of a slow acoustic wave. However, we verified that their propagation speed is equal to c_S, indicating their acoustic nature. The analysis of their wavenumbers indicates that the direction of propagation of these waves is close to the inclination of the magnetic field lines. Thus, we came to the conclusion that these waves are slow acoustic waves created from the continuous transformation of the fast acoustic mode which moves away from the driver across the field lines below $v_A^2 = c_S^2$ (visible in Figure 5.2(b) in transversal velocity and in Figure 5.2(e) in pressure variations from a radial distance of ±2 Mm to ±6 Mm) when it reaches this layer. As the wavefront closer to the axis of the sunspot gets to the surface $v_A^2 = c_S^2$ earlier, the slow acoustic wave that it produces has the wavefront inclined in the direction to the axis. Due to this fact, it looks like its propagation is across the field lines. This hypothesis also explains the nodes located at a radial distance of ±1.5 and ±3 Mm.

Acoustic and magnetic wave energy fluxes

Figure 5.5 shows the acoustic and magnetic fluxes averaged over the stationary stage of the simulations. Around 95% of the flux at the location of the driver is acoustic flux and it corresponds to the fast mode. At the center of the sunspot, where the magnetic field is almost vertical, the fast to slow transformation is very effective and the region above the layer $v_A^2 = c_S^2$ at the axis is dominated by the slow acoustic mode. When the angle between the direction of propagation of the wave and the magnetic field is different from zero, the fast-to-fast transmission is produced and it forms the two lobes which are visible in the magnetic flux just above the layer $v_A^2 = c_S^2$. The magnetic flux reaches a height of 0.5 Mm before the fast waves are refracted back toward the photosphere. In the low-β region, the fast magnetic mode has an important contribution from $z = 0$ Mm to $z = 0.5$ Mm for radial distances below 2 Mm, except at the axis of the sunspot. The transformation of the refracted fast magnetic wave when it comes back toward the photosphere generates acoustic as well as magnetic flux in the high-β region, corresponding to the new fast and slow modes, respectively, which propagate downward. As expected, we do not find any propagating magnetic flux along the field lines that may be associated with an Alfvén mode.

Saw-tooth wave formation

Figure 5.4 displays the evolution in time of the longitudinal velocity at the center of the sunspot at different heights, starting from the photospheric level $z = 0$ km until 750 km above the photosphere. Velocity is shown in units of the local sound speed (Mach number), and positive velocities indicate downflows while negative velocities are upflows. During the first five minutes after the start of the simulation the amplitudes of the consecutive wavefronts are quite different because at the beginning of the calculations the atmosphere is in an equilibrium state. Multiple wave transformations happen at the beginning of the simulations. Once this initial time has passed, the wave at the axis reaches a stationary state and at z=0 km it has a sinusoidal behavior. As the wave propagates upward, its amplitude increases. Note that velocities are much larger at higher layers, since the plotted velocities are normalized to the local sound speed, which changes with height according to Figure 5.6. When the amplitude approaches the sound speed, the nonlinear terms in the equations become important and the oscillation pattern acquires a saw-tooth shape that indicates the presence of weak shock wave trains. At $z = 0$ km the oscillation spends the same time in increasing the velocity from the minimum to the maximum and in the following decrease of the velocity, including more or less three time steps in each slope. At 250 km, the increase spends about four time steps, while the decrease occurs in only two or three. Finally, the two top heights (500 and 750 km) have a clear saw-tooth pattern with slow increases of the velocity followed by sudden drops. This oscillatory pattern shows that, thanks to the diffusivity terms, the code can manage high amplitudes and non-linearities.

Slow acoustic mode phase velocities

The phase velocity of a linear high-frequency slow mode wave in a magnetically dominated region is equal to c_S. In our simulation, a slow acoustic wave appears above the $v_A^2 = c_S^2$

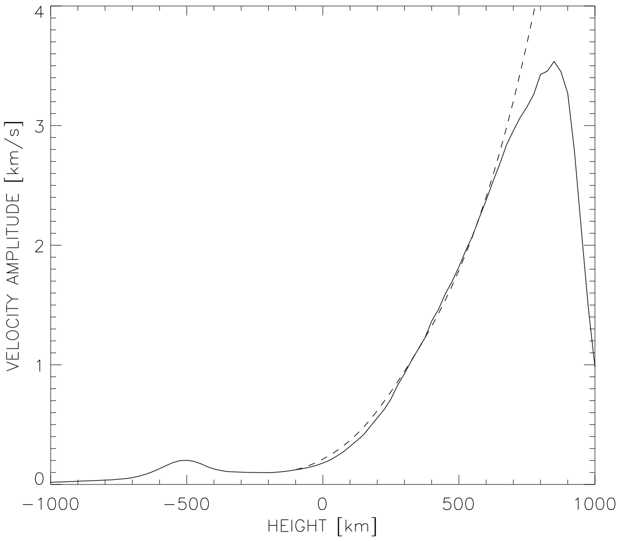

Figure 5.7: Amplitude of the slow acoustic mode vertical velocity (solid line) in the simulations with 50 s harmonic force. Dashed line gives the analytical curve for an acoustic-gravity wave with 50 s period (Mihalas & Mihalas 1984).

layer produced after the mode transformation. This wave allows us to check whether or not the velocity of waves involved in the simulations in this complex sunspot model corresponds to that expected from theoretical considerations.

Figure 5.6 presents the results of this test. The solid line in Figure 5.6 shows the stratification of the sound speed with height at the sunspot axis and diamonds indicate the phase velocity of the slow mode wave measured at each grid point from the simulations. Note that diamonds are only plotted at heights above $z = -200$ km, after the mode transformation has been completed. The velocity of the slow wave matches well the local sound speed at heights from $z = -200$ km to $z = 700$ km. Higher than $z = 700$ km the wave starts to propagate faster than c_S, since the velocity amplitude of the wave approaches the sound speed and non-linearities start playing an important role.

Slow acoustic mode amplitudes

As the slow acoustic wave propagates up in the atmosphere of the sunspot the amplitude of the velocity oscillations increases due to the density drop. The kinetic energy of this wave is proportional to ρv^2 and must be conserved. Thus, a decrease of the density must be accompanied with an increase of the velocity. The atmosphere of the sunspot is very complex and it includes vertical and horizontal gradients in all the magnitudes. Because of that there is no analytical expression for the variation of the amplitudes of the waves with height. However, we can compare the particular case of the wavefront of the slow acoustic mode wave which propagates along the axis of the sunspot with a case of a linear acoustic wave which propagates upward in a gravitationally stratified atmosphere permeated by a magnetic field parallel to the direction of gravity (see Section 2.2.3). In this theoretical

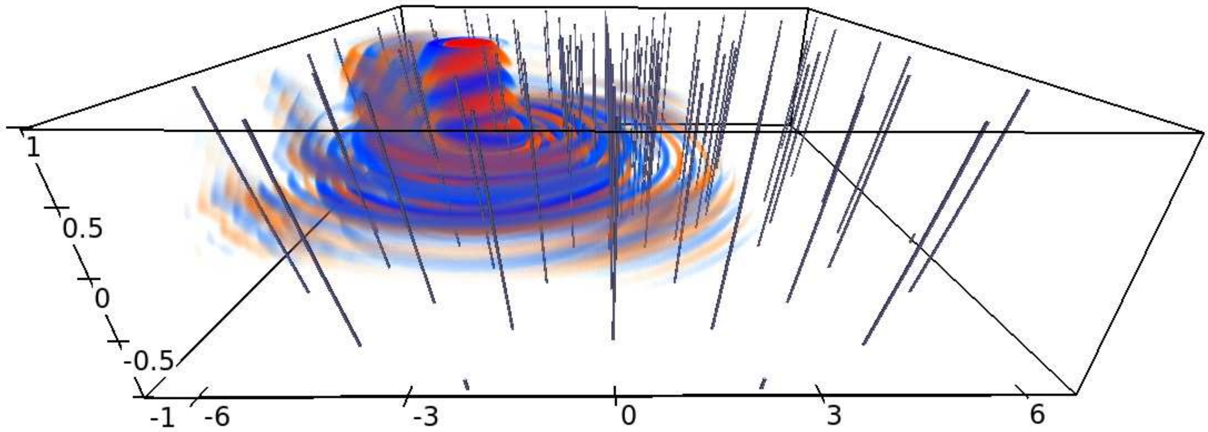

Figure 5.8: Variations of $\sqrt{\rho}v_z$ at an elapsed time $t = 820$ s after the beginning of the simulations for the 50 s harmonic force at 3 Mm from the axis of the sunspot. Gray inclined lines are magnetic field lines. Blue colors represent upward movement while orange/red colors represent downward movement.

case, the amplitude of the wave is given by

$$A(z) = A_0 \exp\left(\int_{z_0}^{z} \frac{dz}{2H_0}\right), \tag{5.8}$$

In Figure 5.7, we show the amplitude of the vertical velocity at each grid point at the axis of the sunspot (solid line) for the stationary stage of the simulations. The force is located at $z = -500$ km and the amplitude of the wave decreases until it reaches $z = -200$ km. This initial decrease is due to the part of the energy of the source that goes into other wave types because of the mode transformations. More or less at this layer the wave is transformed into a slow acoustic mode as it propagates up while its amplitude increases. When the wave reaches the height $z = 850$ km its amplitude drops very fast as a consequence of the large diffusivity that was imposed at high layers in order to stabilize the numerical simulation. In this figure, the expected amplitude according to Equation (5.8) (dashed line) is also overplotted, starting from the height where the wave has already been transformed into a slow acoustic mode in the region $v_A > c_S$. From $z = -200$ km to $z = 700$ km the numerical amplitude agrees with the analytical one, while from $z = 700$ km to $z = 850$ km the numerical amplitude is lower than the analytical one. This happens because the wave develops into weak shocks and the linear approximation for the amplitude increase is no longer valid. Note that the amplitudes of the oscillations (Figure 5.7) as well as the phase velocity (Figure 5.6) show discrepancies with the linear theory at the same heights.

5.4.2 Case of 50 s harmonic force located off the axis

Figure 5.8 gives a 3D view of the vertical velocity in the simulation run with 50 s harmonic force located at $x = -3$ Mm off the sunspot axis. This figure clearly shows the asymmetry of the wavefront with respect to the axis. In the lower part of the domain, the fast (acoustic) waves can be appreciated propagating in circles away from the source with a visibly lower

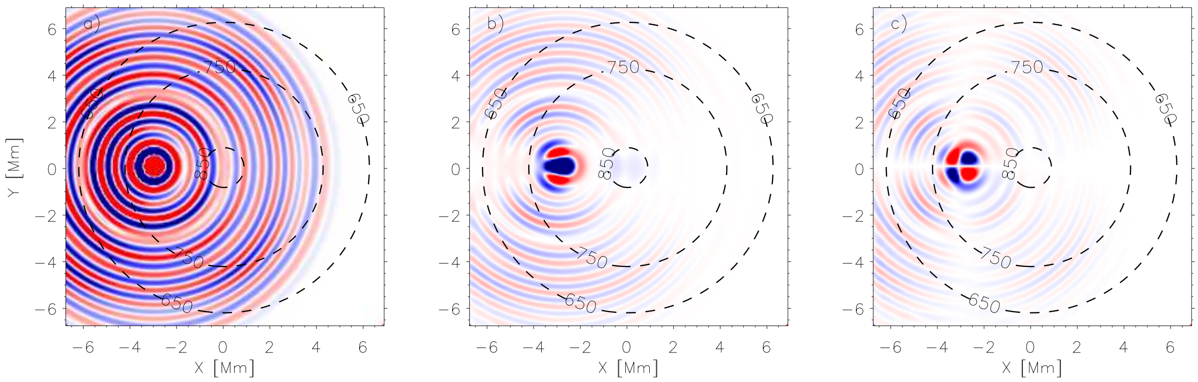

Figure 5.9: Variations of the velocity in the directions $\hat{e}_{\rm long}$ (a), $\hat{e}_{\rm trans}$ (b), and $\hat{e}_{\rm perp}$ (c), all of them scaled with factor $\sqrt{\rho_0}$ of the unperturbed density, at $z = 300$ km and at an elapsed time $t = 820$ s after the beginning of the simulations for the 50 s harmonic force located at $x = -3$ Mm , $y = 0$ Mm and $z = -0.5$ Mm. The image color coding is such that blue colors represent lower values and red colors are higher values with respect to the mean. All images have the same scale. Concentric dashed lines are contours of an equal magnetic field.

amplitude toward the axis. In the upper part of the domain, slow (acoustic) waves are the dominating ones, propagating along the inclined magnetic field lines.

Three-dimensional mode transformation

Figure 5.9 presents the projected velocities in the three characteristic directions at the horizontal cut of the simulation domain taken in the middle photosphere at $z = 300$ km. Figure 5.10 shows the snapshots of some variables in the vertical cut through the domain. Both figures correspond to the same time moment of the simulations at $t = 820$ s. These simulations have many features in common with the previously considered case of the driving force located at the sunspot axis. A set of fast (acoustic) and slow (magnetic) modes is generated below the layer $v_A^2 = c_S^2$, propagating upward and suffering several transformation after reaching this height. Similar to the previous case, slow (acoustic) and fast (magnetic) modes are produced after the mode transformation in the magnetically dominated upper atmosphere. The conversion to slow and fast modes in the low-β region only presents slight changes in comparison with the simulation with the driver placed at the axis. One of these changes is the presence of an asymmetry with respect to the axis. For example, Figure 5.10(a) and contours of Figure 5.10(e) show that the slow acoustic mode is channeled along the field lines and its wavefronts are clearly inclined in that direction in the region above the green lines at a radial distance of −3 Mm.

There are two different fast to fast transmissions. Most of the energy of the vertical driver goes to the mode with $k_x \approx 0$ and when it is transmitted as a fast magnetic wave in the region above $v_A^2 = c_S^2$ the horizontal gradients of the Alfvén speed incline the wavefront away from the axis and it is reflected downward, like in the case of the 50 s harmonic at the axis. This is the case of the wave situated at a radial distance between −4.5 and −3.3 Mm between the two contours of equal ratio c_S^2/v_A^2 in Figures 5.11(e) and 5.11(g).

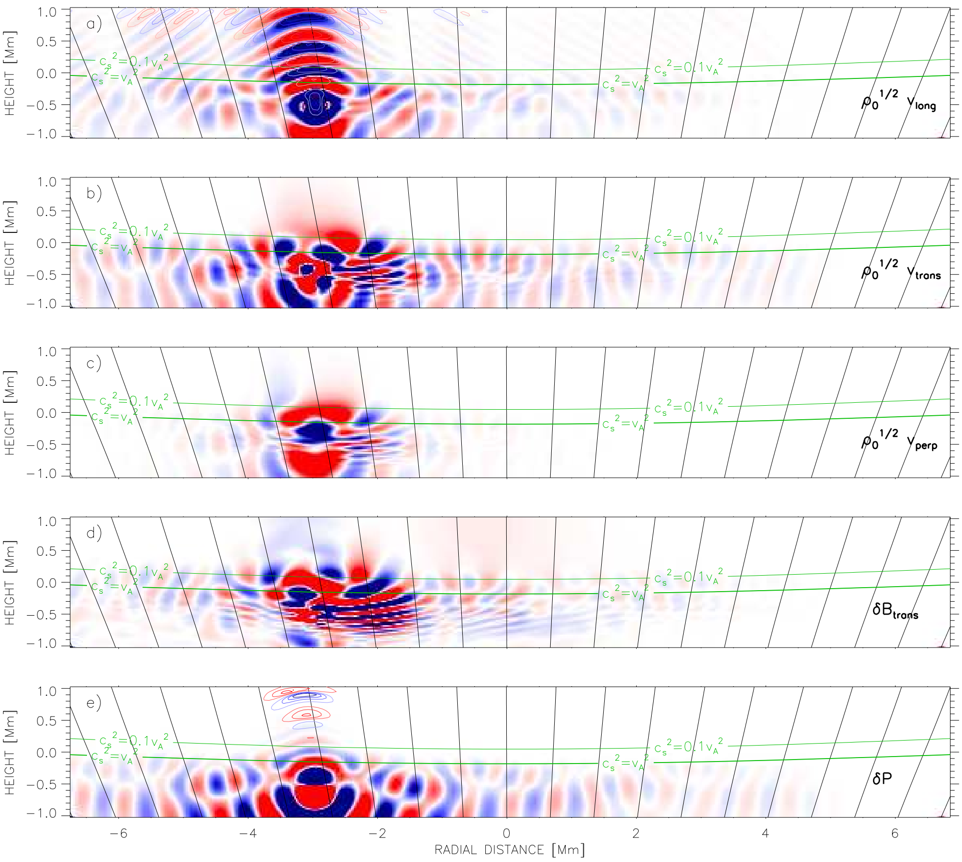

Figure 5.10: Variations of the velocity in the directions $\hat{e}_{\rm long}$ (a), $\hat{e}_{\rm trans}$ (b), and $\hat{e}_{\rm perp}$ (c), all of them scaled with factor $\sqrt{\rho_0}$ of the unperturbed density; the magnetic field in the direction $\hat{e}_{\rm trans}$ (d) and pressure (e) at an elapsed time $t = 820$ s after the beginning of the simulations for the 50 s harmonic force located at $x = -3$ Mm off the sunspot axis. The format of the figure is the same as Figure 5.2.

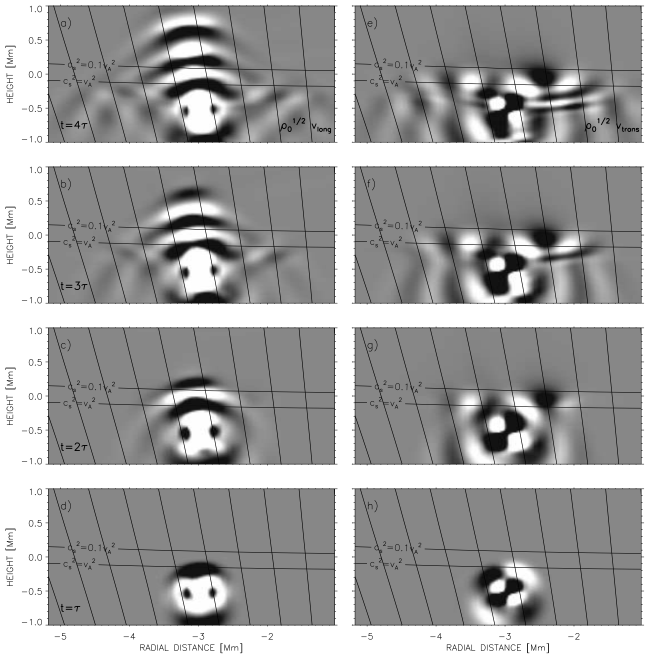

Figure 5.11: Time evolution of $\sqrt{\rho_0}v_{long}$ (left) and $\sqrt{\rho_0}v_{trans}$ (right) for the simulation with 50 s harmonic driver at 3 Mm from the axis of the sunspot. The time increases from bottom to top. The format of the panels is the same as Figure 5.3.

The other transmission is experienced by the components of the pulse with $k_x > 0$ and is visible in Figures 5.11(e) and 5.11(g) at a radial distance between −3 and −1.5 Mm. They propagate to the right with respect to the pulse location in the $v_A > c_S$ region (*i.e.*, toward the axis), so the wavefront is inclined to the right. After the fast to fast transmission, the vertical gradients of the Alfvén speed make the left part of the wavefront propagate faster than the right part, and it refracts toward the sunspot axis. The transformation of the downward propagating refracted fast (magnetic) mode into the slow (magnetic) mode below the surface (Figure 5.10, panels (b)–(d)) also presents an asymmetry. Due to the particular combination of the field inclination and the direction of propagation of the refracted fast mode, this transformation is much more efficient on the right from the source in the direction toward the axis (locations between $x = -3$ and -1 Mm at $z \approx -0.5$ Mm).

The most important changes are present in the velocity component in the direction $\hat{e}_{\rm perp}$ (Figure 5.9(c)). At a height of $z = 300$ km, this component shows variations that do not correspond to the fast (magnetic) mode. The latter has been already reflected down. As demonstrated by the analysis of the magnetic energy flux below, the variations observed in the snapshot of $\hat{e}_{\rm perp}$ at heights above $z \approx 300$ km at locations between $x = -4$ to -2 Mm and $y = -1$ to 1 Mm correspond to the Alfvén wave.

The contours of velocity in Figures 5.10(a)–(b) show at a radial distance between −6 and −4.5 Mm the slow wave that is created from the transformation of the fast waves below $v_A^2 = c_S^2$ which propagate with an important horizontal component, as we proposed in Section 5.4.1. However, at the same heights, but at the right hand side of the driver this wave is much weaker (in Figure 5.10(a) only a small component is seen at a radial distance of

-1 Mm at the top of the domain). The efficiency of the fast to slow transformation is higher for the waves which propagate along the magnetic field at the layer where $v_A^2 = c_S^2$ (Cally 2006). Near the center of the sunspot the angle between the almost vertical field lines and the almost horizontal propagation of waves is big, and the efficiency of the transformation is very low, which agrees with the results of the simulation. This feature is also very clear in the 3D plot in Figure 5.8 and it verifies the hypothesis for the origin of these waves proposed in Section 5.4.1.

Acoustic and magnetic wave energy fluxes

The acoustic and magnetic fluxes are shown in Figure 5.12. These fluxes, in general, show a pattern similar to the case of driving at the axis, but some important asymmetry is also present. The acoustic flux of the slow mode in the low-β region is oriented in the direction of the field lines and it is slightly lower than in the previous simulation due to the larger angle between the direction of propagation of the fast mode before reaching the layer $v_A^2 = c_S^2$ and the magnetic field (φ). An important fraction of the magnetic flux appears in the lobe located at $v_A^2 = c_S^2$ line in the direction toward the axis of the sunspot present due to more efficient fast-to-fast mode transmission with increasing φ (Cally 2005). Compared with Figure 5.5 there is also more magnetic flux present in the upper part of the atmosphere above $v_A^2 = c_S^2$, apparently directed along the magnetic field lines. It is not clear, however, whether this flux corresponds to fast, not yet completely reflected wave, or to the Alfvén wave. To clarify this issue we have calculated the magnetic flux following Equation (5.7), but using only the projections of the velocity and magnetic field perturbations in the direction $\hat{e}_{\mathrm{perp}}$. We expect that this quantity (longitudinal, by definition, as expected for Alfvén waves) may give us indications about presence of the propagating Alfvén waves.

Figure 5.13 illustrates the result. The top panel corresponds to a vertical cut in the plane $y = -0.4$ Mm, normalized at every height to its maximum value at this height. The bottom panel is a horizontal cut in the plane $z = 0.9$ Mm. The white colors (positive flux) mean upward energy propagation, while the black colors (negative flux) mean downward energy propagation. Indeed these plots reveal the energy flux associated with the Alfvén wave, which clearly propagates upward along the field lines. The Alfvén mode has a node at the plane $y = 0$ Mm, where the driver was located, so conversion to this mode is only produced when the wavevector forms a certain angle with the magnetic field (different from zero). This result is in qualitative agreement with the recent investigation of the conversion to Alfvén waves by Cally & Goossens (2008). However, even at the location where the contribution of the Alfvén wave energy flux to the total energy flux is maximum, its flux is still around 20 times lower than the acoustic flux at this location. So it means that in the sunspot magnetic field configuration and for the driver location considered here, the transformation from the fast (acoustic) to Alfvén wave is much less effective than the transformation to the slow (acoustic) wave in the magnetically dominated upper atmosphere.

5.4.3 Case of 180 s harmonic force located at the axis

This simulation corresponds to the source placed at the same position as in Section 5.4.1, that is, at the axis of the sunspot 500 km below the photosphere, but in this case with a

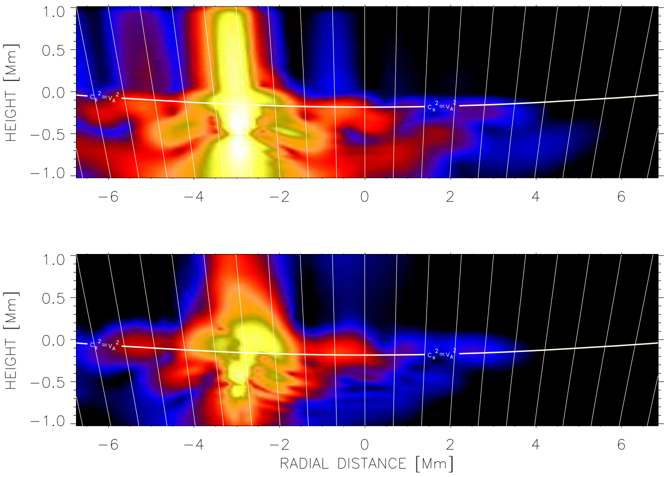

Figure 5.12: Average acoustic (top) and magnetic (bottom) flux for the 3D simulation with a 50 s harmonic driver located at 3 Mm from the axis of the sunspot averaged over the stationary stage of the simulations. The format is the same as Figure 5.5.

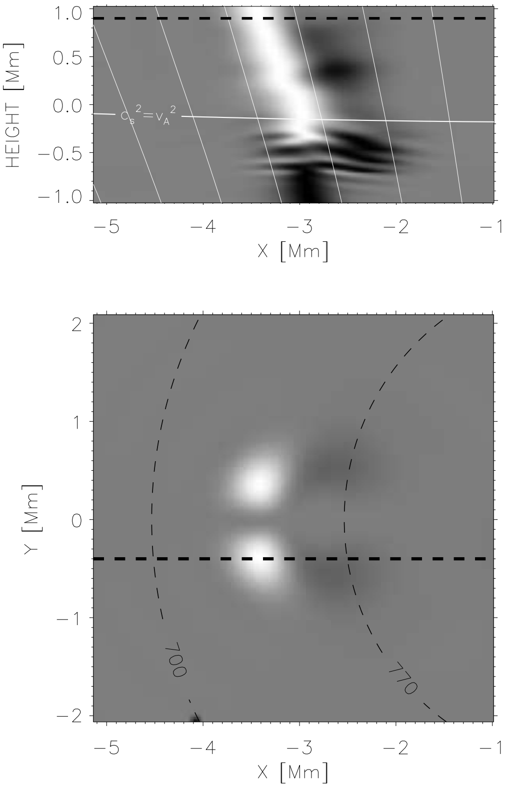

Figure 5.13: Magnetic flux of the Alfvén mode. Top: vertical cut in the plane $y = -0.4$ Mm, normalized at every height. Vertical white lines are magnetic field lines and the horizontal white line is the layer where $c_S^2 = v_A^2$. Bottom: horizontal cut in the plane $z = 0.9$ Mm. Thin dashed lines are contours of equal magnetic field. In both panels, thick dashed lines mark the location of the other plot.

period of 180 s and $R_{\text{src}} = 540$ km. A larger source size is needed because the wavelength of this longer period waves is larger, and in this way we can compare the results with the simulation of Section 5.4.1. The snapshots of several variables and the temporal evolution of the velocities are plotted in Figures 5.14 and 5.15, respectively. This simulation shows many features which also appeared in the 50 s harmonic case, since the response of the magnetic atmosphere is quite similar at both frequencies because they are above the cutoff frequency, with differences in the wavelengths and periods of the wave modes involved.

Three-dimensional mode transformation

The vertical force introduced below the photosphere generates an acoustic fast mode and a magnetic slow mode. The first one can be seen in the longitudinal velocity, as field aligned oscillations of the wavefront propagating upwards, together with fluctuations in density and pressure. At photospheric levels, the longitudinal velocity oscillates with an amplitude of almost 400 m s^{-1}. Figure 5.14(b) shows the magnetic slow mode oscillations in the transversal velocity with an amplitude of 90 m s^{-1} at $z = -250$ km (between a radial distance of -1 and 1 Mm just below the green line $v_A^2 = c_S^2$). This mode is also present in the transversal magnetic field in Figure 5.14(c) with a maximum displacement from the equilibrium state of 8 G.

The acoustic fast wave propagates with sound speed, and on its way to the chromosphere it reaches a height where the sound speed and Alfvén speed are similar. The fast mode is transformed into a slow acoustic mode in the region above $v_A^2 = c_S^2$. The slow mode is visible in 5.14(a) in the longitudinal velocity around the axis above the surface $v_A^2 = c_S^2$ and it is channeled along the field lines higher up to the chromosphere. Its amplitude increases with height from the layer where it is formed at $z = -100$ km to $z = 1000$ km in accordance with the density falloff and it develops into saw-tooth waves with amplitudes of 5 km s^{-1}. This acoustic slow wave does not produce fluctuations in magnetic field, but it is accompanied by density and pressure oscillations whose relative amplitudes (*i.e.*, normalized to the local density/pressure) increase with height (see the contours in Figure 5.14(d)), as expected for an acoustic wave.

The acoustic fast mode reaching the layer $v_A^2 = c_S^2$ is also transformed in a fast magnetic mode in the region where $v_A > c_S$. This mode is evident in the transversal velocity and magnetic field variations in Figures 5.14(b) and 5.14(c), respectively, and, as in the simulation of the 50 s harmonic source, it is reflected back to the photosphere. When this fast magnetic wave comes back to the photospheric height where $v_A^2 = c_S^2$, it is again transformed into a slow magnetic wave (visible in the region between ±1 and ±6 Mm below the layer $v_A^2 = c_S^2$ in Figures 5.14(b) and 5.14(c)) that propagates downward at slow speed (see the temporal evolution of the transversal velocity in Figure 5.15). Due to the small value of the Alfvén speed the wavelength of this wave becomes smaller and its amplitude decreases as the density increases. After the reflected fast magnetic wave comes back to $v_A \approx c_S$ a part of its energy is also transmitted as fast wave, that is, below $v_A \approx c_S$ there is a new fast acoustic wave (see Figures 5.15(a)–(e) between a radial distance of 1 and 2 Mm) similar to the one mentioned in the simulation of the 50 s harmonic source.

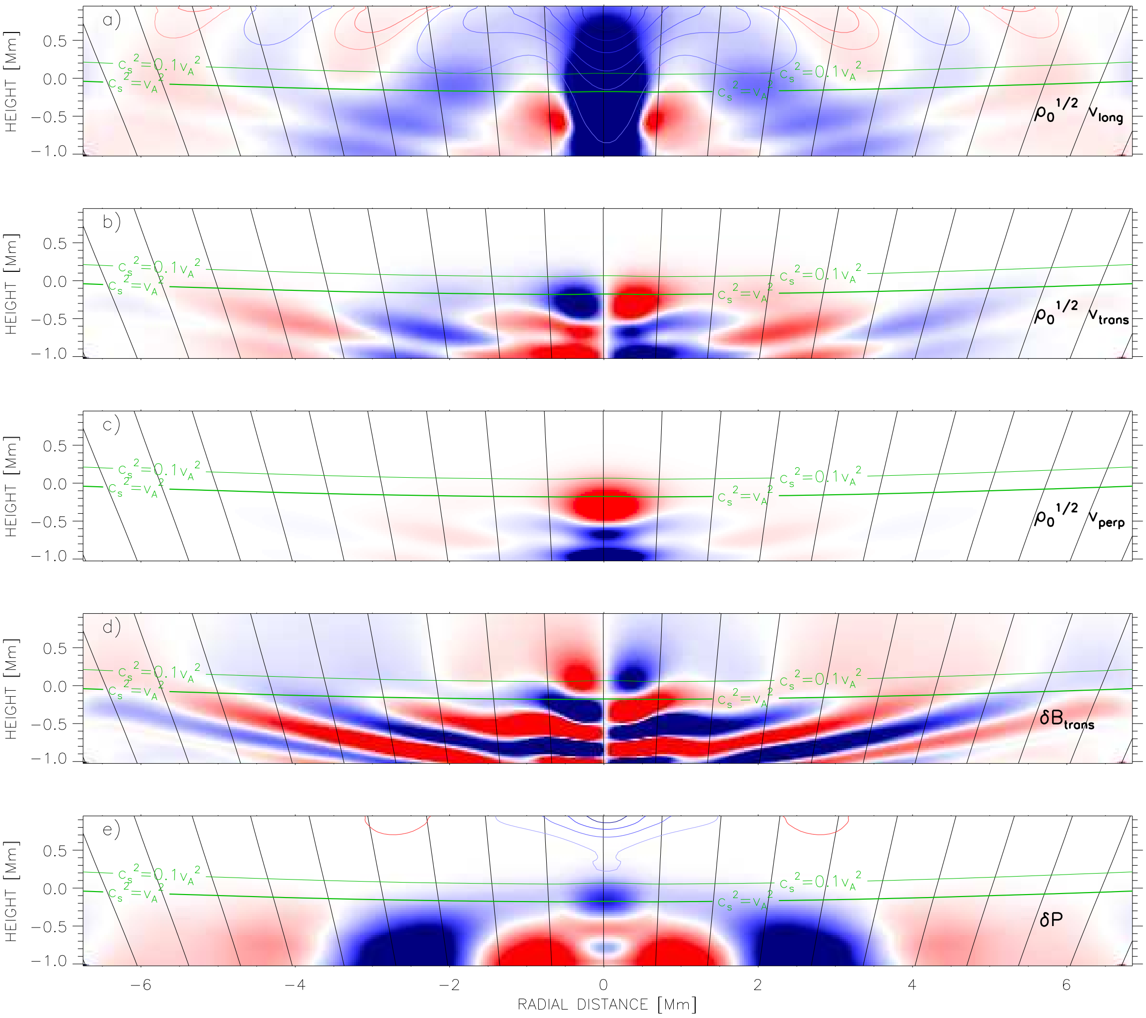

Figure 5.14: Variations of the velocity in the directions $\hat{e}_{long}$ (a), $\hat{e}_{trans}$ (b), and $\hat{e}_{perp}$ (c), all of them scaled with factor $\sqrt{\rho_0}$ of the unperturbed density; the magnetic field in the direction $\hat{e}_{trans}$ (d) and pressure (e) at an elapsed time $t = 820$ s after the beginning of the simulations for the 180 s harmonic force located at $x = 0$ km, $y = 0$ km and $z = -500$ km. The format of the figure is the same as Figure 5.2.

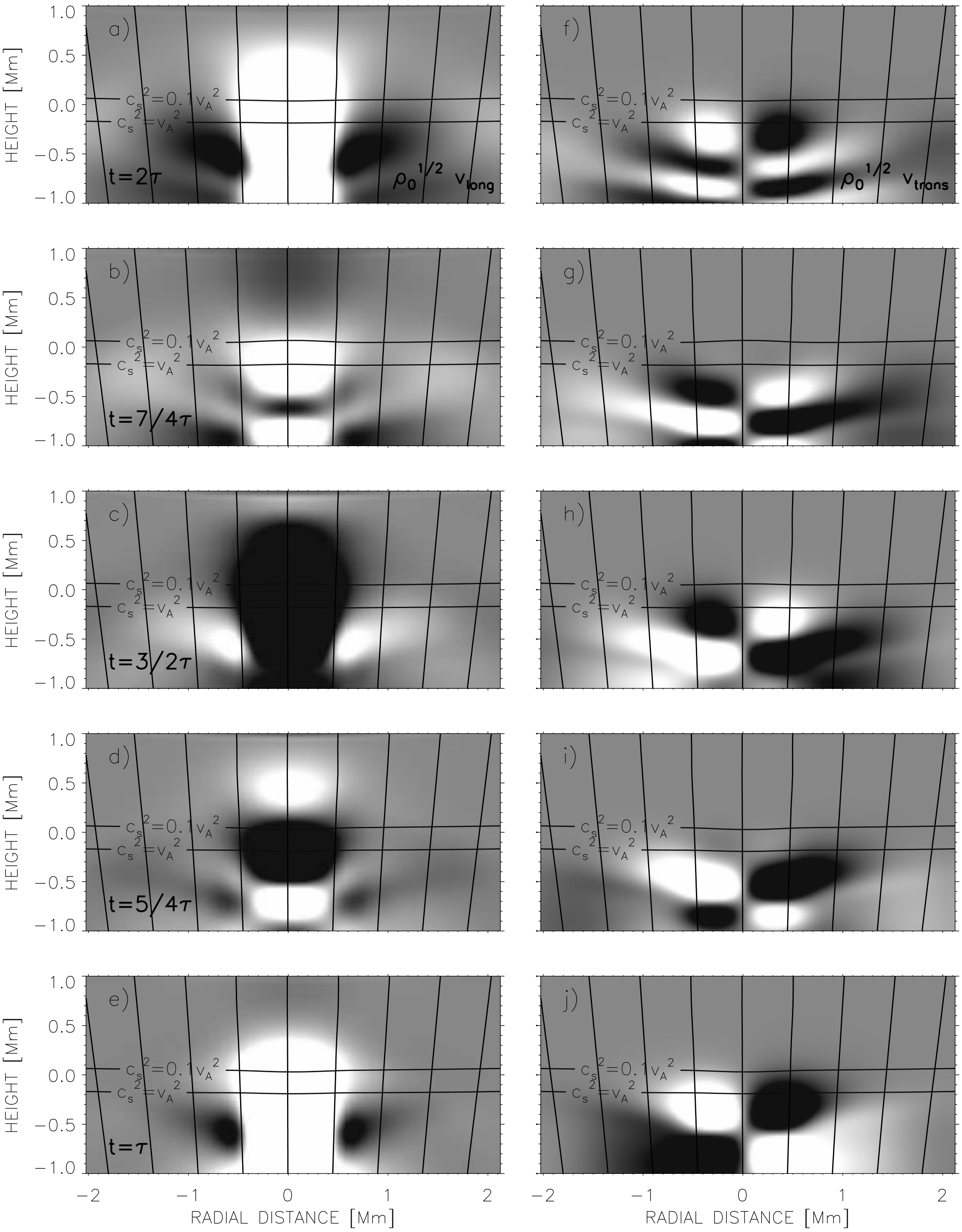

Figure 5.15: Time evolution of $\sqrt{\rho_0}v_{long}$ (left) and $\sqrt{\rho_0}v_{trans}$ (right) for the simulation with 180 s harmonic driver at the axis of the sunspot. Time increases from bottom to top. The format of the panels is the same as Figure 5.3.

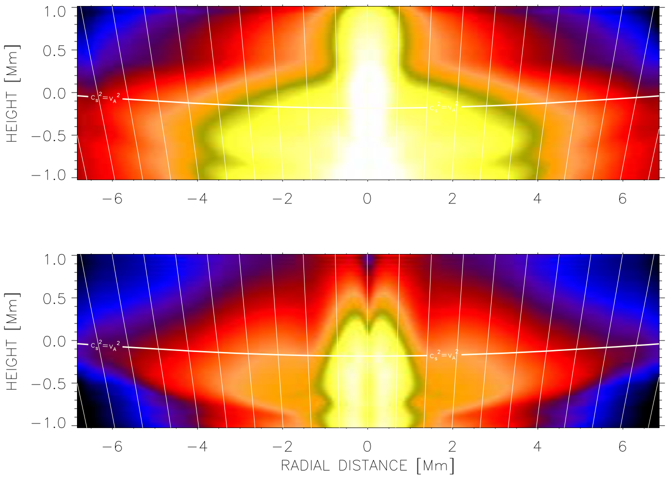

Figure 5.16: Acoustic (top) and magnetic (bottom) flux for the simulation with a 3 min harmonic driver located at the axis of the sunspot averaged over the stationary stage of the simulations. The format is the same as Figure 5.5.

Acoustic and magnetic wave energy fluxes

The fluxes are presented in Figure 5.16. It is very similar to Figure 5.5, except for the much larger wavelength of the fluctuations, in agreement with the larger temporal period of waves. The average acoustic flux shows that at the axis of the sunspot the fast to slow mode transformation is also effective for waves with 180 s period. After the transformation, slow (acoustic) waves propagate acoustic energy upward. The fast mode visible in the magnetic flux above the $v_A^2 = c_S^2$ also has longer wavelengths than in the 50 s harmonic simulation. The magnetic flux vanishes at the axis of the sunspot at high layers. Due to the reflection of the fast (magnetic) wave, there is no magnetic flux above the certain height, also away from the axis. In this simulation we find no traces of the Alfvén mode.

5.4.4 Case of 300 s wavelet force located at the axis

Figure 5.17 shows vertical snapshots of several variables after 820 s of the simulation with the driver emitting a spectrum of waves with a central frequency at 3.33 mHz given by Equation (5.2).

According to the stratification of the atmosphere, at the axis of the sunspot at $z = -700$ km the cutoff frequency is $\nu_c = 3.3$ mHz. It increases with height reaching a maximum at the height of $z = 0$ km, where its value is $\nu_c = 5.8$ mHz. It means that 5 minute acoustic waves cannot propagate upward above $z = 0$ Mm, since they are evanescent in the vertical direction, and can only propagate horizontally. Therefore, the cutoff frequency is a critical value for the wave propagation in this case, and the behavior of waves below and above the cutoff layer is expected to be completely different.

The source located at $z = -500$ km drives waves with frequencies below as well as above ν_c, but most of its energy goes to the band around 3.33 mHz. This generates a fast acoustic wave with an amplitude below 100 m s^{-1} and 5 minute period, which can propagate upward only until the height $z = 0$ Mm. Waves with this frequency are evanescent at higher layers

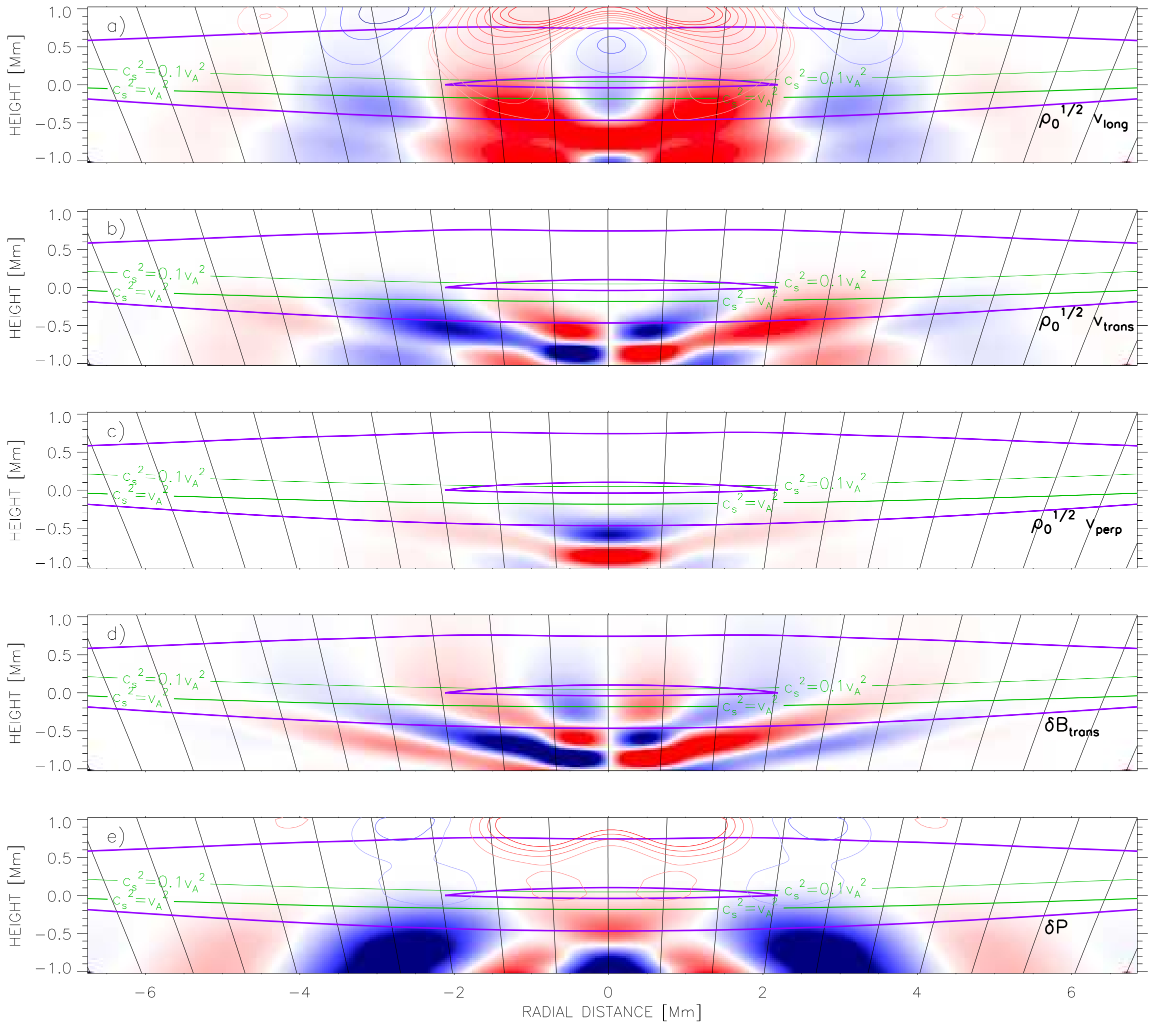

Figure 5.17: Variations of the velocity in the directions $\hat{e}_{\rm long}$ (a), $\hat{e}_{\rm trans}$ (b), and $\hat{e}_{\rm perp}$ (c), all of them scaled with factor $\sqrt{\rho_0}$ of the unperturbed density; the magnetic field in the direction $\hat{e}_{\rm trans}$ (d), and pressure (e) at an elapsed time t=820 s after the beginning of the simulations for the 300 s wavelet force located at $x=0$ km, $y=0$ km and $z=-500$ km. The format of the figure is the same as Figure 5.2. Violet lines represent contours of equal cutoff frequency. The inner one is $\nu_c=5.6$ mHz and the outer one is $\nu_c=4$ mHz.

and their vertical wavelength occupies the whole upper part of the simulated atmosphere. The amplitude of their longitudinal velocity slightly increases with height.

Three-dimensional mode transformation

Part of the energy of the driver which reaches the surface $v_A^2=c_S^2$ is transformed into a fast wave above this height. Due to its magnetic nature it becomes unaffected by the cutoff frequency. As in the previous simulations, the transversal velocity in Figure 5.17(b) and the transversal magnetic field in Figure 5.17(d) show that the fast magnetic wave in the region $v_A>c_S$ is reflected because of the gradients in the Alfvén speed. Once the wave

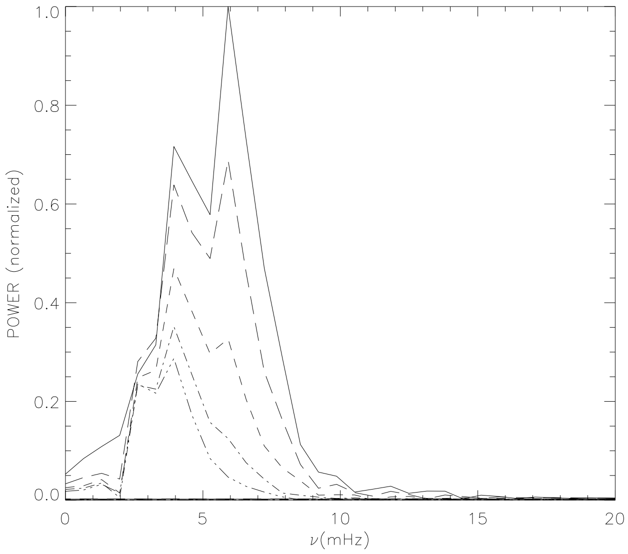

Figure 5.18: Power spectra at different heights at the axis of the sunspot for the simulations with 300 s wavelet force, normalized to the maximum power at the highest height. From bottom to top: $z = -250$ km, $z = 0$ km, $z = 250$ km, $z = 500$ km and $z = 750$ km.

comes back to the sub-photospheric layers below $v_A^2 = c_S^2$, it keeps its magnetic nature and propagates downward in a form of a slow wave with decreasing wavelength due to the drop of the Alfvén speed, but keeping its 5 minute period.

The maximum cutoff frequency at the axis in this sunspot model is $\nu_c = 5.8$ mHz, so waves with higher frequencies can still propagate upward through the atmosphere. The fast acoustic modes generated by the driver with frequencies higher than ν_c are transformed into propagating slow acoustic modes in the region above $v_A^2 = c_S^2$. The contours in Figure 5.17(a) represent constant longitudinal velocity. At a height around $z = 900$ km, the longitudinal velocity has maximum power at 3 minute period, which corresponds to the frequency above ν_c receiving more energy from the driver.

Frequency change with height

The increase of the amplitude of 3 minute waves according to the drop of the density (compared to much weaker increase of the amplitude of the evanescent 5 minute waves) leads to the power spectrum at chromospheric heights dominated by 3 minute waves. There, their amplitudes reach almost 400 m s^{-1} . They do not develop into a saw-tooth waves because at the photosphere the driver generates low power at this frequency band and their amplitude increase is not enough to produce significant non-linearities.

Figure 5.18 shows the power spectra at different heights, from $z = -250$ to $z = 750$ km. At $z = 750$ km it shows a clear peak at $\nu = 5.9$ mHz, corresponding to a period of 170 s. At the lower layers, a peak below 4 mHz dominates. One can see in this figure how the amplitude of the low-frequency peak increases with height. However, this increase is weaker than that of the peak at high-frequency around $\nu \approx 6$ mHz. Due to this behavior,

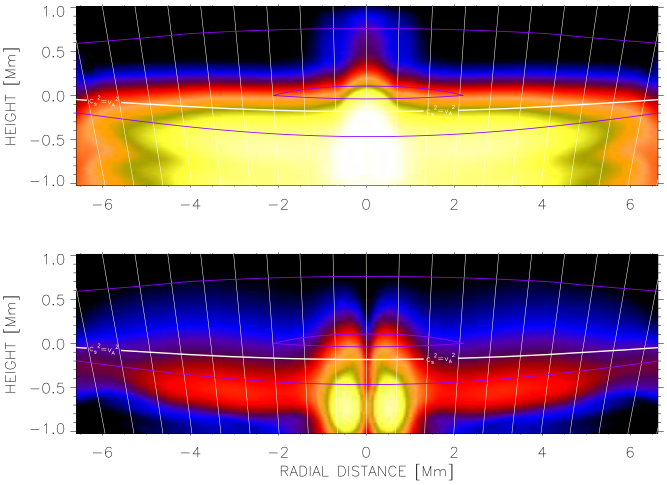

Figure 5.19: Acoustic (*top*) and magnetic (*bottom*) flux for the simulation with a 5 min wavelet driver located at the axis of the sunspot averaged over the stationary stage of the simulations. The format is the same as Figure 5.5. Violet lines represent contours of equal cutoff frequency. The inner one is $\nu_c = 5.6$ mHz and the outer one is $\nu_c = 4$ mHz.

the high layers are dominated by oscillations with period around 3 minutes.

A simulation with a 300 s harmonic driver was also performed. In this case high layers develop evanescent 5 minutes period waves, but there is no trace of 3 minute oscillations at the chromosphere, so power in this frequency band cannot be produced if these frequencies are not excited by the driver. Thus, we can conclude that the mechanism that produces the change in frequency of oscillations in the umbra from the photosphere to the chromosphere is the linear propagation of waves with 3 minute power which come directly from the photosphere and dominate over the evanescent long period waves. This conclusion goes in line with the results of the observational study of sunspot waves simultaneously at the photosphere and the chromosphere by Centeno et al. (2006).

Acoustic and magnetic wave energy fluxes

The magnitudes $\sqrt{\rho_0}v_{\rm long}$, $\sqrt{\rho_0}v_{\rm tran}$ and $\sqrt{\rho_0}v_{\rm perp}$ plotted in Figure 5.17 (panels a–c), respectively, show that most of the kinetic energy remains in the photosphere and below. Most of the energy introduced by the driver goes into the waves in the 5 minute band. Propagating to higher layers, they form evanescent waves or are transformed into fast magnetic mode waves. The first ones do not carry energy, while the second ones are reflected back to the photosphere. Thus, waves in the 5 minute band cannot supply energy to the chromosphere, if the driving force is located at the sunspot center.

This case differs from the simulations with shorter periods described in Sections. 5.4.1, 5.4.2 and 5.4.3, where the slow acoustic wave transports to the high layers part of the energy injected by the driver (or, in the case of 50 s off-axis driver, a smaller part of the energy is also transported upward in the form of the Alfvén wave). In the simulation with the 5 minute wavelet force located at the axis, waves with frequencies higher than ν_c represent a small fraction of the energy introduced by the driver.

The acoustic flux in Figure 5.19 shows that most of the energy keeps below the layer

$c_S^2 = v_A^2$. The wavelet mainly drives 5 minute power in a fast acoustic mode, and since it is evanescent, it does not propagate energy upward and this 5 minute power is distributed horizontally. Only waves with frequency higher than the cutoff frequency are transformed into slow acoustic modes in the low-β region and carry energy to the chromosphere. They correspond to the low acoustic flux which appears at the center of the sunspot between $z = 0$ Mm and $z = 1$ Mm. The high-β region contains the energy of the slow magnetic modes generated from the secondary transformation of the reflected fast magnetic modes. In the magnetic flux, the energy of these slow modes appears in red for radial distances below 6 Mm. Note that, interestingly, the maximum of this energy is not located just at the $c_S^2 = v_A^2$ line it was in the case of 50 s simulations, but it located below this line. This new location follows the line of constant $\nu_c = 4$ mHz meaning that the cutoff effects also influence the penetration of the magnetic energy into the higher layers. The fast mode waves in the high-β region contribute to the high acoustic flux there. Like in all the simulations with the driver located at the center of the sunspot, magnetic flux along field lines is negligible, and there is no conversion to Alfvén waves.

Propagation in the upper atmosphere

Contours in Figure 5.17(a) in the region above $v_A^2 = c_S^2$ (upper part of the domain) far from the axis of the sunspot show longitudinal waves with 5 minute period which apparently move across field lines at the sound speed. Similar to Section 5.4.1, we tried to analyze their wavenumber and phase velocity behavior with height. However, the wavelength of these waves in the upper layers is comparable to the size of our simulation domain in the vertical direction (~ 1 Mm above $v_A^2 = c_S^2$). Because of that, we cannot be completely sure if these waves propagate along or across the field lines.

Another difficulty to understand the behavior of these waves lies in the fact that their frequency is below the cutoff frequency ν_c of the atmosphere. In principle, the cutoff frequency in the magnetically dominated atmosphere is lowered for the acoustic wave propagating along inclined field lines. We calculated the cutoff frequency taking into account the effect of the field inclination. We found this inclination to be insufficient to reduce the cutoff frequency enough to allow for the propagation of the 5-minute waves. Simulations in a larger spatial domain (both in the horizontal and vertical directions) will be needed in the future to clarify the nature of these waves.

5.4.5 Case of 300 s wavelet force located off the axis

Figures 5.20 and 5.21 show the longitudinal and transversal components of the velocity, respectively, of the simulation with the driver located at 5 Mm from the axis of the sunspot. Similar to the simulations presented in previous sections, the driver mainly excites a fast acoustic mode below the $c_S = v_A$ layer. When it reaches this layer it is transformed into a slow acoustic mode (visible in blue in high layers at $x = -5$ Mm in the longitudinal velocity, Figure 5.20), which propagates upwards to the chromosphere; and a fast magnetic mode (visible in the transversal velocity, Figure 5.21), which is reflected back to the photosphere due to the gradients of the Alfvén speed. When the later fast mode reaches the $c_S = v_A$ layer, it is transformed again into a fast acoustic mode and a slow magnetic mode in the

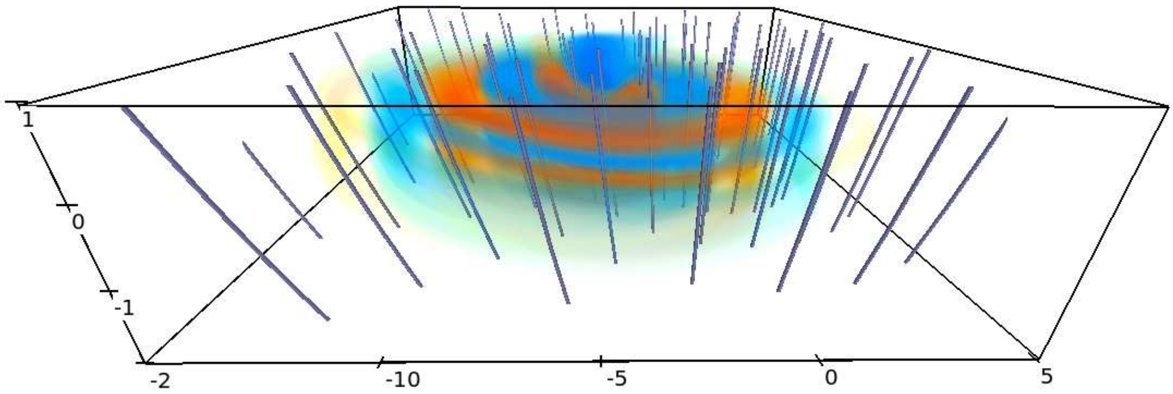

Figure 5.20: Variations of longitudinal velocity scaled by a factor $\rho^{1/2}$ at an elapsed time $t = 820$ s after the beginning of the simulations with the driver force at 5 Mm from the axis of the sunspot. Gray inclined lines are magnetic field lines.

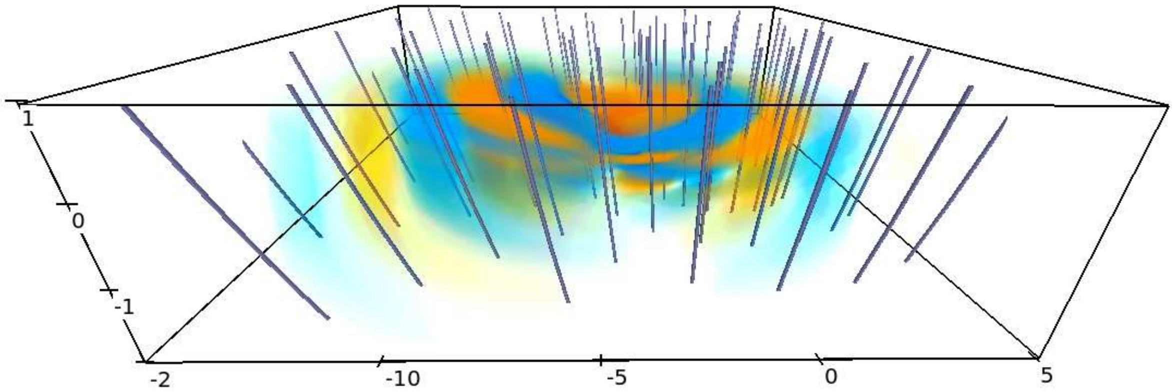

Figure 5.21: Variations of transversal velocity scaled by a factor $\rho^{1/2}$ at an elapsed time $t = 820$ s after the beginning of the simulations with the driver force at 5 Mm from the axis of the sunspot. Gray inclined lines are magnetic field lines.

high-β region. The new fast acoustic and slow magnetic modes in the high-β region appear in Figures 5.20 and 5.21, respectively, as concentric rings around and below $z = 0$ Mm. There is also conversion to the Alfvén mode, although it is not visible in these figures. We will discuss it in Section 5.4.5.

Frequency change with height

Figure 5.22 shows the power spectra of the longitudinal velocity at two different heights at the location of the driver for the simulation with $X_0 = 10$ Mm. The blue line corresponds to the photospheric height $z = -1$ Mm, where the driver was imposed, while the red line is the power spectra at $z = 1$ Mm, *i.e.*, at the chromosphere. The photospheric power spectra peaks at 3.3 mHz (5 min) and it has a secondary peak around 5.4 mHz. The maximum contribution to the power at the chromosphere is at 5.3 mHz (3 min), so the simulation

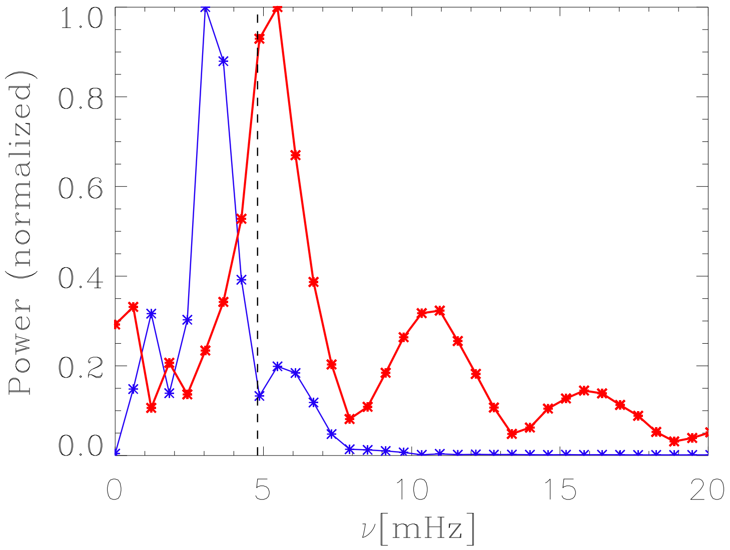

Figure 5.22: Normalized power spectra of the longitudinal velocity at the photosphere (blue line) and the chromosphere (red line) at the location of the driver for the simulation with $X_0 = 10$ Mm. Asterisks mark the measured values. The vertical dashed line marks the maximum value of the cutoff frequency at this position.

reflects the observed change of frequency with height. Note that interestingly the frequency of the power peak in the chromosphere is lower than the one obtained from Figure 5.18 (see discussion to Figure 5.23 below).

The power spectra at the chromosphere in Figure 5.22 shows some secondary peaks, which correspond to the harmonics of the 3 minute signal, due to the importance of the non-linearities at these high layers, where the longitudinal velocity reaches an amplitude of 4.5 km s^{-1}. Waves with freqecies below the cutoff (dashed vertical line) form evanescent waves, which can not propagate energy upwards, while waves with frequencies above the cutoff (as the secondary peak of the photospheric power spectra) do propagate energy upwards. Their amplitude increases according to the drop of the density.

Figure 5.23 shows the frequency of the dominant power peak at all atmospheric heights at the location of the driver for the three simulations with a wavelet driver out of the axis. At photospheric deeper layers the dominant frequency is around 3.3 mHz (5 min) for all simulations, increasing abruptly around $z = 0$ Mm (depending on the case), when the power at frequencies above the cutoff becomes more important than the evanescent 3 mHz oscillations. At the chromosphere, in the case of the simulation with the driver at 5 Mm from the axis of the sunspot (red line), the frequency of the maximum power peak is around 5.5 mHz, while it decreases to 5.2 mHz for the driver located at 10 Mm (green line), and 5 mHz for the driver at 15 Mm (blue line). The frequency of the peak at the chromosphere decreases with the radial distance, since the cutoff frequency is higher near the center of the sunspot.

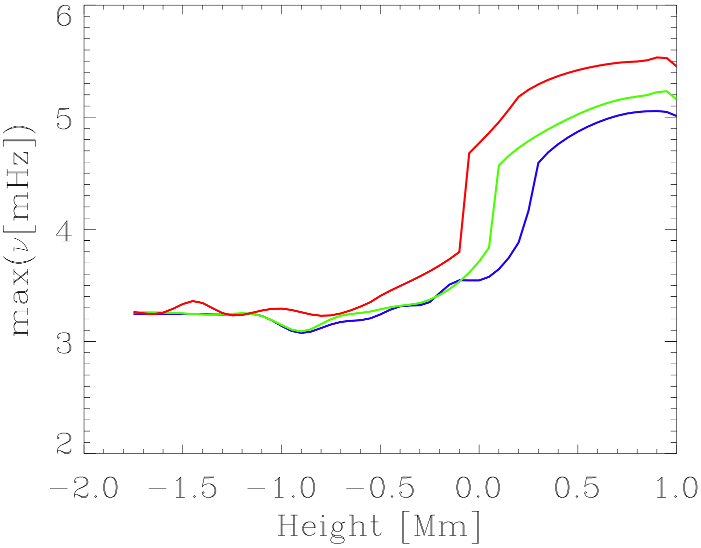

Figure 5.23: Height variation of the dominant frequency of oscillations for the 3 simulations with the driver located at 5 (red line), 10 (green line) and 15 (blue line) Mm of the sunspot axis. The spectra are taken at the location of the driver of the corresponding simulation.

Acoustic and magnetic wave energy fluxes

Figures 5.24, 5.25, and 5.26 present the acoustic (top panels) and magnetic (bottom panels) energy fluxes obtained from Eqs. 5.6 and 5.7. They clearly show that most of the energy introduced by the driver keeps below the layer $c_S = v_A$ (white horizontal line), since the low frequency (3.3 mHz band) slow acoustic mode can only propagate horizontally, and the fast magnetic mode above this layer returns toward the photosphere and generates new acoustic and magnetic flux after its transformation. Only the slow acoustic mode with frequencies above the cutoff frequency that propagates upward along field lines, visible in top panel of Figures 5.24 – 5.26 at a radial distance around the location of the driver and z between 0.5 and 1 Mm, supplies energy to the chromosphere, since the energy of the Alfvén mode is negligible, as we will show later. Most of the magnetic flux above the layer $c_S = v_A$ corresponds to the fast magnetic waves which are being reflected.

The Alfvén mode is visible in Figure 5.27. It shows the longitudinal magnetic energy flux calculated from Equation 5.7 when $\mathbf{v}$ and $\mathbf{B}_1$ are projections along the polarization direction of the Alfvén wave (Equation 5.4), for the driver located at 5 Mm from the axis of the sunspot. The top panel is a cut in the plane $x-z$ at $y = -1.3$ Mm, and it is normalized to its maximum at every height. The bottom panel is a horizontal cut in the plane $x-y$ at $z = 0.5$ Mm. The Alfvén direction projections from Cally & Goossens (2008) are valid only in asymptotic case $\beta \ll 1$. It means that in the top panel we can only indentify the Alfvén mode energy flux in the layers above the line $c_s^2 = v_A^2$, and the flux below this height is not meaningful. The Alfvén wave propagates upward along field lines. The transformation from the fast acoustic mode to the Alfvén wave does not take place in the plane $y = 0$ Mm,

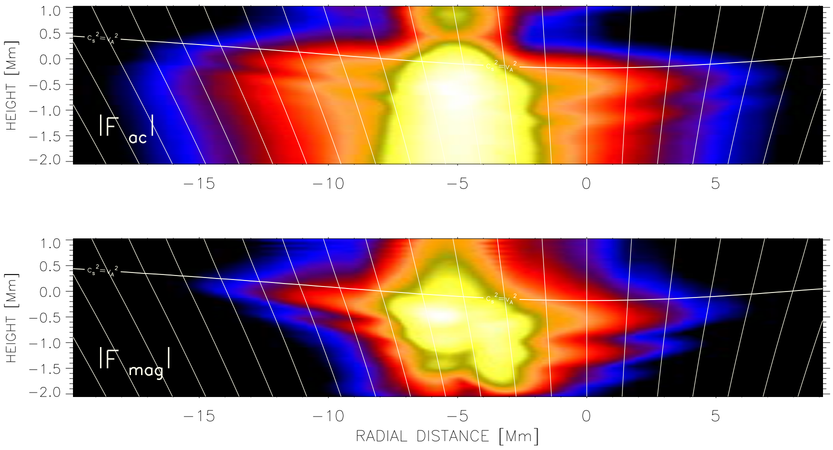

Figure 5.24: Acoustic (top) and magnetic (bottom) flux for the simulation with $X_0 = 5$ Mm averaged over the stationary stage of the simulations in logaritmic scale. Horizontal white line is the height where sound velocity and Alfvén velocity are equal.

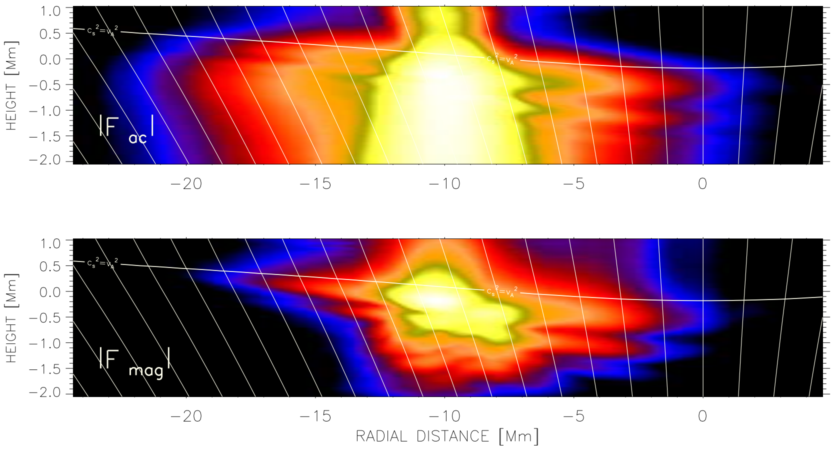

Figure 5.25: Acoustic (top) and magnetic (bottom) flux for the simulation with $X_0 = 10$ Mm averaged over the stationary stage of the simulations in logaritmic scale. Horizontal white line is the height where sound velocity and Alfvén velocity are equal.

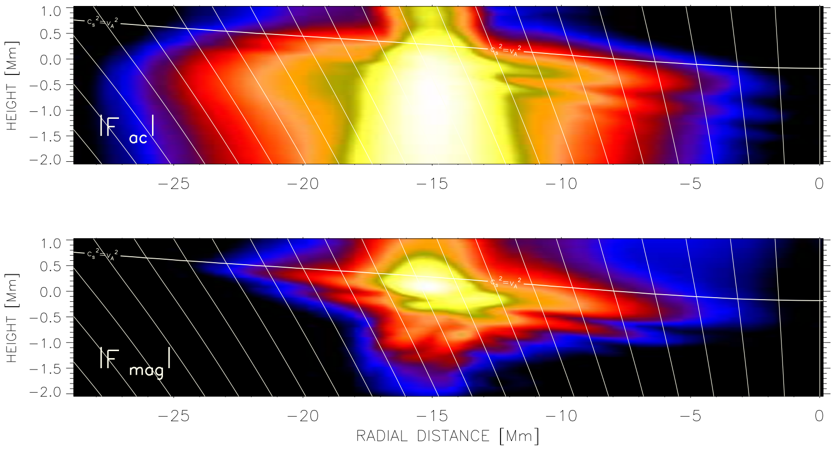

Figure 5.26: Acoustic (top) and magnetic (bottom) flux for the simulation with $X_0 = 15$ Mm averaged over the stationary stage of the simulations in logaritmic scale. Horizontal white line is the height where sound velocity and Alfvén velocity are equal.

where the driver is located, but out of this plane there is energy flux in the Alfvén mode, as can be seen in the bottom panel. However, for the inclination of the magnetic field and the direction of propagation of the wave in these simulations, the trasformation to the Alfvén mode is very ineffective, and the magnetic flux of this wave at the height $z = 0.5$ Mm and at $y = -1.3$ Mm is around 20 times lower than the acoustic flux of the slow mode at the same position. However, it is 40 times lower than the maximum of the acoustic flux at this height (which corresponds to $y = 0$ Mm).

5.5 Discussion and conclusions

In this chapter, we have addressed the problem of the 3D wave propagation and mode transformation of the MHD waves in the upper atmosphere (photosphere and chromosphere) of a sunspot model, by means of numerical simulations.

We have presented the analysis of several simulations where the sunspot atmosphere was perturbed by different pulses, varying their location and temporal behavior. The simulations of short period waves in the 3D sunspot model clearly show several phenomena that are predicted by wave theory. We confirmed that our code correctly describes the propagation of slow and fast modes, both in regions dominated by the magnetic field and the gas pressure.

The conversion between fast and slow magneto-acoustic waves happens in 3D in a qualitatively similar way as in two dimensions. Waves with frequencies down to the cutoff frequency behave in the same way. The driver located in the gas pressure dominated region generates mostly the fast acoustic mode. The fast mode which propagates upwards is transformed at the height where the Alfvén and sound velocities are similar. After this mode conversion, a slow acoustic mode propagates upwards along the field lines in the region $v_A > c_S$. The fast magnetic mode undergoes refraction due to the gradients of the Alfvén velocity and it is reflected back to the photosphere. When it reaches again the

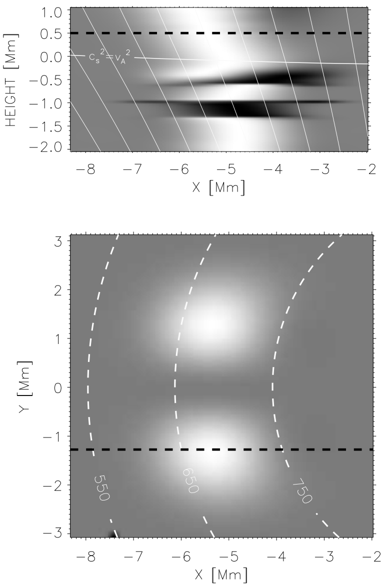

Figure 5.27: Longitudinal magnetic flux of the Alfvén mode at $t = 330$ s for the simulation with the driver located at 5 Mm from the axis of the sunspot. Top: Vertical cut in the plane $y = -1.3$ Mm, normalized at every height. Vertical white lines are magnetic field lines and horizontal white line is the layer where $c_S^2 = v_A^2$. Bottom: Horizontal cut in the plane $z = 0.5$ Mm. Thin dashed lines are contours of equal magnetic field, with its value indicated in Gauss. In both panels, black dashed lines mark the location of the other plot.

surface $v_A = c_S$, it is transformed into new fast acoustic and slow magnetic modes in the region $v_A < c_S$.

High-frequency field-aligned propagating acoustic waves are constantly produced in the upper magnetically dominated atmosphere at locations away from the source. These waves appear due to the continuous transformation from the fast (acoustic) waves moving horizontally, across the field lines, away from the source in the gas pressure dominated region. On their way, the fast waves constantly touch the $c_S = v_A$ layer producing slow (acoustic) waves in the upper atmosphere in the horizontal locations far from the source. We observe this behavior in all simulations with different driving frequencies and source position.

The 3D simulations allow us to identify an Alfvén mode. This mode appears only in the simulations with the source located away from the sunspot axis. It is produced after the transformation from the fast (acoustic) mode. Its conversion rate is low compared to the fast to slow transformation, and the eventual energy of the Alfvén wave in the magnetically dominated region is much lower than that of the slow mode. In the simulations with the driver located at the axis of the sunspot, where the angle between the direction of the upward propagating wave and the magnetic field is zero, we find no indications of the transformation to the Alfvén mode.

From the study of the wave energy fluxes we have found that in the case of waves with frequency above the cutoff the wave energy can reach the upper atmosphere as slow acoustic field aligned propagating waves. On the other hand, the fast magnetic waves are reflected, and there is no magnetic flux corresponding to them above a certain height in the middle chromosphere. When the driver is located out of the axis, some small part of the energy can also propagate upward in the form of an Alfvén wave.

A realistic driver mainly excites waves in the 5 minute band, whose frequency is below the cutoff. In this case, most of the energy is confined to the region below the height where the sound and Alfvén velocity are similar. The energy of the fast magnetic modes in the upper layers is reflected, while the evanescent acoustic slow modes do not propagate any energy at these frequencies. The comparison between the magnetic fluxes at high and low frequencies shows that the magnetic flux reaches smaller heights for the low-frequency waves.

The sunspot model used in this work has a maximum cutoff frequency at $\nu_c = 5.8$ mHz, and waves with frequencies below this value cannot propagate to the chromosphere and become evanescent waves. We have shown that high-frequency waves are able to propagate upward along field lines. Due to their amplitude increase with height (caused by the density falloff) the 3-minute waves ($\nu \approx 5.9$ mHz) dominate the power spectrum in the chromosphere. This behavior, obtained in the simulations, is similar to the observed one. These simulations also show that the dominant wave frequency in the chromosphere decreases with the radial distance, due to the reduction of the cutoff frequency far from the axis.

One of the questions that arises from these results is the evaluation of the validity of the decomposition performed to separate the fast mode from the Alfvén mode in the low-β plasma. The decoupling following Cally & Goossens (2008) is valid for an idealized case when considering a uniform magnetic field, for a plane wave with a constant wavenumber perpendicular to gravity, and it is obtained asymptotically in the limit of infinite Alfvén speed. Although the realistic atmosphere used in our calculations does not fulfill these restrictions, a coherent picture is retrieved from the magnetic flux of the velocity and magnetic field components in the direction given by Equation 5.4, showing upward propagation along magnetic field lines. The result that naturally emerges from this decomposition justifies the application of the method.

Another issue that complicates the decoupling of both magnetic modes is the excitation of small horizontal wavenumbers due to the limited horizontal extent of the driver. The fast mode is refracted due to the rapid increase of the Alfvén speed with height, but the altitude at which it happens depends on the wavenumber, being higher for lower wavenumbers. Since most of the power excited by our driver lies in the range of wavenumbers below $\sim 1/R_{scr}$, some of the fast mode waves might still be partially refracted in the limited 1 Mm atmosphere above the $c_S = v_A$ surface. The magnetic flux of these waves may reach high layers, complicating the separation of the fast and Alfvén modes. In this scenario, we would expect a continuous transition between the upward longitudinal magnetic flux and the refracted one at different heights where all these waves are being refracted. However, the magnetic flux of the Alfvén wave that we retrieve is clearly delimited along magnetic field lines, confirming that this flux mostly corresponds to the Alfvén mode.

The most important achievement reached by the development of our numerical code is the possibility to investigate the 3D mode transformation in realistic conditions imitating a sunspot atmosphere. This, together with the possibility to study long-period waves in the layers where they are observed, gives an opportunity for the direct comparison between our numerical simulations and solar spectropolarimetric observations. Simulations of sunspot high layers represent a hard challenge due to the exponential increase of the Alfvén speed with height. Our sunspot model presents an Alfvén speed of almost 1000 km s^{-1} close to the upper boundary of the domain, limiting the time step and making the calculations very expensive. Despite this, our code manages to describe the waves well, including the correct performance of the boundary PML layer. Note that other works on waves in non-trivial magnetic configurations have been restricted either to two-dimensional high-frequency cases (Cargill et al. 1997; Rosenthal et al. 2002; Hasan et al. 2003; Bogdan et al. 2003; Khomenko & Collados 2006) or to the study of helioseismic waves, where the problem of high Alfvén speed is avoided (Cally & Bogdan 1997; Parchevsky & Kosovichev 2009; Hanasoge 2008; Cameron et al. 2008; Moradi et al. 2009b; Khomenko et al. 2009).

The strategy applied in our code allows the direct comparison with observations by means of spectral synthesis. The simulations presented in this chapter reproduce the frequency change with height, actually observed in the sunspot atmospheres (Centeno et al. 2006). In Chapter 7 we will perform a more detailed comparison with solar data, by exciting a MHS sunspot model with velocities obtained from spectropolarimetric observations, and by comparison of the simulated wave parameters in the photosphere and chromosphere with those obtained from simultaneous observations in different spectral lines.

Perhaps the most interesting simulations considered in this chapter are the ones with the source exciting a spectrum of waves close to the solar one. These cases have a special relevance because theoretical models of wave transformation, existing as of today, are best valid in the high-frequency limit and do not address the behavior of waves at frequencies below the cutoff frequency (Schunker & Cally 2006). Our initial results show that almost no energy of the 5 minute waves propagates into the higher layers, at least in the situation of the sunspot model and location of the sources considered in these simulations. In particular, an interesting question is under which conditions 5 minute Alfvén waves can be excited by the mode transformation. These waves can still propagate some energy into the upper atmosphere of solar active regions, and thus understanding the conditions of transformation to these waves and their energetics in sunspots is important. The number of works in the literature with numerical calculations including the transformation to Alfvén waves is scarce. The most relevant study is the one by Cally & Goossens (2008), who find that the transformation to an Alfvén mode is effective at certain angles of inclination and azimuth of the magnetic field. Our code will give us a possibility in the future to perform a more detailed study of the transformation to Alfvén waves under realistic conditions.

6

Multi-layer observations of waves

Simultaneous observations in different spectral lines give us information about different heights in the solar atmosphere. It is thus interesting to perform a detailed sampling of the sunspot atmosphere, using a set of spectral lines formed between the photosphere and the chromosphere. One of the pionering papers of this subject is the work by Kneer et al. (1981). On the one hand, observationally detected spatial wave patterns in sunspots are rather complex (Bogdan & Judge 2006), and several studies have pointed out the presence of fine structure in chromospheric umbral oscillations (Socas-Navarro et al. 2001, 2009; Centeno et al. 2005). On the other hand, recent numerical simulations of waves in sunspots also suggest a complex picture of the fast and slow magneto-acoustic waves propagating simultaneously in the same layers but in different directions and with different phase speeds (Khomenko & Collados 2009, Chapter 5 of this thesis). This requires a more refined multi-layer study of sunspot waves. Studies of this kind often represent an observational challenge since several spectral lines have to be detected simultaneously not only in intensity but also in polarized light. In this chapter, we report on such multi-line spectropolarimetric observations. Our aim is to cover the gap between the photospheric and chromospheric signals and analyze sunspot oscillations at the formation heights of several spectral lines. Apart from information about waves, we also aim to estimate the structure of the sunspot atmosphere and the formation heights of the spectral lines used in this study: Ca II H line, several Fe I blends in the wing of this line and the infrared lines of Si I at λ 10827 Å and He I at λ 10830 Å. The works by Lites (1986) and Centeno et al. (2006), for example, have used these spectral lines.

The structure of this chapter is the following. In Section 6.1 the observations and data reduction are explained. Section 6.2 describes the analysis of the velocity oscillations at several heights. The results are discussed in Section 6.3, which also presents our conclusions.

6.1 Observation and data reduction

The observations analyzed in this work were obtained on 2007 August 28 with two different instruments, the POlarimetric LIttrow Spectrograph (POLIS, Beck et al. 2005b) and the Tenerife Infrared Polarimeter II (TIP-II, Collados et al. 2007), attached to the German

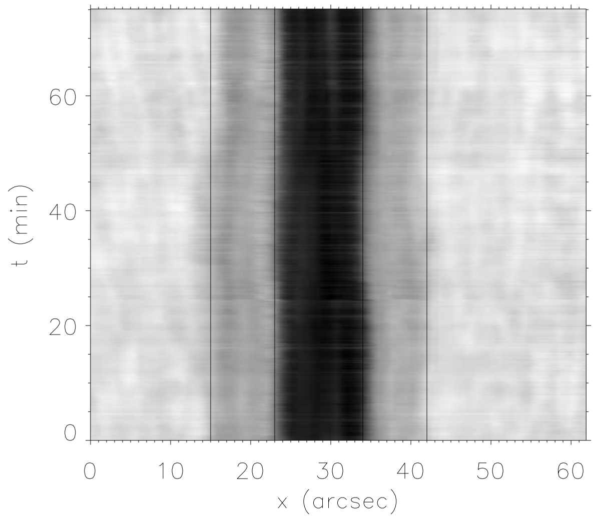

Figure 6.1: Temporal evolution of the IR continuum along the slit. Vertical lines mark the position of quiet Sun-penumbra and penumbra-umbra boundaries. Time increases from bottom to top.

Vacuum Tower Telescope at the Observatorio del Teide in Tenerife. Simultaneous and co-spatial scans of a sunspot located near the center of the Sun ($\mu = 0.96$) were taken with both instruments. The slit was placed over the center of the sunspot. The observations were obtained with real-time seeing correction by the Kiepenheuer-Institute adaptive optics system (von der Luehe et al. 2003).

The spectra of the blue channel of POLIS include Ca II H λ 3968 Å intensity profiles and some photospheric line blends in the wings of Ca II H, covering a spectral range from 3964.9 Å to 3971.3 Å with a spectral sampling of 20 mÅ pixel^{-1} and a spatial sampling of $0''29$ per pixel. The Ca spectra were reduced for the flatfield (Beck et al. 2005a,b), and were also corrected for the transmission curve of the order-selecting interference filter in front of the camera. For the wavelength calibration, the line-core positions of the iron lines at 3965.45, 3966.07, 3966.63, 3967.42 and 3969.26 Å in an average quiet Sun region were determined by a second order polynomial fit. We then determined the wavelength scale that matched best all the position values.

TIP-II yielded the four Stokes parameters $IQUV$ in a spectral range from 10822.7 Å to 10833.7 Å with a spectral sampling of 11 mÅ pixel^{-1} and a spatial sampling of $0''18$ per pixel. This spectral region contains information about two different heights of the solar atmosphere due to the presence of two spectral lines. The Si I line at 10827.09 Å is formed at photospheric heights, whereas the He I λ 10830 triplet, which includes a weak blue component at 10829.09 Å and two blended red components at 10830.25 and 10830.34 Å, forms in the chromosphere (Centeno et al. 2008). In this case, the wavelength calibration was done using the Si I and He I lines as references.

The full data set consists of three temporal series; each of them lasting about one hour. Three scan steps with $0''5$ step width were taken for the two first series, while in the last series only two spatial positions were used. The cadence was different for all series. Table

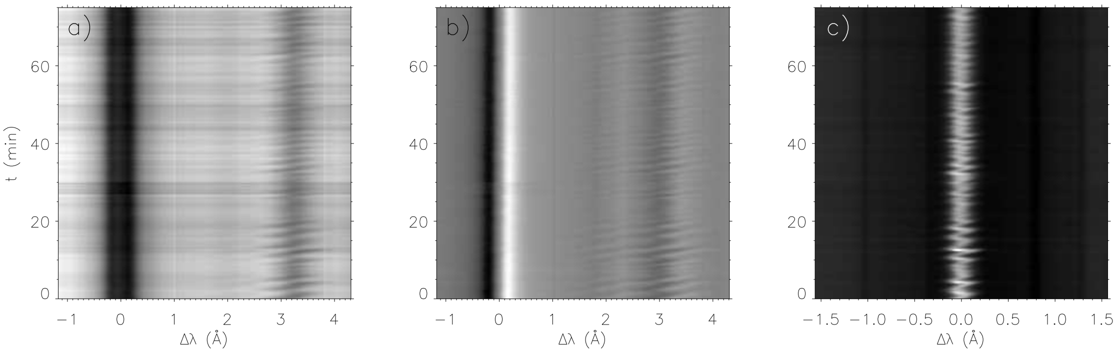

Figure 6.2: Temporal evolution of the spectra obtained at one position in the umbral region of series #2. *Left*: Si I and He I intensity; *center*: Si I and He I Stokes V; *right*: Ca II H intensity. The horizontal axis represents wavelength, with the origin at the position of the Si I λ 10827 Å rest wavelength in (a) and (b) and at the position of the Ca II H λ 3968 Å rest wavelength in (c). The vertical axis represents time, increasing from bottom to top.

6.1 shows the time step between two spectra taken at the same spatial position, the time when the observation were obtained and the number of repetitions of each series.

Table 6.1: Summary of observations:

Series No	t_{start} (UT)	t_{end} (UT)	Δt (s)	N spectra
Series 1	07:55:02	08:54:48	21	170
Series 2	09:01:02	10:15:25	18	250
Series 3	10:43:34	11:58:43	7.5	600

Due to the differential refraction in the earth atmosphere (e.g., Filippenko 1982), the spectra of POLIS and TIP-II are not fully co-spatial. The spatial displacement of the two wavelengths (3968 Å, 10830 Å) perpendicular to the slit depends on the date and time of the observations, the slit orientation, and the location of the first coelostat mirror (see Appendix A of Beck et al. 2008). On the first day of the observation campaign, we took a set of large-area scans at different times for an accurate determination of the displacement. The solid line in Figure 6.3 shows the theoretically predicted spatial displacement perpendicular to the slit due to differential refraction, while the asterisks are the measured displacements; the match between both is remarkable. To guarantee an overlap between the observations in the two wavelengths, we thus positioned the scan mirror inside of POLIS at the beginning of each observation such that it compensated the spatial displacement for about the middle of the observation. Moreover, small repeated scans of 2-3 slit spatial positions, separated by $0''5$, were taken in order to sample a wider region of the Sun and prevent possible errors between the theoretical differential refraction and the actual one.

Figure 6.1 shows the temporal evolution of the intensity in a wavelength from the IR continuum. The regions of quiet Sun, penumbra, and umbra of the sunspot are well defined. The vertical lines in the figure indicate the boundaries between these areas. The temporal evolution of the Stokes I and Stokes V spectra for the TIP data and the intensity around the Ca II H core in the POLIS data are plotted in Figure 6.2 at a fixed position inside the

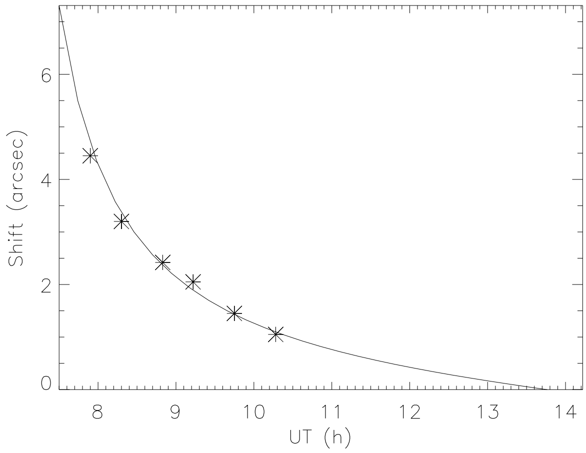

Figure 6.3: Temporal variation of the theoretical spatial displacement perpendicular to the slit due to differential refraction *(Solid line)*. *Asterisks* mark the values measured at the telescope.

umbra. The Stokes I and V profiles from TIP contain the Si I line at $\Delta\lambda$ =0 Å (the rest wavelength of the silicon line was determined from the quiet Sun region and was set as the origin) and the He I line at $\Delta\lambda$ =3.25 Å. The helium line profile shows periodic shifts with large displacements to the blue and the red. The core of the Ca II H line shows a strong emission peak inside the umbra. The Doppler shift of this emission peak develops a saw-tooth pattern, similar to the He I line (see also Rouppe van der Voort et al. 2003).

6.2 Data analysis and results

We focus our analysis on the line-of-sight (LOS) velocities. For all the spectral lines except for Ca II H, Doppler velocities were inferred by measuring the position of the intensity minimum. The wavelengths close to the core of the line were fitted with a second order polynomial. The location of the minimum of the parabola was taken as the line-core position. This procedure was performed to obtain the Doppler shifts of Si I, He I, and the Fe I lines at 3965.45, 3966.07, 3966.63, 3967.42 and 3969.26 Å. In the case of the TIP data, the Doppler shift of the Stokes V zero crossing, where the polarization signal intersects the zero level, was derived as well. The Doppler shifts from the intensity and Stokes V profiles are very similar due to the large magnetic filling factor in the sunspot umbra.

The behavior of the Ca II H core is different. It exhibits a prominent peak at the center of the line in highly magnetized regions (top line of Figure 6.4), while in a field-free atmosphere the center of the line has a minimum between two lobes at both sides with their corresponding maxima (bottom line of Figure 6.4) (see also, e.g., Liu & Smith 1972). In the umbra, the Doppler shift was retrieved from the spectral displacement of the maximum of the core emission. In the low magnetized region it was obtained from the shift of the central minimum. All in all, we have obtained maps of the LOS velocity at each spatial point covered by the slit at the formation heights of the eight spectral lines, except for He I, whose line depth in the non-magnetized regions is too small to determine its location.

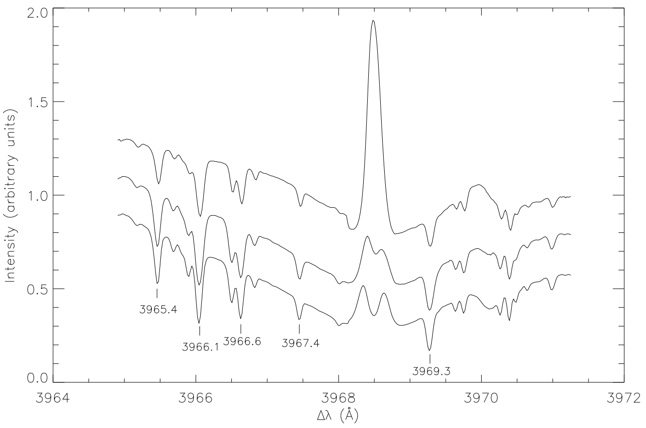

Figure 6.4: Averaged intensity profile of the Ca II H line at different locations. From bottom to top: quiet Sun, penumbra, and umbra. The intensity scale is different for all of them. The profiles have been displaced from each other. The Fe I lines analyzed in this work are marked.

We have selected the scan steps which give the best alignment of the data from both instruments to obtain a better correction of the differential refraction. The use of different steps introduces a systematic delay between the oscillatory signals from POLIS and TIP-II, since the same spatial location is observed with a time lag. However, in the case of the data from series 3, the theoretical correction of the differential refraction worked perfectly and the optimal alignment was found using the simultaneous scan steps. This data set has been chosen to calculate the phase difference spectra, as shown in Section 6.2.3. An additional finer alignment along the slit between TIP and POLIS was done by cross-correlation of the velocity maps of two spectral lines formed at similar heights, using the line pair Ca II H and He I for the chromosphere, and Si I and Fe I λ 3969.26 Å for the photosphere. Finally, we resampled all velocity maps with the sampling of the POLIS Ca II H data, *i.e.*, $0''\!.29$ per pixel.

6.2.1 LOS velocity

Figure 6.5 shows an example of the temporal evolution of the LOS velocities in the sunspot region obtained from the Doppler shift of several spectral lines. Negative velocities (appearing as black shaded regions) indicate upflows, where matter is approaching the observer, while white regions are downflows. Figures 6.5(a-d) reveal a similar pattern since all these lines are formed at photospheric heights. The velocity maps of the Fe I line blends of Ca II H have lower quality than the Si I maps, especially inside the umbra, due to the coarser spectral sampling and the small line depth of the lines.

The velocity field at chromospheric heights is given in Figure 6.5e (Ca II H) and 6.5f (He I). Both figures show a similar wave pattern and similar amplitudes, but, as a more detailed analysis will reveal, the velocity oscillations of the He I line are slightly retarded relative to those in Ca. The wave pattern measured at chromospheric heights in the umbral region has a smaller spatial coherence than that observed in the photosphere. It also differs in its larger peak-to-peak variations of about 8 km s^{-1} and its period of about three minutes.

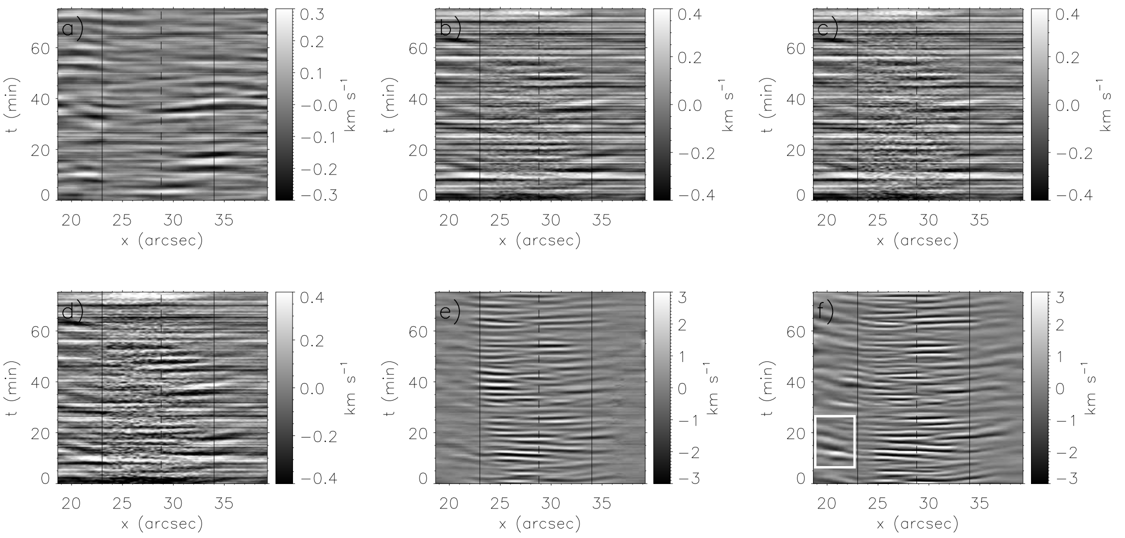

Figure 6.5: Velocity maps in the sunspot during series #2 for the different spectral lines. The horizontal axis represents the position along the slit and the vertical axis represents time. Black color indicates negative velocities (upflow), white color positive velocities (downflow). Top row, left to right: Si I λ 10827 (a), Fe I λ 3966.1 (b), Fe I λ 3966.6 (c). Bottom row, left to right: Fe I λ 3969.3 (d), Ca II H 3968.5 (e), He I λ 10830 (f). Vertical solid lines represents the limits of the umbra. The vertical dashed line denotes the location of the velocity shown in Figure 6.7. The white rectangle in (f) marks an area of running penumbral waves.

In the region of the penumbra, which can be seen in Figure 6.5f at a position between 19″ and 23″ and between 34″ and 39″, there is also a characteristic pattern of alternating positive and negative velocities, but with lower amplitudes than the waves in the umbra and with longer periods, corresponding to running penumbral waves (see, e.g., Giovanelli 1972; Zirin & Stein 1972; Bloomfield et al. 2007). They start at the inner penumbra, and their wave front is delayed in the regions of the outer penumbra, so their propagation through the penumbra appears as a slope in the diagram. An example of such a slope can be seen in an area between 19″ and 23″ during the first 22 minutes (white rectangle). This slope is smaller near the outer penumbra, indicating a decrease of the propagation speed as the disturbance travels from the inner to the outer penumbral boundary. The estimation of the velocity for the Ca II H line core (Figure 6.5e) in the penumbral region is poorer due to the change of the shape of the line that does not have a prominent emission peak any more (see middle curve in Figure 6.4).

The left panels of Figure 6.6 show the histograms of the LOS velocities in the umbra of the sunspot obtained from all the spectral lines used in this study. We fitted a Gaussian to the distributions to estimate the root-mean-square (rms) velocity value. The histograms are sorted from bottom to top with increasing rms velocity, with Si I having the smallest and He I the largest rms velocity. The Fe I lines at 3966.0 and 3966.6 Å have an identical rms velocity value, indicating that they are formed at close heights. This is also suggested by their nearly identical line depth (see Figure 6.4). From these histograms and the variation of the rms velocities, we obtain the first estimate of the relative formation height of the spectral lines since we expect a monotonic increase of the rms velocity with height, according to the density drop.

For comparison, the right panels of Figure 6.6 show the histograms of LOS velocities for the same lines in a region of the quiet Sun. The He I histogram is not shown because the He I absorption in quiet Sun is too low to retrieve a velocity. The quiet Sun histograms also show the increase of the rms velocity with increasing formation height, although the order of the rms velocity slightly differs from the one obtained in the sunspot, since all the Fe I lines form in a thin layer. As the oscillatory power in sunspots is suppressed (see, for example, Hindman et al. 1997), the rms velocities in the quiet Sun are larger. Another possible source of the broadening of the quiet Sun velocity histogram can come from the granulation velocities not present inside the umbra. We did not remove the granular component from the velocity variations in the quiet Sun and it can contribute to some extent to the overall rms velocity variations (see, *e.g.* Kostyk & Khomenko 2002).

Figure 6.7 shows an example of the temporal evolution of the LOS velocity obtained from the chromospheric He I line and the Ca II H line core, the four photospheric Fe I lines, and the photospheric Si I line at one location inside the umbra of the sunspot, indicated in all panels of Figure 6.5 with a vertical dashed line at $x = 28''$. The plots are sorted from bottom to top with increasing formation height, as retrieved from Figure 6.6. A comparison between the bottom and top panels (which show the Si I and He I velocities, respectively) reveals the differences in period and amplitude of the waves at photospheric and chromospheric heights. Between these two layers, the rest of the spectral lines sample different heights of the atmosphere. At photospheric heights (panels c-g), the pattern of waves is similar and the signals of the lines with higher formation heights are slightly delayed (see *e.g.* the peak at $t = 49$ min marked with a dashed line). We can see that higher layers have larger amplitudes (note that the top two panels have a different scale for the velocity). The temporal evolution of the LOS velocity of the two chromospheric lines (panels a-b) is almost identical, but the amplitudes are higher in the case of the He I line. For instance from minute 10 to 25, it is clearly seen that the oscillations measured with the He I line and Ca II H core have a saw-tooth profile that indicates the presence of a shock wave train, with a slow increase of the velocity followed by a sudden decrease. There is a phase difference of about 20 s between the Ca II H line core and the He I line velocities, in the sense that the oscillatory signal reaches the formation height of the Ca II H line core 20 s before that of the He I line.

Table 6.2: Rms velocities in ms^{-1} in the sunspot and the quiet Sun, and their ratio (3rd column).

Line	Umbra	QS	Ratio QS/umbra
Si I	90	250	2.80
Fe I 3965.4	170	256	1.51
Fe I 3966.1	174	275	1.58
Fe I 3966.6	180	273	1.52
Fe I 3969.3	201	306	1.53
Ca II H	510	659	1.29
He I	726	–	–

Table 6.2 lists the rms velocities in the quiet Sun (except He I) and in the sunspot

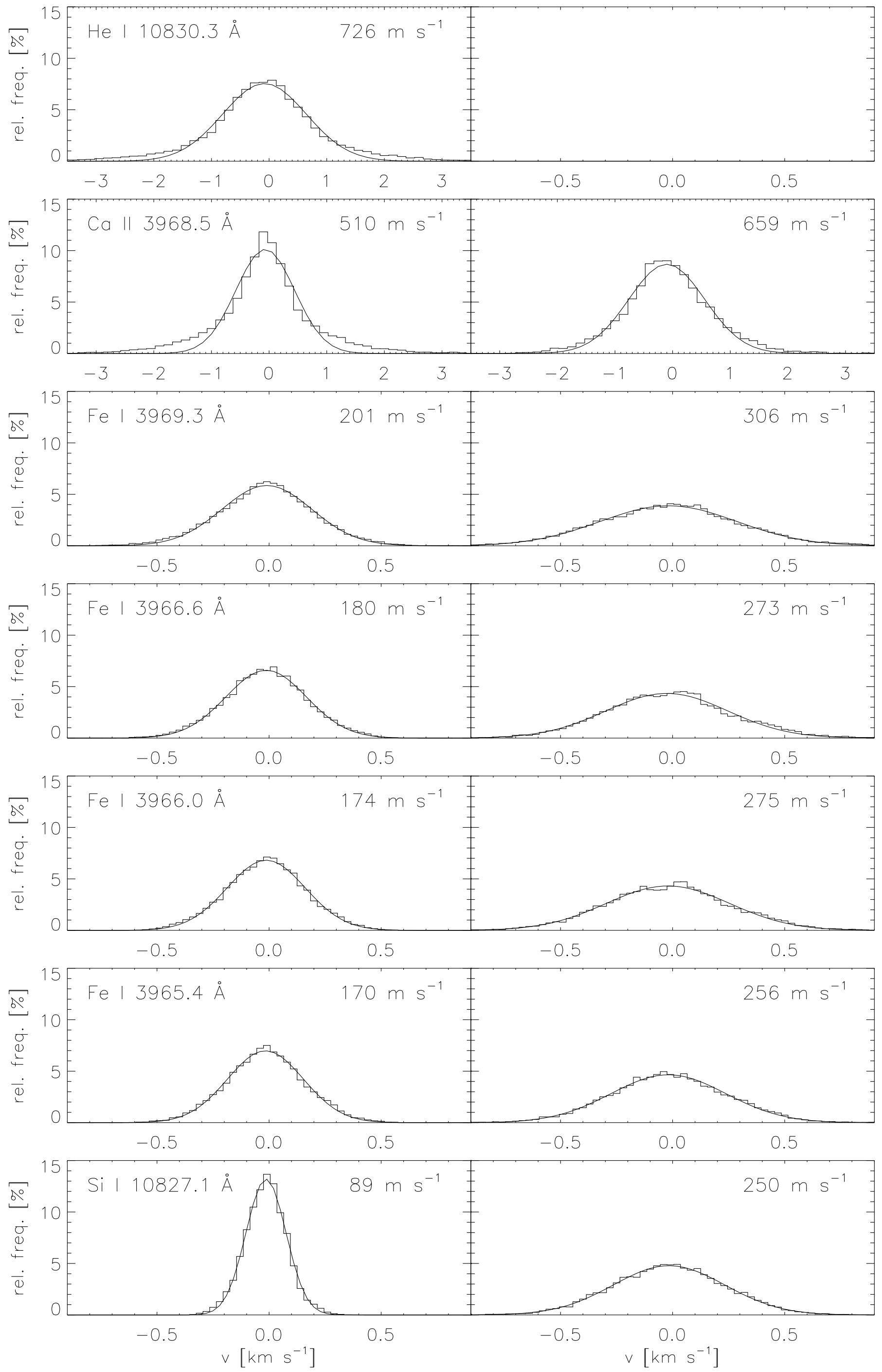

Figure 6.6: Histograms of LOS velocity measured with several spectral lines. The left column corresponds to the umbra, the right column to the quiet Sun. From bottom to top: Si I, Fe I λ 3965.4, Fe I λ 3966.1, Fe I λ 3966.6, Fe I λ 3969.3, Ca II H and He I. Solid lines represent the Gaussian fit; its width is indicated in each plot.

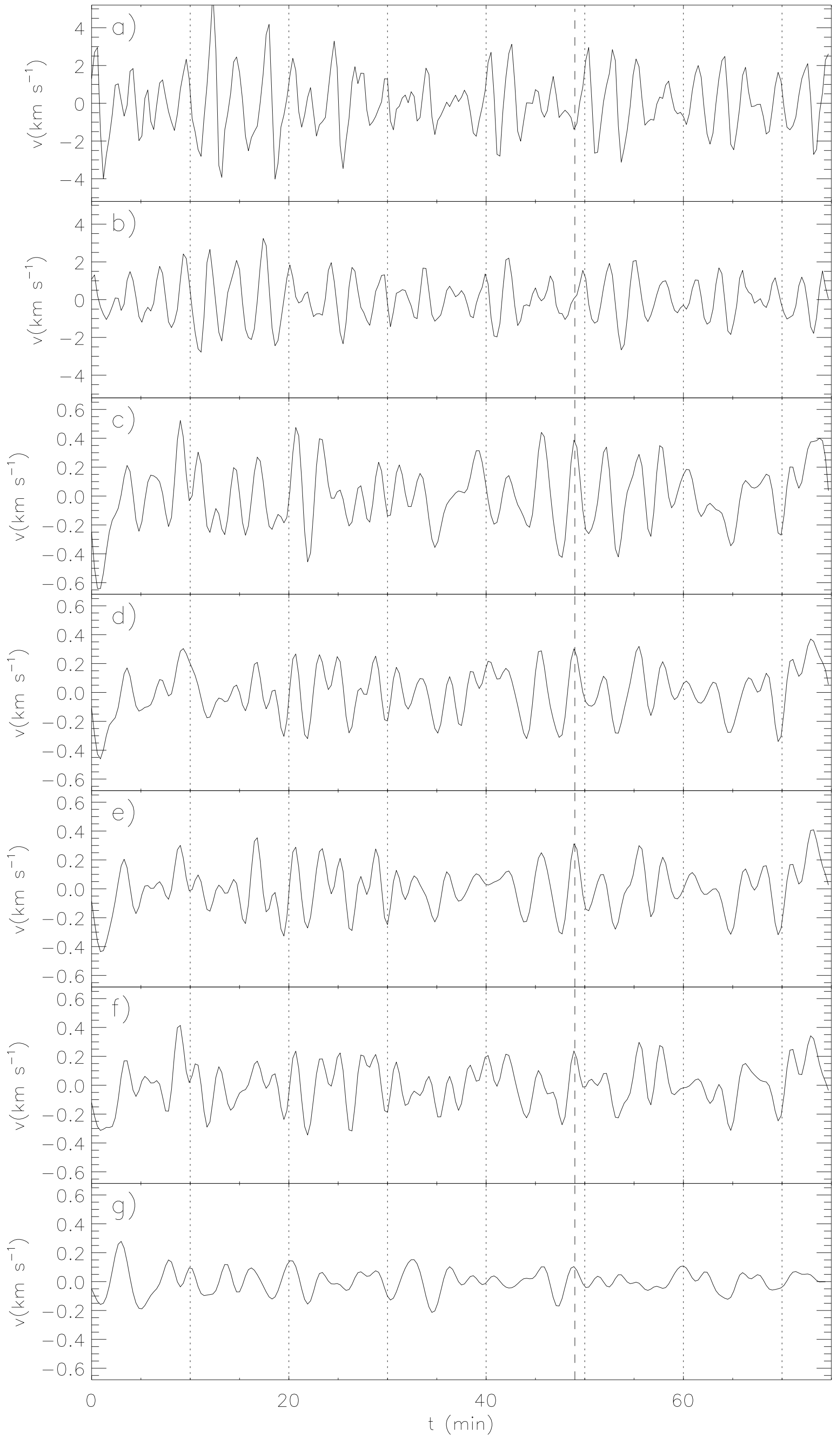

Figure 6.7: Velocity at a fixed position in the umbra for different spectral lines, sorted by formation height: He I λ 10830 (a), Ca II H 3968.5 (b), Fe I λ 3969.3 (c), Fe I λ 3966.6 (d), Fe I λ 3966.1 (e),Fe I λ 3965.4 (f), Si I λ 10827.1 (g). The vertical dashed line at $t = 49$ min marks a prominent velocity peak. The dotted lines are drawn at fixed times for comparison purposes.

for all the spectral lines, together with the ratios between the quiet Sun and the sunspot velocities. The relative increase of the rms velocity of the quiet Sun to the rms velocity of the sunspot decreases with the height in the atmosphere, from 2.80 at the photospheric height of the formation of Si I to 1.29 at the chromospheric height of the formation of Ca II H line core. The rate of the increase of the rms velocity in the sunspot is faster, and the difference between velocities from lines formed at higher layers is smaller. The growth of the amplitude of the oscillations with height is scaled with the pressure scale height, $H_0 = RT/\mu g$, where T is the temperature, R is the gas constant, g is the gravity and μ is the mean weight of the atoms. In the umbra the temperature is lower and H_0 is smaller than in the quiet Sun atmosphere, so the amplitude of umbral oscillations rises faster.

6.2.2 Power Spectra

Figure 6.8 shows the normalized average power spectra of LOS velocity of the two chromospheric (He I and Ca II H) and two of the photospheric (Si I and Fe I λ 3969.3) lines inside the umbra of the sunspot. We chose this iron line because it has better signal to noise and its formation height is distant from the layer where Si I is formed. In the photosphere (bottom panel), the power is concentrated between 2 and 4 mHz, corresponding to the 5 minute band, with a maximum peak at 3.5 mHz. Both spectral lines peak at the same frequency, although the power of the Fe I line is slightly higher. The increase of the power at frequencies above 4.5 mHz is more important than the one for frequencies below this value.

The velocity power spectra of both chromospheric lines (top panel) have a broad distribution of frequencies, with the largest power being in the band from 5 to 10 mHz. The chromospheric power spectrum has a maximum at 6.2 mHz and several secondary peaks around it (see for comparison Lites 1986). These frequency peaks correspond to the chromospheric 3 minutes oscillations. At the highest peak of the power spectra, both Ca II H and He I have almost the same power, but for those frequencies with lower power, the power of the He I is increased comparing to the Ca II H. Note that at the heights sampled by our spectral lines we do not find a continuous transition from the peak at 3.5 mHz to the one at 6.2 mHz, but rather a discontinuous behavior between the photospheric and chromospheric power spectra. However, the prominent secondary peak around 5.5 mHz in the power spectra of the Fe I line is much more obvious than the corresponding in the Si I power spectra, which could indicate some transition towards higher frequencies in the power spectra as the waves propagate upward from the formation height of the Si I line to the Fe I lines.

6.2.3 Phase spectra

A phase diagram gives the phase difference ($\Delta\phi$) between two signals. In our study, we use $\Delta\phi$ to measure the time delay between the oscillatory velocity signals from two spectral lines and assume that the difference between them is mainly due to the difference of the formation height of the two lines. In the following, we show the phase difference spectra between different combinations of pairs of spectral lines used in this work. To obtain the phase spectra, we treated each spatial point separately and calculated the Fourier-transform of the temporal evolution of the respective velocities. We derived the phases, and from them

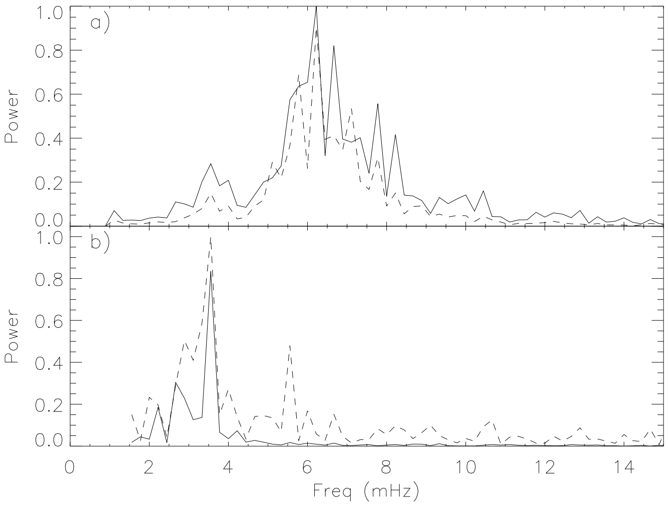

Figure 6.8: Average umbral power spectra of the LOS velocities. *Top:* chromospheric lines, He I (*solid line*) and Ca II H (*dashed line*), both are normalized to the maximum power of the He I line; *bottom:* photospheric lines, Si I line (*solid line*) and Fe I 3969.3 Å (*dashed line*), both are normalized to the maximum power of the Fe I line.

the phase difference of the two signals as a function of the frequency. There is a 2π ambiguity in the computation of the phase value, so all phase differences have been projected in the range $\pm\pi$. Then we calculated histograms of the relative occurrence of a given value of the phase differences at each frequency taking into account all the corresponding spatial points (see also Krijger et al. 2001, and references therein). We obtained the data displayed in Figures 6.9–6.15.

In addition to the phase difference spectra, we calculated the coherence spectra. They provide an estimate of the statistical validity of the phase and power spectra. Considering n pairs of signals $x_k(t)$ and $y_k(t)$, whose Fourier transforms are $\bar{X}_k(\omega)$ and $\bar{Y}_k(\omega)$, respectively, the coherence is defined as

$$P_{xy}(\omega) = \frac{\left| \sum_k^n |\bar{X}_k(\omega)||\bar{Y}_k(\omega)|e^{i\Delta\phi_k(\omega)} \right|}{\sum_k^n \sqrt{|\bar{X}_k(\omega)|^2|\bar{Y}_k(\omega)|^2}} \qquad (6.1)$$

where $\Delta\phi_k(\omega) = \phi_{xk}(\omega) - \phi_{yk}(\omega)$. In our case, the sub-index k covers the spatial position. The coherence evaluates statistically for every frequency ω the relation of the $\Delta\phi_k(\omega)$ for the n k-signals. It takes the value 1 when $\Delta\phi_k(\omega)$ is the same for all the k. If the phase difference of the different k is arbitrary, the coherence takes very low values. We selected a confidence limit at 0.7, and for frequencies with coherence above this value we consider the phase spectra to be reliable.

We also analyzed the increase of the amplitude of the oscillations. We calculated the amplification spectra as the ratio between the power at two layers, both of them averaged all over the umbra:

$$A_{xy} = \frac{\sum_k^n |\bar{Y}_k(\omega)|^2}{\sum_k^n |\bar{X}_k(\omega)|^2}. \qquad (6.2)$$

Theoretical model

Following Centeno et al. (2006), the observations were compared with a model of linear vertical propagation of slow magneto-acoustic wave in an isothermal atmosphere that includes radiative losses described by Newton's cooling law (Mihalas & Mihalas 1984). Assuming that the amplitude of the vertical velocity changes with height by

$$V(z) = V_0 e^{z/(2H_0)} e^{ik_z z}, \tag{6.3}$$

the dispersion relation for such waves is

$$k_z^2 = \frac{\omega^2 - \hat{\omega}_{ac}^2}{\hat{c}^2}, \tag{6.4}$$

where

$$\hat{\omega}_{ac} = \hat{c}/2H_0, \hat{c}^2 = \hat{\gamma} g H_0, \hat{\gamma} = \frac{1 - \gamma i \omega \tau_R}{1 - i \omega \tau_R}, \tag{6.5}$$

and τ_R is the radiative cooling time for an optically thin perturbation (Spiegel 1957):

$$\tau_R = \rho c_v / (16 \chi \sigma_R T^3). \tag{6.6}$$

The phase difference between oscillations at two heights is calculated as the difference of the imaginary part of the argument of the complex exponential in Equation 6.3, that is, $\Delta\phi = k_R \Delta z$, where Δz is the geometric distance between the two heights and k_R is the real part of k_z. The amplification spectrum is given by the ratio between the amplitude at the two layers and is obtained as $A = e^{2(1/(2H_0) - k_I)\Delta z}$, with k_I being the imaginary part of k_z.

This model allows us to fit the phase and amplification spectra with three free parameters: the temperature of the atmosphere, T, the difference in height between two lines, Δz, and the typical time scale in which the temperature fluctuations are damped radiatively, τ_R. These free parameters are manually tuned to match the effective cut-off frequency and the slope (including its variations) of the phase difference spectra in the regime of propagating waves above the cut-off frequency.

Si I-He I phase spectra

Figure 6.9 shows the phase difference between the velocity signals measured in the photospheric Si I line and the chromospheric He I line. The phase difference is zero for frequencies below 4 mHz. At these frequencies the coherence is high, except in the range between 1 and 2.5 mHz, and the atmosphere oscillates as a whole, *i.e.*, the waves are stationary. From 4 mHz to 7 mHz, the phase difference increases linearly with the frequency and the coherence is (more or less) above the confidence limit. It indicates that waves at these frequencies propagate from the photospheric layer, where the Si I line forms, to the chromospheric layer, where He I forms. The phase difference spectra for higher frequencies are very noisy, and no meaningful conclusions are possible.

We fit both the phase difference and the amplification spectra simultaneously. The parameters of the fit are listed in Table 6.3. The bottom panel of Figure 6.9 shows the ratio of chromospheric to photospheric power as a function of frequency. The solid red line

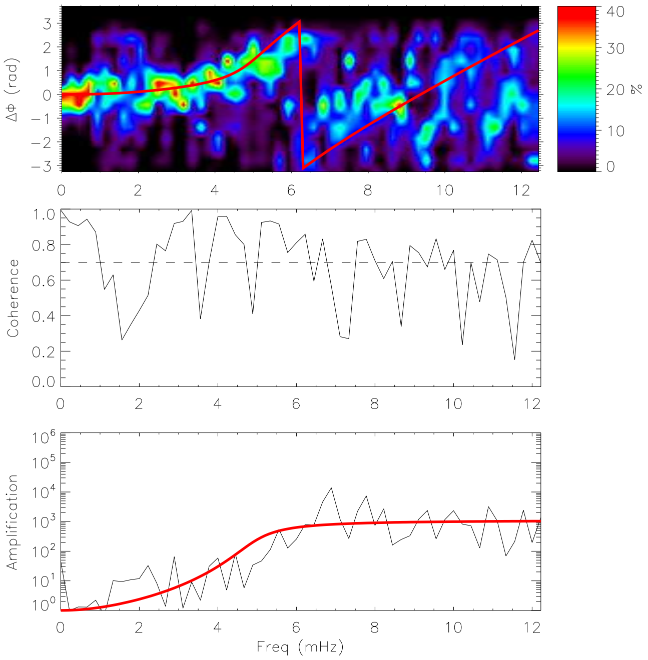

Figure 6.9: *Top*: Phase spectra between the LOS velocities of the Si I and the He I lines. The color code shows the relative occurrence of a given phase shift. The red line represents the best fit from the theoretical model. *Middle*: Coherence spectra. The horizontal dashed line at 0.7 marks the confidence limit. *Bottom*: Amplification spectra. The red line represents the best fit from the theoretical model.

in the phase diagram in Figure 6.9 represents the phase difference according to the model presented in Section 6.2.3, calculated with the parameters that best fit the observations. The theoretical amplification spectra matches rather well the observational one, with an order of magnitude agreement in the amplification factor.

Si I-Ca II H phase spectra

Figure 6.10 shows the phase, coherence and amplification spectra between the velocity measured with the Si I line and the core of Ca II H line. Frequencies below 1 mHz have a very low coherence, so these values are not reliable. Surprisingly, frequencies in the range between 1 and 2.5 mHz present an anomalous behavior, with a phase difference around 2.5 rad and a high amplification, while their coherence is remarkably high. The long period of waves with these frequencies hinders their analysis, so further observations with longer temporal series are required to study this behavior. The rest of the phase spectra is similar to the one between Si I and He I, with zero phase difference between 2.5 and 4 mHz, indicating stationary waves, and an almost linear increase of the phase difference between 4 and 7 mHz, corresponding to upwards propagating waves. In all this frequency range, the coherence is high. However, in this case the slope of the increase of the phase difference is smaller than in the previous one, and the amplification also has lower values. It means that the phase delay between the velocities at the formation height of these two lines is smaller than the delay between Si I and He I and the amplitude of the waves at the formation height

Table 6.3: Best-fit parameters of the theoretical model

Line pair	T (K)	Δz (km)	τ_R (s)
Si-He	4500	900	45
Si-Ca	4000	650	45
Fe 3969.3-He	4000	450	45
Fe 3969.3-Si	4000	-280	30
Fe 3969.3-Si (quiet sun)	4500	-200	30
Fe 3965.4-Fe 3969.3	3500	30	45
Fe 3966.0-Fe 3969.3	3500	20	45
Fe 3965.4-Fe 3966.0	3500	10	45
Ca-He	6000	100	15

of He I is larger than that of waves at the layer where Ca II H forms. Both the phase and amplification spectra locate the formation height of the Ca II H core below the He I line.

The parameters retrieved from the fit of the phase and amplification spectra to the theoretical model are listed in Table 6.3. Comparing the ones retrieved for the line pair Si I-He I with the pair Si I-Ca II H, the Ca II H core formation height in the umbra is around 250 km below the He I line. The temperature obtained for the phase difference between Si I and Ca II H is smaller by 500 K; waves traveling from the formation height of Ca II H core to that of He I pass presumably through a region where the temperature is increasing.

Fe I-Fe I phase spectra

To study the properties of oscillations at photospheric heights, phase diagrams between pairs of the photospheric lines were calculated. We can assume that the Fe I lines in the Ca II H wing form at three different heights according to their line depth (Figure 3) and to the width of the velocity histograms (Figure 6.6). We take the lines Fe I λ 3965.4, Fe I λ 3966.0 and Fe I λ 3969.3 as representative of these heights, since Fe I λ 3966.6 and Fe I λ 3967.4 seem to form at a similar height as Fe I λ 3966.0. As an example, Figure 6.11 shows the phase spectra, coherence and amplification spectra obtained between between Fe I λ 3966.0 and Fe I λ 3969.3. The phase spectrum shows that the phase difference is almost zero for all the frequencies that can be trusted according to the coherence spectra (from 0 to 10 mHz). We conclude that we can not retrieve the phase shift between the Fe I lines reliably, as the geometrical difference in their heights of the formation is too small. However, the amplification spectra reflects some increase of the amplitude with height. We managed to fit both the phase and the amplification spectra with the wave model described in the previous section. These fits yield, indeed, a small geometrical height difference between the Fe I lines. The temperature and the cooling time obtained from the fit are identical for all pairs of iron lines (Table 6.3).

Fe I-Si I phase spectra

The phase difference spectrum between the Fe I λ 3969.3 line and the Si I λ 10827 line is shown in the top panel of Figure 6.12. For frequencies below 2 mHz, the phase spectrum

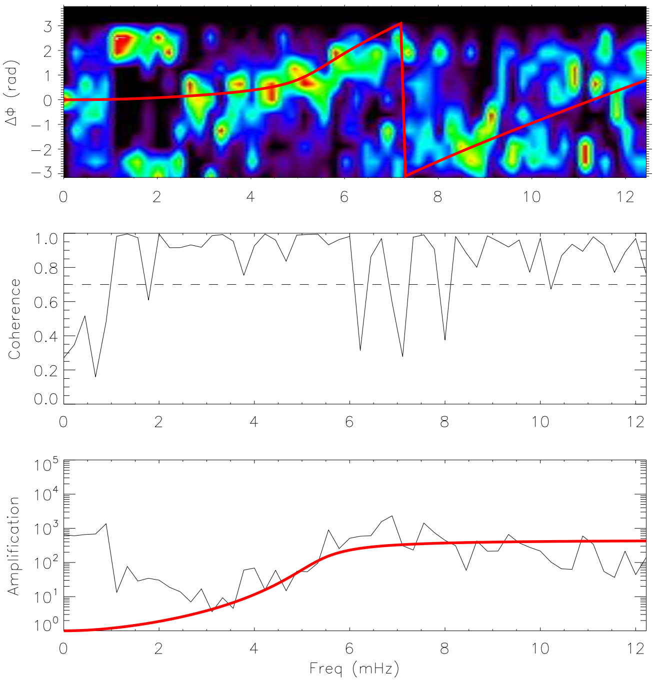

Figure 6.10: Phase, coherence and amplification spectra between Si I and Ca II H. The format of the figure is the same as Figure 6.9.

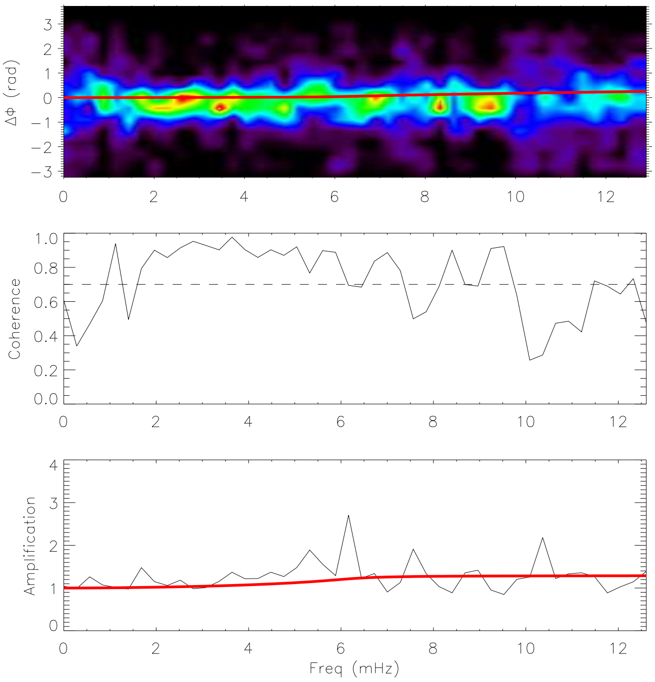

Figure 6.11: Phase, coherence and amplification spectra between Fe I λ 3966.0 and Fe I λ 3969.3. The format of the figure is the same as Figure 6.9.

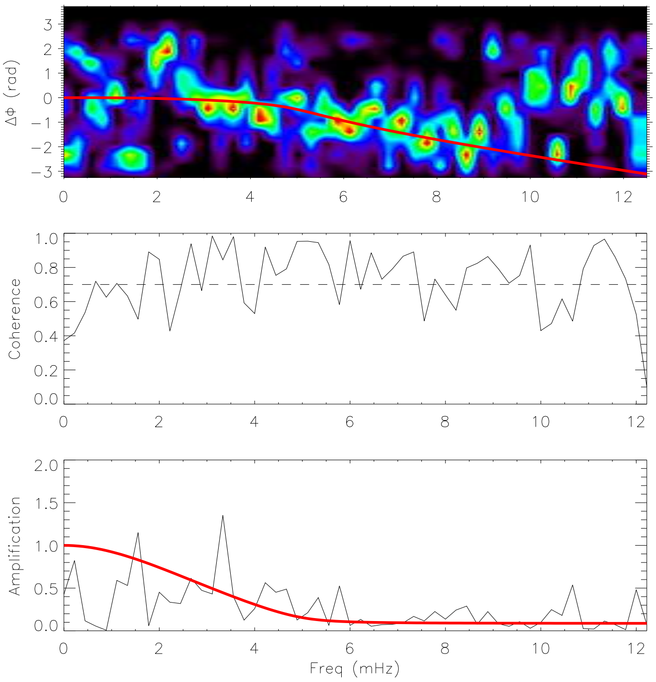

Figure 6.12: Phase, coherence and amplification spectra between Fe I 3969.3 and Si I. The format of the figure is the same as Figure 6.9.

is very noisy and has no coherence (see middle panel), indicating that waves at the heights of formation of these two lines are not related. At frequencies in the band of 2.5 – 4 mHz, some oscillatory power is present, the coherence is high and the phase difference is close to zero, so these waves are evanescent. The phase difference spectrum for high frequencies in the range from 4 to 9 mHz shows a decreasing tendency, indicating that the waves reach the formation height of the Si I line before the Fe I line. This phase spectrum was also fitted with the wave propagation model. The solid red line in top and bottom panels of Figure 6.12 shows the result of this fit. The amplification spectrum is not reliable at frequencies below 3 mHz due to the low coherence, but above this value the agreement of the theoretical and observational spectra is good, indicating that the amplitude of the oscillations measured in Si I is about twice lower than the amplitude measured in the Fe I 3969.3 line.

As a summary of the propagation at photospheric heights, we conclude that all observed photospheric spectral lines (five Fe I lines and the Si I line) fluctuate with a dominant period of 5 minutes. While all the Fe I lines have similar velocity amplitudes, with a maximum peak-to-peak amplitude of around 800 m s^{-1}, the velocity amplitude measured in Si I is clearly smaller (maximum peak-to-peak amplitude around 400 m s^{-1}). According to the phase diagram between the Fe I lines (Figure 6.11) and the amplification and phase diagram between a Fe I line and Si I (Figure 6.12), we conclude that waves with frequencies above 4 mHz propagate upwards at photospheric heights. They first reach the height where Si I is formed. As they propagate upward, their amplitudes increase due to the density fall-off. Then the waves reach the formation height of all the Fe I spectral lines, that all come from a thin layer and for this reason all show similar amplitudes.

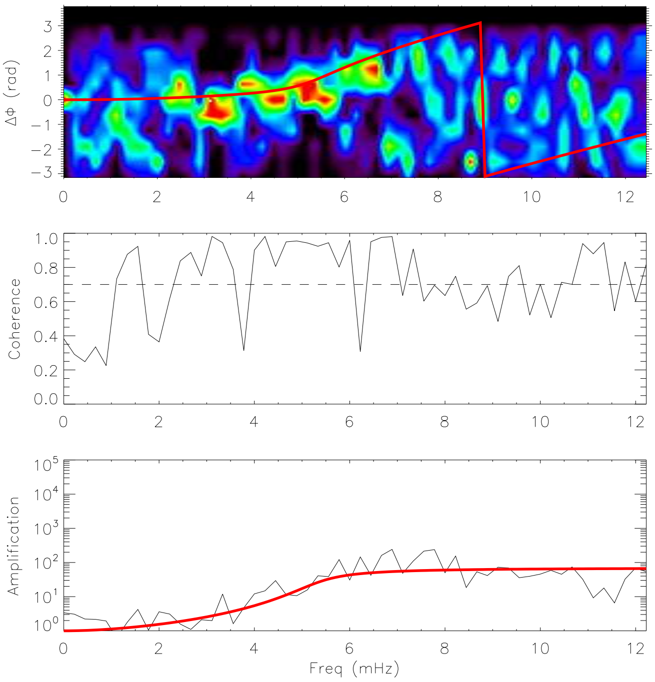

Figure 6.13: Phase, coherence and amplification spectra between Fe I λ 3969.3 and He I. The format of the figure is the same as Figure 6.9.

Fe I-He I phase spectra

According to the results extracted from the velocity statistics and the phase spectra presented before, the Fe I lines form at some height between the formation height of the Si I line and the chromospheric He I line and the Ca II H core. This means that they give information about a high photospheric layer, located at an intermediate height in the propagation of the waves from the photosphere to the chromosphere. Figure 6.13 shows the analysis of the phase differences and amplification between the velocity signal measured at the formation height of the Fe I λ 3969.3 line and the He I line. The phase spectrum is similar to the other two between photospheric and chromospheric lines (Si I-He I and Si I-Ca II H). For frequencies between 2 and 4 mHz, the phase difference is about zero, and it increases with the frequency between 4 and 7 mHz, but the slope is smaller than for Si I-He I. In the range between 2 and 7 mHz, the coherence is significant. The amplification spectrum also shows a lower amplification, compared to the Si I-He I case. The temperature, height difference and radiative damping time retrieved from the fit are listed in Table 6.3.

Ca II H -He I phase spectra

At chromospheric heights, we have the Doppler velocities obtained from the cores of the Ca II H line and the He I λ 10830 line. The top panel of Figure 6.14 shows the phase difference diagram between them. At frequencies between 1-2 mHz, the coherence (middle panel of Figure 6.14) is low and the phase spectrum is noisy. The coherence spectrum shows that the phase spectrum is reliable between 2 and 12 mHz. In the frequency band between

2 and 4 mHz, the phase difference is about 0, indicating that there is no propagation and the waves are evanescent. From ν=4 mHz to ν=11 mHz, the phase difference increases, starting from $\Delta\phi = 0$ and showing a small positive slope. It means that as waves propagate upwards, they reach the Ca II H core formation height just before the He I one. The same conclusion was obtained previously from comparing the temporal variations of the Ca II H core and He I velocities presented in Figure 6.7(a–b), where the oscillatory signal of He I is delayed by 20 s with respect to the Ca II H one.

The differences in the amplitudes between Ca II H core and He I velocities are in line with their phase spectra (top panel in Figure 6.14), since the amplitude of the He I velocity is bigger than the Ca II H. A more detailed inspection of the amplification spectra between both chromospheric lines (bottom panel of Figure 6.14) reveals that the oscillatory signal is amplified between 2 and 4 mHz, but there is no amplification for frequencies in the range from 4.5 to 10 mHz (the ratio between the amplitudes is around unity). Waves in the 2–4 mHz frequency range are evanescent, and the increase of their amplitude from the photosphere to the chromosphere is not so high, keeping them in a linear regime. At the high layers, their amplitude still increases due to the drop of the density with height. On the other hand, waves with frequencies between 4 and 10 mHz propagate upwards to the chromosphere and develop into shocks (top panels of Figure 6.7). In this non-linear regime, their amplitudes do not increase with height, explaining the observational amplification spectrum around unity for frequencies in the range 4-10 mHz. The model of linear wave propagation in an isothermal stratified atmosphere predicts a higher amplification. In the case of waves with frequencies above 10 mHz, they do propagate upwards, but their amplitude at the photosphere is so low that they do not reach a non-linear regime and their amplitude still increases with height at chromospheric layers. All in all, the model is not suitable for the description of waves at heights of Ca II H core and He I formation where the non-linearities start to become important.

It is expected that the propagation of non-linear waves happens at a higher speed compared to the linear case. This would decrease the phase difference between two layers. Therefore, we can expect that the height difference between the formation layers of Ca II H and He I lines presented in Table 6.3 is underestimated by our linear model; the value of about 100 km is the lower limit of this difference. One of the issues that arises from this fact is the evaluation of the height range where the linear model of wave propagation is valid. It is clear that it fails between the formation height of the Ca II H core and the He I line due to the non-linearities. However, in previous sections we have applied successfully this model to the propagation between the photospheric Si I line and the chromospheric Ca II H core and He I line, and between one of the Fe I lines and the He I line. It means that in most of their way from the photosphere to the chromosphere, the linear regime is a good approximation for these waves. At some layer between the formation height of the Fe I 3969.3 and the He I lines the wave propagation departs from the linear regime (cf. Carlsson & Stein 1997).

Fe I-Si I phase spectra in quiet Sun

We calculated the phase difference spectra for a region of quiet Sun around the sunspot as well. In this region, the Stokes parameters QUV are below the level of noise, so we suppose

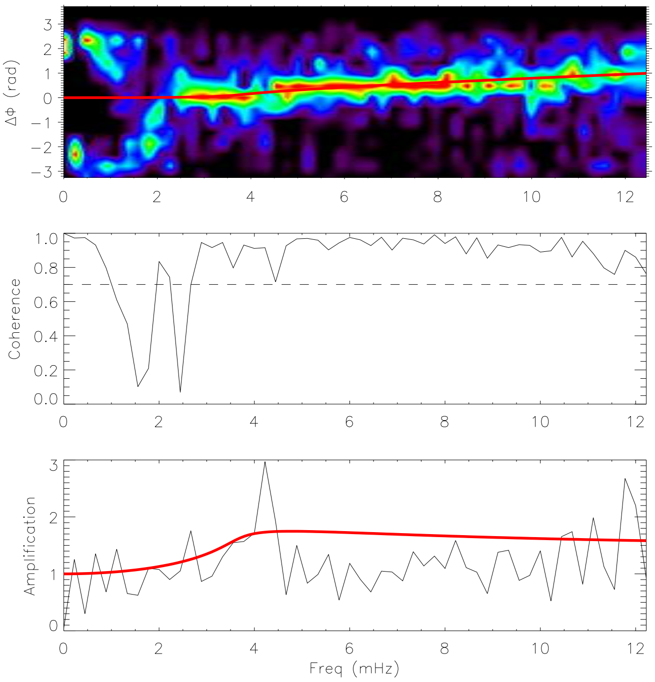

Figure 6.14: Phase, coherence and amplification spectra between Ca II H and He I. The format of the figure is the same as Figure 6.9.

there is no significant magnetic field. Figure 6.15 (top) shows the phase spectrum between the photospheric Fe I λ 3969.3 and Si I λ 10827 lines in the quiet Sun. The coherence spectrum shows high values for frequencies below 9 mHz. For frequencies below 2 mHz, the phase diagram is very noisy due to the low oscillatory power of the two velocity signals, and we do not find any clear relation between them. In the spectral range from 2 mHz to 4 mHz, the phase difference takes a constant value around zero, while for frequencies above 4 mHz, $\Delta\phi$ decreases with increasing frequency. However, the low power at the photosphere at frequencies between 6 and 8 mHz (Figure 6.8) results in a noisy phase spectrum in this band.

Comparing the phase difference diagrams between the same two lines inside the umbra of the sunspot (top panel in Figure 6.12) and in the quiet Sun, we find that in quiet Sun the negative slope of the phase difference is less steep. We also fitted the quiet Sun phase difference and amplification spectra with our wave propagation model. Inside the umbra of the sunspot, the magnetic field imposes wave propagation along field lines, and thus the hypothesis of vertical propagation is justified. However, in the quiet Sun waves can propagate in different directions and this approximation may not be true. Still, we were able to find a fit matching reasonably the phase spectrum. We retrieve a formation height difference of 200 km, lower than in the umbra, and a higher temperature of 4500 K. For a comparison between the parameters in the quiet Sun and the umbra see Table 6.3.

The bottom panel of Figure 6.15 shows the amplification spectrum for this case. For frequencies in the band of 2-7 mHz, the theoretical amplification matches the observational one.

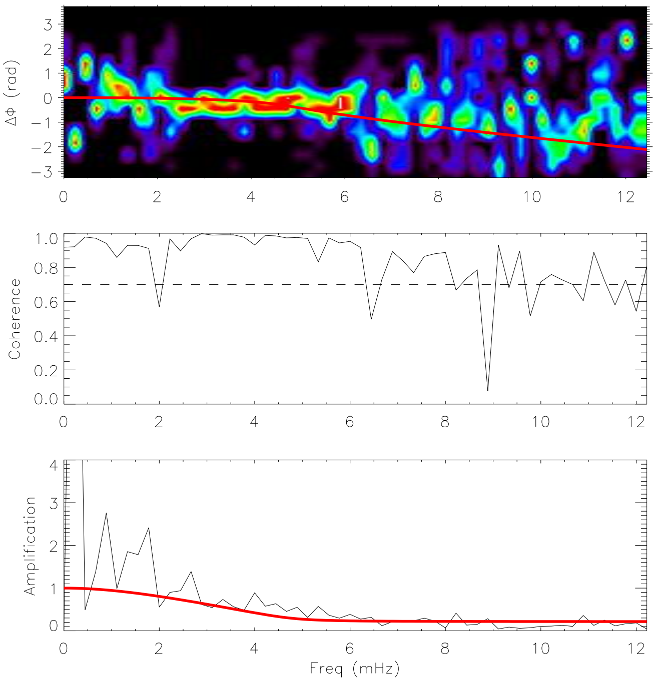

Figure 6.15: Phase, coherence and amplification spectra between Fe I λ 3969.3 and Si I in a quiet Sun region. The format of the figure is the same as Figure 6.9.

6.2.4 Comparison of the parameters of the fit with a model of sunspot

From the fit to the phase and amplitude spectra of all the pairs of lines we obtain the temperature, the difference between the formation heights of two lines, and the cooling time that best match the observational data. Obviously, our model is simplified and has several important limitations. It only describes linear wave propagation in an isothermal stratified atmosphere, not taking into account a realistic temperature stratification of the sunspot atmosphere. In a real sunspot, the temperature varies with height, so the temperature that we obtain from the fit represents a mean value between two heights of formation. In the case of spectral lines formed at a similar height (*i.e.*, the Fe I lines), the temperature that we find should be close to the real temperature in the layer. However, when the formation height difference (Δz) obtained from the fit is larger (*i.e.*, Si I-He I), we can not assign the temperature to a certain height. The presence of shocks in the temporal evolution of the He I and Ca II H velocities (Figure 6.7), together with the difficulties of the model to fit the amplification spectra between Ca II H and He I (Figure 6.14), show that the propagation at these heights is non-linear. Thus our determination of the height difference between these two layers must be somewhat affected by the deviations from the linear regime.

Despite these limitations, we plotted the deduced temperature values over the temperature stratification of the sunspot model M of Maltby et al. (1986) (Figure 6.16). The symbols in this figure mark the values retrieved from the fit to our observations. From the fit, we obtain the relative difference between the formation heights of spectral lines, not the absolute values. As reference point, we set the height of the Si I line to z=308 km, as given

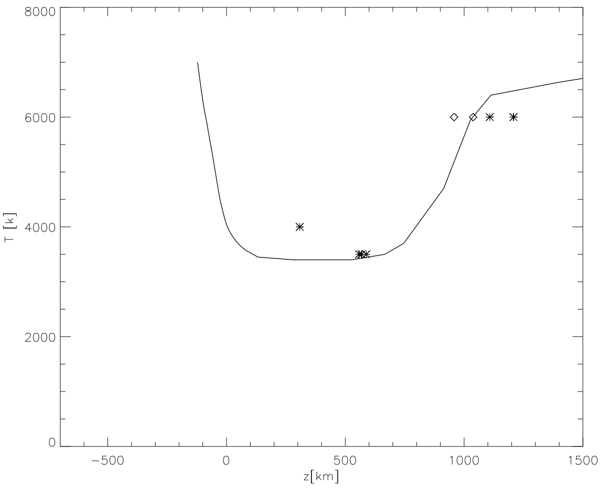

Figure 6.16: Temperature stratification in the sunspot model M of Maltby et al. (1986). Asterisks represent our best-fit values to the phase difference and amplification spectra of the line pairs. Diamonds mark an alternative estimate of the formation height of the Ca II H core and the He I line.

by Bard & Carlsson (2008) for the sunspot atmosphere model of Maltby et al. (1986). The formation heights of the other lines then follow from their relative distance to the Si I line (Table 6.3). Table 6.4 lists the resulting height values and the corresponding temperature.

In the case of the Fe I lines, we obtained from the low phase difference (top panel of Figure 6.11) that the distances between them are very small, but the amplification spectra (bottom panel of Figure 6.11) or the histograms of velocities (Figure 6.6) show a certain increase of the amplitude with height. This amplification in spite of the small geometrical distance indicates a low pressure scale height H_0 and consequently a low temperature T. The height of the Fe I line close to the temperature minimum agrees with the results from the fit of the model to the phase and amplification spectra.

In the case of the chromospheric signals (Ca II H core and He I line), we assign to both formation heights the temperature retrieved from the fit of the phase spectra between Ca II H and He I velocities. According to the geometrical differences of Table 6.3, there is an uncertainty in the formation height of these two lines. On the one hand, we have set them from their Δz with respect to the Si I line, locating the formation height of the Ca II H core at 958 km and the formation height of the He I line at 1208 km. On the other hand, we have obtained an alternative height for the Ca II H core by considering its Δz to the He I line, and subtracting it from the previous estimate of the He I formation height. In the same way, we have located the formation height of the He I line taking into account the geometrical differences between the pairs Si I-Fe I λ 3969.3 and Fe I λ 3969.3-He I. Thus, we retrieved a range of heights for both chromospheric lines, as it is shown in Table 6.4. The height ranges we find are comparable to previous works (e.g., Lites et al. 1993; Carlsson & Stein 1997; Centeno et al. 2009; Beck et al. 2009), even if some of these articles deal with the quiet Sun solely.

Table 6.4: Formation heights and temperature for the spectral lines

Spectral line	z [km]	T[k]
Si I	308	4000
Fe I 3965.4	558	3500
Fe I 3966.0	568	3500
Fe I 3969.3	588	3500
Ca II H	958-1108	6000
He I	1038-1208	6000

6.3 Discussion and conclusions

In this chapter, we have presented an analysis of the LOS velocities obtained from at set of spectropolarimetric data in the near-IR spectral region around 10830 Å and the optical region around 3969 Å in a sunspot atmosphere and its vicinity. From these two spectral ranges, we retrieve on the one hand the Doppler velocities of the photospheric Si I λ 10827 and the chromospheric He I λ 10830 line. On the other hand, we also sample several layers between these two heights, using the Doppler shifts of the chromospheric Ca II H line core and the photospheric Fe I lines from the wings of the Ca II H line.

The histograms of LOS velocities show that the width of the velocity distribution increases with height, both in the sunspot and the quiet Sun atmosphere. Quiet Sun rms velocities are larger than those in the sunspot due to the higher power of oscillations in the quiet Sun. The growth of the amplitude of the oscillations with height is scaled by the pressure scale height H_0. It is smaller in the umbra than in the quiet Sun atmosphere, so the amplitude of umbral oscillations rises faster. This yields the fact that the ratio of the quiet Sun and umbral rms velocities of the same lines decreases with the formation height of the lines.

The phase difference spectra of LOS velocities between several pairs of lines show upward propagating waves for frequencies higher than 4 mHz. The power at lower frequencies does not propagate up, since waves with these frequencies are evanescent. The slope of the phase spectra, together with the histograms of LOS velocity, allows us to sort all the spectral lines used in this work by their formation height.

Phase and amplification spectra were fitted to a model of linear wave propagation in a stratified atmosphere with radiative losses following the Newton cooling law. The model works reasonably well in layers below the formation height of the Ca II H line core, where waves propagate in a linear regime, while it fails in the fit of the amplification spectrum between the He I velocity and the Ca II H line core velocity, due to the importance of nonlinearities at these chromospheric heights.

From the fit to the model, we retrieved the temperature, the difference in geometrical height between the formation heights of both spectral lines, and the radiative relaxation time. Setting the height of the lowermost forming line (Si I) to agree with Bard & Carlsson (2008), the formation height of all the lines in sunspots was inferred. The Fe I lines from the wings of the Ca II H line are formed about 250 km above the photospheric Si I line. The relative position of the lines is well determined by the observations, since the rms velocities (Figure 6.6), the power spectra (Figure 6.8), and the phase and amplification spectra (Figure 6.12) all indicate that the Fe I lines are formed in the upper photosphere above the Si I line. The temperatures obtained for the spectral lines then show a good agreement with the temperature stratification of the Maltby et al. (1986) sunspot model M, and the formation heights are coherent with previous estimates. It must, however, be taken into account that the estimate of the formation height from response functions in Bard & Carlsson (2008) was performed for a static atmosphere and has a strong dependence on the model atmosphere employed.

Most of the power of the photospheric lines is concentrated in a prominent peak at 3.5 mHz, in the 5 minute band. From a comparison between the power spectra of the Si I and one of the Fe I lines, it is interesting to note that the power peak is exactly at the same position, although the iron line forms at around 200 km above the silicon one. The same behavior was found for the chromospheric He I line and the Ca II H line core, which peak at around 6 mHz, corresponding to the 3 minute band. The maximum of the power spectra is not shifted gradually from 3.5 mHz at the photosphere to higher frequencies at larger heights, but the photospheric and chromospheric group of lines show a discontinuous behavior. The analysis of the simulations presented in the previous chapter also shows that the transition between 3 and 5 mHz waves is clearly discountinuous and occurs in a few kilometers (Figure 5.23). This observational result shows a perfect agreement with the simulations presented in Chapter 5. Waves at frequencies above the cut-off increase their amplitude with height faster than evanescent waves below the cut-off, resulting in larger power of 3-minute waves at chromospheric heights. Yet, as follows from Figure 6.8b, the LOS velocity power at frequencies above 4 mHz measured from of the Fe I line is higher than the one from the Si I line; it means that already in the upper photosphere the high-frequency power becomes important. This finding suggests that high-frequency waves prominent in the chromosphere have to be generated in the photosphere or below and their dominance at the chromospheric height is the result of their large amplitude increase. These results are consistent with those obtained from observations by Socas-Navarro et al. (2001) and Centeno et al. (2006), and from numerical simulations in Chapter 5 of this thesis.

From the compatibility between our observations and a simple wave model, we conclude that we observe a continuous field-aligned propagation of slow magneto-acoustic waves in the upper atmosphere of the sunspot. These waves first reach the formation height of Si I, then the formation height of the Fe I lines from the Ca II H line wing located in the upper photosphere, then the formation height of the Ca II H line core and finally that of the He I line. The propagation becomes non-linear at heights between the formation of Fe I lines and Ca II H line core.

7

Combination of observations and simulations

Simulating wave propagation in realistic sunspot atmospheres with the properties of observed oscillations is a challenge. There are several issues which hinder their calculation. In a typical sunspot, the Alfvén speed at the chromosfere is about 1000 km s^{-1}, limiting the time step and making the calculations very expensive. This high characteristic velocity, together with the strong shocks and nonlinearities, also makes difficult the stability of the top boundary but, thanks to the PML, our code is able to manage these hard conditions without reflections and develop long enough simulations. Many wave periods are needed for a correct analysis of the wave propagation. It makes the time length of the simulation critical due to the long 3 and 5 minute periods observed in sunspot atmospheres. Our code has proven its capability to study long period waves in the atmospheric layers where they are observed. In this chapter we present the results from simulations which reproduce the wave pattern analysed in Chapter 6. We have constructed a MHS sunspot model based on the observational data presented in Chapter 6 and have introduced an observed velocity in the photosphere as a driver. The aim of this Chapter is to perform a direct comparison between simulations and observations of all available lines.

In Section 7.1 we show the methods developed to construct a MHS model representative of that sunspot and discuss its properties. Section 7.2 presents several alternatives which have been tested to introduce the photospheric observed velocity as a driver. Section 7.3 summarizes the set up of the simulations performed, while Section 7.4 includes the first tests that we have developed to reproduce the observations. Finally, in Section 7.5 we analyze the simulation that best matches the observations and in Section 7.6 we discuss the results.

7.1 MHS model of the sunspot

The MHS model is constructed following the method of Khomenko & Collados (2008). They developed a technique to calculate a thick sunspot structure in magnetostatic equilibrium with distributed currents, *i.e.*, showing a continous variations of field strength and gas pressure across the spot, from sub-photospheric to chromospheric layers. In current-distributed models, the field falls off from its value at the magnetized atmosphere at the axis of the sunspot to almost zero at the nonmagnetic atmosphere located at large radial distances. These models are constructed by combining the advantages of two different methods: in the first, the magnetic topology is set and the thermodynamic variables are forced to match with this structure (Schlüter & Temesváry 1958; Low 1975, 1980), constructing the so-called "self-similar" models; in the second type of models, the pressure distribution is prescribed as boundary condition at the axis of the sunspot and in the distant quiet Sun atmosphere and at the rest of the model the pressure and magnetic field are iteratively changed until the system reaches an equilibrium state (Pizzo 1986).

Khomenko & Collados (2008) identified several advantages in a method that uses both approaches. In photospheric layers they take the Pizzo (1986) solution, since the pressure distributions at the magnetized atmosphere and at the quiet Sun atmosphere which are needed for the boundaries can be retrieved from observations. In the case of deeper levels, the method of Pizzo (1986) is very sensitive to the pressure distribution at the sunspot axis, but there are almost no suitable models for deep subphotospheric layers. For this reason, the procedure proposed by Low (1980) works better at these heights where the gas pressure dominates over the magnetic pressure, although it has problems at the photosphere, where the method often leads to negative pressures, and it does not produce models at high layers with the high magnetic field strength representative of sunspots. The method proposed by Khomenko & Collados (2008) joins smoothly the subphotospheric deep layers obtained from the Low approach with the photospheric model retrieved from the Pizzo solution, avoiding the problems related with both methods and taking the advantages of both approaches.

7.1.1 Method

In the case of a magnetohydrostatic (MHS) atmosphere, velocities are zero and the temporal derivatives are also zero, so the full set of MHD equations (Equations 2.22 - 2.25) is reduced to an equilibrium force balance equation

$$-\nabla P_0 + \rho_0 g + \frac{1}{\mu_0}(\nabla \times \mathbf{B}_0) \times \mathbf{B}_0 = 0. \tag{7.1}$$

This equation represents the different forces that play a role in the atmosphere. From left to right, it includes the pressure gradient, the force per unit volume produced by the gravitatory field, and the magnetic pressure and magnetic stress. The system of equations required to solve the MHS atmosphere is completed by means of the Maxwell equation (Equation 2.26), that is, with divergence-free condition for the magnetic field:

$$\nabla \mathbf{B}_0 = 0. \tag{7.2}$$

The equations are solved in cylindrical coordinates (r, ϕ, z) and with axial symmetry, so none of the variables have dependence on ϕ. This allows us to write the magnetic field in terms of the field line constant u:

$$\mathbf{B} = \Big(-\frac{1}{r}\frac{\partial u}{\partial z}, \frac{G(u)}{r}, \frac{1}{r}\frac{\partial u}{\partial r} \Big), \tag{7.3}$$

where the component G(u) represents the twist of the field. As in this model the field is untwisted, the azimuthal component B_ϕ is zero and it is equivalent to set $G(u) = 0$.

Following Low (1980), the field-line constant u can be expressed as a function of a variable φ:

$$u(r,z) = u(\varphi) \tag{7.4}$$

$$\varphi = r^2 F(z) \tag{7.5}$$

$$F(z) = (z^2 + a^2)^{-1} \tag{7.6}$$

where a is a constant parameter. Introducing Equations (7.4)–(7.6) into Equation (7.3), the magnetic field vector can be expressed as a function of φ

$$\mathbf{B} = \Big(-r\frac{dF(z)}{dz}\frac{du}{d\varphi}, 0, 2F(z)\frac{du}{d\varphi}\Big). \tag{7.7}$$

The form of the derivative $du/d\varphi$ is imposed by the force balance equation and it yields the expression

$$\frac{du}{d\varphi} = B_0^L h^2 \exp(-\eta\varphi), \tag{7.8}$$

where the parameter B_0^L controls the magnetic field strength, h is a suitable length scale, and η is a constant parameter. From Equations (7.8) and (7.7) we can retrieve the horizontal and vertical components of the magnetic field vector in Low's model, which are written as

$$B_r(r,z) = 2B_0^L \frac{(z-z_d)rh^2}{[(z-z_d)^2+a^2]^2} \exp\Big[\frac{-\eta r^2}{(z-z_d)^2+a^2}\Big], \tag{7.9}$$

$$B_z(r,z) = 2B_0^L \frac{h^2}{(z-z_d)^2+a^2} \exp\Big[\frac{-\eta r^2}{(z-z_d)^2+a^2}\Big]. \tag{7.10}$$

The parameter z_d corresponds to the height where the magnetic field is vertical, and it is taken as a reference height. Equation (7.10) is similar to the one used in Pizzo (1986) as a boundary condition at the bottom boundary of the domain,

$$B_z(r,z_0) = B_0^P \exp(-r^2/r_e^2), \tag{7.11}$$

where B_0^P is the field strength at the axis of the model at $z = z_0$ and r_e is a convenient scaling for the magnetic field variations with the radius. From a comparison of these two expressions we can see that both models can be joined at an arbitrary height $z = z_0$, and the parameters of the models should be related as

$$B_0^P = B_0^L \frac{2h^2}{(z_0-z_d)^2+a^2}, \tag{7.12}$$

$$r_e^2 = [(z_0-z_d)^2+a^2]/\eta. \tag{7.13}$$

The model was constructed following the steps described in Khomenko & Collados (2008): (1) Generation of a self-similar solution in deep subphotospheric layers; (2) generation of a potencial solution in the overlying atmosphere; (3) generation of a magnetostatic solution in the high layers following the strategy described by Pizzo (1986); and (4) concatenating both solutions. The method was modified in order to create an atmosphere which resembles the sunspot from our observations. The following procedures were performed with this aim:

Obtaining the pressure distribution at the boundaries and estimation of Wilson depression

For the construction of a magnetostatic solution at the photosphere and higher layers it is necessary to introduce the pressure distributions along the axis of the sunspot and in the field-free quiet atmosphere as boundary conditions. In both cases the pressure stratification of the surrounding quiet photosphere was retrieved from the inversion of the Stokes parameters measured for the Si I λ 10827 line. Stokes profiles were averaged over all the time steps and several spatial positions from one of the temporal series. In the case of the sunspot axis atmosphere, the average includes 1 arcsec around the center of the umbra, while for the quiet Sun atmosphere a region was selected at 30 Mm from the axis of the sunspot. The inversion of the silicon line of these two averaged Stokes vectors was carried out using SIR (Ruiz Cobo & del Toro Iniesta 1992). Figure 7.1 shows the four Stokes parameters for the sunspot axis observations (black solid line) and the synthetic profiles obtained from the inversion (red dashed line). In this inversion we have performed three cycles, with a variable number of nodes in several parameters. In the temperature, we have used 2 nodes in the first cycle, 3 nodes for the second and 5 nodes for the last cycle. In the parameters defining the magnetic field, including its strength and orientation, we have chosen one node for the first cycle and 2 nodes for the rest of the cycles, while for the LOS velocity we have forced SIR to use just one node for all the cycles.

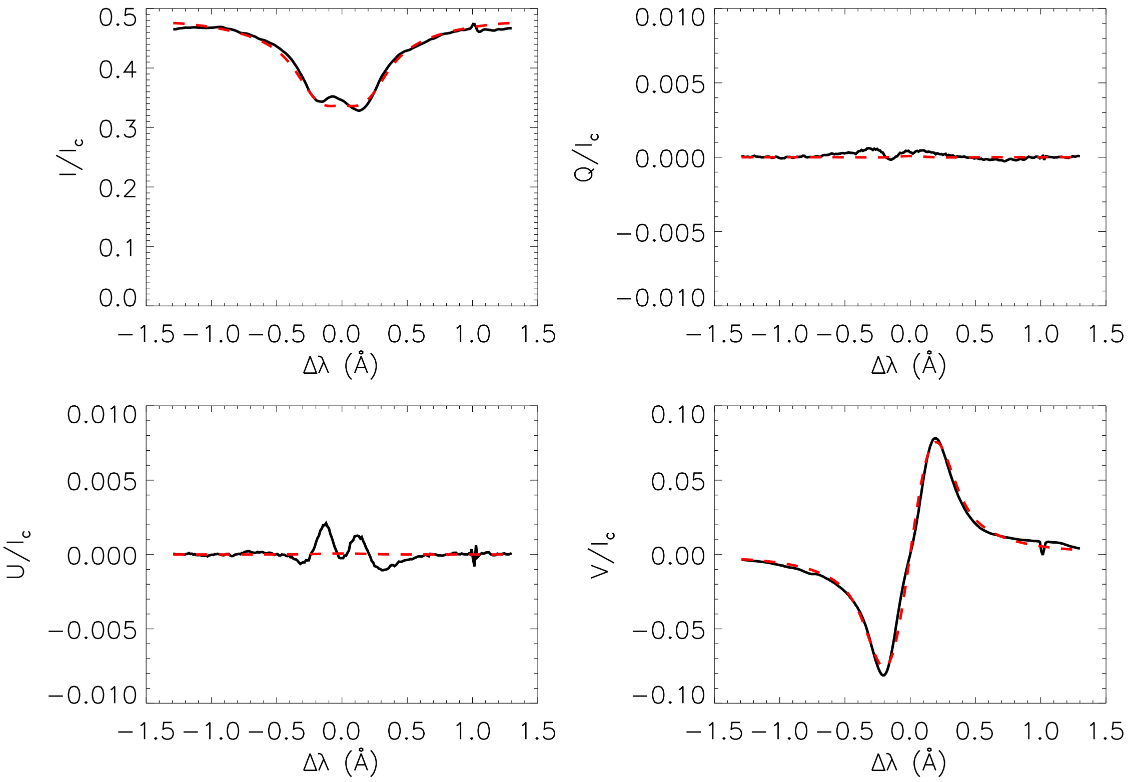

Figure 7.1: Stokes parameters IQUV for the Si I 10827 Å line for the averaged atmosphere at the axis of the sunspot. Black solid line: observed profiles; red dashed line: synthetic profiles retrieved from the inversion.

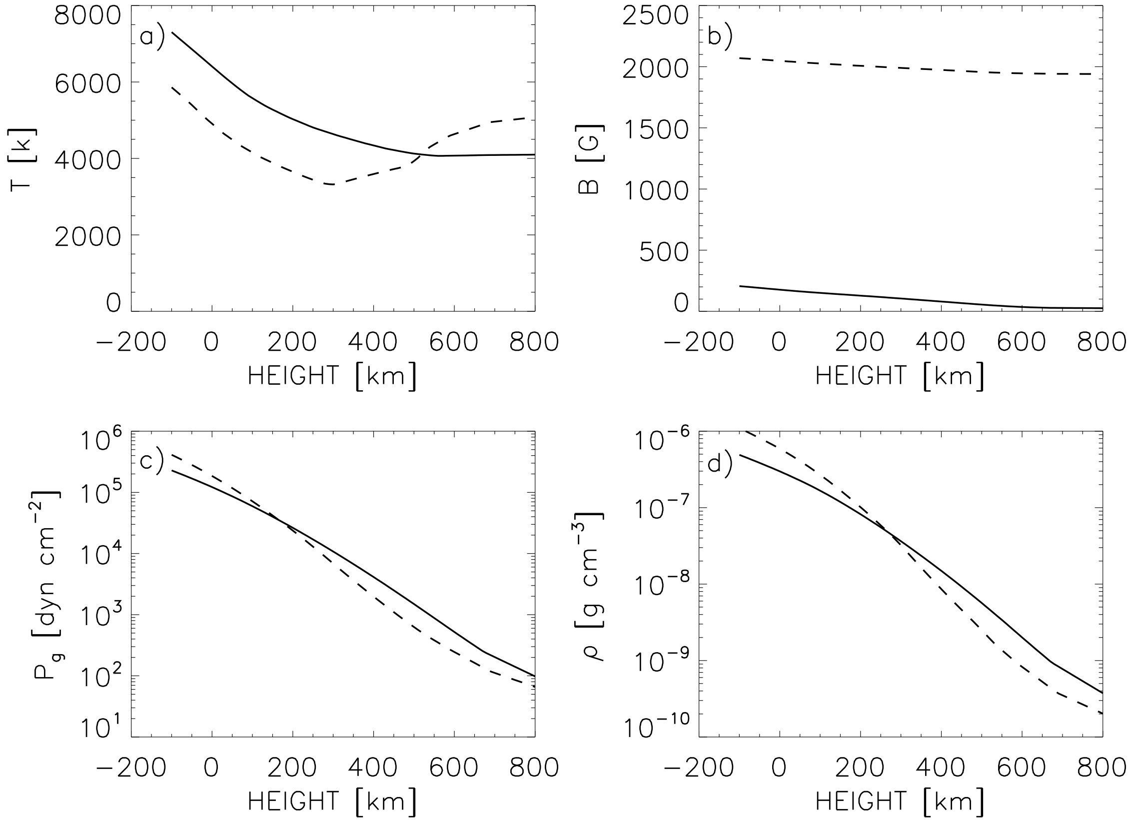

Figure 7.2: Stratification of the temperature (a), magnetic field (b), gas pressure (c), and density (d) in the atmosphere of the quiet Sun (solid line) and sunspot (dashed line) retrieved from the inversion. The height $z = 0$ km is set at the height where $\log\tau_{5000} = 1$ for each model, so the Wilson depression is not taken into account and they correspond to a different geometrical height. The sunspot stratification should be shifted downward 350 km.

Once the stratification of temperature, magnetic field strength and direction, gas pressure and density is retrieved from the inversion for the axis of the sunspot and the quiet Sun (Figure 7.2), it is posible to calculate approximately the Wilson depression of the observed sunspot. In a simple model of thin flux tube we can define a region inside the tube with vertical magnetic field and a region outside with no magnetic field. A condition for the lateral force balance imposes that at a fixed height z_0 the pressure inside the flux tube, including the gas pressure (P_g^{sp}) and the magnetic pressure ($P_m^{sp} = B^2/(2\mu_0)$), must be equal to the gas pressure outside (P_g^{ph}),

$$P_g^{sp} + B^2/(2\mu_0) = P_g^{ph}. \tag{7.14}$$

From the inversion we obtain the stratification of all the variables with height, but in both atmospheres the height $z = 0$ km is located at the height where the continuum optical depth at 5000 Å (τ_{5000}) is unity and they correspond to different geometrical heights due to the Wilson depression. We set the height $z = 0$ km for the quiet Sun and derive the Wilson depression Δz from Equation (7.15). Taking into account all the possible values of the Wilson depression, the magnetic field can be calculated as a function of the height z and Δz:

$$B(z,\Delta z)=\sqrt{2\mu_0\Big[P_g(z)^{ph}-P_g(z+\Delta z)^{sp}\Big]}. \tag{7.15}$$

The formation height of silicon core is around the optical depth $\log\tau_{5000}=-1.8$ and it was chosen as the height z for reference. We look for the appropiate value of Δz which according to Equation (7.15) gives a magnetic field strength equal to the one infered from the inversion at the formation height of the Si I line at the sunspot axis. The obtained Wilson depression was $\Delta z=350$ km.

From the inversion of the Si I Stokes profiles we can retrieve the stratification of magnetic field and thermodynamic variables up to a height of almost 800 km in the atmosphere of the observed sunspot and its surroundings. Since the method needs the distribution of gas pressure deeper in the atmosphere as well as at higher chromospheric layers, we have smoothly joined our estimation of the photospheric variables with other models from the literature. As field-free atmosphere we used model S of Christensen-Dalsgaard et al. (1996) at deeper layers and the VAL-C model of the solar chromosphere (Vernazza et al. 1981). For the axis of the sunspot we use the Avrett (1981) model in the upper layers, while the deep layers were extracted from a model by Kosovichev et al. (2000) obtained from helioseismic inversions of the phase speed in sunspots. The resulting sunspot atmosphere was shifted down 350 km in the vertical direction in order to account for the Wilson depression measured before.

Obtaining the parameters which chraracterize the magnetic structure

The magnetic field vector in the Low's model that we use for the deep layers is calculated from Equations (7.9) and (7.10). It depends on several parameters. The lower boundary is taken at height z_d, where $B_r(r,z_d)=0$ at all radial distances. It was set to $z_d=-10$ Mm, with the origin for the z-axis at the base of the photosphere. The parameters η, a and B_0^L can be chosen freely, and in this case we have estimated those which closely resemble the parameters of the observed sunspot. According to Equation (7.11), the vertical magnetic field at the bottom boundary of the Pizzo's model has a horizontal gaussian profile. At each spatial position from one of the series of our observations we have averaged the Stokes parameters of the Si I 10827 for all the time steps, and we have inverted the resulting Stokes vectors with SIR. Asterisks in Figure 7.3 represent the magnetic field obtained from the inversion at the formation height of the silicon line, and the red line corresponds to a gaussian fit. From this fit we can retrieve the parameters B_0^P and r_e from Equation (7.11), with z_0 being the formation height of Si I. In our sunspot we obtain $B_0^P=2040$ G and $r_e=4.65$ Mm. The selected height of the Si I line was chosen at the same optical depth for all the spatial positions. Due to the Wilson depresion, it corresponds to a different geometrical height for each spatial point. However, we have not taken into account this effect.

Equations (7.12) and (7.13) relate B_0^P and r_e with the required parameters to contruct the Low's model at deep layers. The parameter h was set with the length scale at $z=z_d$, so we have three unknown parameters (B_0^L, η and a) and only two equations. We introduce a fixed B_0^L and retrieve η and a from the system of two equations. An appropiate value of

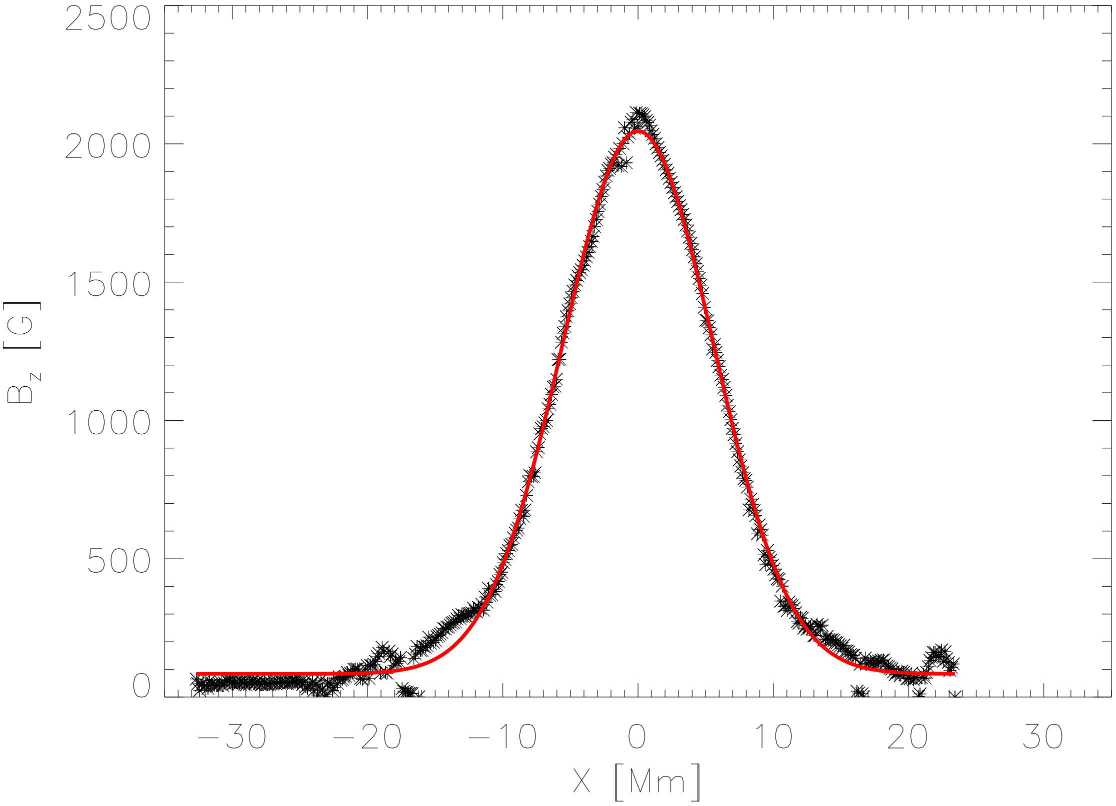

Figure 7.3: Vertical magnetic field at the formation height of the Si I 10827 Å line for all the spatial positions. The red line indicates the result of a gaussian fit.

B_0^L was selected with the criterion that after all the process to construct the sunspot the Alfvén and sound velocities at the axis of the model should match those obtained from the inversion. The top and middle panel of Figure 7.4 show the comparison between both sound and Alfvén velocities, showing a perfect match. The bottom panel of the figure includes the comparison of the pressure scale heights, which also show an exceptional agreement. The parameters η and a account for the topology of the magnetic field, while B_0^L indicates its strength. Since it is easier to verify if the resulting strength is correct (it is measured directly), we find that it is preferable to impose the value of B_0^L rather than the value of the other parameters η and a. Once we have obtained a suitable model, the parameters that better resemble the observed sunspot are $B_0^L = 32000$ G, $\eta = 4.38$ and $a = 3.74$ Mm.

7.1.2 Properties of the MHS model of the observed sunspot

Figures 7.5 and 7.6 show distributions of some variables in the complete sunspot model. Most of the magnetic field is concentrated around the axis of the model, inside a radius of 10 Mm, and it is weaker at farther distances from the center. The squared ratio of the sound velocity to the Alfvén velocity at the axis is unity just below the height $z = 0$ km, and the height of the contour $c_S^2/v_A^2 = 1$ increases with the distance to the axis. This layer

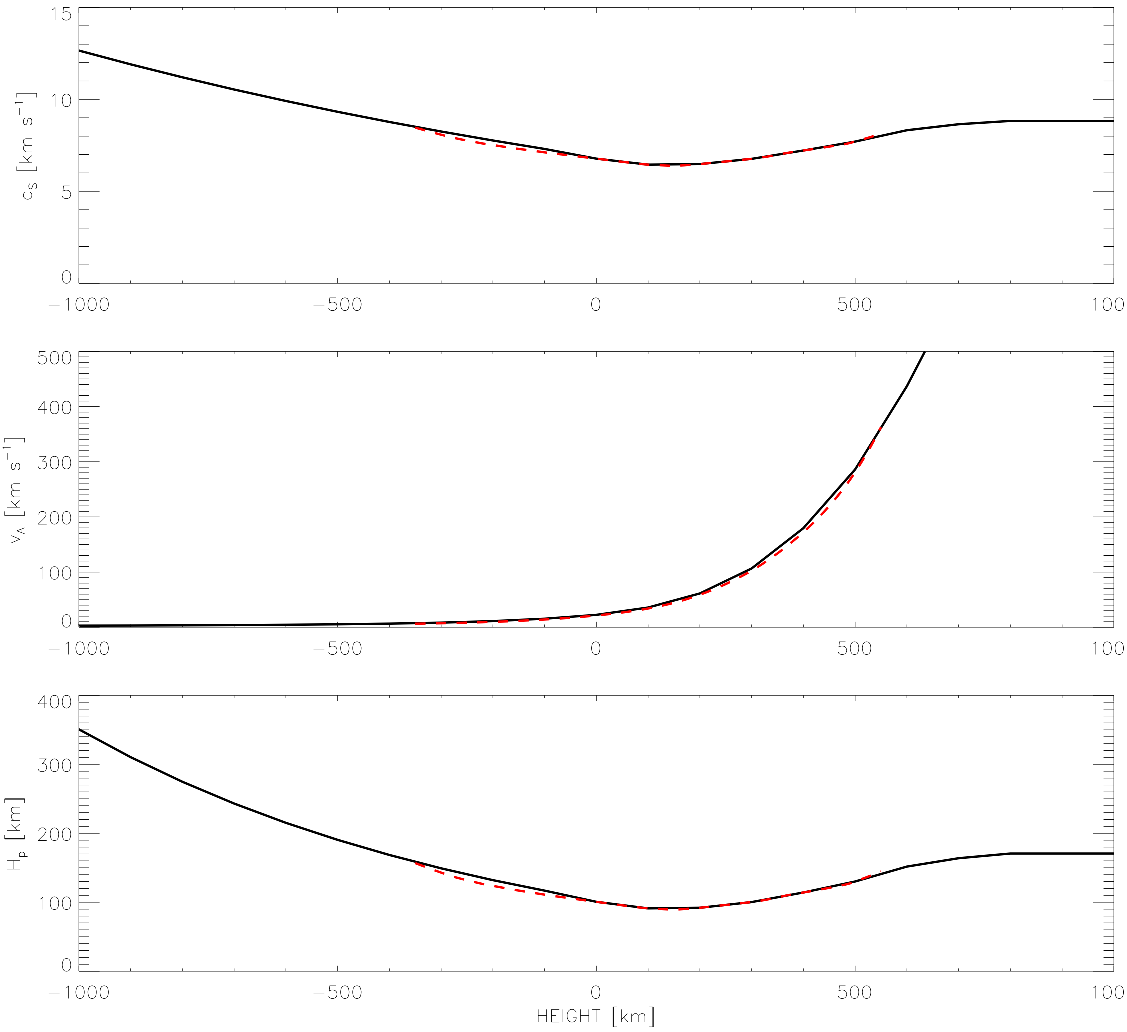

Figure 7.4: Comparison between the computed model of sunspot (black solid line) and the inversion (red dashed line) at the axis of the sunspot for a range of heights around the photosphere. From top to bottom: Sound velocity, Alfvén velocity and pressure scale height.

is very important for the analysis of the wave modes involved in the atmosphere, since the mode transformation is produced at the height where both characteristic velocities are similar. The orientation of the magnetic field lines changes very fast from being vertical at the axis to almost horizontal at radial distances larger than 15 Mm below $z = 0$ km. Above this layer the magnetic field lines spread increasing their inclination with the distance to the axis.

The properties of the model are shown in more detail in Figure 7.7, where the distribution with radius at several heights (left panels) and the stratification with height at different distances from the axis of the sunspot (right panels) are plotted. At the axis of the sunspot the magnetic field drops from 4 kG at $z = -10$ Mm to 1.1 kG at $z = 1$ Mm. It is vertical at $r = 0$ Mm and its inclination at photospheric layers increases with the radius,

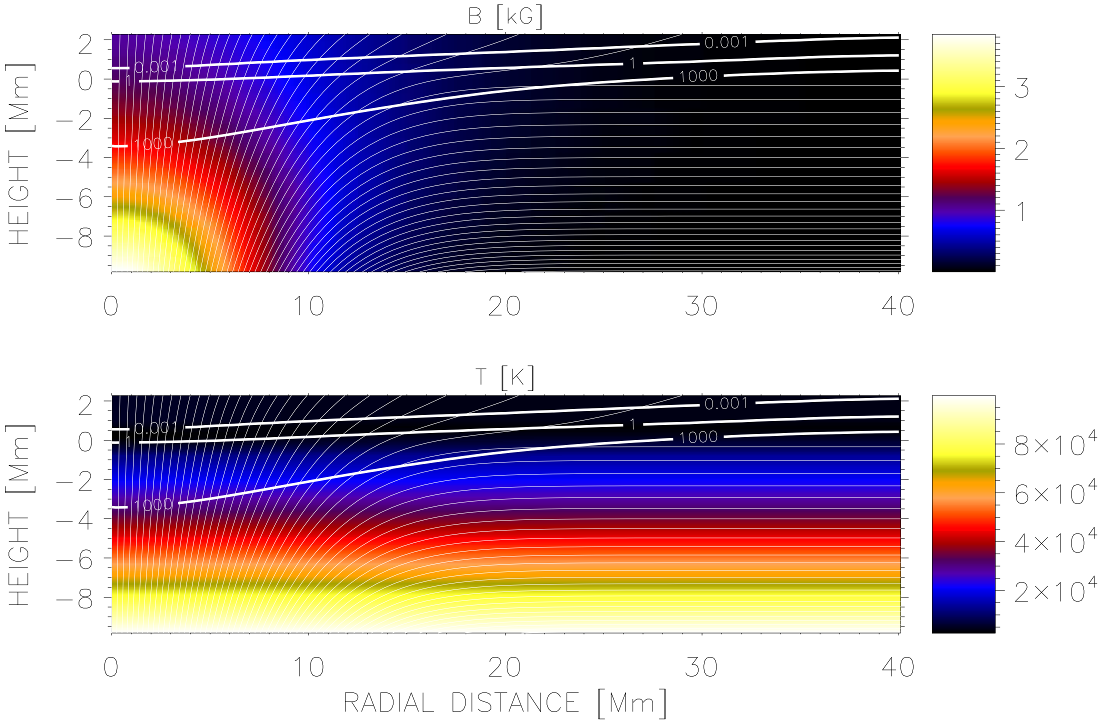

Figure 7.5: Topology of the obtained sunspot model. Top: Magnetic field strength; bottom: Temperature. White thin lines are magnetic field lines. White thick lines with labels are the contours of c_S^2/v_A^2.

being horizontal at the rightmost point of the domain. The gas pressure has a deficit at the magnetized regions around the center of the sunspot. Below $z = 0$ km this deficit decreases with depth, as can be seen from the radial distribution of gas pressure at $z = -1$ Mm, and it almost disappears at about -2 Mm depth, according to the assumption of self-similarity of the MHS solution at larger depths. The gas pressure changes by 12 orders of magnitude from its value at the bottom boundary at $z = -10$ Mm to $z = 2$ Mm. The squared ratio between the sound speed and the Alfvén speed also gives the ratio of the gas pressure to the magnetic pressure. It has very strong variations, from 10^5 at $z = -10$ Mm to 10^{-7} at $z = 2$ Mm.

Comparing the magnetic field and the thermodynamic variables of the obtained model at the axis of the sunspot with the values infered from the inversion, we find that the model has lower values in all these variables. This happens because the density and gas pressure obtained from the inversion are too high for the model of deeper layer introduced and, in order to produce a magnetostatic solution, the density and gas pressure is decreased after the iterative process. According to the drop of the gas pressure in the quiet sun atmosphere, the magnetic pressure also has to be reduced and the final magnetic field is lower than the infered from the observations. Another cause of this difference could be the limitation in the estimation of the radial variation of the magnetic field at a fixed height in Figure 7.3, since we did not account for the variation of the formation height of the Si I line produced by the Wilson depresion. However, as it is shown in Figure 7.4, the Alfvén and sound velocities that characterize the velocity of propagation of waves and the scale length in

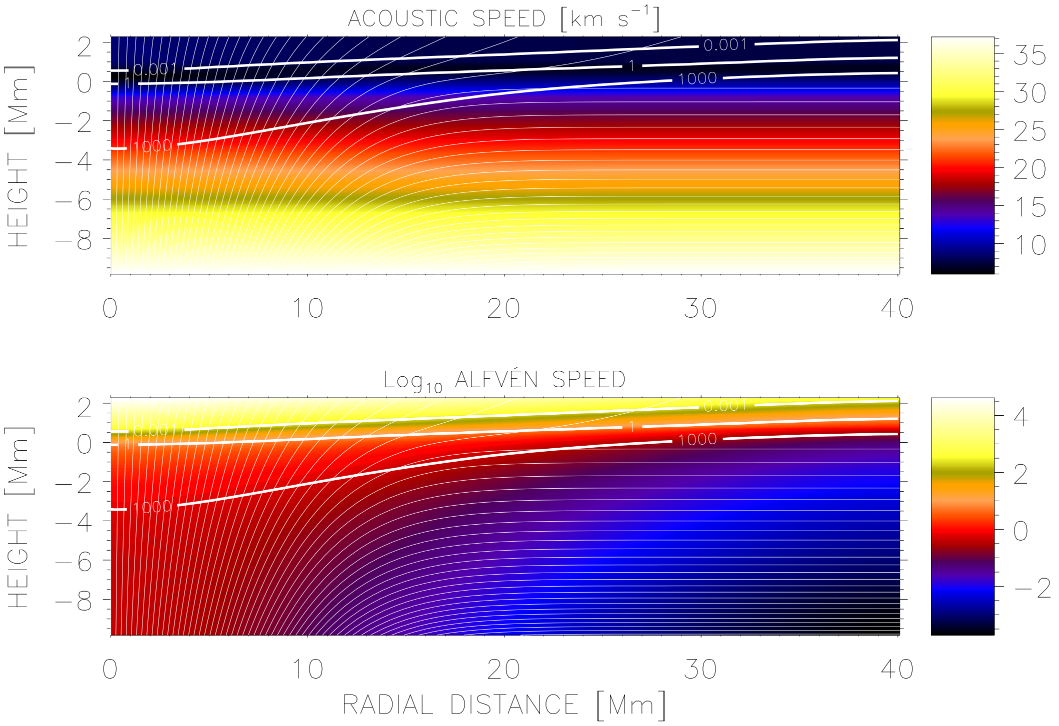

Figure 7.6: Topology of the obtained model of sunspot. Top: acoustic speed; bottom: log of the Alfvén speed. Thin white lines are magnetic filed lines. Thick white lines with labels are the contours of c_S^2/v_A^2.

which the amplification of the amplitude is produced are very similar in the model and the observations, so we expect that our model is suitable to study the propagation of waves in the atmosphere of the observed sunspot.

7.2 Introduction of the driver

With regard to the reproduction of the real wave pattern by means of numerical calculations, one of the key aspects is the introduction of some observed velocity as a driver. We have chosen the velocity measured with the Si I line as the driver of the simulation, since it is the line which is formed deeper of the set of lines that we have observed. At the formation height of Si I, the numerical simulation should have a vertical velocity as close as possible to the measured LOS velocity. The photospheric oscillations are dominated by waves in the 5 minute band and, thus, the power at this band excited in the simulation must resemble the observed one. However, it is even more critical to introduce correctly the power at higher frequencies. Frequencies above the cutoff propagate upward and dominate the higher layers. The wave pattern at the chromosphere will depend on the power introduced by the driver at those high frequencies and on their phase shift.

Several strategies may be developed to use the oscillations of the silicon line as a driver: on the one hand, it is posible to set the observed oscillations as a boundary condition in a computational domain where the bottom boundary coincides with the formation height of the Si I; on the other hand, we may calculate the force which corresponds to the velocity

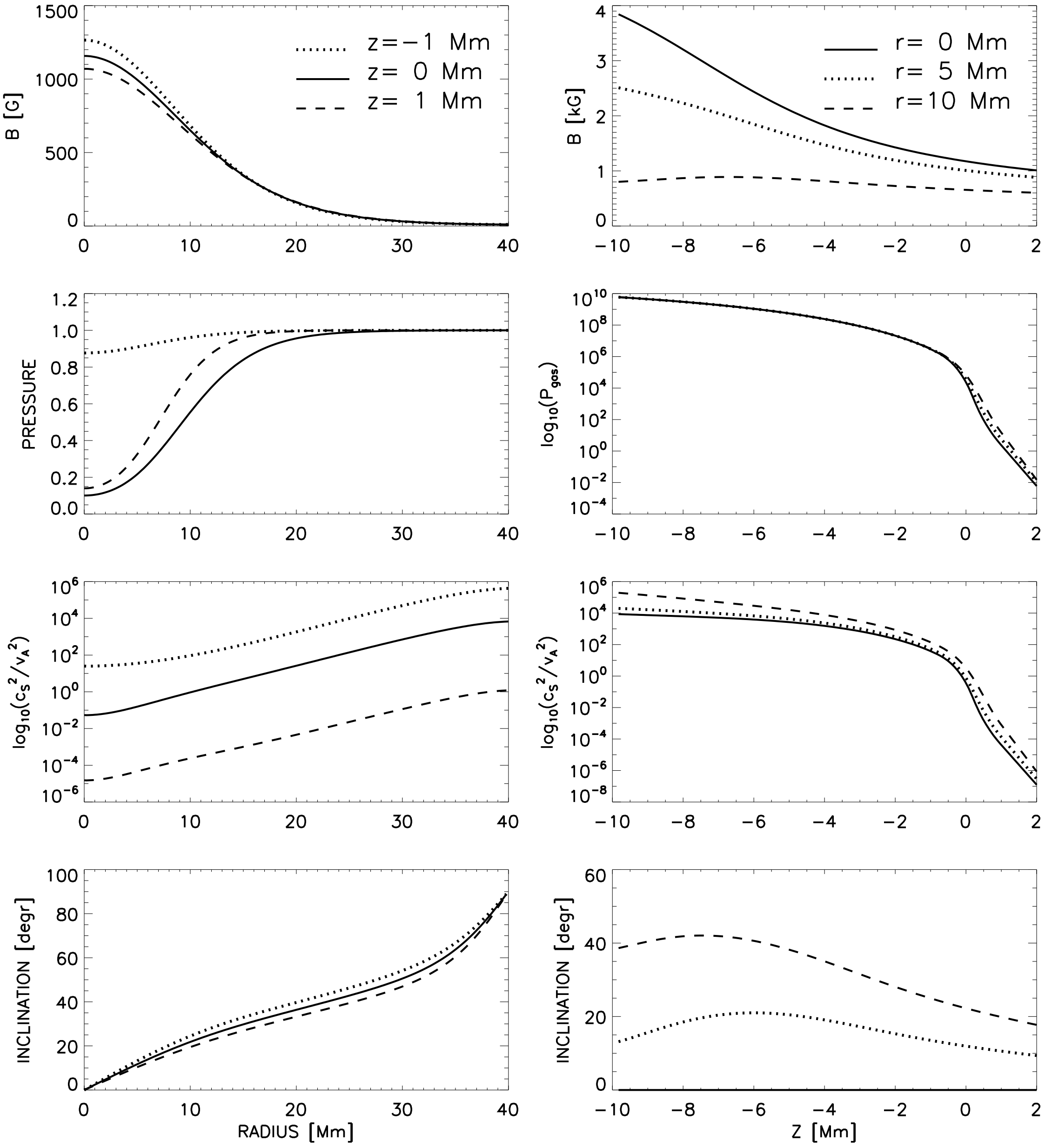

Figure 7.7: Distribution with radial distance (left panels) and with depth (right panels) of the magnetic field strength, pressure, ratio c_s^2/v_A^2, and the magnetic field inclination for the obtained sunspot model. The radial pressure distributions are normalized to their values at the right boundary.

measured and introduce it directly in the motion equation. In the case of the first approach, several problems arise. It is not valid just to set the vertical velocity, since it is necessary to impose at the bottom boundary the fluctuations of all the variables self-consistently. From the inversion of the Stokes profiles we can retrieve the variations of all these magnitudes, but it is difficult to obtain reliable values with a good spatial and time resolution related to a single layer in geometrical height, not optical depth (see Rodríguez Hidalgo et al. 2001).

Another option is to calculate the polarization relations of all the variables which agree with the vertical velocity measured from the Doppler shift, but it is a tough work in such a realistic case. For these reasons, we found more convenient to introduce the retrieved force as a source function $S_z(t)$ in the MHD equations, although the calculation of this force is not obvious.

7.2.1 Force driver

Our first attempt for deriving the force from the velocity measured with the Si I line consisted on a simple calculation of its derivative, obtaining the force $S_z(x,y,z,t)$ as

$$S_z(x,y,z,t)=\rho_0(x,y,z)\frac{\partial v_{obs}(x,t)}{\partial t}P(x,y,z), \tag{7.16}$$

where ρ_0 is the mass density of the MHS model, and v_{obs} is the observed velocity. In the case of v_{obs}, we only have its dependence with the x coordinate, that we consider along the slit, so we suppose that it is constant with y and z. The function $P(x,y,z)$ indicates the region where the driver is introduced, and its value is unity at the formation height of the Si I line ($z=z_{Si}$) and at a selected $y=y_0$ for a wide range of x. It decreases smoothly in all directions, dropping to zero at a certain distance R_{src}. In this manner, the driver only acts in a narrow layer around the formation height of the silicon line for an elongated region in the x direction. Once the initial numerical simulation was performed, we found that the power spectra of the vertical velocity at the height where the driver was introduced did not match the observed one, from which the source force was retrieved. The power at the high frequencies of the simulated velocity was too high in comparison with the original velocity. This gave us clues that the velocity generated by a force in a stratified atmosphere might have some dependence on the frequency.

7.2.2 Analytical relation between the velocity and a source force

As a next step, we investigated analytically the dependence between the source properties and the velocity produced by a perturbation. The set of MHD equations for perturbations (Equations 2.30–2.34) is the adequate system (simplified enough) to study this problem, where the fluctuations in all the variables are produced by a force $\mathbf{S}(x,y,z,t)$ which is introduced at the right hand side of the motion equation (Equation 2.31). Our aim is to obtain a relation between the source force $\mathbf{S}(x,y,z,t)$ and the velocity $\mathbf{v}_1$. For simplicity, we consider a one dimensional atmosphere, and the equations are reduced to

$$\frac{\partial\rho_1}{\partial t}+v_{1z}\frac{d\rho_0}{dz}+\rho_0\frac{\partial v_{1z}}{\partial z}=0, \tag{7.17}$$

$$\rho_0\frac{\partial v_{1z}}{\partial t}=-\frac{\partial p_1}{\partial z}-\rho_1 g+S(z,t), \tag{7.18}$$

$$\frac{\partial p_1}{\partial t}+v_{1z}\frac{dp_0}{dz}-c_s^2\Big(\frac{\partial\rho_1}{\partial t}+v_{1z}\frac{d\rho_0}{dz}\Big)=0. \tag{7.19}$$

$$\frac{\partial B_{1z}}{\partial t}=0. \tag{7.20}$$

$$\frac{\partial B_{1z}}{\partial z} = 0. \tag{7.21}$$

In the 1D case, Equations (7.20) and (7.21) show that the magnetic field is constant in time and space, so $B(z, t) = B_0(z)$, where $B_0(z)$ is the initial magnetic field. The rest of the equations have no dependence on the magnetic field. If we suppose that the atmosphere is vertically stratified by gravity, from the equation of hydrostatic equilibrium (Equation 2.27), and taking into account that the sound speed is $c_s^2 = \gamma p_0/\rho_0$ and the pressure scale height is $H_0 = c_s^2/(\gamma g)$, it is easy to see that in the 1D case the density and pressure in equilibrium vary with height as

$$\rho_0(z) = \rho_0(z = 0)e^{-\frac{z}{H_0}}, \tag{7.22}$$

$$p_0(z) = p_0(z = 0)e^{-\frac{z}{H_0}}. \tag{7.23}$$

Thus, the spatial vertical derivatives may be replaced according to

$$\frac{d\rho_0}{dz} = -\frac{1}{H_0}\rho_0, \tag{7.24}$$

and the same applies to the pressure. In this way, for an isothermal atmosphere stratified by gravity permeated by a vertical magnetic field, Equations (7.17-7.19) may be written as

$$\frac{\partial \rho_1}{\partial t} - v_{1z}\frac{\rho_0}{H_0} + \rho_0\frac{\partial v_{1z}}{\partial z} = 0, \tag{7.25}$$

$$\rho_0\frac{\partial v_{1z}}{\partial t} = -\frac{\partial p_1}{\partial z} - \rho_1 g + S(z, t), \tag{7.26}$$

$$\frac{\partial p_1}{\partial t} - v_{1z}\frac{p_0}{H_0} - c_s^2\Big(\frac{\partial \rho_1}{\partial t} - v_{1z}\frac{\rho_0}{H_0}\Big) = 0. \tag{7.27}$$

The next step is to seek for monochromatic plane-wave solutions in the form given by Equation (2.37), which gives

$$\frac{\partial v_{1z}}{\partial t} = -i\omega v_{1z}, \tag{7.28}$$

$$\frac{\partial v_{1z}}{\partial z} = ikv_{1z}, \tag{7.29}$$

and in an equivalent way for the perturbations in the pressure and density. The system of Equations (7.25)–(7.27) reduces to:

$$-i\omega\rho_1 - v_{1z}\frac{\rho_0}{H_0} + ik\rho_0 v_{1z} = 0, \tag{7.30}$$

$$-i\omega\rho_0 v_{1z} = -ikp_1 - \rho_1 g + S(z, t), \tag{7.31}$$

$$-i\omega p_1 - v_{1z}\frac{p_0}{H_0} - c_s^2\Big(- i\omega\rho_1 - v_{1z}\frac{\rho_0}{H_0}\Big) = 0. \tag{7.32}$$

From Equation (7.30) we easily retrieve the following relation between the fluctuation in the velocity and the density:

$$\rho_1 = v_{1z}\frac{\rho_0}{\omega}\Big(k + \frac{i}{H_0}\Big). \tag{7.33}$$

Introducing Equation (7.33) in Equation (7.32), we find that the perturbation of the pressure depends on the velocity as

$$p_1 = v_{1z}\frac{p_0}{\omega}\Big(\gamma k + \frac{i}{H_0}\Big), \tag{7.34}$$

and finally, from Equations (7.31), (7.33), and (7.34), after some trivial calculations, we obtain that the velocity is related to the driving force as

$$v_{1z} = -i\frac{S(z,t)}{\rho_0}\frac{\omega H_0}{k^2\gamma H_0^2 g + g - \omega^2 H_0}. \tag{7.35}$$

Taking into account the dispersion relation of the acoustic waves in a stratified atmosphere (Section 2.2.3):

$$k = \sqrt{\frac{\omega^2 - \omega_c^2}{c_s^2}}, \tag{7.36}$$

where $\omega_c = c_s/(2H_0)$ is the cutoff frequency of the atmosphere, we may replace the wavevector k of Equation (7.35), obtaining the expression

$$v_{1z}(z,t) = -i\frac{S(z,t)}{\rho_0}\frac{\omega H_0}{g - \omega_c^2 H_0}, \tag{7.37}$$

which shows that the velocity depends linearly on the frequency of the source force. According to this equation, if two harmonic forces of the same module $|S(z,t)|$ but with different frecuency ω are applied to the atmosphere, the one with higher frequency produces higher velocity amplitudes. This fact agrees with the results of the simulations obtained by introducing the force driver calculated from Equation (7.16).

All in all, since we attempt to find the proper force which reproduces the Doppler velocity measured with the Si I line, we may retrieve it from Equation (7.37). Considering z_{Si} the formation height of the silicon line, the force which generates the observed velocity $v_{\omega,obs}$ at this height at every position of the slit x is given by

$$S_\omega(x, z_{Si}, t) = i\frac{v_{\omega,obs}(x, z_{Si}, t)}{\omega}\rho_0\Big(\frac{g}{H_0} - \omega_c^2\Big) \tag{7.38}$$

for each frequency ω. The velocity v_{obs} contains variations in a wide range of frequencies, with a prominent peak at $\nu = 3.3$ mHz. The total force $S(z_{Si}, t)$ will be the sum of Equation (7.38) over all frequencies ω_i which can be sampled from the observational temporal series, that is

$$S(x, z_{Si}, t) = i\sum_{\omega_j}\frac{v_{\omega_j,obs}(x, z_{Si}, t)}{\omega_j}\rho_0\Big(\frac{g}{H_0} - \omega_c^2\Big). \tag{7.39}$$

Considering that the temporal series is sampled with n time steps with an interval Δt, for an even n the sampled frequencies are given by

$$\omega_j = \frac{-n/2+1}{n\Delta t}, \frac{-n/2+2}{n\Delta t}, ..., \frac{-1}{n\Delta t}, 0, \frac{1}{n\Delta t}, ..., \frac{n/2-1}{n\Delta t}, \frac{1}{2\Delta t}, \tag{7.40}$$

while for an odd n

$$\omega_j = \frac{-(n-1)/2}{n\Delta t}, \frac{-(n-1)/2+1}{n\Delta t}, ..., \frac{-1}{n\Delta t}, 0, \frac{1}{n\Delta t}, ..., \frac{(n-1)/2}{n\Delta t}. \tag{7.41}$$

The highest frequency corresponds to the Nyquist critical frequency $1/(2\Delta t)$.

The force $S(x, z_{Si}, t)$ was evaluated by separating each of these frequencies of the velocities and summing all of them following Equation (7.39). The complex i of Equation (7.39) introduces a delay of $\pi/2$ in the resulting force. The force includes a broad spectrum of frequencies, and a delay of $\pi/2$ in their phase produces a different time delay for each of them, depending on their period.

Thus, to that aim, we have calculated the Fourier Transform of the temporal series of the velocity and added the $\pi/2$ phase in the transformed domain. If $F(s)$ is the Fourier Transform of a real function $f(t)$, $F(s)$ is hermitic and it satisfies the following condition:

$$F(-s) = F^*(s), \tag{7.42}$$

where $F^*(s)$ indicates the conjugate complex of $F(s)$. According to this, if we add a $\pi/2$ phase to the positive frequencies of the Fourier Transform, in the case of the negative frequencies we have to substract the $\pi/2$ phase to produce the same effect. Once this procedure is completed, the force $S(x, z_{Si}, t)$ is ready to be introduced in the simulations.

The spatial distribution of the force is given by the same function $P(x, y, z)$ described at the beginning of Section (7.2.1). We set the force $S(x, z_{Si}, t)$ for all the heights inside a layer of a chosen thickness in the y and z directions, but smoothly modulated to be zero after a few grid points, and covering the slit of the observations in the x direction.

We have performed several numerical simulations using the above method to calculate the driver, showing no completely satisfactory results. In the simulations we carried out, the power in the vertical velocity in the 5 minute band at the height where the driver was located matched the observed one, but at high frequencies the power was lower than required. As the power was low at high frequencies, the oscillations that we simulate at the photosphere reproduced the wave pattern of the Si I observations more or less well. However, is it not the case for oscillations measured in other lines formed higher up. The match of the power in the band between 5 and 8 mHz is critical to reproduce the oscillations in higher layers, since they propagate upward and their amplitude increases with height. Another problem is the phase delay. According to Equation (7.39) the response of the velocity to the force must be delayed $\Delta\phi = \pi/2$ with respect to the force. In simulations, however, we find that it was the case only for frequencies below 4 mHz. Due to some reason, this delay decreases linearly until reaching $\Delta\phi = 0$ at 6 mHz. Thus, with this driver we have not been able to reproduce the observations. We concluded that we need a higher power at frequencies above 5 mHz and these high frequency waves must be in phase with the force that generates them.

7.2.3 Empirical relation between the velocity and a source force

Since the previous attempts to obtain a force driver which generates the correct observed velocity pattern were not entirely succesful, we replaced the source force of Equation (7.38) by a new one of the form:

$$S_\omega(x, z_{Si}, t) = v_{\omega,obs}(x, t)\frac{1}{A(\omega)}\Delta(\omega), \tag{7.43}$$

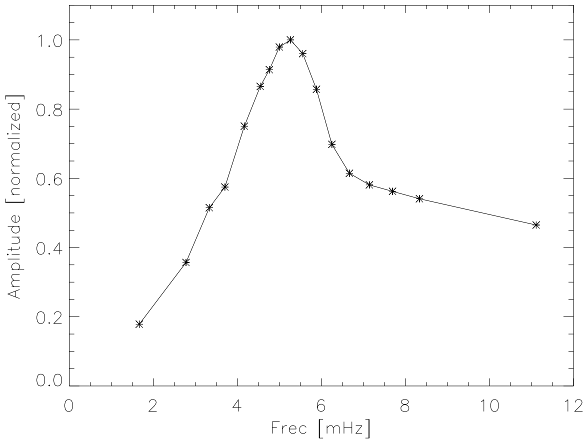

Figure 7.8: Variation of the amplitude of the velocity with the frequency of the force driver, normalized to the maximum value.

where the functions $A(\omega)$ and $\Delta(\omega)$ include the dependence of the force amplitude and phase delay with frequency, respectively. The $A(\omega)$ dependence was evaluated by analyzing numerically the response of the atmosphere to a force driver with a certain period. We have carried out a set of simulations using a harmonic driver located at the photosphere with different periods, but all of them with the same force amplitude. The amplitude of the velocity retrieved after reaching the stationary regime of the simulations is chosen as the response of the atmosphere to a harmonic wave. Figure 7.8 shows the values obtained for all the simulations performed, normalized to the maximum amplitude. The amplitude increases almost linearly from the lower frequency to a frequency around 5.2 mHz, and for higher frequencies it decreases as the inverse of the frequency. Its maximum is located at a frequency close to the local cutoff frequency. The particular form of this dependence varies with the parameters of the sunspot atmosphere, and it critically depends on the location of the driver. We found that a change in the height of the driver shifts the frequency of the maximum response. At those frequencies for which the response of the velocity to the force is very efficient (for example, at 5.3 mHz) the factor which multiplies the velocity to obtain the force from Equation (7.43) must be lower than for those frequencies with a poorer response (for example, at 3 mHz). For this reason $A(\omega)$ appears dividing v_{1z} in Equation (7.43).

Note that the analytical relation obtained in the previous section reproduces the linear behavior of the response at low frequencies. As mentioned previously, in this frequency range Equation (7.37) is a good aproximation of the dependence between velocity amplitude and frequency.

We have carried out a simulation using Equation (7.43) to introduce the observed driver in the simulations, including the expression of $A(\omega)$ from Figure 7.8 but ignoring the phase dependence $\Delta(\omega)$. The analysis of the phase difference between the observed velocity and the obtained in this simulation at the height where the driver was introduced shows the same phase delay infered in the previous section, that is, $\Delta\phi = \pi/2$ for frequencies below 4 mHz and $\Delta\phi = 0$ for frequencies higher than 6 mHz, with a linear variation between 4 and 6 mHz. The function $\Delta(\omega)$ has been constructed in order to characterize this behavior. As the velocity at low frequencies needs a quarter of a period to account for the variations of the force, at these frequencies $\Delta(\omega)$ shift the source driver backwards. From 4 to 6 mHz, the shift of the phase decreases from $\pi/2$ to zero. This simulation has also been used to correct $A(\omega)$, comparing the power spectra of the Si I observed velocity and the simulated one with the better frequency sample that it produces (only 17 frequencies were used in the previous estimation of $A(\omega)$).

7.3 Set up of the simulations

We have introduced the driver from Section 7.2.3 as a force perturbation in the MHS model of the observed sunspot obtained in Section 7.1. The height where the optical depth at 5000 Å is unity in the quiet Sun atmosphere was chosen as $z = 0$ Mm. According to Bard & Carlsson (2008), in a model of sunspot the Si I line forms at a geometrical height of 308 km above the height where $\tau_{5000} = 1$, which corresponds to $z = -42$ km for the adopted Wilson depression of 350 km. We have to take into account that we need at least $0.9 - 1$ Mm of atmosphere above the location of the driver to reproduce the travel of the wave from the Si I line to the He I line, according to the geometrical height difference between these two layers (see Table 6.4). In those high layers, the Alfvén speed of the MHS sunspot model takes very high values, which produces a extremely small time step. In order to save computational time and avoid problems with the top PML boundary, we have located the driver slightly deeper, at $z = -100$ km.

In order to compare the numerical simulation with the observational data, we have assigned a fixed z to the formation height of each spectral line, and we have assumed that the vertical velocity at that location corresponds to the velocity measured from the Doppler shift of the line. Following the heights retrieved from Table 6.4 and taking into account that the velocity obtained from the observations of the Si I line was imposed as a driver at $z_{Si} = -100$ km, the layers of the computational domain selected as representative of the rest of the spectral lines are $z_{Fe} = 175$ km, $z_{Ca} = 600$ km and $z_{He} = 725$ km for the Fe I λ 3969.3 line, Ca II H core, and He I line, respectively.

The details of the configuration are shown in Table 7.1, including the section where the simulation is discussed, the radiative relaxation time, the length of the driver, the duration of the simulation, the size of the computational domain, the frequencies drived by the source force, and the numbers of the corresponding figures.

The size of the x and y directions of the computational domain are different, and we have used different boxes in these simulations. The big computational domain covers 14.8×8.4 Mm in the horizontal directions, while the small one covers 8.4×5.2 Mm. Both domains have horizontal spatial steps of $\Delta x = \Delta y = 100$ km. There are also some differences in the vertical direction. For the two first simulations the computational domain spans from $z = -0.6$ Mm to $z = 0.8$ Mm, excluding the PML layer, with a spatial step of $\Delta z = 25$ km. The last run extends 200 km higher. The radiative transfer is implemented following Newton's cooling law. In Sections 7.4.1 and 7.4.2 we discuss the limitations of the runs without radiative transfer and with constant relaxation time, respectively. Section 7.5 describes the analysis of the run with the radiative relaxation time as given by Spiegel (1957).

Table 7.1: Summary of the simulation runs

Section	τ_R	Driver length (Mm)	Duration (s)	Domain (Mm)	Frequency (mHz)	Figures
7.4.1	∞	10	4465	$14.8 \times 8.4 \times 1.4$	1.5–8	7.9–7.10
7.4.2	45 s	4	3916	$8.4 \times 5.2 \times 1.4$	1.5–8	7.11–7.12
7.5	Spiegel	4	4465	$14.8 \times 8.4 \times 1.6$	1.5–20	7.14–7.26

7.4 Simulation of the observed wave propagation

We have performed three numerical simulations. These simulations differ in some aspects. First, we vary the horizontal length of the driver in x direction. We chose either only an umbral region of the observed sunspot (X=4 Mm) or include also part of the penumbra (X=10 Mm). The parameters of the MHS model of sunspot vary slowly, and this model cannot account for a realistic penumbra. The simulations of Sections 7.4.1 and 7.5 cover the whole umbra, but the simulation of Section 7.4.2 only includes 4 Mm of the umbra. The second different parameter between the runs is the radiative relaxation time. As described in Section 3.1.4 our code has the posibility to account for radiative losses due to the coupling between the plasma and radiation following the simple Newton cooling law, valid for optically thin media. The run with relaxation time according to Spiegel formula shows more promising results, and for this reason we have introduced a driver with a broader range of frequencies and we have spanned the computational domain 200 km higher, in order to avoid possible problems with the top boundary.

7.4.1 Run with no energy exchange

The parameter Q_{rad} from the energy equation (Equation 3.25) is set to zero. Since no radiative losses are taken into account, the propagation of waves is adiabatic. Figures 7.9 and 7.10 show a comparison between the observations and the numerical simulations. Figure 7.9 represents the phase and amplification spectra between two photospheric lines, the Si I and the Fe I lines, while Figure 7.10 presents the results obtained between the Si I and the He I lines. In the top panels of these figures, the background color indicates the relative occurence of a given phase shift in the observational data (same as in Section 6.2.3), and the green crosses correspond to the phase shift at every spatial position in the umbra, obtained from the simulations. The solid lines of the bottom panels show the amplification spectra of the observed data, while the dashed lines represent the values retrieved from the simulation. From the comparison of the data presented in Figure 7.9, we find that in the numerical simulation the phase shift is zero for frequencies below 6 mHz, and it increases rapidly in such a way that at 7 mHz it matches the observational data and the model. In the range between 4.5 and 6 mHz the behavior of the simulation differs from the observations, since the phase difference increases more slowly for observations. The amplification spectra of both observations and simulations are similar for frequencies below 6 mHz, but they greatly differ at higher frequencies. The simulation presents a much higher amplification between 6 and 7 mHz.

The phase and amplification spectra between the photospheric Si I line and the chromo-

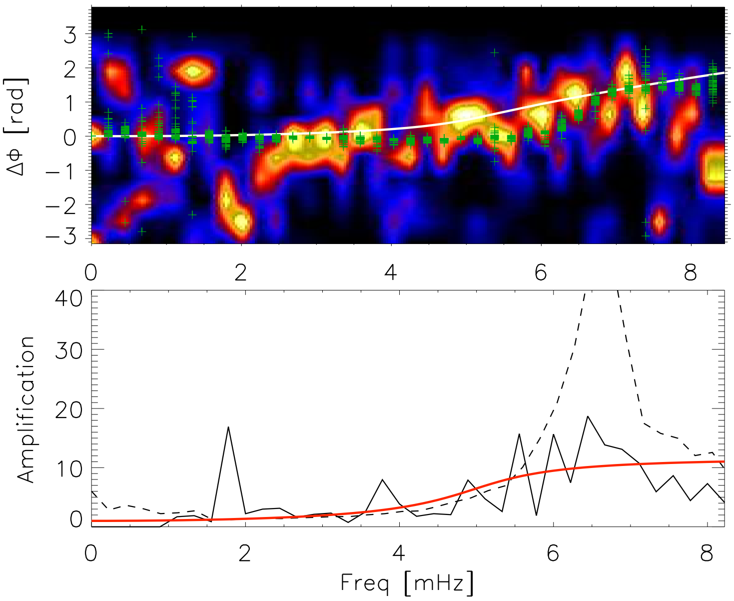

Figure 7.9: Top: Phase spectra between the observed LOS velocity of the Si I and the Fe I λ 3969.3 lines. The color code shows the relative occurence of a given phase shift. The green crosses are the results of the simulation with no radiative transfer for all the spatial points. The white line represents the best fit from the theoretical model used in Chapter 6. Bottom: Amplification spectra for the observation (black solid line), the simulations (black dashed line) and the model (red line).

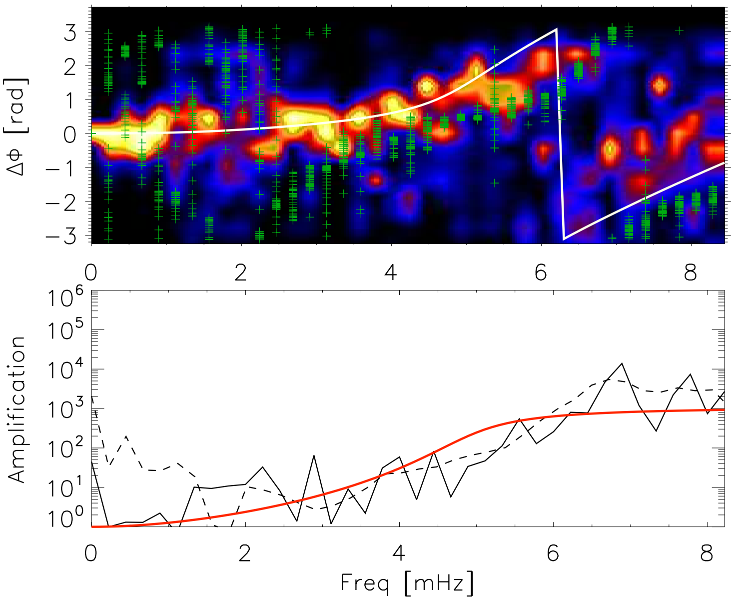

Figure 7.10: Top: Phase spectra between the LOS velocity of the Si I and the He I lines and comparison with the simulation without radiative transfer. Bottom: Amplification spectra. The format is the same as Figure 7.9.

spheric He I line also show some critical differences between simulations and observations. The phase shift of the simulation is lower than that of the observation, while the amplification at frequencies higher than 5.5 mHz is larger in the simulation. Note that the amplification spectra is plotted in a logarimic scale, so the differences are significant.

The discrepancies between these simulations and the observations clearly point out that some important ingredient is missing in the simulations. A good candidate to improve the simulations can be the introduction of radiative energy losses. Several arguments point in that direction. First, in the simulation, the oscillations at heights above the formation height of the Si I have amplitudes much higher than the observed ones. The radiative losses should produce some damping of the waves, especially at high frequencies. Secondly, the cutoff of the simulation is located at 6 mHz (see Figure 7.9), which is higher than the one inferred from the observations (around 4.5 mHz). When the radiative timescale τ_R is small enough, the cutoff frequency is expected to decrease, compared to the adiabatic case. Finally, the inclusion of radiative losses also produces an increase of the phase difference compared to adiabatic case (see Figure 7 from Centeno et al. 2006).

7.4.2 Run with constant relaxation time

We implemented the energy exchange with a simple Newton's cooling law and assumed a constant cooling time. Taking into account the value retrieved from the fit of the observed phase spectra to the model (Table 6.3) obtained between the deeper (Si I) and the higher (He I) lines in Chapter 6, we have selected $\tau_R = 45$ s.

Now the phase and amplification spectra between the photospheric Si I and Fe I λ 3969.3 lines agree much better with the observations (Figure 7.11). The cutoff of the simulated phase spectra is shifted toward lower frequencies, and the phase shift shows a better qualitative match with the observations for frequencies below 7 mHz. The amplification is much lower than in the previous adiabatic simulation, and it also fits well to the observations for all frequencies.

Figure 7.12 shows the comparison between observations and simulation for the Si I and He I lines. Again, the agreement in the phase spectra is remarkable, although for frequencies higher than 5 mHz the amplification of the simulation is much lower than the observed one.

These results suggest that, while the energy exchange is fundamental for a proper reproduction of the observations, a constant and short cooling time as $\tau_R = 45$ s produces too large energy losses, and the amplitude of waves at high chromospheric layers has been damped too much. At the same time, between the formation height of the photospheric Si I and Fe I lines the imposed cooling time looks reasonable, as it allows to reproduce the phase and amplification spectra between these layers.

In order to obtain a better agreement between the observations and the simulations we need a variable τ_R, with relatively low values at the low photosphere but increasing with height toward the chromosphere. It means that the cooling time must increase at layers above the formation height of the Fe I lines, producing an almost adiabatic upward propagation. Note that this conclusion, obtained from the comparison of the observations with the numerical simulations, was previously reached independently in Chapter 6 from the observational analysis fitting a simple wave model (see Table 6.3). From these fits we have found that τ_R at the photosphere is around 30 s, and at the chromosphere its value is 15 s.

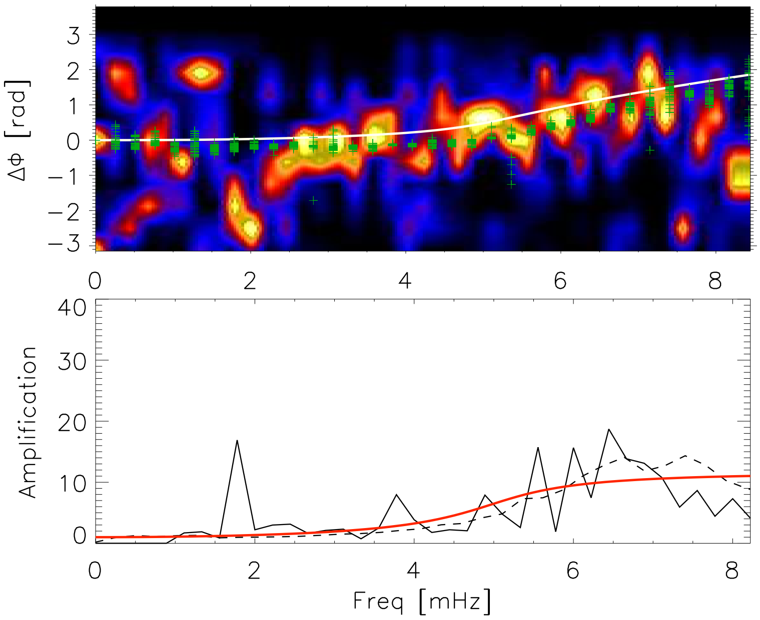

Figure 7.11: Top: Phase spectra between the LOS velocity of the Si I and the Fe I λ 3969.3 lines and comparison with the simulations with constant relaxation time. Bottom: Amplification spectra. The format is the same as in Figure 7.9.

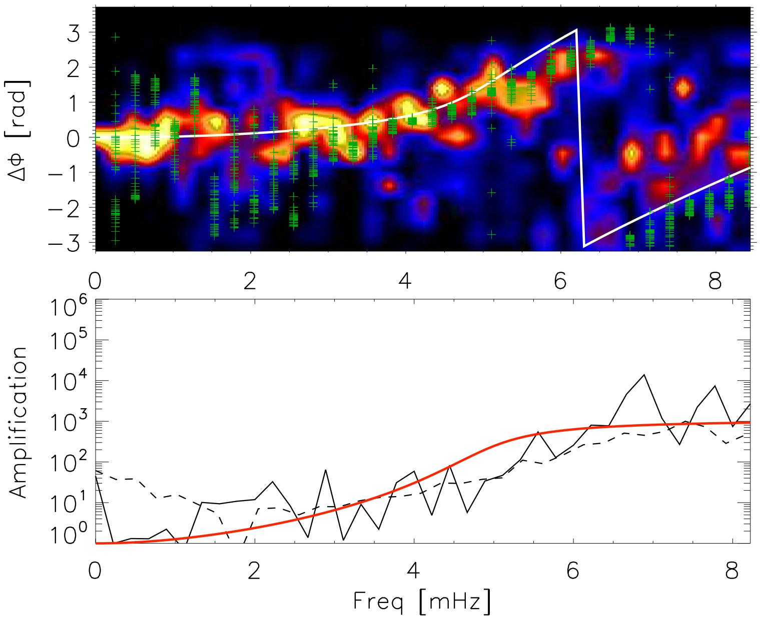

Figure 7.12: Top: Phase spectra between the LOS velocity of the Si I and the He I lines and comparison with the simulations with constant relaxation time s. Bottom: Amplification spectra. The format is the same as in Figure 7.9.

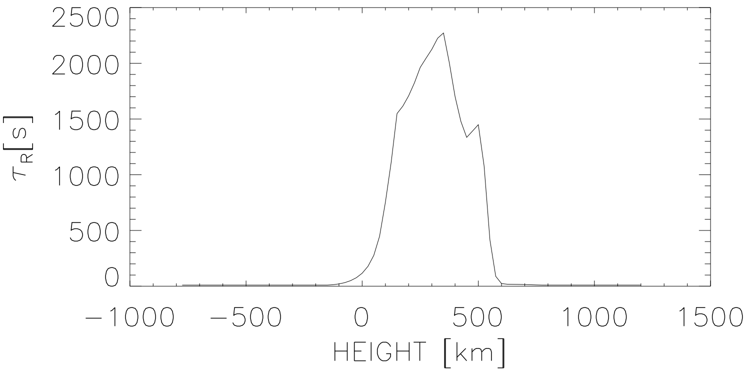

Figure 7.13: Variation of the radiative relaxation time with height according to Spiegel (1957), modified above $z = 500$ km.

In the case of pairs of lines with one of them formed at the photosphere and the other at the chromosphere, we have obtained a higher value of 45 s. Taking into account that these τ_R are estimated for an isothermal atmosphere, and thus constant τ_R, the retrieved values should indicate an average through the atmosphere between the two formation heights of the corresponding lines. Since both the photosphere (30 s) and the chromosphere (15 s) has lower values than the average of all the travel (45 s), the τ_R at these intermediate layers must be higher than the obtained $\tau_R = 45$ s, *i.e.*, there must be a local maximum of τ_R at intermediate heights.

7.5 Run with relaxation time according to Spiegel formula

In this section we compare the results of the simulation with the observed wave propagation using the radiative damping time following Spiegel (1957), which is given by

$$\tau_R = \frac{\rho c_v}{16\chi\sigma_R T^3}, \tag{7.44}$$

where c_v is the specific heat at constant volume, χ is the mean absorption coefficient, and σ_R is the Stefan-Boltzmann constant. This expression is valid at photospheric heights, but not in the chromosphere as it was derived by Spiegel in the approximation of local thermodynamic equilibrium. As the values of τ_R given by the Spiegel formula are not certain at chromospheric heights, we took the freedom to modify them above $z = 500$ km, in order to mimic the low $\tau_R = 10$ s obtained for chromospheric lines in Chapter 6 from observations. Figure 7.13 shows the variation of the cooling time applied in our simulations with height at the axis of the sunspot.

7.5.1 Oscillatory signal at the height of the driver

Figure 7.14 shows a comparison between the LOS velocity map of the umbra observed with the Si I line (top panel) and the vertical velocity of the simulation at the height where the driver was introduced (middle panel). Negative velocities (appearing as black shaded regions) indicate upflows, where the matter moves toward the observer, while white

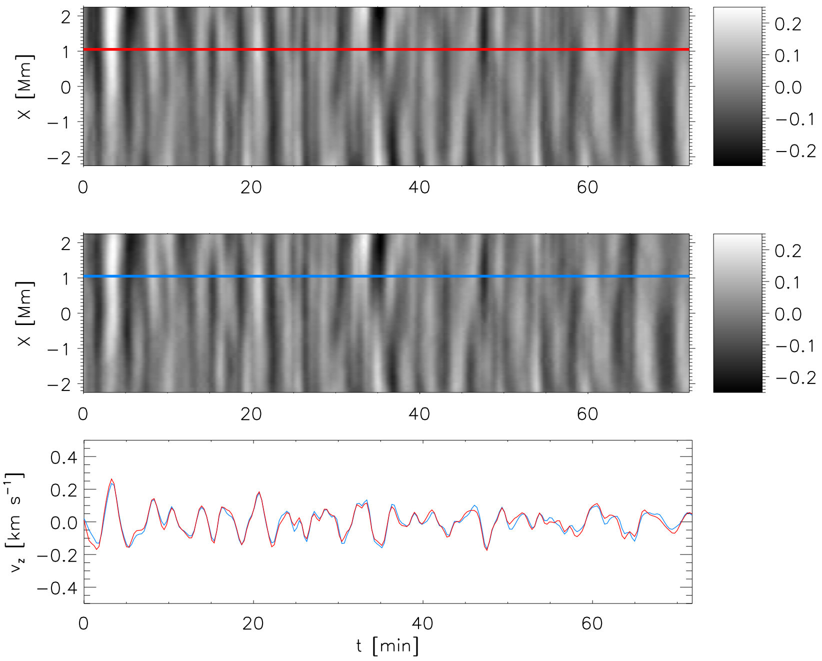

Figure 7.14: Velocity maps of the Si I line. Top: Observational, measured from the Doppler shift of the Si I line; middle: numerical, vertical velocity at the formation height of the Si I line; bottom: comparison of the observational (red line) and numerical (blue line) velocity at x=1.1 Mm.

regions are downflows. Both wave patterns are almost identical, with an amplitude below 0.3 km s^{-1}. The bottom panel shows the time evolution of the velocity at a certain location inside the umbra, confirming once again that the simulation fits well the observations.

To perform a more detailed comparison between the velocities at the height of the driver, we show in Figure 7.15 a spectral analysis of the simulation and the observation. Top panel illustrates the power spectra of the observed velocity (red dashed line) and vertical velocity at the height of the driver (blue solid line). The ratio between the amplitudes of both velocities (simulated/observed) is given in the middle panel. In all the frequency range the ratio is around unity, indicating a good match between the driver and the real oscillation. The power peak at 3 mHz is a bit lower in the simulation. For frequencies above 7 mHz, where the power is very low, the ratio departs slightly from unity, but it varies between 0.7 and 1.3. Bottom panel of Figure 7.15 shows the phase difference between the measured and simulated velocity. At each frequency we have calculated histograms of the phase difference in all the spatial points inside the umbra. The color scale of the panel indicate the relative occurrence of a given phase shift, spanning from black (low) to red (high). Negative phase difference means that the simulated velocity lags the observed one. Both oscillatory signals are in phase for all frequencies.

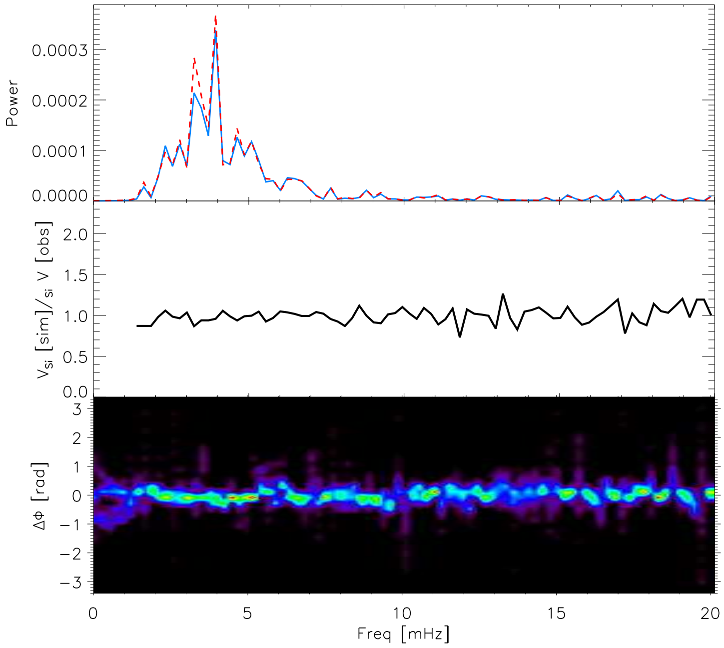

Figure 7.15: Top: Power spectra of the Si I velocity (red dashed line) and the simulated velocity at the height where the driver is introduced (blue solid line); middle: ratio of the simulated amplitude to the observed one; bottom: differences in phase.

7.5.2 Simulated velocity at the formation heights of the other spectral lines

Now we can compare the observed velocities obtained from different spectral lines in Chapter 6 with the simulated ones at heights defined in Section 7.3.

The Fe I lines are formed about 280 km above the Si I line, where the driver is introduced. Figure 7.16 shows the velocity map observed with the Fe I λ 3969.3 line and the simulated one at the corresponding height. The Doppler velocity map retrieved from the Fe I line is quite poor, especially in this region of the umbra where the intensity is lower. However, the strongest wavefronts, with an amplitude of almost 0.5 km s^{-1}, can be recognized and compared with the simulated wave pattern, showing a good agreement. For example, the wavefronts around t = 20 min or the ones between t = 47 and t = 55 min can be clearly identified in the simulation, with a similar amplitude (bottom panel of Figure 7.16).

The power spectrum of the simulation at the formation height of the Fe I λ 3969.3 line is given in Figure 7.17. The power peak at 3 mHz is stronger in the observations, while the power peak at 6 mHz is more significant in the simulations. At frequencies above 8 mHz the observational power spectra shows higher power. But we suspect that this high fequency power corresponds to the noise present in the velocity signal of the Fe I lines. The problems of the simulation to reproduce the power spectra at this height in the 3 and 5 minute bands could indicate a deficiency in the MHS umbral model to mimic the observed one.

Figure 7.18 illustrates the observational and numerical velocity maps in the case of the LOS velocity measured with the Ca II H core. The Ca II H core is formed in the chromosphere, so these waves have propagated upward about 700 km from the formation height

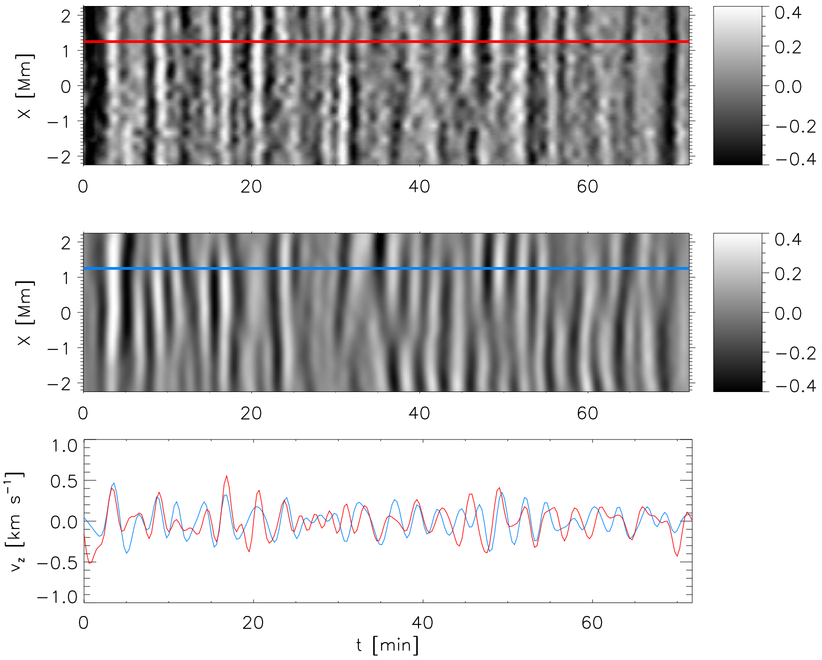

Figure 7.16: Velocity maps of the Fe I λ 3969.3 line. Top: Observational, measured from the Doppler shift of the Fe I line; middle: numerical, vertical velocity at the formation height of the Fe I line; bottom: comparison of the observational (red line) and numerical (blue line) velocity at x=1.1 Mm.

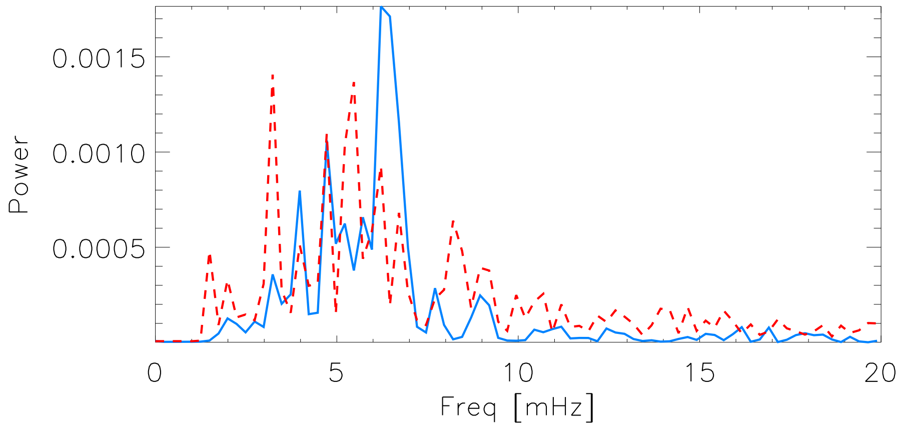

Figure 7.17: Power spectra of the observed Fe I λ 3969.3 velocity (red dashed line) and the simulated velocity at its corresponding height (blue solid line), averaged over the umbra.

of the Si I line in order to reach this layer. Note that in the simulated velocity map (middle panel) the velocity signal is almost zero during the first 2 minutes, due to the time spent by the slow waves to cover the distance between the driver and this height travelling at the sound speed. During this travel the period of the waves is reduced to around 3 minutes and their amplitude increases, reaching peak-to-peak values of almost 8 km s^{-1}. The bottom panel of Figure 7.18 shows that the oscillations develop into shocks. This behavior is well reproduced by the numerical simulation. The simulated velocity map reproduces reasonably well the observed oscillatory pattern. Only in the temporal lapse between $t = 27$ and $t = 40$ min the simulated pattern differs significantly from the observations. Most of the observed wavefronts can be identified in the simulation, although their spatial coverage of the umbra can be slightly different. For example, in the observations at $t = 50$ min a wavefront shaded in white covers from the limit of the plotted velocity map at $x = 2$ Mm to around $x = 0$ Mm, while in the simulations it extends from $x = 2$ Mm to almost $x = 1$ Mm. These little differences may be due to the limitations in the configuration of the numerical simulation: on the one hand, the MHS atmosphere is an axisimetric model, which is obviously not the case of the real sunspot. Thus, the distance travelled by the waves along field lines may be different, producing a phase lag. On the other hand, we have only introduced the driver in a region of the umbra along the slit of the observations, so we have ignored the driving of waves in the rest of the (non observed) umbra.

During the first 20 minute of the simulation there is some phase shift with respect to the observation, and the amplitude of the simulation is lower. Note that this time lag is evident in the wavefronts with the largest amplitude, where the nonlinearities are clear. It will be discussed in Section 7.6.

The highest spectral line observed is the He I line, which is formed around 100 km above the Ca II H core. The comparison between the Doppler velocity of this line and the vertical velocity of the simulation at the corresponding height is given in Figure 7.19. Like in the case of the Ca II H, most of the wavefronts of the observation can be clearly identified in the simulation, except in the temporal range between $t = 27$ and $t = 40$ min. The match between the observed and simulated amplitudes is also remarkable. Both maps seem to be almost in phase. There is some phase delay which coincides with the strongest shocks, but it is smaller than the one obtained for the Ca II H core.

Only those waves with frequecy above the cutoff can reach the chromosphere. The increase of the amplitude of these waves with height is higher than the one corresponding to the evanescent low frequency waves, and the power spectra at the chromosphere is dominated by a peak at 6 mHz. For example, in the case of the power spectra of the He I line (Figure 7.20), both the observations and simulation have their power concentrated around this frequency. The observational power has three power peaks in the 3 minute band, located at 5.5, 6 and 7 mHz. The simulated power is concentrated at a single peak between the two highest peaks of the observations. The simulated peak at 5.5 mHz is lower than the observed one. The simulations also reproduce the power peaks at 7.7 mHz and 9 mHz, and the low power at frequencies below 5 mHz. At frequencies above 13 mHz the simulated power is higher than the observational one.

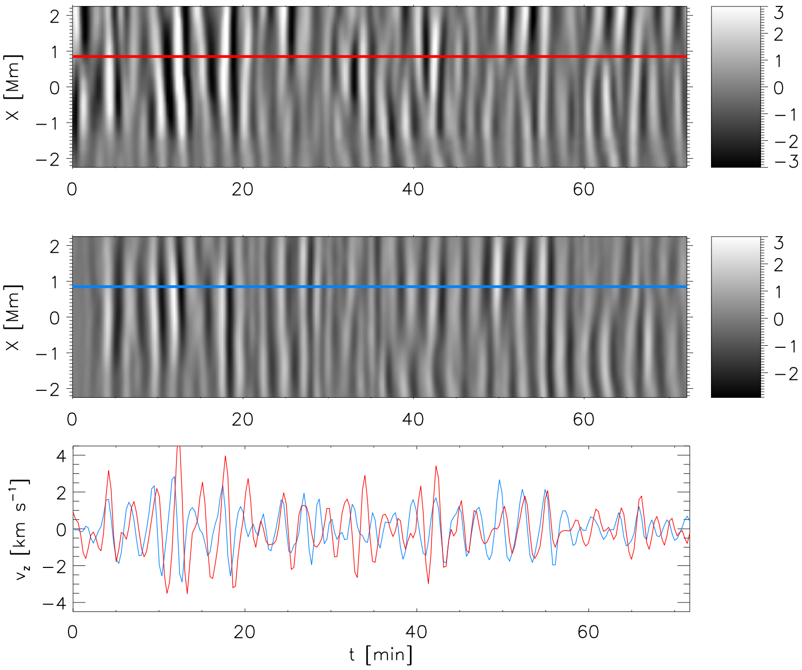

Figure 7.18: Velocity maps of the Ca II H core. Top: Observational, measured from the Doppler shift of the Ca II H line; middle: numerical, vertical velocity at the formation height of the Ca II H line; bottom: comparison of the observational (red line) and numerical (blue line) velocity at x=0.9 Mm.

7.5.3 Propagation from the photosphere to the chromosphere

Figure 7.21 shows the spectra between the photospheric Si I line and the chromospheric He I line. From 0 to 7 mHz, where the coherence of the observations is high, the simulated phase difference precisely matches the observed one, with a null phase difference for frequencies below 4 mHz and an almost linear increase between 4 and 7 mHz. At higher frequencies the coherence of the observed phase difference is lower, but the simulated one keeps its linear increase. With regards to the amplification spectra, for frequencies above 1.5 mHz the simulated spectra reproduces properly the observed one. The smallest frequencies show a high numerical amplification, which is due to the difficulties of the PML to damp these long period waves. The thickness of the PML layer should be proportional to the wavelength of the wave that must be absorbed, and the employed PML is obviously not optimized for such a long period waves.

A similar result is found between the velocity obtained with the Si I and the Ca II H core (Figure 7.22), since the last one is formed just around 100 km below the He I line. The simulated phase difference is zero for frequencies below 4 mHz, and it increases at higher frequencies. It matches the observed phase shift between 2.5 and 9 mHz. At higher frequencies the observed phase difference is noisier, while in the frequency range between 1 and 2.5 mHz it takes a value of π or $-\pi$. In the analysis of the observations we expressed our doubts about the reliability of this phase shift, so we are not surprised that the simulation does not reproduce it.

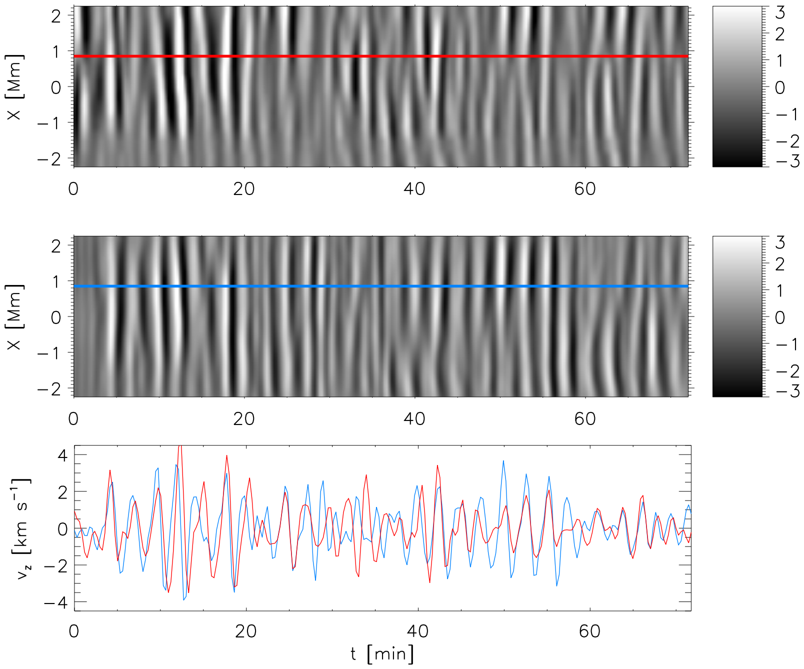

Figure 7.19: Velocity maps of the He I line. Top: Observational, measured from the Doppler shift of the He I line; middle: numerical, vertical velocity at the formation height of the He I line; bottom: comparison of the observational (red line) and numerical (blue line) velocity at x=0.9 Mm.

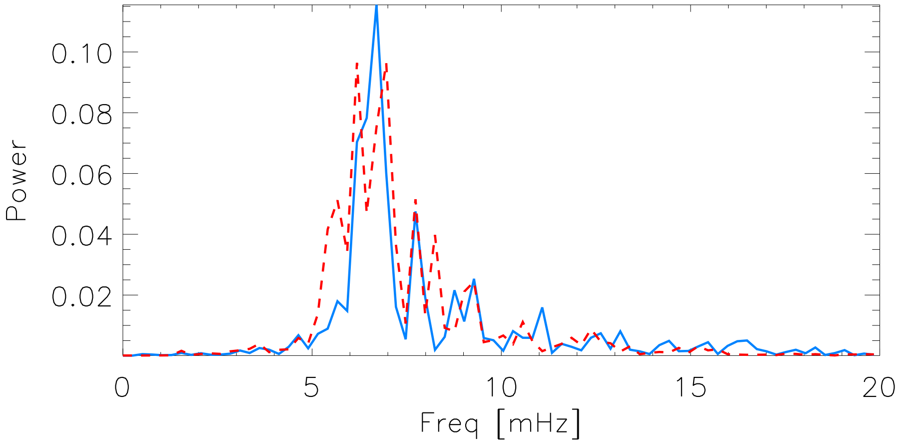

Figure 7.20: Power spectra of the observed He I velocity (red dashed line) and the simulated velocity at its corresponding height (blue solid line).

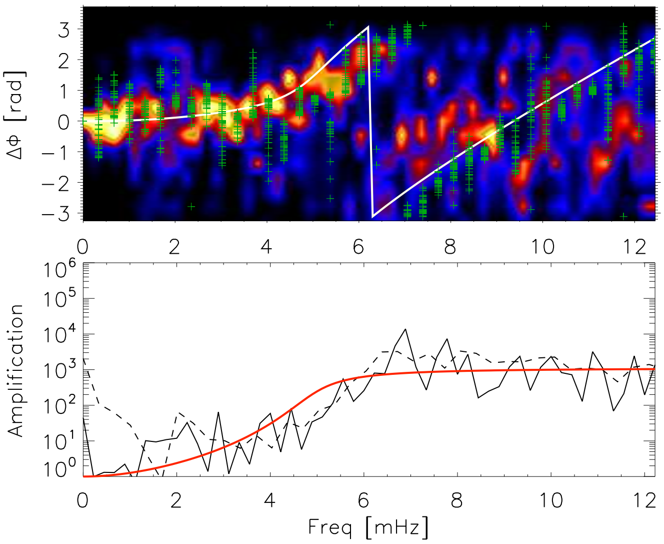

Figure 7.21: Top: Phase difference spectra between Si I and He I velocities in the umbra. Bottom: Amplification spectra. The format is the same as in Figure 7.9.

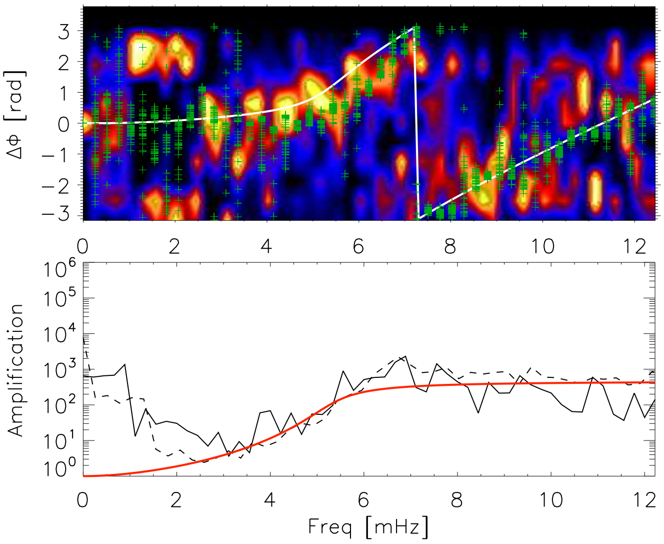

Figure 7.22: Top: Phase difference spectra between Si I and Ca II H velocities in the umbra. Bottom: Amplification spectra. The format is the same as in Figure 7.9.

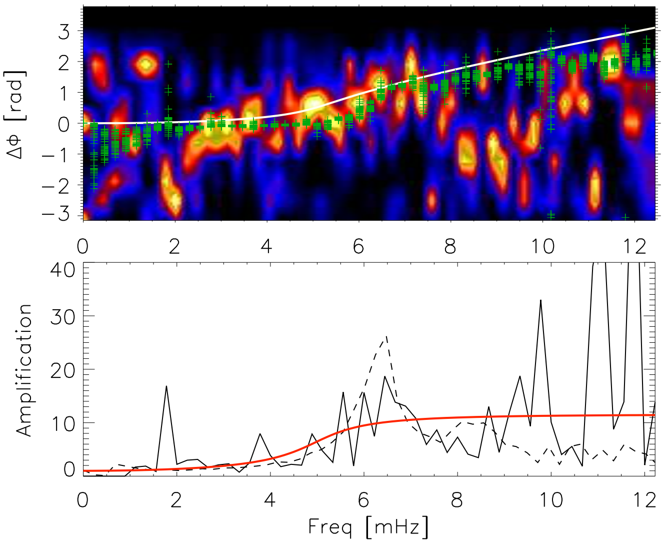

Figure 7.23: Top: Phase difference spectra between Si I and Fe I λ 3969.3 velocities in the umbra. Bottom: Amplification spectra. The format is the same as in Figure 7.9.

Figure 7.23 shows the phase and amplification spectra between two photospheric lines, the Si I and the Fe I λ 3969.3 lines. The observed phase difference has high coherence between 2 and 8 mHz, and in this frequency range the simulated phase delay fits the observational one reasonably well, showing a $\Delta\phi = 0$ for frequencies below 4 mHz and a slow increase for higher frequencies. For frequencies below 2 mHz and above 8 mHz the observed phase difference spreads out and has lower coherence. The behavior of the simulated amplification spectra is similar to the observed one between 0 and 8 mHz, but the numerical amplification is significatively larger at the peak around 6.5 mHz. Note also that around 3.5 mHz the observed amplification shows a peak, not reproduced in simulations. This was also seen in the power spectra in Figure 7.17. At higher frequencies, the observed amplification has some high peaks, but they are not trustable due to the poor quality of the Fe I velocity map.

The spectra between Fe I λ 3969.3 and He I shown in Figure 7.24 are similar to the ones from Figures 7.21 and 7.22, since all of them correspond to pairs of lines including one photospheric and one chromospheric line. The numerical phase and amplification spectra match the observational ones in the frequency range between 2 and 8.5 mHz. Out of this range the observational phase spectra is very noisy and has a lower coherence, meaning that these phase shifts are not reliable. At frequencies above 8 mHz the observational amplification seems to decrease, but this tendency is not reproduced by the simulated one.

7.5.4 Energy balance

The driver is located just above the layer where the Alfvén speed is equal to the sound speed. At this height the c_s^2/v_A^2 parameter is 0.8. Since our driver is a vertical force, it mainly generates oscillations in the vertical velocity. Inside the umbra the magnetic field is vertical, and most of the energy introduced by the vertical force has an acoustic nature,

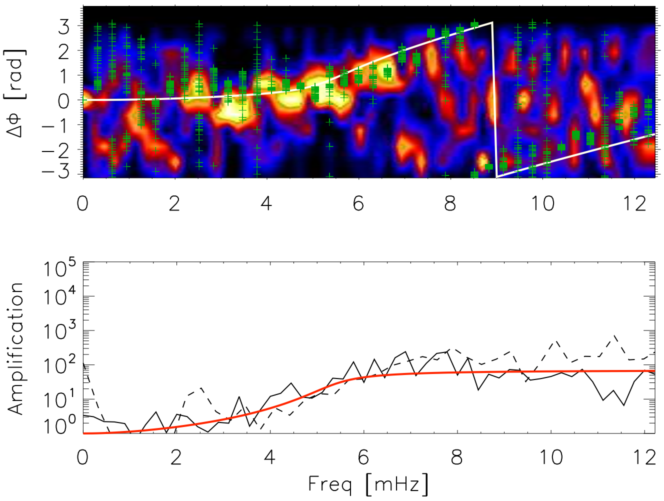

Figure 7.24: Top: Phase difference spectra between Fe I λ 3969.3 and He I velocities in the umbra. Bottom: Amplification spectra. The format is the same as Figure 7.9.

which corresponds to a slow mode in this low-β region. Because of the vertical thickness of the driver, some part also acts at $c_S = v_A$ or below, and it produces some fast acoustic waves in the region just below the layer $c_S = v_A$. These waves are partially transformed into a fast magnetic mode above the height where $c_S = v_A$, which is reflected towards deeper layers due to the gradients of the Alfvén speed. The energy of this mode is very low. However, it must be taken into account that in this simulation we are introducing the observed velocity at the formation height of the Si I line and, thus, the wave pattern below this layer is not reliable. In the real sunspot, waves propagate from deeper layers and in their upward propagation they reach the layer where $c_S = v_A$. Some significative part of the energy of these waves is transformed into fast magnetic waves at this height, and the contribution of the fast modes in the low-β region must be higher than the one estimated in this simulation.

The slow acoustic mode generated directly by the driver propagates upwards along the field lines. According to Figure 7.15, at $z = -100$ km most of its power is concentrated in the 5 minute band, with a frequency between 3 and 4 mHz. At this layer the cutoff frequency is $\nu_c = 4.7$ mHz, and it increases with height until it reaches $\nu_c = 6$ mHz at $z = 200$ km. It means that the oscillations in the 5 minute band introduced by the driver cannot propagate upwards, and they form evanescent waves which do not supply energy to the higher layers. Only those waves with frequency above the cutoff can propagate to the chromosphere. As it was pointed before, the behavior of the simulation between the formation height of the Si I and the Fe I lines is different from the observations. In the observational data, waves with frequency below 5 mHz can propagate upward and they have more power at the formation height of the Fe I line. Although in the real sunspot there are some propagation of low frequency energy at the photospheric layers, this difference does not affect the balance of energy at the higher layers, since in both, the simulations and the observations, only the waves with frequency above 6 mHz reach the chromosphere (Figure 7.20).

During the travel of high frequency waves to high layers their amplitude increases due to

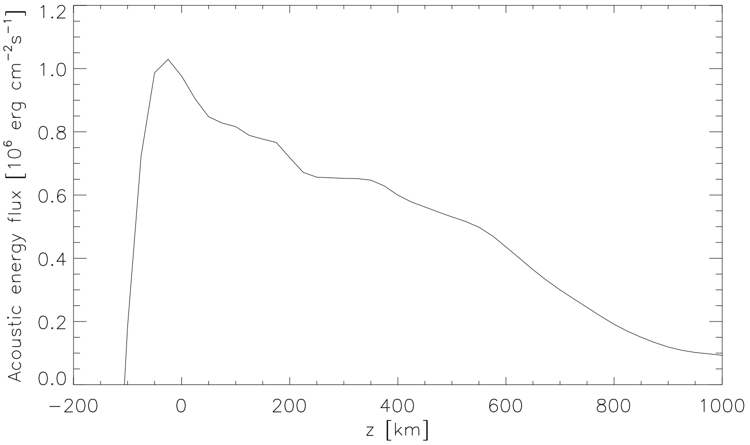

Figure 7.25: Average acoustic energy flux inside the umbra in the simulation.

the drop of the density and they develop into shocks with peak-to-peak amplitudes around 8 km s^{-1} at the formation height of the Ca II H core and the He I line. These waves supply energy to the chromosphere, but, is this acoustic energy enough to balance the radiative losses of the chromosphere? According to Withbroe & Noyes (1977), the radiative energy losses in the chromosphere of active regions amount to 2×10^7 erg cm^{-2} s^{-1}, and these losses should be balanced by some energy source. Figure 7.25 illustrates the variation of the acoustic flux with height, which was calculated following Equation (5.6) and was averaged in time for all points inside the umbra at the stationary stage of simulations. At the position of the driver it reaches 10^6 erg cm^{-2} s^{-1} and then decreases with height. It shows a steep decrease at $z = 200$ km, where the cutoff frequency reaches its maximum value. The acoustic flux presents important variations with time. For example, Figure 7.26 shows the temporal evolution of the acoustic flux inside the umbra at the formation height of the He I line. Positive values (shaded in white) represent upward flux. The wavefronts of the slow acoustic waves in the 6 mHz band are accompanied by acoustic energy which reaches almost 5×10^6 erg cm^{-2} s^{-1} for the strongest shocks. The average value of the acoustic flux at this height is 3×10^5 erg cm^{-2} s^{-1}, which is two orders of magnitude below the required value to balance the radiative losses. Only at the moments when shocks reach the chromosphere the energy supplied by the slow acoustic waves is close to the chromospheric radiative losses, being half of its value.

7.6 Discussion and conclusions

We have presented numerical simulations which closely reproduce the real wave propagation observed in the umbra of a sunspot on 2007 August 28. The analysis of these observations was done in Chapter 6. As is proved in Chapter 5, our code is able to manage the propagation of waves with long realistic periods, even in the hard conditions imposed by the high Alfvén speed at the sunspot chromosphere.

The similarity between the simulations and the observations is achieved in two steps. Firstly, we have contructed a MHS model of a sunspot with the properties of the observed

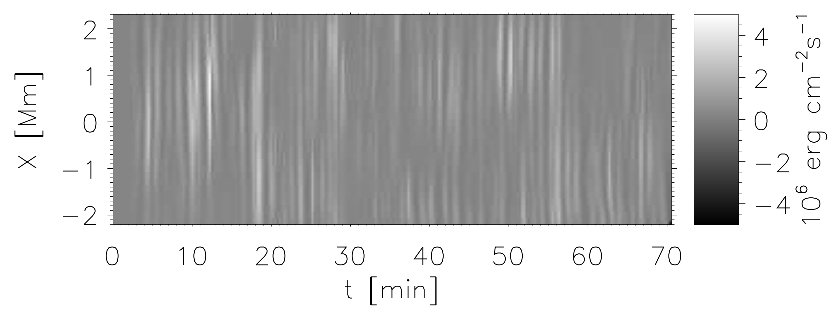

Figure 7.26: Acoustic energy flux map. Positive values (white) indicate upward flux.

one. We have followed the methods described in Khomenko & Collados (2008), but introduced some modifications in order to take into account some of the atmospheric properties of the sunspot retrieved from the inversion of the Si I line. This static model is perturbed by a force which drives a vertical velocity similar to the LOS velocity measured from the Doppler shift of the Si I line. This force is imposed around the estimated formation height of the photospheric Si I line. We have discussed several methods to infer the force driver which best matches the observed velocity.

Once the observed velocity is introduced in the MHS atmosphere, it mainly drives slow acoustic waves in the low-β region. Most of their power is concentrated in the 5 minute band, with frequencies between 3 and 4 mHz, and they form standing waves due to the higher cutoff frequency of the atmosphere. The driver also generates high frequencies waves, which propagate upward to the chromosphere. In their travel through the sunspot atmosphere, they reach the formation height of several observed spectral lines. The simulated velocity maps and power spectra at their corresponding formation heights reproduce reasonably well those obtained for the chromospheric Ca II H core and He I line. In the case of the Fe I λ 3969.3 line, the comparison is hindered due to the poor quatility of the observed velocity map, but it presents some differences in the power spectra. The fact that the simulated power spectra has lower power than the observational one for frequencies below 5 mHz, while the opposite is valid for frequencies above it, indicates that the real stratification of the sunspot may produce a lower cutoff frequency than the one corresponding to the MHS model at these photospheric layers. However, since the power at the chromospheric lines peaks at 6 mHz, we expect that the maximum value that the cutoff frequency reaches in the real sunspot agrees with the 6 mHz obtained for the MHS model.

The comparison between the simulated and observed velocity maps at chromospheric heights reveals some phase delay at the strongest wavefronts, in the sense that the observed wavefronts lag the simulated ones. In the case of the Ca II H core the phase lag is 0.4π, but the delay between the observed and simulated He I velocities is smaller. These delay, together with the higher amplitude of the observed strongest shocks, indicates that in the dynamical sunspot chromosphere the nonlinear waves shift the formation height of spectral lines to higher layers, specially the Ca II H core. In the analysis of these simulations, we have chosen a certain height representative of the layer from which the information about the velocity measured with the observed line comes. Obviously, this procedure is a simplification, since the contribution function from every spectral line spans over a thick layer. The height that we are considering corresponds to the average height derived in Chapter 6. This approximation seems to be good for the photospheric lines, but not for the highly nonlinear chromospheric region.

Our simulations reproduce the phase and amplification spectra between several pairs of lines with a remarkable match. For those spectra between a photospheric and a chromospheric signal, the phase difference shows stationary waves with $\Delta\phi = 0$ below 4 mHz, and at higher frequencies they progressively develop propagating waves, whose $\Delta\phi$ increases with the frequency. This empirical cutoff is assigned from the estimation of the frequency at which the phase difference starts to depart from $\Delta\phi = 0$. In the solar atmosphere, the cutoff is a local parameter which depends on the temperature and is stratificated with height. In our MHS model its maximum value is 6 mHz, and only waves with frequencies above this value can propagate all over the atmosphere. However, in most of the atmosphere the local cutoff is below 6 mHz, and for this reason the phase difference spectra show propagation for frequencies in the range between 4 and 6 mHz.

The only strong discrepancy is found in the amplification spectra at frequencies above 8 mHz (Figures 7.22 and 7.24). The amplification is cleary higher in the simulation than in the observations, and the observed power spectra of the chromospheric lines show lower power than the simulated equivalent (Figure 7.20). There are several causes that could account for this discrepancy. The comparison of the power spectra of the velocity retrieved from the Si I line and the one obtained in the simulation at its formation height (middle panel of Figure 7.15) shows some slight differences which are specially significant above 8 mHz. Since the amplitude of the waves increases exponentially with height, these small discrepancies could be the origin of the larger ones that appear at greater heights. For example, Figure 7.15 shows that the simulation has an excess of power at the height of the driver at 13 mHz and 17 mHz, and these frequencies also present higher power than the observations at the chromosphere (Figure 7.20). However, some frequencies where the power of the photospheric velocity in the simulation is not higher than the power of the Si I line also present a significative difference at higher layers. It is possible that all the power generated by the driver (which match the power obtained in the observations) does not correspond to real photospheric oscillations, but it is introduced by some observational limitations. In this case, the simulation would propagate upward some oscillatory power which is not present in the Sun, and although it vanishes at deep layers, its contribution in the chromosphere is important. Another possible cause of the different power of the high frequency waves at the chromosphere is the simple energy exchange implemented in this simulation. A more realistic method could produce a stronger radiative damping of the high frequency waves.

The analysis of the energy flux carried by magnetoacoustic waves to high layers reveals that it is not enough to heat the chromosphere. The energy supplied by slow acoustic waves is 70 times lower than the amount required to balance the radiative losses. Moreover, the simulation overestimates the power of the waves with frequencies between 8 and 20 mHz at the chromosphere, and the contribution of waves to chromospheric heating in sunspot could be even lower. In this simulation we have rejected the waves with frequencies above 20 mHz. According to Fossum & Carlsson (2005) and Carlsson et al. (2007) their power can be assumed to be negligible for chromospheric heating, but Wedemeyer-Böhm et al. (2007) and Kalkofen (2007) have pointed out that this question depends on the spatial resolution of the data used.

Previous works have found that the acoustic wave energy is too low, by a factor of at least ten, to balance the radiative losses in the non-magnetic solar chromosphere (Fossum & Carlsson 2005; Carlsson et al. 2007). The fraction of the required energy supplied by acoustic waves in the magnetized atmosphere of a sunspot seems to be even lower. The chromospheric energy losses in active regions are 5 times higher than in quiet Sun. Not only the acoustic wave flux is unable to balance this extra needed energy, but also the energy supplied by these waves in the sunspot atmosphere is scarcer. At the photosphere, the surface amplitude of solar p-modes in magnetic regions are reduced below those in magnetically quiet regions in the 5 minute band (Woods & Cram 1981). Brown et al. (1992) showed that the suppression is frequency dependent, peaking at 4 mHz. The reduction of the amplitude occurs for frequencies below 5 mHz, while the amplitude of waves above 5.5 mHz is enhanced. Since the waves that propagate energy to higher layers are those above the cutoff frequency, the reduction of p-modes in regions of magnetic activity does not explain the lower efficience of acoustic energy propagation in sunspots. In Chapter 5, we have found that the fast magnetic mode in the low-β region is reflected back toward the photosphere and it is unable to supply energy to higher layers. This result agrees with previous numerical calculations (Khomenko & Collados 2006). According to Cally (2005), the fast-to-fast conversion is more efficient for higher frequencies and, thus, waves with frequencies above the cutoff are significantly transformed into fast magnetic waves above the height where $v_A = c_S$ and cannot carry energy to the chromosphere. The LOS velocity oscillations measured with the Si I line correspond to the slow acoustic waves in the low-β region, after the transformation of the upward propagating waves. Their power has already been reduced by the transformation to the fast magnetic mode. Figure 7.25 shows that at the formation height of the Si I line the average acoustic energy flux is around 10^6 erg cm^{-2} s^{-1}, so even at this photospheric height the energy contained in form of acoustic flux is too low to supply the amount required by the chromospheric radiative losses. This case differs from the quiet Sun, where the acoustic wave energy is found to be enough to maintain the temperature stratification until a height of 500 km (Beck et al. 2009).

8

Conclusions and future prospects

In this thesis we have investigated the propagation of waves in sunspots using observations and numerical simulations. From the analysis of this data set we retrieve a coherent picture of the oscillations between the photosphere and the chromosphere of sunspots, and we are able to evaluate the different wave modes involved and their energy contribution, model and reproduce numerically several observed features, and infer the properties of the sunspot atmosphere. The conclusions are summarized in the next section, while in Section 8.2 we briefly present the future steps which could be performed as a continuation of this work.

8.1 Conclusions

Mode transformation in 3D numerical simulations

We have performed a set of numerical simulations with several drivers, which differ in their location and temporal behavior. Our main findings can be summarized as follows:

- The driver located in the gas pressure dominated region generates mostly a fast acoustic mode. This mode, propagating to the upper layers, is transformed at the height where $c_S = v_A$. After the transformation, a slow acoustic mode propagates upward along the field lines in the magnetically dominated atmosphere. The fast magnetic mode undergoes refraction and it is reflected back to the sub-photosphere. When it reaches again the surface $c_S = v_A$, new transformations take place producing other fast acoustic and slow magnetic modes in the region $v_A < c_S$.

- We have been able to identify an Alfvén mode. This mode appears only in the simulations with the source located away from the sunspot axis. The transformation efficiency from the fast to the Alfvén mode is much lower than that from the fast to the slow mode.

- The analysis of the wave energy fluxes suggests that in the high-frequency cases (above the cutoff) the wave energy can reach the upper atmosphere most efficiently in the form of slow (acoustic) field aligned propagating waves. After some height in the middle photosphere there is no magnetic flux corresponding to the fast (magnetic) waves as their energy is reflected. If the driver is located away from the axis, some small part of the energy also can propagate upward in the form of an Alfvén wave.

- Both magnetic and acoustic energy of the low-frequency waves (smaller than the cutoff) remain almost completely below the level $c_S = v_A$ and do not reach upper layers. This happens because the energy of the fast magnetic modes in the upper layers is reflected, and the evanescent acoustic slow modes do not propagate any energy at these frequencies.

- Simulations with a driver which excites a spectrum of waves reproduce the observed change of the dominant frequency of oscillations with height from the photosphere to the chromosphere. Waves with frequency below the cutoff value are evanescent in the atmosphere, while at higher frequencies the waves can propagate upward along the field lines. Due to the larger amplitude increase with height of the propagating waves compared to the evanescent waves, the 3 minute waves dominate the power spectrum in the chromosphere.

- The dominant wave frequency in the chromosphere decreases with the radial distance, due to the reduction of the cutoff frequency far from the axis.

Multi-layer observations of waves

We have presented an analysis of the LOS velocities obtained from at set of spectropolarimetric data in the near-IR spectral region around 10830 Å and the optical region around 3969 Å in a sunspot atmosphere and its vicinity. We have extracted the following conclusions:

- The phase difference spectra of LOS velocities between several pairs of lines show upward propagating waves for frequencies higher than 4 mHz. The power at lower frequencies does not propagate up, since waves with these frequencies are evanescent. The slope of the phase spectra, together with the histograms of LOS velocity, allows us to sort all the spectral lines used in this work by their formation height.

- Phase and amplification spectra were fitted to a model of linear wave propagation in a stratified atmosphere with radiative losses following the Newton cooling law. The model works reasonably well at layers below the formation height of the Ca II H line core, where waves propagate in a linear regime, while it fails in the fit of the amplification spectrum between the He I velocity and the Ca II H line core velocity due to the importance of nonlinearities at these chromospheric heights.

- From the fit to the model we retrieved the temperature, the difference in geometrical height between the formation heights of pairs of spectral lines, and the radiative relaxation time. The obtained values agree with previous estimations of the formation heights and with the stratification of a standard model of sunspot.

- The maximum of the power spectra is not gradually shifted from 3.5 mHz at the photosphere to higher frequencies at larger heights, but the photospheric and chromospheric group of lines show a discontinuous behavior. This phenomenon is also shown by the numerical simulations.

- High-frequency waves prominent in the chromosphere have to be generated in the photosphere or below and their dominance at the chromospheric height is the result of their large amplitude increase, since the increase of their amplitude with height is faster than the one of evanescent waves below the cutoff.
- We observe a continuous field-aligned propagation of slow magneto-acoustic waves in the upper atmosphere of sunspot. These waves first reach the formation height of Si I, then the formation height of the Fe I lines from the Ca II H line wing located in the upper photosphere, then the formation height of the Ca II H line core, and finally that of the He I line. The propagation becomes non-linear at heights between the formation of Fe I lines and Ca II H line core.

Combination of observations and simulations

We have performed numerical simulations based on the observations analyzed in Chapter 6. These are the main achievements extracted from its study:

- We have constructed a magnetohydrostatic model which resembles in its properties the observed sunspot umbra. The analysis of wave propagation shows that the synthetic model accounts for the observed wave amplification, cutoff frequency, and velocity of propagation, although the stratification of the photospheric layers is not exactly corresponding to the observed sunspot.
- The simulation reproduces reasonably well the oscillations measured at different atmospheric heights, spanning from the photosphere to the chromosphere, where the observed wave pattern was obtained from the simultaneous observations in several spectral lines.
- The strongest shock waves shift the average response height to velocity perturbations of the chromospheric lines toward higher layers, specially the one of the Ca II H core.
- We identify high frequency propagating waves. The phase and amplification spectra obtained from the numerical simulation match with the observed one, and indicate that only waves with frequency above a 6 mHz can propagate upward through all the umbral atmosphere, while waves with frequency between 4 and 6 mHz can propagate at certain heights.
- The acoustic energy flux supplied by the slow mode high frequency waves is 70 times lower than the amount required to balance the chromospheric radiative losses in an active region. In sunspots the contribution of acoustic waves to the chromospheric heating is even lower than in quiet Sun regions.

8.2 Future prospects

The results presented in this thesis shed light upon the issue of wave propagation in realistic magnetized atmospheres with the observed periods, and allow us for the first time to perform a direct comparison with observations. Future steps to go beyond these results can be divided in two different kinds. Firstly, we aim to improve the numerical code introducing the following modifications:

- Include a more detailed physical description in the solution of the equations. The code uses as equation of state a simple ideal gas equation, and the energy exchange is implemented with the approximation of Newton's cooling law. Both approaches seem to be a poor simplification of the physics of stellar atmospheres, specially at the chromosphere. At this height, the effects of partial ionization should be taken into account by the introduction of a pretabulated equation of state. The energy exchange should also be improved by including realistic opacities from several atomic species.
- The top boundary condition is a hard challenge for wave propagation simulations, and the extremely high Alfvén speed at the chromosphere of active regions hinders the obtaining of stable and long enough simulations. The PML boundary has proven to be a good solution, but for the study of some cases we need to reach a better performance.

Secondly, we have the subsequent scientific objetives:

- We plan to develop new simulations with different driving conditions and exciting other magnetic structures. In the present work we have obtained a very inefficient conversion from slow to Alfvén modes. According to Cally & Goossens (2008), at some inclination angles the transformation into the Alfvén wave is even more important than the fast-to-slow transformation. With the configuration of the simulations that we have studied, the energy transported by the Alfvén mode is negligible. However, in magnetic field structures with different topology, or using different drivers, new Alfvén like modes can appear, such as kink and sausage modes in flux tubes.
- The study of velocity oscillations measured at the photosphere and the chromosphere for structures with different size and magnetic fluxes (large spots, small spots, pores and facuale) performed by Centeno et al. (2009) has revealed an intrinsic difference between all these features. These results were obtained only for two reference spectral lines, the Si I and the He I lines in the 10830 Å spectral region, which does not allow them to trace continuously the properties of waves with height. We aim to repeat the same kind of observations, including the Ca II H line (and its accompanying Fe I lines) with POLIS. However, the low solar activity during the period of this thesis has prevented us from obtaining such observations until present.
- The code is also suitable for local helioseismic purposes. The intepretation of the full wave field observed around active regions is one of the greatest challenges for local helioseismology. Numerical modeling is the ideal tool to complement the observations obtained with new observing facilities, like the Helioseismic and Magnetic Imager (HMI) instrument which was launched recently on-board Solar Dynamics Observatory (SDO).

9

Conclusiones y perspectivas futuras

En esta tesis hemos investigado la propagación de ondas en manchas solares utilizando observaciones y simulaciones numéricas. Del análisis de este conjunto de datos hemos obtenido una escena coherente de las oscilaciones entre la fotosfera y la cromosfera de manchas solares, y hemos podido evaluar los diferentes modos de onda involucrados, modelar y reproducir numéricamente varios rasgos observacionales e inferir las propiedades de la atmósfera de la mancha. La siguiente sección resume las conclusiones, mientras que en la Sección 9.2 presentamos brevemente futuros pasos que se podrían realizar como continuación de este trabajo.

9.1 Conclusiones

Transformación de modos en simulaciones numéricas en 3D

Hemos realizado un conjunto de simulaciones numéricas con varias fuerzas excitadoras, que se diferencian en su posición y comportamiento temporal. Nuestros principales hallazgos pueden ser resumidos como se muestra a continuación:

- La fuerza excitadora situada en la región dominada por la presión del gas genera principalmente un modo acústico rápido. Este modo, que se propaga hacia capas superiores, se transforma a la altura donde la velocidad del sonido (c_S) y la velocidad Alfvén (v_A) son iguales. Después de la transformación, un modo acústico lento se propaga hacia arriba a lo largo de las líneas de campo en la región de la atmósfera dominada por el campo magnético. El modo magnético rápido es refractado y se dirige nuevamente hacia la fotosfera. Cuando alcanza otra vez la superficie $c_S = v_A$ aparecen nuevas transformaciones, produciendo otros modos acústico rápido y magnético lento en la región $v_A < c_S$.
- Hemos podido indentificar el modo Alfvén. Este modo aparece sólo en las simulaciones con la fuente situada fuera del eje de la mancha. La eficiencia de la transformación del modo rápido al Alfvén es mucho más baja que la del modo rápido al lento.
- El análisis del flujo de energía sugiere que en los casos de ondas con frecuencias altas (por encima de la frecuencia de corte) la energía de la onda puede alcanzar la parte alta

de la atmósfera más eficientemente en forma de ondas acústicas lentas propagándose a lo largo de las líneas de campo. Por encima de una cierta altura en la fotosfera media no hay flujo magnético correspondiente a las ondas magnéticas rápidas, debido a que su energía es reflejada. Si la fuerza excitadora está situada fuera del eje, una pequeña parte de la energía se puede propagar hacia arriba en forma de onda Alfvén.

- Tanto la energía magnética como la acústica de la ondas con baja frecuencia (más baja que la frecuencia de corte) se quedan casi completamente por debajo de la altura donde $c_S = v_A$ y no alcanzan capas superiores. Esto sucede debido a que la energía del modo magnético rápido en las capas superiores es reflejado, mientras que el modo acústico lento es evanescente y no propaga energía a estas frecuencias.

- Las simulaciones en las que actúa como fuerza excitadora un espectro de ondas con diferentes frecuencias reproducen el cambio observado con la altura en la frecuencia dominante de las oscilaciones. Las ondas cuya frecuencia es inferior a la frecuencia de corte son evanescentes, mientras que las frecuencias más altas se pueden propagar hacia arriba a lo largo de las líneas de campo. Debido al mayor incremento de la amplitud con la altura de las ondas que se propagan en comparación con las ondas evanescentes, las ondas de 3 minutos de periodo dominan el espectro de potencias en la cromosfera.

- La frecuencia dominante en la cromosfera disminuye con la distancia radial, debido a la reducción del valor de la frecuencia de corte lejos del eje de la mancha.

Observaciones de ondas en diferentes alturas

Hemos presentado un análisis de la velocidad en la líneas de visión de un conjunto de datos espectropolarimétricos en la región del infrarrojo cercano en torno a 10830 Å y en la región visible alrededor de 3969 Å en la atmosfera de una mancha solar y sus alrededores. Hemos extraído las siguientes conclusiones:

- El espectro de diferencia de fase de la velocidad en la línea de visión entre varios pares de líneas muestra propagación de ondas hacia arriba para frecuencias superiores a 4 mHz. La potencia a frecuencias más bajas no se propaga hacia arriba, ya que las ondas con estas frecuencias son evanescentes. La pendiente del espectro de diferencia de fase, junto con los histogramas de velocidad en la líneas de visión, nos permite ordenar según su altura de formación todas las líneas spectrales utilizadas en este trabajo.

- Los espectros de diferencia de fase y de amplificación fueron ajustados con un modelo de propagación lineal de ondas en una atmósfera estratificada con pérdidas radiativas siguiendo la ley de enfriamiento de Newton. El modelo funciona razonablemente bien en capas por debajo de la altura de formación del núcleo de la línea de Ca II H, mientras falla en el ajuste del espectro de amplificación entre las velocidades medidas con el He I y el núcleo de la línea de Ca II H debido a la importancia de las no linealidades a estas alturas cromosféricas.

- Del ajuste al modelo obtenemos la temperatura, la diferencia en altura geométrica entre la altura de formación de ambas línas espectrales y el tiempo de relajación radiativo. Los valores obtenidos muestran un buen acuerdo con estimaciones previas de las alturas de formación y con la estratificación de un modelo estándar de mancha solar.

- El máximo del espectro de potencias no se desplaza gradualmente de 3.5 mHz en la fotosfera hacia frecuencias más altas en alturas superiores, sino que los conjuntos de líneas fotosféricas y cromosféricas muestran un comportamiento discontinuo. Las simulaciones numéricas también muestran este fenómeno.

- Las ondas de alta frecuencia que dominan en las capas cromosféricas deben ser generadas en la fotosfera o a mayor profundidad, y su importancia en la cromosfera es el resultado de su gran incremento de amplitud, dado que el aumento de su amplitud con la altura es más rápido que el correspondiente a ondas evanescentes con frecuencia inferior a la de corte.

- Observamos una propagación continua de ondas magneto-acústicas lentas en la atmósfera de la mancha solar. Estas ondas primero alcanzan la altura de formación del Si I, luego la de las líneas de Fe I de las alas de la líneas de Ca II H que se forman en la alta fotosfera, a continuación la altura de formación del núcleo de la líneas de Ca II H y finalmente la de He I. La propagación se vuelve no lineal a una cierta altura entre la formación de las líneas de Fe I y el núcleo de la línea de Ca II H.

Combinación de las observaciones y las simulaciones

Hemos realizado simulaciones numéricas basadas en las observaciones analizadas en el Capítulo 6. Estos son los principales logros extraídos de su estudio:

- Hemos construido un modelo magnetohidrostático con las propiedades de la umbra de la mancha observada. El análisis de la propagación de ondas muestra que el modelo sintético da cuenta de la amplificación de la onda, la frecuencia de corte y la velocidad de propagación, aunque la estratificación de las capas fotosféricas no es exactamente la que corresponde a la mancha solar observada.

- La simulación reproduce razonablemente bien las oscilaciones medidas a diferentes alturas atmosféricas, desde la fotosfera hasta la cromosfera, donde el patrón de ondas observado fue obtenido a partir de la observación simultánea de varias líneas espectrales.

- Las ondas de choque más fuertes desplazan la altura de repuesta promedio a perturbaciones en la velocidad de las líneas cromosféricas hacia capas más altas, especialmente en el caso del núcleo de la línea de Ca II H.

- Identificamos propagación de ondas de alta frecuencia. Los espectros de fase y de amplificación obtenidos a partir de la simulación numérica se ajustan a los observados, e indican que sólo las ondas con frequencia superior a 6 mHz pueden propagarse hacia arriba a través de toda la atmósfera de la umbra, mientras las ondas con frecuencia entre 4 y 6 mHz se pueden propagar a determinadas alturas.

- El flujo de energía acústico suministrado por las ondas de alta frecuencia correspondientes al modo lento es 70 veces inferior a la cantidad necesaria para compensar las pérdidas radiativas de la cromosfera en regiones activas. En manchas solares la contribución de las ondas acústicas al calentamiento cromosférico es incluso inferior a la de regiones de Sol en calma.

9.2 Perspectivas futuras

Los resultados presentados en esta tesis ayudan a esclarecer el estudio de la propagacion de ondas en atmósferas magnetizadas realistas con los periodos observados, y nos permiten realizar una comparación directa con observaciones. Los futuros pasos para profundizar en este temar se pueden dividir en dos tipos. En primer lugar, pretendemos mejorar el código numérico introduciendo las siguientes modificaciones:

- Incluir una descripción física más detallada en la resolución de las equaciones. El código utiliza como ecuación de estado la ley de los gases ideales, y el intercambio de energía está implementado con la aproximación de la ley de enfriamiento de Newton. Ambos son una simplificación pobre de la física de atmósferas estelares, especialmente en la cromosfera. A esta altura, los efectos de la ionización parcial deben ser tenidos en cuenta mediante la introducción de una ecuación de estado pretabulada. El intercambio de energía también debe ser mejorado incluyendo las opacidades realistas de varias especies atómicas.
- La condición de contorno superior es un reto duro para las simulaciones de propagación de ondas, y la extremadamente alta velocidad Alfvén en la cromosfera de regiones activas dificulta la obtención de simulaciones estables y suficientemente largas. La capa PML ha demostrado ser una buena solución, pero para el estudio de algunos casos necesitamos alcanzar un mejor rendimiento.

En segundo lugar, tenemos los siguientes objetivos científicos:

- Planeamos obtener nuevas simulaciones con diferentes condiciones de excitación y en otras estructuras magnéticas. En este trabajo hemos obtenido una conversión muy ineficiente entre los modos lento y Alfvén. De acuerdo con Cally & Goossens (2008), a determinados ángulos de inclinación la transformación al modo Alfvén es incluso más importante que la transformación de rápido a lento. Con la configuración de las simulaciones que hemos estudiado, la energía transportada por el modo Alfvén es despreciable. Sin embargo, en estructuras magnéticas con diferente topología, o utilizando diferentes perturbaciones excitadoras, aparecen nuevos modos Alfvén, como los modos “kink” y “salchicha” en tubos de flujo.
- El estudio de las oscilaciones de velocidad medidas en la fotosfera y la cromosfera para estructuras con diferente tamaño y flujos magnéticos (manchas grandes y pequeñas, poros y fáculas) realizado por Centeno et al. (2009) ha revelado una diferencia intrínseca entre todas estas estructuras. Estos resultados fueron obtenidos únicamente para dos líneas espectrales de referencia, las líneas de Si I y He I de la región

espectral de 10830 Å, lo que no les permite trazar continuamente las propiedades de las ondas con la altura. Pretendemos repetir el mismo tipo de observaciones, incluyendo la línea de Ca II H (y las líneas de Fe I que la acompañan) medida con POLIS. Sin embargo, la baja acividad solar existente durante el periodo de esta tesis ha evitado que obtengamos estas observaciones.

- El código también puede ser utilizado para estudios de helioseismología local. La interpretación del campo de ondas observado alrededor de regiones activas es uno de los grandes retos de la helioseismología local. El modelado numérico es la herramienta ideal para complementar las observaciones obtenidas con nuevas facilidades observacionales, como el instrumento Helioseismic and Magnetic Imager (HMI) que fue lanzado recientemente a bordo de Solar Dynamics Observatory (SDO).

Bibliography

Abdelatif, T. E., Lites, B. W., & Thomas, J. H. 1986, ApJ, 311, 1015

Avrett, E. H. 1981, in The Physics of Sunspots, ed. L. E. Cram & J. H. Thomas, 235–255

Balsara, D. S. & Spicer, D. S. 1999, J. Comp. Phys., 149, 270

Balthasar, H., Schleicher, H., Bendlin, C., & Volkmer, R. 1996, A&A, 315, 603

Balthasar, H. & Wiehr, E. 1984, Sol. Phys., 94, 99

Bard, S. & Carlsson, M. 2008, ApJ, 682, 1376

Beck, C., Khomenko, E., Rezaei, R., & Collados, M. 2009, A&A, 507, 453

Beck, C., Schlichenmaier, R., Collados, M., Bellot Rubio, L., & Kentischer, T. 2005a, A&A, 443, 1047

Beck, C., Schmidt, W., Kentischer, T., & Elmore, D. 2005b, A&A, 437, 1159

Beck, C., Schmidt, W., Rezaei, R., & Rammacher, W. 2008, A&A, 479, 213

Beckers, J. M. & Tallant, P. E. 1969, Sol. Phys., 7, 351

Bellot Rubio, L. R., Balthasar, H., Collados, M., & Schlichenmaier, R. 2003, A&A, 403, L47

Bellot Rubio, L. R., Collados, M., Ruiz Cobo, B., & Rodríguez Hidalgo, I. 2000, ApJ, 534, 989

Berenger, J. P. 1994, Journal of Computational Physics, 114, 185

Berenger, J. P. 1996, Journal of Computational Physics, 127, 363

Biermann, L. 1948, ZAp, 25, 161

Bloomfield, D. S., Lagg, A., & Solanki, S. K. 2007, ApJ, 671, 1005

Bogdan, T. J., Carlsson, M., Hansteen, V. H., et al. 2003, ApJ, 599, 626

Bogdan, T. J. & Judge, P. G. 2006, Royal Society of London Philosophical Transactions Series A, 364, 313

Bogdan, T. J., Rosenthal, C. S., Carlsson, M., et al. 2002, Astronomische Nachrichten, 323, 196

Bray, R. J. & Loughhead, R. E. 1974, The solar chromosphere, ed. Bray, R. J. & Loughhead, R. E.

Brio, M. & Wu, C. 1988, J. Comp. Phys., 75, 400

Brown, T. M., Bogdan, T. J., Lites, B. W., & Thomas, J. H. 1992, ApJ, 394, L65

Brynildsen, N., Maltby, P., Fredvik, T., & Kjeldseth-Moe, O. 2002, Sol. Phys., 207, 259

Brynildsen, N., Maltby, P., Leifsen, T., Kjeldseth-Moe, O., & Wilhelm, K. 2000, Sol. Phys., 191, 129

Cally, P. S. 1995, ApJ, 451, 372

Cally, P. S. 2005, MNRAS, 358, 353

Cally, P. S. 2006, Royal Society of London Philosophical Transactions Series A, 364, 333

Cally, P. S. & Bogdan, T. J. 1997, ApJ, 486, L67

Cally, P. S. & Goossens, M. 2008, Sol. Phys., 251, 251

Cameron, R., Gizon, L., & Daiffallah, K. 2007, Astronomische Nachrichten, 328, 313

Cameron, R., Gizon, L., & Duvall, Jr., T. L. 2008, Sol. Phys., 251, 291

Cargill, P. J., Spicer, D. S., & Zalesak, S. T. 1997, ApJ, 488, 854

Carlsson, M., Hansteen, V. H., de Pontieu, B., et al. 2007, PASJ, 59, 663

Carlsson, M. & Stein, R. F. 1997, ApJ, 481, 500

Caunt, S. E. & Korpi, M. J. 2001, A&A, 369, 706

Centeno, R., Collados, M., & Trujillo Bueno, J. 2006, ApJ, 640, 1153

Centeno, R., Collados, M., & Trujillo Bueno, J. 2009, ApJ, 692, 1211

Centeno, R., Socas-Navarro, H., Collados, M., & Trujillo Bueno, J. 2005, ApJ, 635, 670

Centeno, R., Trujillo Bueno, J., Uitenbroek, H., & Collados, M. 2008, ApJ, 677, 742

Christensen-Dalsgaard, J., Dappen, W., Ajukov, S. V., & 30 co-authors. 1996, Science, 272, 1286

Collados, M., del Toro Iniesta, J. C., & Vazquez, M. 1988, A&A, 195, 315

Collados, M., Lagg, A., Díaz Garcí A, J. J., et al. 2007, in Astronomical Society of the Pacific Conference Series, Vol. 368, The Physics of Chromospheric Plasmas, ed. P. Heinzel, I. Dorotovič, & R. J. Rutten, 611

Dai, W. & Woodward, P. R. 1998, ApJ, 494, 317

Duvall, Jr., T. L., Jefferies, S. M., Harvey, J. W., & Pomerantz, M. A. 1993, Nature, 362, 430

Ferraro, C. A. & Plumpton, C. 1958, ApJ, 127, 459

Filippenko, A. V. 1982, PASP, 94, 715

Fossum, A. & Carlsson, M. 2005, Nature, 435, 919

Giovanelli, R. G. 1972, Sol. Phys., 27, 71

Giovanelli, R. G., Harvey, J. W., & Livingston, W. C. 1978, Sol. Phys., 58, 347

Gizon, L. & Birch, A. C. 2005, Living Reviews in Solar Physics, 2, 6

Goldreich, P. & Keeley, D. A. 1977, ApJ, 211, 934

Goldreich, P. & Kumar, P. 1988, ApJ, 326, 462

Goldreich, P. & Kumar, P. 1990, ApJ, 363, 694

Gurman, J. B. & Leibacher, J. W. 1984, ApJ, 283, 859

Hammerschlag, R. H. & Bettonvil, F. C. M. 1998, , 42, 485

Hanasoge, S. M. 2008, ApJ, 680, 1457

Hasan, S. S., Kalkofen, W., van Ballegooijen, A. A., & Ulmschneider, P. 2003, ApJ, 585, 1138

Hasan, S. S. & Ulmschneider, P. 2004, A&A, 422, 1085

Hasan, S. S., van Ballegooijen, A. A., Kalkofen, W., & Steiner, O. 2005, ApJ, 631, 1270

Hesthaven, J. S. 1998, J. Comp. Phys., 142, 129

Hill, F. 1988, ApJ, 333, 996

Hindman, B. W., Jain, R., & Zweibel, E. G. 1997, ApJ, 476, 392

Hu, F. Q. 1996, Journal of Computational Physics, 129, 201

Hu, F. Q. 2001, J. Comp. Phys., 173, 455

Kalkofen, W. 2007, ApJ, 671, 2154

Khomenko, E. 2009, ASPCS, 416

Khomenko, E. & Collados, M. 2006, ApJ, 653, 739

Khomenko, E. & Collados, M. 2008, ApJ, 689, 1379

Khomenko, E. & Collados, M. 2009, A&A, 506, L5

Khomenko, E., Collados, M., & Felipe, T. 2008, Sol. Phys., 251, 589

Khomenko, E., Kosovichev, A., Collados, M., Parchevsky, K., & Olshevsky, V. 2009, ApJ, 694, 411

Khomenko, E. V., Collados, M., & Bellot Rubio, L. R. 2003, ApJ, 588, 606

Kneer, F., Mattig, W., & v. Uexkuell, M. 1981, A&A, 102, 147

Kobanov, N. I. 1990, Sol. Phys., 125, 25

Kobanov, N. I. & Makarchik, D. V. 2004, A&A, 424, 671

Kosovichev, A. G., Duvall, Jr., T. L. ., & Scherrer, P. H. 2000, Sol. Phys., 192, 159

Kostyk, R. I. & Khomenko, E. V. 2002, Astronomy Reports, 46, 925

Krijger, J. M., Rutten, R. J., Lites, B. W., et al. 2001, A&A, 379, 1052

Kumar, B., Jain, R., Tripathy, S. C., Vats, H. O., & Deshpande, M. R. 2000, Sol. Phys., 191, 293

Lindsey, C. & Braun, D. C. 1990, Sol. Phys., 126, 101

Lites, B. W. 1984, ApJ, 277, 874

Lites, B. W. 1986, ApJ, 301, 1005

Lites, B. W. 1988, ApJ, 334, 1054

Lites, B. W. 1992, in NATO ASIC Proc. 375: Sunspots. Theory and Observations, ed. J. H. Thomas & N. O. Weiss, 261–302

Lites, B. W., Rutten, R. J., & Kalkofen, W. 1993, ApJ, 414, 345

Lites, B. W. & Thomas, J. H. 1985, ApJ, 294, 682

Lites, B. W., Thomas, J. H., Bogdan, T. J., & Cally, P. S. 1998, ApJ, 497, 464

Lites, B. W., White, O. R., & Packman, D. 1982, ApJ, 253, 386

Liu, S. & Smith, E. V. P. 1972, Sol. Phys., 24, 301

Londrillo, P. & Del Zanna, L. 2000, ApJ, 530, 508

Low, B. C. 1975, ApJ, 197, 251

Low, B. C. 1980, Sol. Phys., 67, 57

Maltby, P., Avrett, E. H., Carlsson, M., et al. 1986, ApJ, 306, 284

Maltby, P., Brynildsen, N., Fredvik, T., Kjeldseth-Moe, O., & Wilhelm, K. 1999, Sol. Phys., 190, 437

Maltby, P., Brynildsen, N., Kjeldseth-Moe, O., & Wilhelm, K. 2001, A&A, 373, L1

Ruiz Cobo, B. & del Toro Iniesta, J. C. 1992, ApJ, 398, 375

Mihalas, D. & Mihalas, B. W. 1984, Foundations of Radiation Hydrodynamics (Oxford: Oxford University Press)

Moradi, H., Baldner, C., Birch, A. C., et al. 2009a, ArXiv e-prints

Moradi, H., Hanasoge, S. M., & Cally, P. S. 2009b, ApJ, 690, L72

Orszag, M. & Tang, C. 1979, J. Fluid Mech., 90, 129

Parchevsky, K., Kosovichev, A., Khomenko, E., Olshevsky, V., & Collados, M. 2010, ArXiv e-prints

Parchevsky, K. V. & Kosovichev, A. G. 2007, ApJ, 666, L53

Parchevsky, K. V. & Kosovichev, A. G. 2009, ApJ, 694, 573

Pizzo, V. J. 1986, ApJ, 302, 785

Rodríguez Hidalgo, I., Ruiz Cobo, B., Collados, M., & Bellot Rubio, L. R. 2001, ApJ, 547, 491

Rosenthal, C. S., Bogdan, T. J., Carlsson, M., et al. 2002, ApJ, 564, 508

Rouppe van der Voort, L. H. M., Rutten, R. J., Sütterlin, P., Sloover, P. J., & Krijger, J. M. 2003, å, 403, 277

Ryu, D., Jones, T. W., & Frank, A. 1995, ApJ, 452, 791

Scharmer, G. B., Bjelksjo, K., Korhonen, T. K., Lindberg, B., & Petterson, B. 2003, in Presented at the Society of Photo-Optical Instrumentation Engineers (SPIE) Conference, Vol. 4853, Society of Photo-Optical Instrumentation Engineers (SPIE) Conference Series, ed. S. L. Keil & S. V. Avakyan, 341–350

Scharmer, G. B., Pettersson, L., Brown, D. S., & Rehn, J. 1985, Appl. Opt., 24, 2558

Schlüter, A. & Temesváry, S. 1958, in Electromagnetic Phenomena in Cosmical Physics, ed. B. Lehnert, Vol. 6, International Astronomical Union. Symposium (Cambridge University Press), 263

Schunker, H. & Cally, P. S. 2006, MNRAS, 372, 551

Schwarzschild, M. 1948, ApJ, 107, 1

Shelyag, S., Fedun, V., & Erdélyi, R. 2008, A&A, 486, 655

Shibata, K. 1983, PASJ, 35, 263

Socas-Navarro, H., McIntosh, S. W., Centeno, R., de Wijn, A. G., & Lites, B. W. 2009, ApJ, 696, 1683

Socas-Navarro, H., Trujillo Bueno, J., & Ruiz Cobo, B. 2001, ApJ, 550, 1102

Sod, G. A. 1978, J. Comp. Phys., 27, 1

Spiegel, E. A. 1957, ApJ, 126, 202

Spruit, H. C. 1981, A&A, 98, 155

Stein, R. F. & Nordlund, Å. 1998, ApJ, 499, 914

Stix, M. 1989, The Sun. an Introduction, ed. Stix, M.

Stone, J. & Norman, M. 1992, ApJS, 80, 791

Terradas, J., Andries, J., Goossens, M., et al. 2008, ApJ, 687, L115

Thomas, J. H., Cram, L. E., & Nye, A. H. 1982, Nature, 297, 485

Thomas, J. H., Lites, B. W., Gurman, J. B., & Ladd, E. F. 1987, ApJ, 312, 457

Thomas, J. H. & Scheuer, M. A. 1982, Sol. Phys., 79, 19

Tóth, G. 1996, Astrophysical Letters Communications, 34, 245

Tziotziou, K., Tsiropoula, G., Mein, N., & Mein, P. 2006, A&A, 456, 689

Vernazza, J. E., Avrett, E. H., & Loeser, R. 1981, ApJS, 45, 635

Vögler, A., Shelyag, S., Schüssler, M., et al. 2005, A&A, 429, 335

von der Luehe, O., Soltau, D., Berkefeld, T., & Schelenz, T. 2003, in Proceedings of the SPIE, Vol. 4853, Innovative Telescopes and Instrumentation for Solar Astrophysics, ed. S. L. Keil & S. V. Avakyan, 187–193

Wedemeyer-Böhm, S., Steiner, O., Bruls, J., & Rammacher, W. 2007, in Astronomical Society of the Pacific Conference Series, Vol. 368, The Physics of Chromospheric Plasmas, ed. P. Heinzel, I. Dorotovič, & R. J. Rutten, 93–+

Westendorp Plaza, C., del Toro Iniesta, J. C., Ruiz Cobo, B., et al. 1997, Nature, 389, 47

Withbroe, G. L. & Noyes, R. W. 1977, ARA&A, 15, 363

Woods, D. T. & Cram, L. E. 1981, Sol. Phys., 69, 233

Zhugzhda, I. D. & Dzhalilov, N. S. 1982, A&A, 112, 16

Zhugzhda, I. D., Locans, V., & Staude, J. 1983, Sol. Phys., 82, 369

Zhugzhda, I. D., Locans, V., & Staude, J. 1985, A&A, 143, 201

Zhugzhda, Y. D. & Dzhalilov, N. S. 1984a, A&A, 132, 45

Zhugzhda, Y. D. & Dzhalilov, N. S. 1984b, A&A, 132, 52

Zirin, H. & Stein, A. 1972, ApJ, 178, L85+

Agradecimientos

En primer lugar, quiero agradecer a mis directores, Lena Khomenko y Manolo Collados, todo el tiempo que han compartido conmigo durante estos cuatro años de tesis, así como durante la beca de colaboración. Gracias por haberme introducido en el maravilloso mundo de la Física Solar y por guiarme a lo largo del camino que me ha conducido hasta la culminación de esta tesis. Ha sido un placer trabajar con ustedes, y espero que lo siga siendo en un futuro. También debo agradecer a Christian Beck, ya que sin sus consejos el capítulo 6 de esta tesis no sería lo que aquí aparece, y por la paciencia que tuvo para mostrarme en detalle el funcionamiento de la VTT. Gracias a Héctor Socas Navarro por haber aceptado la dura tarea de ejercer de revisor interno y por todas sus indicaciones. Sin duda, su contribución ha permitido mejorar la versión previa de este manuscrito. Y aunque no entienda lo que aquí se dice, gracias a Slavik por el tiempo que pasamos juntos en Tenerife, Oslo, Bochum, Friburgo y La Palma, y por todas las fructíferas charlas sobre nuestros respectivos códigos.

No puedo completar estos agradecimientos sin recordar a la gente con la que prácticamente he convivido durante los últimos cuatro años en el IAC y los cuatro años anteriores en la Facultad de Física. Aunque son demasiados para nombrarlos a todos, debo hacer una mención especial a Adal, Alberto, Ariadna, Christoph, Inés, Joni, Luisa y Manu, por todos los momentos que hemos pasado juntos en el despacho y la cafetería, o en las clases y prácticas de la universidad.

Y por último, pero más importante, gracias a mi familia. Sobre todo a mis padres, que aunque probablemente no entenderán ninguna de las 165 páginas anteriores, deben saber que este trabajo no habría sido posible sin la educación, ayuda y cariño que me han proporcionado durante estos 26 años. Gracias a Jonatán, con el que sorpredentemente apenas me he peleado a pesar de que se trata de mi hermano mayor, y a Esther, a la que ya considero parte de la familia. Y de forma especial, gracias a Mar. Porque has puesto tu granito de arena en esta tesis “obligándome” a trabajar un tiempo que yo no hubiese sido capaz de dedicarle por mi propia iniciativa. Por todo lo que has significado para mí durante los últimos 6 años y los 3 anteriores, aunque tú no lo supieses. Y por la suerte que he tenido al encontrarme contigo, que aunque mis limitaciones me impiden transmitirlo con palabras, humildemente me permito parafrasear a Carl Sagan para decirte que “en la inmensidad del espacio y el tiempo, mi alegría es haber compartido un lugar y una época contigo”. Espero que esta época continúe.